The Emission and Transport of Saharan Dust

James Richard Banks

Atmospheric, Oceanic, and Planetary Physics

Lincoln College, University of Oxford

Hilary 2010

Abstract

The Emission and Transport of Saharan Dust

James Richard Banks, Lincoln College, University of Oxford

A thesis submitted for the degree of Doctor of Philosophy

Hilary Term 2010

Tropospheric aerosols have a significant influence on climate and have been recognised by the Intergovernmental Panel on Climate Change as the biggest source of uncertainty in understanding future climate, even the factors controlling their spatial distribution remain unclear.

SHAMAL, a three-dimensional desert dust lifting and transport model, using meteorological fields from ECMWF analyses, is used to compare predicted mineral dust loading over the Sahara with observations of optical depth from AERONET ground stations, and from satellite instruments such as SEVIRI. The model is used to investigate the sensitivity of the predicted aerosol profiles to variations in model parameters, such as dust emission. Estimates of yearly dust activity are presented for the period of March 2006- February 2007. Total emissions from North Africa are estimated to be 1157 Tg, of which 1001 Tg are deposited by gravitational settling and turbulent deposition, and of which 45 Tg are deposited by precipitation scavenging. During the year, 62.0 Tg of dust were transported off the coast of West Africa into the Atlantic.

The period of March 2006 saw particularly intense dust storm activity. From the 6th March, a dust storm started to form in northern Algeria, which propagated south (and to the west and east) over the following two days. At its peak on the 8th March, the dust plume was observed to extend from the Atlantic off the coast of Western Sahara, through Mauritania, Mali and southern Algeria, to northern Niger. Using a data assimilation scheme, improved estimates can be made of dust transport during this event: for the 5 days of the 5th-9th March, 4.38±0.40 Tg of dust were transported off the coast of West Africa into the Atlantic, 70.2±9.6% of the total for March 2006.

Acknowledgements

First and foremost, I should thank my supervisors, Don Grainger and Martin Juckes, for all their help, advice, and time they have given me over the past three and a half years. Their detailed suggestions, comments and criticisms have been invaluable in helping me to motivate, produce and refine this work.

I have also received much advice from various people within EODG and AOPP. Special thanks must go to Elisa Carboni, Andy Sayer, and Gareth Thomas for their expertise in using and interpreting satellite data. Thanks also to the AERONET and DRI projects for their data.

The soil data was produced by Benoit Laurent at the Laboratoire Interuniversitaire des Systèmes Atmosphériques (LISA) in Paris, which has been enormously helpful in producing more accurate estimates of North African dust storms.

Crucially, I have been well served by the use of ECMWF operational analysis meteorological data: thanks go to ECMWF for producing such a complete and reliable data set. Thanks also to everybody at the BADC, for enabling me to access the ECMWF data, and for all their advice.

AOPP has been such an enjoyable place to work in- thanks to everybody here for all the good times. I should also thank all of my friends, in Oxford, London, and around the World, who have kept me sane for the last three and a half years!

I cannot forget the role that my parents have played in all this. My father will never have the chance to read this thesis, but I know that he would have been fascinated by it- my interest in studying the natural world has been inherited from him. Meanwhile, my mum has provided me with much love and support over the past 25 years- I simply could not have made it this far without her.

Finally, I am very grateful to the Natural Environment Research Council (NERC), which has provided the financial backing for this project, without which this thesis could not have been produced.

Contents

1 Introduction **5**
- 1.1 Aerosols, and their impact on climate . . . 5
- 1.2 Desert environments . . . 7
  - 1.2.1 Dust storms . . . 7
  - 1.2.2 Desert surfaces . . . 8
- 1.3 Sources of desert dust . . . 8
  - 1.3.1 Saharan sources . . . 8
  - 1.3.2 The Bodélé Depression . . . 12
  - 1.3.3 West Africa . . . 13
  - 1.3.4 North Sahara: northern Algeria, Tunisia, Libya . . . 14
  - 1.3.5 The Middle East and the rest of the world . . . 14
- 1.4 Trajectories of Saharan desert dust . . . 15
- 1.5 Dust Forecasting . . . 16
- 1.6 Outlook . . . 17

2 Observational Data **20**
- 2.1 Measurement types . . . 20
  - 2.1.1 Satellite measurements of radiance . . . 20
  - 2.1.2 Sun-photometry . . . 21
  - 2.1.3 Lidar measurements of backscattered light . . . 22
- 2.2 Satellite instruments . . . 23
  - 2.2.1 AATSR . . . 23
  - 2.2.2 SEVIRI . . . 24
  - 2.2.3 MODIS . . . 24
  - 2.2.4 MISR . . . 25
  - 2.2.5 OMI . . . 25
  - 2.2.6 CALIPSO . . . 26
  - 2.2.7 DRI . . . 26
- 2.3 Ground-based instruments . . . 28
  - 2.3.1 AERONET . . . 28
- 2.4 Comparison between AERONET and DRI data . . . 30

3 Dust Emission **34**
- 3.1 Model domain . . . 35
- 3.2 Soil data . . . 35
- 3.3 Meteorological data . . . 38
- 3.4 Dust emission parameterisation . . . 39
  - 3.4.1 Wind friction velocity . . . 39
  - 3.4.2 Threshold friction velocity . . . 40
  - 3.4.3 Emission flux . . . 41
  - 3.4.4 Roughness length . . . 44
  - 3.4.5 Sand-blasting efficiency, α . . . 47

3.4.6 Soil moisture . . . 50
3.4.7 Summary of emission scheme . . . 50
3.5 Soil size distribution . . . 51
3.6 Emission at constant wind speed . . . 54
3.7 Sensitivity to model resolution . . . 57
3.8 Emission climatology . . . 59
3.8.1 2006 emissions and meteorological conditions . . . 59
3.8.2 Seasonal emissions and meteorological conditions . . . 61
3.8.3 Inter-annual variability . . . 67
3.8.4 The relationship between emission and wind speed . . . 74
3.9 Comparisons between emission schemes, and between soil data sets . . . 76
3.10 Emission comparison . . . 78

4 The Dust Transport Model 80
4.1 Dust and Aerosol Transport Models . . . 80
4.1.1 DEAD . . . 81
4.1.2 DREAM/SKIRON . . . 81
4.1.3 GOCART . . . 82
4.1.4 Deficiency of current models: motivation for SHAMAL . . . 83
4.2 Model structure . . . 83
4.2.1 ECMWF meteorological data . . . 86
4.3 Processes . . . 87
4.3.1 Advection: wind velocities and the gravitational settling velocity . . . 87
4.3.2 Turbulent diffusion . . . 89
4.3.3 Deposition . . . 90
4.4 Optical depth . . . 92
4.5 Resolution/domain size . . . 93
4.6 Sensitivity analysis . . . 94

5 A year of dust storm activity 98
5.1 Sources and sinks . . . 99
5.1.1 Deposition over North Africa . . . 100
5.1.2 Oceanic deposition . . . 106
5.1.3 Surface concentrations . . . 111
5.2 Dust transport . . . 113
5.2.1 Dust transport across North Africa . . . 113
5.2.2 Dust transport into the Atlantic, and to other regions . . . 116
5.3 Dust storm activity . . . 120
5.3.1 Optical depth of dust storms . . . 120
5.3.2 Dust plume heights . . . 128
5.4 Dust size . . . 131
5.4.1 Dust effective radius . . . 131
5.4.2 Dust aerosol size distributions . . . 132
5.5 AERONET comparisons . . . 138
5.6 Ensemble of model schemes . . . 142
5.7 Summary . . . 144

6 Data Assimilation 147
6.1 Theory of Data Assimilation . . . 147
6.1.1 Least Squares fitting . . . 147
6.1.2 The Cost Function . . . 149
6.1.3 Cressman Analysis . . . 150
6.1.4 Adjoint schemes . . . 151
6.2 Assimilation with data from the Dust Retrieval Intercomparison (DRI) project . . . 151

6.3 Model uncertainty 152
6.4 Summary 154

7 Dust storms in March 2006 **156**
7.1 Overview of March 2006 North African dust weather 157
7.2 Comparison between background model results from SHAMAL-high and SHAMAL-low 158
7.3 Overview of modelled results from March 2006 160
7.3.1 Sources and sinks 162
7.3.2 Optical depth 168
7.3.3 Size distributions and plume heights 174
7.3.4 Atlantic transport and deposition 179
7.4 The effect of data assimilation on the validation against AERONET 183
7.5 The 8th March 2006 dust event: anatomy of a dust storm 192
7.5.1 Origins: the 5th-6th March 192
7.5.2 Growth: the 7th March 195
7.5.3 Maturity: the 8th March 199
7.5.4 Aftermath: the 9th March 201
7.6 Summary 203

8 Conclusion **205**
8.1 Summary of the SHAMAL dust model 205
8.2 Dust emission 205
8.3 Dust storm activity 207
8.4 Dust transport and deposition into the Atlantic 209
8.5 The 8th March 2006 dust event 210
8.6 The value of data assimilation 210
8.7 Directions for future work 211
8.8 Overview 214

Chapter 1

Introduction

The radiative forcing of airborne aerosols is one of the most significant uncertainties in our understanding of climate change (Forster et al., 2007). Airborne aerosols have a number of different sources, for example: soot pollution and biomass burning (anthropogenic), volcanic ash, and desert dust. The emission of desert dust is generally a natural occurrence (unlike pollution); however, human activity may amplify the production of airborne dust aerosol through overgrazing or deforestation, both of which can lead to desertification. The most obvious example of this is the Sahel region in Africa, a semi-arid region which forms the southern boundary of the Sahara desert (Middleton, 1985).

The Sahara desert itself is by far the largest source of desert dust aerosol in the world: it is the largest desert in terms of area, it has the strongest source in the world (the Bodélé Depression in Chad), and emits a total mass of 630-710 Tg of dust per year according to D'Almeida (1986), or 1430 Tg per year according to Ginoux et al. (2004). This compares to the estimated global emission of 1000-3000 Tg per year (Engelstaedter et al., 2006). These figures show that there is still some considerable uncertainty about the annual emission, the burden, and the annual deposition of desert dust.

1.1 Aerosols, and their impact on climate

Aerosols are defined as small solid or liquid particles suspended in a gas (e.g. Seinfeld and Pandis, 2006, amongst others): atmospheric aerosols are aerosol suspended in the atmosphere. Mineral desert dust, such as sand and smaller silt particles, are one example of an aerosol species. Other

examples of aerosols include sea salt, volcanic ash, sulphates, industrial carbon, and organic carbon (from, for example, biomass burning). One global estimate (Stier et al., 2005) suggests that dust contributes 40% of the global aerosol burden. Over North Africa, the dominant species of aerosol is mineral dust (from the Sahara), while in other areas of sub-Saharan West Africa biomass burning becomes an important source of aerosol.

Airborne desert dust has several effects on the global environment. On a global scale, aerosols increase the optical depth, altering the heat budget of the atmosphere. Aerosols scatter and absorb solar and out-going thermal radiation, which affects the climate (Engelstaedter et al., 2006). According to the Intergovernmental Panel on Climate Change (IPCC) in its Fourth Assessment Report (Forster et al., 2007), the dust radiative effect lies somewhere within the range of -0.56 to $+0.1$ W m^{-2}.

The global dust radiative forcing is also influenced by anthropogenic activities (Forster et al., 2007), which can increase the area of erodible desert, and make the surface more vulnerable to wind erosion. Overgrazing and poor agricultural practices (e.g. in the Sahel region) and drying of lakes (e.g. the Aral Sea) can increase the surface area of desert regions. Other human activities such as road-building and war (Goudie and Middleton, 2006) (e.g. in Iraq and Afghanistan, and in North Africa during the Second World War) can disrupt the surface of desert soils, leaving looser material more exposed to wind deflation. According to Forster et al. (2007), the total dust radiative forcing (from anthropogenic activity) lies within the range of -0.3 to $+0.1$ W m^{-2}. This compares to the total aerosol radiative forcing of -0.5 ± 0.4 W m^{-2}

On deposition, desert dust can act as a fertiliser, for example in the Amazon (Swap et al., 1992), where the quantities of sodium, potassium, nitrates, sulphates, and phosphates are enriched by Saharan dust. This may be an important part of the nutrient balance which makes the Amazon rainforest so fertile. Dust deposited into the oceans/seas provides iron, which enhances the production of chlorophyll (Mahowald et al., 2005): this has important implications for the CO_2 budget, since increased productivity will cause a decrease of CO_2 in the atmosphere. Another consequence of airborne desert dust is the weakening of tropical storms (Engelstaedter et al., 2006). Human activity is influenced by desert dust as well, since dust aerosols can spread fungi and bacteria (causing disease), the dust itself can worsen respiratory problems, and the reduced visibility has been responsible for several aviation disasters in North Africa.

1.2 Desert environments

A *desert* is a climate region defined by its aridity, and by its lack of vegetation. The word 'desert' derives from the Latin word *desertum*, which refers to a wasteland or wilderness, a place which is abandoned (Warner, 2004). Interestingly, the Persian word *dasht*, remarkably similar to the Latin and the English words, also refers to a wasteland or a desert: Iran's largest desert is the Dasht-e Kavir. To be a desert, the average surface water loss (the sum of the evaporation and the transpiration, *evapotranspiration*), must be greater than the surface water gain (precipitation). Average yearly precipitation is commonly used to define deserts, though it may be an unreliable indicator of a desert's status: for example, the Nile may have very low rainfall, but the Nile fertilises its flood plain, so permitting the presence of vegetation. However, to be a desert, a region should generally have an annual precipitation of less than 250-500 mm (Miller, 1961). The Sahara desert is the largest hot desert in the world, though it is interesting to note that it is not the largest desert in the world, since Antarctica is also a desert.

1.2.1 Dust storms

A dust storm is a sub-category of weather associated with airborne desert dust. Formally, an event can be considered to be a dust storm if the horizontal visibility is less than 1 km (Warner, 2004). The first distinction to make is between a *dust storm* and a *sand storm* (Bagnold, 1941). A sand storm is a local event, spanning up to a few tens of kilometres in the horizontal and with a height up to a few hundred metres off the ground. They tend to be composed of large sand particles, and so have a short atmospheric lifetime of the order of hours, though they can be very intense for those caught within them. The term 'dust storm', on the other hand, is generally used to denote storms of a much larger scale, with finer silt and clay particles being transported potentially over thousands of kilometres from the source, at an altitude of several kilometres, but with a lower concentration than sand storms. This thesis is concerned mainly with dust storms.

Dust storms are often associated with other types of dust event, which lift the dust from the surface, such as sand storms and *dust devils* (Warner, 2004). As discussed above, sand storms can be particularly intense, and the impact of sand particles striking and lifting particles from the surface ('sand-blasting') is the dominant form of dust lifting. A dust devil can also lift dust: a dust devil is a vortex of dust, similar in scale to a small tornado (of the order of metres across, and tens of metres high), and is associated with atmospheric convection and surface heating.

1.2.2 Desert surfaces

The surface of a desert is not uniform, and is made up of several different types of terrain. A common feature of all desert types is the scarcity of vegetation. Within the Sahara, there are six main types of surface: *regs* and *hamadas* (Mabbutt, 1977), *ergs*, mountains, dried lake beds (such as salt lakes), and *wadis*.

Regs, also known as *serirs*, and *hamadas* are the dominant surface types within the Sahara, and are characterised by their hard and rocky surfaces. They are subsets of *desert pavements*, which are stony deserts. Hamadas, from the Arabic word for 'unfruitful', are particularly difficult to pass, since they are covered by boulders. Regs are more passable, covered by smaller rocks. Figure 1.1 shows an example of a reg.

Ergs are the stereotypical desert surface type, regions dominated by sand and frequently covered by sand dunes. Figure 1.2 shows an example of an erg.

Mountains are also present within the Sahara. The Atlas mountains form the Sahara's northern boundary, running along northern Algeria and through Morocco. Other important mountain areas include the Hoggar in southern Algeria, the Tibesti and the Ennedi in northern Chad, and the Aïr Massif in central Niger. Figure 1.3 shows an example of mountainous deserts.

Endorheic depressions are lakes (or former lakes) which do not have outflow channels. Within the Sahara, many of these have dried up, and are the remnants of ancient lakes. Salt lakes (or *chotts*, as they are known in North Africa) are a type of endorheic depression, and they generally have a crusted surface. *Wadis* are dry river valleys, which are dry either permanently, or seasonally and prone to flash-flooding.

1.3 Sources of desert dust

1.3.1 Saharan sources

The Sahara desert is the pre-eminent desert in the world, due to its size. In fact, the name 'Sahara' comes from the Arabic word for desert, *ṣahra*. For the purposes of this study, the 'Sahara region' encompasses the Sahara desert, which occupies most of North Africa, and extends into the Sahel (which forms the southern boundary of the Sahara; the dividing line between the Sahara and the Sahel is not a distinct boundary, it changes seasonally). The longitude and latitude coordinates which form the bounds of this region are: 20 °W, 11 °N, 35 °E, and 36 °N. The Canary Islands and the Atlantic form the western boundary, the Mediterranean forms the northern boundary, the

Figure 1.1: An example of a reg, Yazd province, central Iran (photograph by the author).

Figure 1.2: An example of an erg, Esfahan province, Iran (photograph by the author).

Figure 1.3: An example of a mountainous desert, Wadi Rum National Park, southern Jordan (photograph by the author). Between the mountains, this region has the characteristics of an erg.

Red Sea forms the eastern boundary, and the countries of the Sahel (Senegal, Mali, Burkina Faso, Niger, Chad, and Sudan) form the southern boundary. Figure 1.4 shows a map of the Sahara's coverage in North Africa.

There are a large number of distinct sources in the Sahara region, too many to be described here. Below are described some of the most significant and interesting sources; for a more complete picture, consult Prospero et al. (2002) or Goudie and Middleton (2006). Aside from the regions descibed below, there are active source regions in Egypt, Sudan, the Ethiopian Rift Valley, and Djibouti.

Through much of the following sections the TOMS (Total Ozone Mapping Spectrometer) aerosol index (TOMS AI) will be used to refer to the strength of dust sources, and to their geographical distribution. According to Ginoux and Torres (2003), the TOMS AI is defined as:

$$AI = -100\Big[\log\left(\frac{I^m_{340}}{I^m_{380}}\right) - \log\left(\frac{I^c_{340}}{I^c_{380}}\right)\Big]. \tag{1.1}$$

The measured backscattering radiance at 340 nm is I^m_{340}, and I^c_{340} is the radiance calculated using a radiative transfer model which assumes a pure Rayleigh atmosphere. It is therefore a measure of how much the backscattered radiance is affected by the aerosol present in the atmosphere.

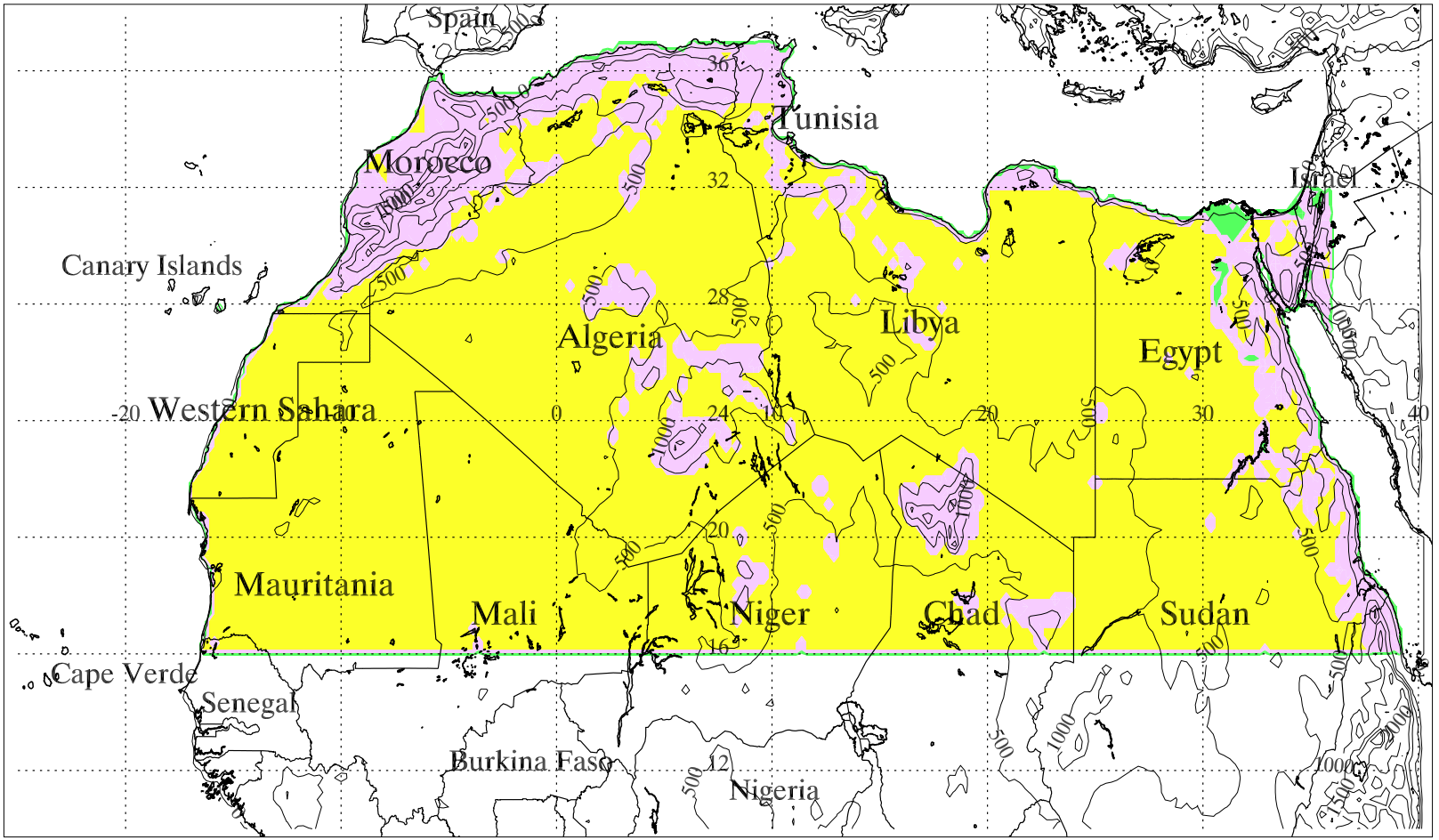

Figure 1.4: Map of North Africa, based on soil data provided by the Laboratoire Interuniversitaire des Systèmes Atmosphériques (LISA) in Paris. The Sahara desert is marked in yellow, mountain ranges and other non-erodible desert areas (defined here with a roughness length cutoff of 2 mm) are marked in pink, and vegetated and cultivated areas are marked in green. The Sahara region has its southern boundary, the Sahel, on the latitude line through southern Mali, southern Niger, and bisecting Chad and Sudan. Contour lines denote elevation, in metres.

1.3.2 The Bodélé Depression

TOMS and MODIS data indicate a significant source of desert dust coming out of Chad (Engelstaedter et al., 2006) in the region of the Bodélé Depression (16 °-18 °N and 15 °-19 °E), with yearly mean AI values exceeding 3.0. One estimate of dust emission from the Bodélé suggests that $1.18 \pm 0.45\,\mathrm{Tg\,day^{-1}}$ are emitted from the Bodélé during strong dust events (Todd et al., 2007). The Bodélé is the best example of a *preferential source region*, or *hot spot*, from where a concentrated plume of dust is emitted. This appears to be the most active dust producing region in the world, and is one of the most significant suppliers of mineral dust to the Amazon rainforest (Koren et al., 2006). Also, unlike most other dust sources in the world, the Bodélé is active year-round, even in the autumn/winter months of October-December when the rest of the Sahara is inactive.

Grini et al. (2005) identifies several important factors which produce a hot spot: (1) reliably strong wind speeds, (2) low threshold wind speed, (3) thin or non-existent crusts, (4) abundance of potential aerosol particles. Lack of crusting is important because crusted surfaces, being very hard, are very resistant to wind erosion. Goudie and Middleton (2006, p.38) refer to *stone/desert pavements*, similar to *duricrusts* (hardened surface crusts found in many arid regions), which are also widespread in arid regions and consist of a hardened coating of coarse particles covering large quantities of fine material, probably caused by dust deposition from the atmosphere. If the crust is disturbed or cracked, perhaps due to human activity, then these areas can become local sources of dust. In general, what we are looking for in a source region is a substantial quantity of exposed fine particles. The latter are usually in the form of silt particles, so we are looking for areas which are fed by streams (to carry alluvium), but which are sufficiently arid that there is very little vegetation. Moreover, soil moisture (Mahowald et al., 2005) increases the cohesion of the soil particles (which hinders erosion), so these streams should be ephemeral, and seasonal.

The Bodélé Depression is such a significant source of dust due to three main factors: it is situated in a region with reliably strong winds, it contains a significant quantity of fine particles, and is downwind of a dune region, the Erg du Djourab, which produces coarse particles which *saltate* (leap forward several metres into the air before impacting onto the surface). The Bodélé Depression is a dried lake bed, and is associated with Lake Chad. The region is very dry, with an average annual rainfall of $\sim$17 mm (Goudie and Middleton, 2006, p.84), which means both that there is very little vegetation (vegetation hinders dust emission) and a low possibility of wet deposition of dust particles. The surface of the Bodélé is composed of diatomite deposits, which were deposited into Palaeolake Mega Chad (Todd et al., 2007; Warren et al., 2007), of the order of

6000 years ago. As a result of this, the Bodélé contains a significant quantity of erodible material (Washington et al., 2006): this means that the soil particles dominating the Bodélé are susceptible to being lifted from the surface, since the particles are so fine. Moreover, as it is surrounded by Saharan desert, the Bodélé gets bombarded by coarser particles saltating down into the depression.

The winds in this region tend to coincide on the Bodélé Depression, since to the north and east of Bodélé are situated the Tibesti and the Ennedi mountain ranges. The effect of this is that north-easterly winds are channelled and focused between the two mountain ranges, downslope and at low altitude, onto the Bodélé Depression (Washington et al., 2006). This characteristic wind is known as the Bodélé Low Level Jet (LLJ) (Washington and Todd, 2005). The LLJ drives the saltation process of coarser particles which initiates the emission of the finer dust particles up into the atmosphere.

1.3.3 West Africa

West Africa is the other main source of airborne dust in the Sahara, though the main emitting region here has a much wider area than does the Bodélé Depression. According to Prospero et al. (2002) there is a large active area from ∼17 °-18 °N, 8 °-10 °W to the ENE to ∼26 °N along the meridian, covering large parts of Mali, Mauritania, and southern Algeria. According to Goudie and Middleton (2006, p.86), the region is an area of low relief bounded to the north and east by highlands. Highlands may not be major dust source regions, but ephemeral wadis draining from them transport silt-rich alluvium. This is comparable to the effect of the Tibesti massif on the Bodélé. Niger is also quite active. Though the average intensity of dust emissions from west Africa is lower than from the Bodélé, the extent of the west African source region means that this area emits a comparable quantity of dust into the atmosphere. West Africa emits dust more seasonally than does the Bodélé, with very low emissions over the winter, from October to March. Between April and September, the TOMS AI is greater than 1.9 on 75% of the days (Goudie and Middleton, 2006, p.92). Satellite observations indicate the primacy of the West African dust sources during the summer months: using the geostationary satellite instrument SEVIRI, described in section 2.2.2, Schepanski et al. (2007) back-tracked dust plumes towards their sources, indicating the significance of topographic depressions to the atmospheric dust budget. Figure 1.5 shows an example of dust transport from West Africa.

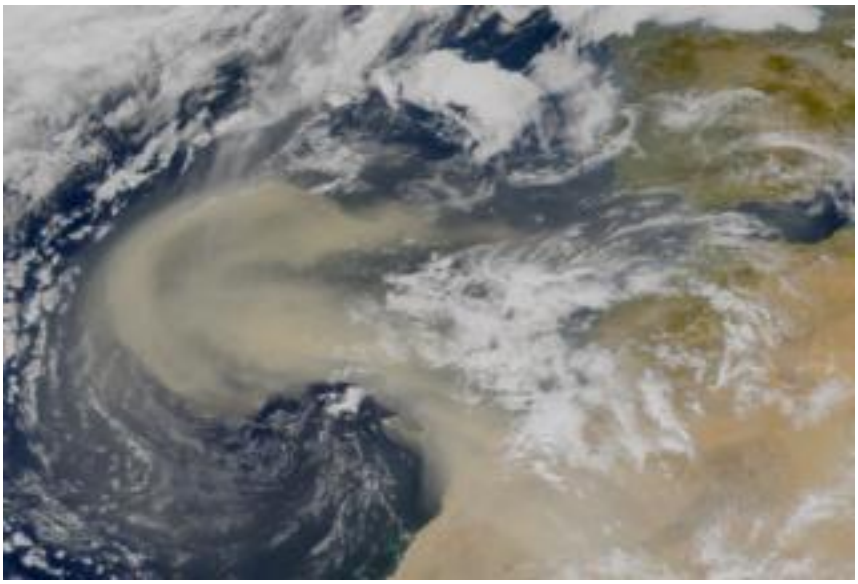

Figure 1.5: Dust plume in the Atlantic off the Western Sahara (SeaWiFs, 26/2/2000, image courtesy of NASA).

1.3.4 North Sahara: northern Algeria, Tunisia, Libya

The source of a large dust event which spread out over a significant fraction of the Sahara in March 2006 (Slingo et al., 2006) appears to be a region just to the south of the Atlas mountains, on the border between Algeria and Tunisia. There are various chotts, or salt lakes (Prospero et al., 2002), and wadis in this area (Chott Melrhir in Algeria and Chott Jerid in Tunisia are particularly large). The region is particularly arid, lying on the other side of the Atlas mountains from the Mediterranean, and has an average annual rainfall of under 100 mm. Meanwhile north-western Libya is cris-crossed by a large network of wadis.

1.3.5 The Middle East and the rest of the world

Most of the Middle East is sandy desert. Goudie and Middleton (2006, p.112) show that the area with the highest dust storm activity in the Middle East is a swathe of land in eastern Saudi Arabia, stretching from the Persian Gulf near Bahrain down to the Rub Al Khali desert in the south. This region is predominantly flat, with relatively fine particles, bordered by a sand sea. Oman is also a significant source. In Iraq, the focus of dust activity appears to be in the Tigris and Euphrates Basin (a source of fines), rather than in the surrounding desert. A particularly strong source is at the mouth of the river system, where there are 43 (Prospero et al., 2002) dust storms per year on

Region	Emission	Dry Deposition	Wet Deposition	Burden
North Africa	1430	1062	60	307
South Africa	22	17	1	3
North America	9	31	12	-34
South America	55	39	5	10
Asia	496	409	29	58
Australia	61	44	2	16

Table 1.1: Simulated mean annual emission, dry deposition, wet deposition and burden (emission - deposition) over various regions of the world, in $\mathrm{Tg\,year^{-1}}$. Data taken from table 2 of Ginoux et al. (2004), which presents results from the GOCART model.

average.

There are other dust sources scattered around the world, such as in China, Iran, Pakistan, Central Asia, Australia, the US (a net sink of dust), Mexico, Bolivia, Argentina, and southern Africa. However, the focus of this study is the Sahara, for the simple reason that the Sahara is by far the largest source of desert dust in the world: an estimate produced by Ginoux et al. (2004), from global model simulations, suggests that over 65% of world dust emissions are from North Africa (Asia emits up to 25%, all other sources account for no more than 10% of global emissions). Table 1.1 shows a regional breakdown of dust emissions and sinks, as simulated by the GOCART model (Ginoux et al., 2004).

1.4 Trajectories of Saharan desert dust

Western trajectories transport Saharan dust across the Atlantic, principally to South America. Goudie and Middleton (2006, p.95) report that 30-50% of the desert dust output from the Sahara passes over the Atlantic. Estimates using MODIS data (Kaufman et al., 2005) suggest that 240±80 Tg of dust per year are transported over the Atlantic. Useful places to measure Saharan dust transport over the Atlantic are on islands, such as Barbados and Cape Verde (Ellis and Merrill, 1995). Cape Verde is particularly useful, since it is so close to the coast of West Africa, and can be used to estimate the total emission into the Atlantic. A dust plume takes about 5-7 days to travel from West Africa to the Caribbean (Middleton and Goudie, 2001), most often during the summer. West Africa is the main source region for the North Atlantic, while Koren et al. (2006) suggest that the Bodélé Depression is a major source to the Amazon Basin, since in winter it is responsible for >40% of dust optical depth over the Amazon.

Northern trajectories transport Saharan dust over the Mediterranean to Europe, and can be

quite frequent: in 1999, every day (Middleton and Goudie, 2001) during the summer the TOMS AI (see equation 1.1) value exceeded 1.9 over the Mediterranean. Northern summer is the most active season for dust events, due to the Sahara, which accounts for 80-120 $\times$ 10^6 tonnes per year (D'Almeida, 1986) over Europe. The sources for these events tend to be from the north-west Sahara. This trajectory can supply dust to northern Europe, to Britain via mid-tropospheric winds in the Bay of Biscay (Middleton and Goudie, 2001), and as far north as Scandinavia. Wet deposition is a common form of deposition over Europe. Saharan dust also has an impact on the mineralogy of the Mediterranean: Guerzoni et al. (1997) report that deep-sea sediments from the Tyrrhenian and Adriatic seas have similar clay mineral signatures to Saharan dust. This is not true in the eastern Mediterranean, where output from the Nile dominates.

Dust transported over the Middle East comes not just from the Middle East itself but also from the Sahara, from as far west as Algeria (Goudie and Middleton, 2006, p.114). Sudan's Red Sea coast is another source of dust transported across the Red Sea to the Middle East, since the region contains two large sources of silt, the Tokar delta, and the ephemeral Baraka river.

There are indications that Saharan dust can travel even further east than Asia. McKendry et al. (2007) report a dust event in British Columbia, Canada, in March 2005, which may have taken two weeks to cross Asia and the Pacific to Canada.

1.5 Dust Forecasting

A number of models to simulate dust storms have been produced, including models such as DREAM (Nickovic et al., 2001), DEAD (Zender et al., 2003), GOCART (Ginoux et al., 2001), and RegCM3 (Zakey et al., 2006), amongst others. Further details on some of these models are described in section 4.1. These aim to simulate dust storm activity, often as a subset of general aerosol activity. Models such as DREAM can also be used for forecasting purposes, if they are attached to weather forecasting models (such as SKIRON, in the case of DREAM). The WMO-SDS (World Meteorological Organisation Sand and Dust Storm) programme is a collaborative project to bring together some of the leading dust and weather forecasting models (e.g. ECMWF, NCEP, and DREAM/SKIRON) in order to improve the forecasting of dust storms, and to provide warnings of dust storm activity (Niu et al. (2008), http://www.wmo.int/pages/prog/arep/wwrp/new/Sand_and_Dust_Storm.html).

Presented in this thesis is an example of an off-line tracer model, as opposed to a coupled climate model (e.g. Meehl (1992)). Coupled models link up various processes in the Earth's climate system, and try to simulate the complex feedbacks that occur between them. An example of this is the heat

transport at the interface between the atmosphere and the ocean: ocean and atmospheric flows can be calculated independently (in off-line models), but this would miss out important details in the global system. Of particular interest is the impact of dust and other aerosols on climate: off-line models may simply just calculate the dust transport, as well as the dust optical depth and radiative impacts. A full coupled model will allow the dust to produce feedbacks on the climate system which will affect the weather systems generating and influencing the dust storms. In terms of this detail, we would expect a coupled model to produce more reliable and complete results. However, off-line models can be much more flexible than coupled models, since they employ fewer processes and feedbacks, and so they are cheaper in processing time. This allows for larger and longer model runs, as well as for more ensemble runs to test various different parameters in the models. Hence off-line models can be used efficiently to test dust emission and transport processes.

1.6 Outlook

Presented in this thesis is the physics and the structure of, and the results from, the SHAMAL (Sa-Haran Aerosol in a Medium-range Assimilation) model. It is named after the Shamal wind (Warner, 2004), which is a north-westerly wind that blows over the Middle East, across Mesopotamia and the Persian Gulf, and is often a dust-bearing wind system. In July 2009 it was responsible for a substantial dust storm which covered large regions of Iraq and western Iran, shown in figure 1.6.

The SHAMAL model is a regional (mesoscale) dust model which is used to simulate dust storm activity over North Africa, and dust transport to the Atlantic, the Mediterranean, and the Sahel and the Sudanian savanna to the south. The focus of the work is primarily on 2006, specifically March, though presented dust emission estimates do extend from 2004-2008. During this time estimates of dust emission, transport (including fluxes and plume heights), and deposition (over North Africa and the Atlantic, in particular) are made. This is done using the dust emission and transport model, which simulates the physics of dust storms, and is enhanced using the data assimilation scheme, which uses satellite observations to initialise and enhance the model dust fields.

The model has been developed to address several science questions:
(1) What are the yearly and seasonal patterns of dust emission from North Africa? Where are the major source areas, when are they active, and how much dust do they emit?
(2) What is the pattern of dust storm activity? How much dust is deposited on a monthly basis, where, and by which removal process? What are the heights of dust plumes, and their size distri-

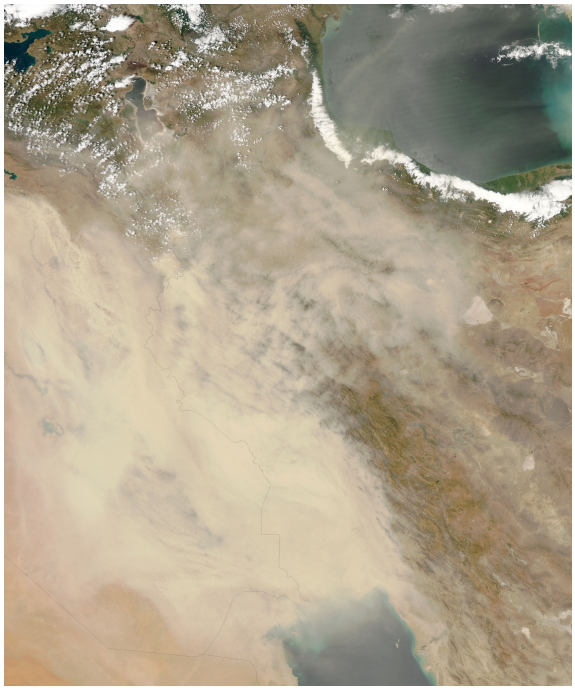

Figure 1.6: Dust storm over Iraq and Iran, caused by the Shamal winds. Image taken by MODIS on 5/7/2009 (image courtesy of NASA).

butions?

(3) How much dust is transported into the Atlantic from the coast of West Africa, and how much of this dust is deposited into the east Atlantic?

(4) How much dust was emitted, transported, and deposited during the 8th March 2006 dust event (which swept across much of North Africa)?

(5) To what extent does data assimilation improve the simulated results?

Note that while a dust model such as SHAMAL can help to improve our understanding of dust sources and dust activity, it can only be one part of our toolkit in learning about dust storm behaviour. Observational evidence is also required, from field campaigns (e.g. direct observations of dust concentrations close to the surface, visibility, etc.) using measurements from ground instruments (and possibly also from aircraft flights), and from satellites (which can provide a much larger spatial picture). The advantage that a full transport model has over any observations, however, is the range of spatial and temporal scales it works on. Whereas a satellite in low Earth orbit may only pass over a swath of the Sahara once or twice a day, a model can simulate dust activity over the entirety of the Sahara at all times of the day. However, observations provide the necessary evidence about the 'true' dust storm activity, and hence any studies carried out using a dust model

must be compared and validated against observations; given the diversity of dust behaviour (we are interested in both the geographical distribution of dust sources and the height profiles of lofted dust plumes, for example), we require a variety of different measurement techniques to measure different dust properties. This will allow us to assess the value of the model, and judge the accuracy of its simulations.

Chapter two introduces the various sources of observational data available from satellite and ground-based observations. Chapter three describes the process of dust emission, how it is parameterised, and presents results from the dust emission model. Chapter four presents the dust transport model, and the physics involved, while chapter five presents the various results output by the model (over the course of a year), such as dust transport into the Atlantic, and the validation of these results. Chapter six presents the data assimilation scheme used to improve and enhance the transport model, and chapter seven describes the dust storm activity in March 2006, as a case study, using the data assimilation technique. Chapter eight summarises the work presented in the thesis, and provides some suggestions for future studies.

Chapter 2

Observational Data

As with other atmospheric aerosols, in order to study atmospheric desert dust, observations are required. These can come in the form of direct in-situ measurements, measuring the dust physically to improve our understanding of dust concentrations and size distributions. The observations are made on the ground (measuring dust saltation and concentration, or deposition) or in the air during aircraft campaigns. Indirect measurements of dust can also be made by remote sensing, observing the optical and radiative effects that dust has on the atmosphere.

2.1 Measurement types

2.1.1 Satellite measurements of radiance

Satellite instruments such as AATSR measure reflected solar radiation from the Earth's surface (Kaufman et al., 1997; Levy, 2009). The reflectance at wavelength λ, ρ_λ, is given by:

$$\rho_\lambda = \frac{L_\lambda \pi}{E_{0,\lambda} \cos \vartheta_0}, \tag{2.1}$$

where L_λ is the measured solar radiance, $E_{0,\lambda}$ is the extra-terrestrial solar irradiance, and ϑ_0 is the solar zenith angle. From a satellite (Levy, 2009), the observed top-of-the-atmosphere (TOA) reflectance, ρ^*_λ, is given by:

$$\rho^*_\lambda(\vartheta_0, \theta_\mathrm{s}, \phi) = \rho^\mathrm{a}_\lambda(\vartheta_0, \theta_\mathrm{s}, \phi) + \frac{T_\lambda(\vartheta_0) T_\lambda(\theta_\mathrm{s}) \rho^\mathrm{s}_\lambda}{1 - s_\lambda \rho^\mathrm{s}_\lambda}, \tag{2.2}$$

where θ_s is the zenith angle of the satellite looking at a point on the Earth's surface ('target angle'), ϕ is the relative azimuthal angle between the sun and the satellite, ρ_λ^a is the atmospheric reflectance, ρ_λ^s is the surface reflectance, s_λ is the atmospheric backscattering ratio, and T_λ are the upward and downward transmissions. To measure the aerosol presence, the satellite retrieval finds first the atmospheric reflectance and then the aerosol reflectance, using a knowledge of the aerosol's spectral reflectance properties.

For measurements of dust storms, we require tropospheric aerosol measurements. Hence all the satellite instruments presented in this chapter are *nadir-viewing* (Andrews, 2000), in which the instrument looks down at the atmosphere against the Earth's surface (at a low zenith angle), rather than *limb-viewing* instruments, in which the instrument observes the atmosphere against space (to observe stratospheric and mesospheric processes).

2.1.2 Sun-photometry

Sun-photometry is a method of observing aerosol particles by measuring the attenuation of solar radiation as it passes through the atmosphere (Kokhanovsky, 2008; Liou, 1980). Sun-photometers measure the solar beam radiance, L, which is related to the optical thickness τ by the *Beer-Bouguer-Lambert Law*:

$$L = L_0 \exp\Big(- \frac{\tau}{\cos\vartheta_0}\Big), \tag{2.3}$$

where L_0 is the TOA radiance. Re-arranging, we can easily find τ:

$$\tau = \cos\vartheta_0 \ln\Big(\frac{L_0}{L}\Big). \tag{2.4}$$

Finding L_0 requires calibrating the instrument by making measurements of L at several different solar zenith angles (with τ assumed to be invariant) and finding the y-intercept of the relation:

$$\ln L = \ln L_0 - M\tau, \tag{2.5}$$

where M is the air-mass factor ($1/\cos\vartheta_0$). This approximation for M is only valid for ϑ_0 being less than $\sim 75\,^\circ$, since the Earth's atmosphere is a spherical shell (Seinfeld and Pandis, 2006); at higher values M must be computed. τ is the *total* optical thickness from all the absorbing and scattering components of the atmosphere: aerosol scattering and absorption, molecular scattering, and gaseous absorption (Dubovik and King, 2000). Observing at wavelengths most sensitive to

the aerosol components of the atmosphere and least sensitive to gaseous absorption, the aerosol optical thickness (AOT) is determined by subtracting molecular and gaseous components of the optical depth.

2.1.3 Lidar measurements of backscattered light

A *lidar* (light detection and ranging) instrument uses an *active* method of remote-sensing, by transmitting pulses of radiation into the atmosphere and then measuring the backscattered radiation (Andrews, 2000). Lidars can be used on the ground, in the air, or from space (such as by CALIPSO).

A lidar system measures the signal $P(z)$ received from a layer of the atmosphere at height z, given by (Fernald et al., 1972):

$$P(z) = ECz^{-2}\beta(z)T^2(z), \tag{2.6}$$

where E is the output monitor pulse, C is a calibration constant for the instrument optics and receiver, $\beta(z)$ is the back-scattering cross-section at z, and $T(z)$ is the transmittance to height z. In the atmosphere, there are two types of scattering: molecular Rayleigh scattering (subscript R) and Mie scattering from particulates (subscript P). Using the ratio, S, of the extinction cross-section ($\sigma(z)$) to the back-scattering cross-section, we can find the transmittance due to particulates, $T_{\mathrm{P}}(z)$:

$$T_{\mathrm{P}}^2(z) = T_{\mathrm{R}}(z)^{3\mathrm{S}/4\pi}\left[1 - \frac{2S}{C}\int_0^{\mathrm{z}} \frac{P(z)z^2}{E} T_{\mathrm{R}}(z)^{(3\mathrm{S}/4\pi)-2} dz\right]; \tag{2.7}$$

and the back-scattering cross-section of the particulates, $\beta_{\mathrm{P}}(z)$:

$$\beta_{\mathrm{P}}(z) = \frac{P(z)z^2}{CE} T_{\mathrm{R}}(z)^{(3\mathrm{S}/4\pi)-2}\left[1 - \frac{2S}{C}\int_0^{\mathrm{z}} \frac{P(z)z^2}{E} T_{\mathrm{R}}(z)^{(3\mathrm{S}/4\pi)-2} dz\right]^{-1} - \beta_{\mathrm{R}}(z). \tag{2.8}$$

The atmospheric components $T_{\mathrm{R}}(z)$ and $\beta_{\mathrm{R}}(z)$ can be estimated using standard atmospheric data, or using local measurements. If S is unknown, then it can found by the relation:

$$S = C\left[1 - T_{\mathrm{P}}^2(z) T_{\mathrm{R}}(z)^{3\mathrm{S}/4\pi}\right]\left[2\int_0^{\mathrm{z}} \frac{P(z)z^2}{E} T_{\mathrm{R}}(z)^{(3\mathrm{S}/4\pi)-2} dz\right], \tag{2.9}$$

assuming that $T_{\mathrm{P}}(z)$ can be found using a sunphotometer. The principal advantage of the lidar technique is that it provides measurements of the vertical distribution of aerosols in an atmospheric column.

2.2 Satellite instruments

Satellite instruments have the advantage over ground-based instruments of a high spatial coverage, covering large regions of the planet during their orbits. Using such instruments, the spatial extent of a dust storm can be observed, not just the local intensity.

2.2.1 AATSR

The AATSR (Advanced Along Track Scanning Radiometer) instrument is located on the ESA satellite Envisat (Curier et al., 2009). The principal advantage of AATSR over other satellite instruments is that it utilises two views, the forward view and the nadir view, which allows for separation of the surface and the atmospheric contributions to the observed radiance. Both views observe radiances from the atmosphere and from the surface; however, the forward view is preferred for retrieving radiance from the atmosphere (since the view has a longer path length through the atmosphere, and an inclined surface), whilst the nadir view is preferred for retrieving radiance from the surface (since it views through a shallower atmosphere, perpendicular to the surface). Its aims are to measure sea surface temperatures (SST) to an accuracy of more than 0.5 K, land surface temperature, vegetation and atmospheric chemistry, as well as aerosol retrieval.

Envisat is in a Sun-synchronous polar orbit (Sayer, 2008), at an altitude of ∼800 km, and an inclination of 98.55 °. The orbital period is 101 minutes, orbiting just over 14 times per day. The repeat cycle of the nominal orbit is 35 days. AATSR uses 7 channels in the visible and the infrared, at 0.55, 0.66, 0.87, 1.6, 3.75, 11 and 12 μm. The resolution is ∼1×1 km at nadir (increasing towards the edges of the swath), ∼1.5×1.5 km in the forward view, and the swath width is ∼500 km. The forward view is inclined at an incidence angle (from the nadir) of 53-55 °, in the direction of ENVISAT's motion. It observes a point over 1000 km ahead of ENVISAT's current position, and it covers this distance in ∼150 s, when the nadir view observes the point.

AATSR data files produced by the Oxford-RAL Aerosol and Cloud (ORAC) retrieval algorithm (Thomas et al., 2009; Sayer, 2008) contain several pieces of information relevant to aerosol retrievals. There are data from each channel for surface albedo, radiances and brightness temperatures. Most useful is the optical depth (at 550 and 870 nm) and the effective radius information, to classify the size of the observed aerosols. The data can be analysed to look specifically for desert, biomass, maritime, continental, or urban aerosol. For desert aerosols, AATSR generally retrieves effective radius values of between 1-2 μm over the Sahara.

2.2.2 SEVIRI

The SEVIRI (Spinning Enhanced Visible and Infra-Red Imager) instrument is located on the ESA satellite Meteosat-8 (Sayer, 2008; Thomas et al., 2009). The satellite has been put into geostationary orbit (altitude 35,600 km) at a longitude of 0 °, and at an inclination of 0 °. Meteosat-8's geostationary orbit enables it to take measurements of one particular region of the Earth at all times of the day (except at night), rather than having to wait for the satellite to return from the other side of the orbit. This is especially useful in the case of Saharan dust, since Meteosat-8 is located at longitude 0 °, latitude 0 °, over the Gulf of Guinea. The disadvantage of the geostationary orbit, however, is that SEVIRI's optics require a larger diameter (it has a primary mirror of 0.5 m diameter) to maintain the same resolution as instruments in Low-Earth orbit (LEO), since it is much higher up than LEO satellites (over 40 times higher than AATSR). SEVIRI has a better resolution observing at nadir than it does towards the limb, which is of benefit to observations of North Africa. SEVIRI employs 12 channels in the visible and the infrared, at 0.6, 0.8, 1.6, 3.9, 6.2, 7.3, 8.7, 9.7, 10.8, 12, and 13.4 μm, as well as a twelfth high-resolution visible (HRV) band. The HRV band has a resolution of 1 km, while the other 11 channels have a resolution of 3 km. Thus SEVIRI generally has a poorer resolution than most other instruments currently used for aerosol retrieval. Data are taken every 15 minutes, which is one of SEVIRI's main advantages. As with AATSR, SEVIRI data from ORAC include albedo, effective radius and radiance information, from which the aerosol optical depth (AOD) can be found. Optical depth information can be distinguished between the various classes of aerosol. To retrieve AOD, data are taken from 5 channels, at 0.67, 0.87, 1.6, 10.8 and 12.0 μm.

2.2.3 MODIS

The MODIS (MODerate resolution Imaging Spectroradiometer) instrument is located on the NASA satellites TERRA and AQUA (Levy, 2009). These satellites orbit at an altitude of 705 km, with an orbital period of 98.8 minutes. It is designed to investigate numerous properties of the atmosphere, land, and ocean, such as aerosol properties. MODIS operates using 36 channels, in the visible to the infrared (from 410 nm to 14.235 μm). Aerosol boundaries and properties are measured using two different algorithms over land and over the ocean: over land, aerosol is measured at 470 and 660 nm (Abdou et al., 2005), while over ocean 550, 660, 860, 1240, 1630 and 2130 nm are used. MODIS' principal advantage over other instruments is its resolution: two of the visible bands have a resolution of 250 m, a further 5 bands have 500 m, while the rest have 1 km. The swath width

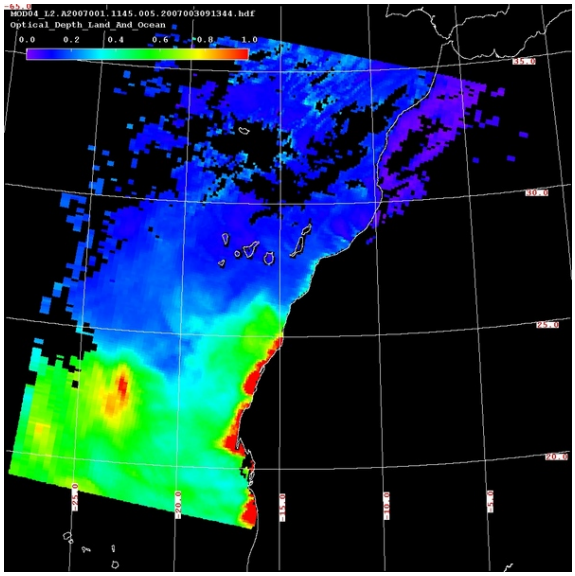

Figure 2.1: Plot of aerosol optical depth, showing dust being blown off west Africa. Image acquired by MODIS on 1/1/07. Image courtesy of NASA (http://ladsweb.nascom.nasa.gov/).

is 2,330 km, and global coverage is achieved once every one to two days. An example of MODIS imagery is presented in figure 2.1.

2.2.4 MISR

The MISR (Multi-angle Imaging SpectroRadiometer (Martonchik et al., 2009)) instrument is also located on TERRA. Imaging at four wavelengths (446, 558, 672, and 867 nm), MISR carries nine cameras, each at a fixed angle, such that MISR has a total of 36 channels. There is a camera in the nadir view (0 °), then there are eight cameras at ±26.1 °, ±45.6 °, ±60.0 °, and ±70.5 °, in the forward and aft directions. Each view has specific purposes: nadir is used for precise determination of MISR's geographical location, ±45.6 ° is sensitive to aerosols, and ±60.0 ° is used for measurements of albedo. The number of views is one of the principal advantages of MISR. The cameras have a maximum resolution of 250 m, though typically an array of, say, 4×4, pixels is averaged over: this reduces the required data transmission rate.

2.2.5 OMI

The Ozone Monitoring Instrument (OMI) is located on NASA's AURA satellite (Tanskanen et al., 2006). Designed to observe atmospheric ozone, OMI can also be used to observe mineral dust

aerosol. Measurements are primarily made in the UV (at 305, 310, 324, and 380 nm), although there are also channels up to 500 nm in the visible. OMI has a wide swath of 2600 km, which means that OMI can make daily observations of most of the Earth's surface, although the horizontal resolution is just 13×24 km at nadir. OMI data is provided in terms of aerosol optical depth (AOD), a standard product from satellite instruments, and the 'aerosol index' (AI), defined in section 1.3.1.

2.2.6 CALIPSO

The NASA satellite CALIPSO (Cloud-Aerosol Lidar and Infrared Pathfinder Satellite Observation [www-calipso.larc.nasa.gov (last accessed 5/4/2010)]) carries the CALIOP (Cloud-Aerosol Lidar with Orthogonal Polarization) instrument. CALIPSO is held at an altitude of 705 km, an inclination of 98 °, and an orbital period of 99 minutes. The CALIOP lidar uses backscattered light at two wavelengths, 532 nm and 1064 nm, and is polarisation sensitive. The output of the CALIOP data is a contour plot (figure 2.2) of the observed backscatter on a graph of the geographical position of CALIPSO (i.e. latitude/longitude) against the altitude of the retrieval. Regions in yellow, orange, red or grey primarily indicate the presence of clouds, but may also indicate atmospheric aerosols.

CALIPSO is a quite different intrument to those discussed above, because it uses a lidar, rather than being a passive observer of atmospheric radiation. The main use of CALIPSO in dust transport modelling is to locate the height and intensity of a dust plume.

2.2.7 DRI

The Dust Retrieval Intercomparison (DRI) project is a collaborative effort, based at the University of Oxford, which has sought to average and compare satellite observations over North Africa during March 2006 (Carboni et al., 2009). Nine satellite instruments are used: SEVIRI, AATSR, AIRS, OMI, MISR, MERIS, SeaWiFS, MODIS, and POLDER. It does not include CALIPSO data. Different retrieval algorithms are included as well: for example, SEVIRI is represented by four retrieval algorithms from the ORAC (Oxford-RAL Retrieval of Aerosols and Clouds) project, the GlobAEROSOL project, and the visible and infrared algorithms developed at Imperial College London. The DRI project has two main purposes: to compare and validate each of the satellite instruments against each other and against AERONET; and to provide as complete a picture as possible for dust storm activity in March 2006.

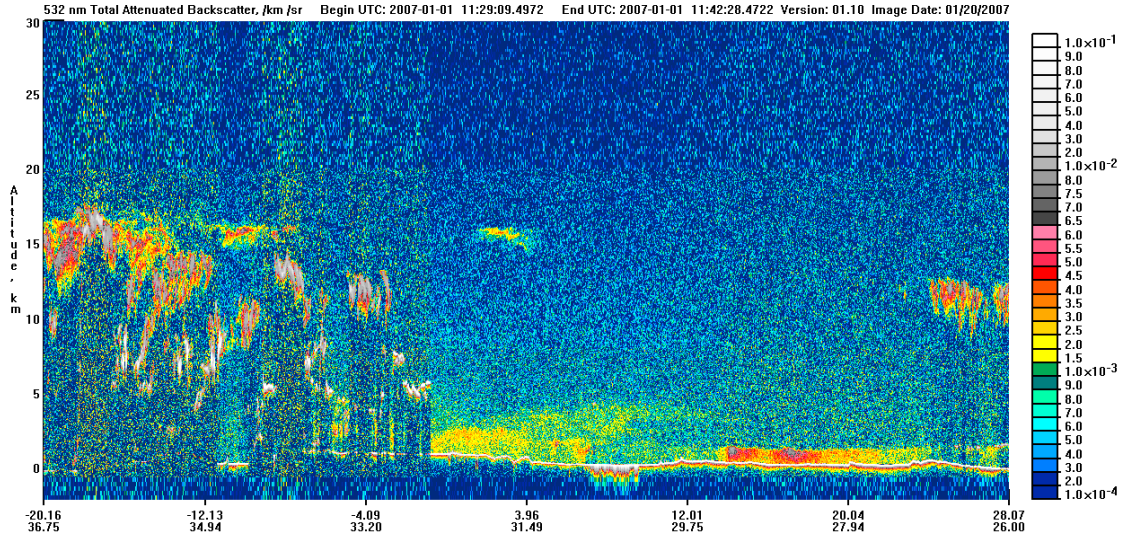

Figure 2.2: CALIPSO data from 1/1/07 (11:28-11:42 UT). The track is heading north from Mozambique to Egypt and Libya. Surface elevation shows up as a red line hovering around the line of 0 km altitude. Data courtesy of NASA [www-calipso.larc.nasa.gov].

For the purposes of studying dust storms, the advantage that DRI data have over the component satellite data sets is their spatial coverage. Data from the component instruments are averaged onto a standard spatial grid (Carboni et al., 2009), with a resolution of $0.5 \times 0.5\,^{\circ}$, finding optical depths at a wavelength of 550 nm. The averaged data are an arithmetic mean of the available satellite data sets, with uncertainties specified by the standard deviation of the data sets. Satellite instruments such as MISR and AATSR have quite poor spatial coverage, since they pass over North Africa in swaths, but provide good quality observations where they do observe; whereas instruments such as SEVIRI have good spatial coverage, but relatively poor quality observations. The purpose of DRI is to get the widest spatial coverage, and the best quality observations, so a composite of all the observations is an effective method of doing this. For an example of the differences in observations, some retrieval algorithms (e.g. POLDER-Ocean, visible SEVIRI data from Imperial, etc.) are optimised to observe dust over the ocean, whereas others (e.g. POLDER-Land, infrared SEVIRI data from Imperial, etc.) are designed to observe dust over land. The retrieval algorithms can be very different over ocean compared with over land, because of the very different surface radiative properties. By comparison, the transport processes over the ocean are much the same as over the land; there is not such a discontinuity in dust transport between land and ocean as there is in surface radiative properties.

The observations are averaged on a daily basis, which means that there is a temporal discontinuity between the observations, varying between 10:00 and 16:12 on each day (Carboni et al., 2009). This is a long enough period that there may have been some evolution in dust activity between the first and last observations in a day: hence DRI data is averaged over time as well as over the satellite instruments.

2.3 Ground-based instruments

2.3.1 AERONET

The AERONET (AErosol RObotic NETwork) is a NASA project which utilises a ground-based network of sun-photometers to measure solar light intensity, globally distributed, with several sites in North Africa (figure 2.3) (Holben et al., 1998). It would be preferable for there to be more AERONET sites in some of the larger sources of aerosols (e.g. the Sahara), however, it is of course more practical to set up photometers in more heavily populated areas rather than in the remote areas which are typical dust sources. The network is a standardised system, graded into three levels of quality assurance for each site. The main objective of the project is to take long-term measurements of the optical, microphysical and radiative properties of atmospheric aerosol.

Each photometer has eight filters at 340, 380, 440, 500, 670, 870, 940, and 1020 nm to measure AOT at various times during the day. AERONET sun-photometers only make observations when the air-mass factor is less than 7 (Kokhanovsky, 2008), where the solar zenith angle is less than 81.8 °. The field of view (FOV) is 1.2 °, about twice the angle of the solar disk. Since AOT is measured in just one direction, this is referred to as 'columnar optical depth'.

There are twenty-two AERONET sites within the North African region, as described in table 2.1. Quality-control can be applied to ignore sites that may be unrepresentative of their surroundings. For example, Izana, on the island of Tenerife, is located on a mountain plateau at an altitude of over 2 km: at this altitude the air will be rather thinner, and the aerosol optical depth will be correspondingly lower. Just a few kilometres away on the coast, the Santa Cruz site can observe the whole atmospheric column from close to sea-level.

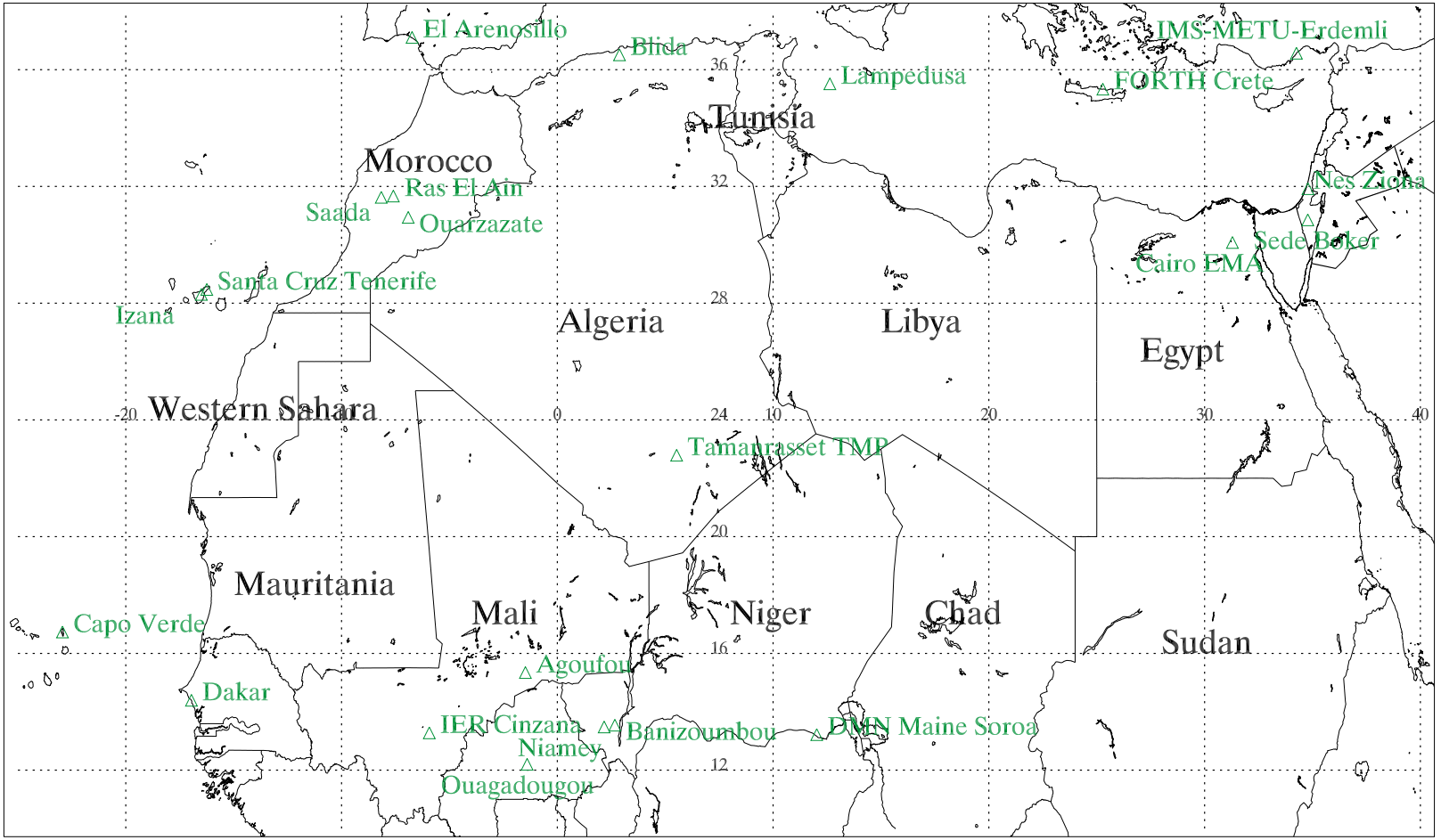

Figure 2.3: Saharan AERONET sites.

Site name	Country/Location	Latitude (°N)	Longitude (°E)	Altitude (m)
Agoufou	Mali	15.35	-1.48	305
Banizoumbou	Niger	13.54	2.67	250
Blida	Algeria	36.51	2.88	230
Cairo EMA	Egypt	30.08	31.29	70
Capo Verde	Cape Verde	16.73	-22.94	60
Dakar	Senegal	14.39	-16.96	0
DMN Maine Soroa	Niger	13.22	12.02	350
El Arenosillo	Spain	37.11	-6.73	0
Forth Crete	Greece (Mediterranean)	35.33	25.28	20
IER Cinzana	Mali	13.28	-5.93	285
IMS-Metu-Erdemli	Turkey	36.57	34.26	3
Izana	Canary Islands	28.3	-16.5	2391
Lampedusa	Italy (Mediterranean)	35.52	12.63	45
Nes Ziona	Israel	31.92	34.79	40
Niamey	Niger	13.48	2.17	205
Ouagadougou	Burkina Faso	12.2	-1.4	290
Ouarzazate	Morocco	30.94	-6.91	1150
Ras El Ain	Morocco	31.67	-7.6	570
Saada	Morocco	31.63	-8.16	420
Santa Cruz Tenerife	Canary Islands	28.47	-16.25	52
Sede Boker	Israel	30.86	34.78	480
Tamanrasset TMP	Algeria	22.79	5.58	1377

Table 2.1: AERONET sites.

2.4 Comparison between AERONET and DRI data

AERONET and DRI data are both used extensively in this thesis within the data assimilation scheme and for validation. Hence the level of the agreement between these two sources of data will be crucial in assessing the output from, and the validity of, the assimilation model.

Figure 2.4 shows a comparison between the AERONET data in March 2006 with the corresponding DRI data for that location. The baseline trend agrees well between DRI and AERONET for all sites, though there are several outlying points for particular events. Generally AERONET observes higher optical depths than do the DRI observations. This is particularly true during the 8th-10th for the AERONET sites in the south and west: this corresponds to the period when a stong dust storm was transported from northern Algeria across West Africa into the Atlantic and into sub-Saharan Africa.

Table 2.2 lists the root mean square (RMS) differences and the correlations between the AERONET sites and the local DRI observations for March 2006, and figure 2.5 maps the correlation. There is most agreement in the south and the west, in the Sahel area, and especially over Dakar. Further north the agreement is rather poorer, with the worst correlations over Saada in Morocco.

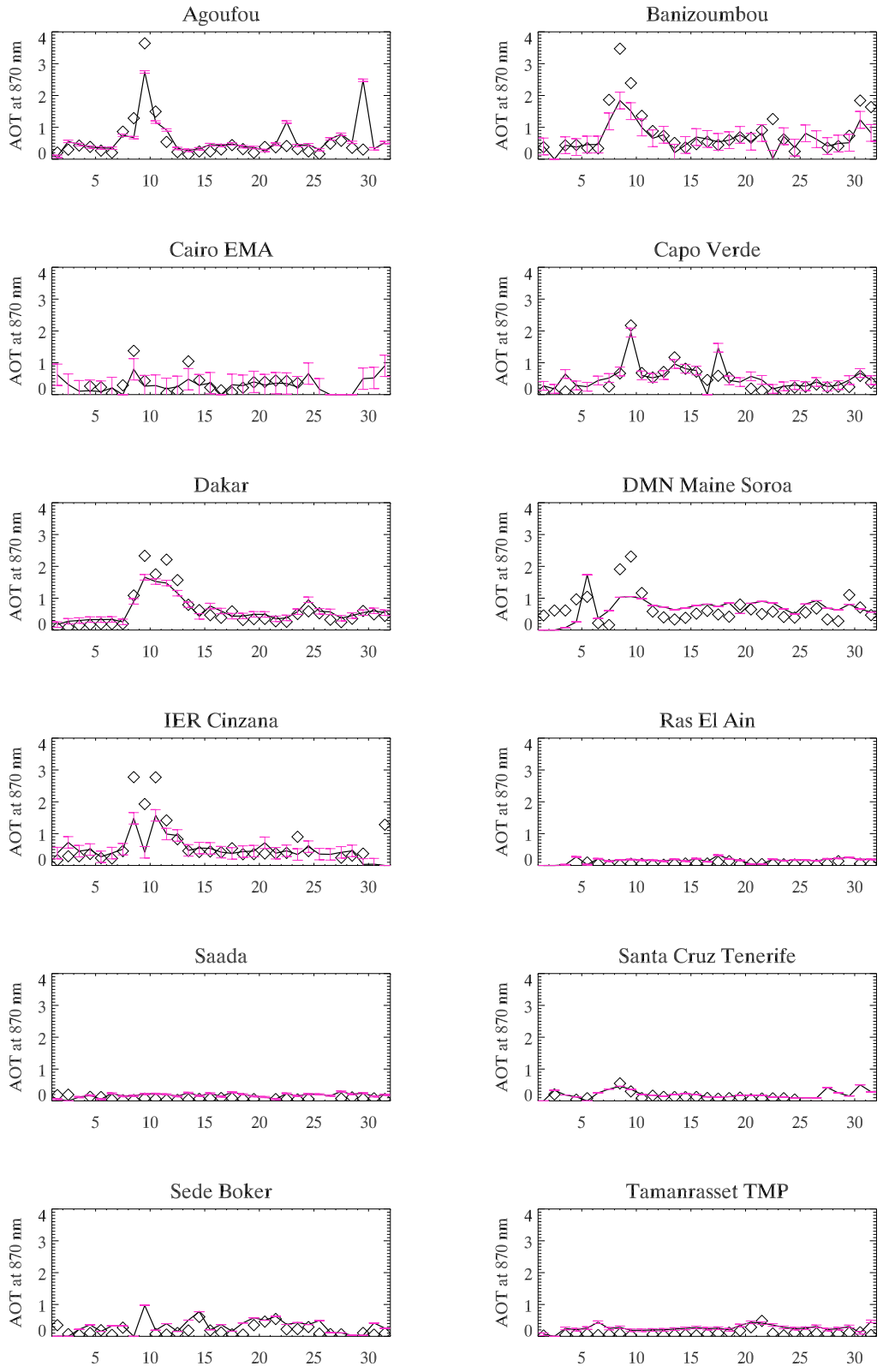

Figure 2.4: AERONET observations (black diamonds) during March 2006 compared with the local DRI observations (black line, pink error bars) for twelve sites with coincident AERONET and DRI data. Nes Ziona has only a small number of days of AERONET data during March 2006.

Site name	RMS difference	Correlation
Agoufou	0.331	0.77
Banizoumbou	0.495	0.80
Blida	No DRI data	-
Cairo EMA	0.202	0.81
Capo Verde	0.357	0.58
Dakar	0.233	0.94
DMN Maine Soroa	0.470	0.24
El Arenosillo	No AERONET data	-
Forth Crete	No DRI data	-
IER Cinzana	0.642	0.49
IMS-Metu-Erdemli	No DRI data	-
Izana	AERONET site too high	-
Lampedusa	No DRI data	-
Nes Ziona	0.134	0.37
Niamey	No AERONET data	-
Ouagadougou	No AERONET data	-
Ouarzazate	No AERONET data	-
Ras El Ain	0.126	0.32
Saada	0.132	-0.32
Santa Cruz Tenerife	0.112	0.71
Sede Boker	0.247	0.50
Tamanrasset TMP	0.188	0.46
Domain	0.314	0.42

Table 2.2: Comparison of daily averaged AERONET and DRI data, for March 2006.

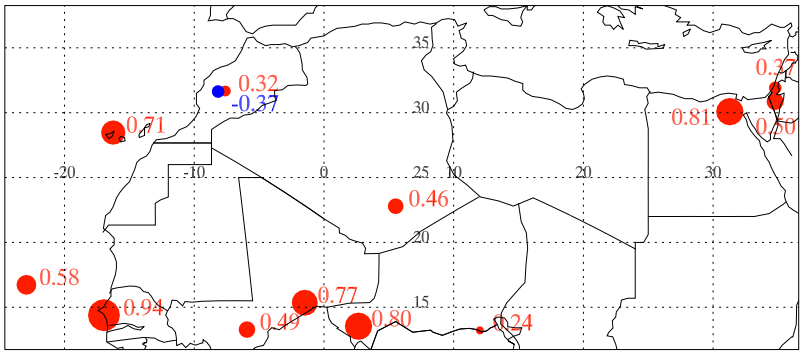

Figure 2.5: Map of correlations between AERONET and DRI data.

These differences in agreement indicate a limitation of the observations, since there is an inherent uncertainty to the observations. No one observational data source can provide complete information about a dust storm. AERONET provides very accurate, but highly localised, observations of AOD; SEVIRI provides regional observations, at high temporal, but low spatial, resolution; instruments such as AATSR provide high resolution observations, but only over a swath, only a few times a day; CALIPSO provides vertical aerosol profiles, but only along a very narrow swath. This means that there is a substantial amount of unavailable information, such as the dust aerosol mass, its size and horizontal/vertical distributions. For this reason, modelling can provide valuable extra information about the nature of dust storms, which observations alone cannot provide.

Chapter 3

Dust Emission

Dust emission is the process by which desert dust aerosol is lifted from the surface and entrained in the atmosphere. Emission is the process that is at the interface between the two states that a dust particle can be in: the surface state, in which it is subject to surface processes (e.g. river flow), and the atmospheric state, in which the dust aerosol is subject to atmospheric processes (e.g. turbulence).

Long-distance dust transport relies on the *suspension* of dust particles (Shao, 2000), generally with radius smaller than 35 μm. Dust *emission* is driven by the process of *saltation*, which triggers *sand-blasting*, enabling emission of small particles to higher altitudes, above the frictional boundary layer in which saltation occurs. Saltation (Marticorena and Bergametti, 1995) is the motion of a particle that is thrown up into the air through horizontal wind (and the impact of other saltating particles) but which quickly falls back to the ground since the updraught velocity and the turbulence are not sufficient to lift and suspend the particle: the maximum height of the saltation layer is of the order of 1 m. Saltating particles are thrown forward (horizontally) by the wind (Bagnold, 1941; Shao, 2000), describing a trajectory that is steep at first ($\sim$55 °), then travelling more horizontally (following the wind, while air drag acts against gravity), dropping at a shallow gradient and hitting the ground at an angle of $\sim$10 °. These particles tend to be the larger particles, since these have larger fall velocities than finer particles, with radii greater than 35 μm. A third dust transport mechanism is *creep*, the motion of the largest particles (radius $>$ 500 μm), too heavy to be lifted, rolling along the surface after being pushed by either the wind or saltating particles.

3.1 Model domain

This thesis is concerned with emission and transport of desert dust from North Africa, the most significant source of desert dust in the world. In order to calculate total emissions from North Africa, the model domain must include the entirety of the dust emitting regions of North Africa, including both the Sahara desert and the Sahel, running in a belt to the south of the Sahara. Another point of interest is the transport of dust away from North Africa; for example, over the Atlantic, or over Europe. Hence the model domain should be large enough to include non-emitting regions to the north, south, east, and west. The Middle Eastern deserts are beyond the scope of the current work (though the model could be extended to include them), so the eastern boundary of the model domain is the Red Sea.

Emissions have been calculated over the model domain, extending from 24 °W to 36 °E and from 12 to 38 °N. This domain stretches from the Atlantic in the west (as far west as Cape Verde, a measurement site), to the Red Sea and Israel in the east. In the south-north direction it stretches from just south of the Sahel region (e.g. northern Nigeria, Burkina Faso) in the south to the Mediterranean in the north, cutting across the southernmost reaches of Spain, Greece, and Turkey. Two different resolutions have been used: the 0.5 ° resolution atmospheric transport model, and a higher resolution of 0.25 ° as a sensitivity study.

In order to study and quantify desert dust emissions, knowledge is required of several initial conditions. Firstly, knowledge of the surface properties is required to know the size distribution of the emitted dust aerosol, the geographical variability of these distributions, and the geographical variability of surface features which may hinder (e.g. mountains, vegetation) and which may promote (e.g. dried lake beds) emission. Secondly, we need to know about the meteorological conditions in North Africa, specifically surface wind speeds (which drive emission) and precipitation (which hinders emission). From these parameters, and from formulating the dependence of emission on these parameters, emissions can be calculated.

3.2 Soil data

Two soil data sets have been used by the model.

The IGBP-DIS (International Geosphere-Biosphere Programme Data Information System) data set (Hall et al., 2005) has been obtained from the International Satellite Land Surface Climatology Project (ISLSCP II) via the British Atmospheric Data Centre (BADC), based on the work by

Index	Soil type	% Sand	% Silt	% Clay	α (cm^{-1})
0	Water	-	-	-	-
1	Silty fine sand (SFS)	82.6	11.5	5.9	6.15E-6
2	Medium sand (MS)	94.2	5.1	0.7	1.25E-6
3	Coarse sand (CS)	95.8	4.2	0.0	1.00E-6
4	Coarse medium sand (CMS)	94.9	4.7	0.4	1.12E-6
5	Fine sand (FS)	87.7	8.7	3.6	3.04E-6
6	Silty medium sand (SMS)	85.1	10.1	4.8	4.35E-6
7	Moderately salty silt (SEM)	85.6	9.9	4.5	4.04E-6
8	Highly salty silt (SEF)	87.4	8.9	3.7	3.18E-6
9	Clayey soil	-	-	-	-
10	Salt waste (SW)	81.3	12.2	6.5	7.35E-6
11	Agricultural soil (AGS)	74.0	16.3	9.7	19.9E-6
12	Salty fine sand (SES)	86.6	9.3	4.1	3.50E-6
13	Silty coarse sand (SCS)	87.1	9.0	3.9	3.31E-6
21	Mountains, rocks, urban areas	-	-	-	-
22	Rivers, water basins	-	-	-	-
23	Cultivated land	-	-	-	-
24	Irrigated land	-	-	-	-

Table 3.1: Soil size mass percentages and sand-blasting efficiencies for each soil type, from the LISA soil data set.

Zobler (1986). It is a global data set, at a resolution of $1\times1\,^{\circ}$, and contains percentages of clay, silt and sand. The distributions are normalised so that the total distribution over all particle sizes is 1. Results from the emission model using IGBP data are presented in section 3.9.

The regional soil data set produced by the Laboratoire Interuniversitaire des Systèmes Atmosphériques (LISA) in Paris, and described in Laurent et al. (2008) (based on the work of Marticorena et al. (1997) and Callot et al. (2000)), has a finer resolution, at $0.25\times0.25\,^{\circ}$. Data are provided for North Africa and the Middle East as far south as $16\,^{\circ}$N, and as far east as $60\,^{\circ}$E, bound by the Mediterranean to the north and the Atlantic to the west. Each grid point is described by two constituent components (classes) of soil, and a prediction is made for the fraction of the surface covered by each class. The soil *type* specifies the nature of the soil, e.g. coarse sand (type 3). The percentages of sand, silt, and clay can be predicted from these soil types, while various other surface properties (e.g. roughness length, sand-blasting efficiency, and residual soil moisture) can be inferred from the soil type. Here, sand is defined as particles with radii between 25 and 500 μm, silt has radii between 1 and 25 μm, while clay has radii less than 1 μm. Table 3.1 defines the properties of each soil type, while figure 3.1 maps the soil type for the two soil classes.

The LISA soil data set is the preferred data set (used in the current model) for three main reasons:

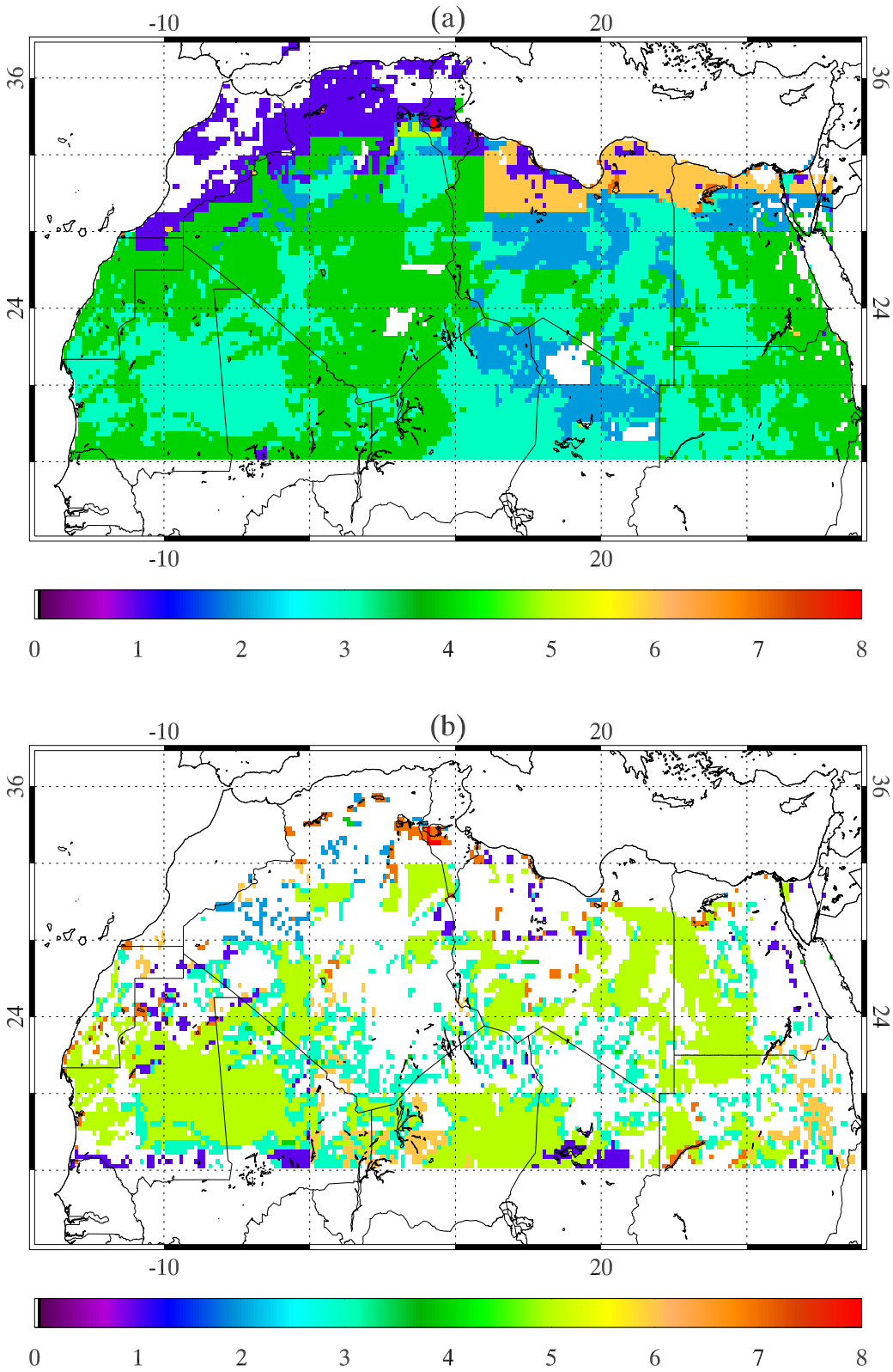

Figure 3.1: Maps of the soil types present at each grid point. The scale refers to the indices in column 1 of table 3.1. Types 10-13 are not specified as being present within the Saharan domain. (a) is the first soil class, which generally is the dominant soil, (b) is the second soil class.

(1) The resolution is 4 times that of the IGBP-DIS soils;
(2) As well as soil texture, data are included for the fraction of the surface covered by soil, surface roughness length (total and smooth, see section 3.4.4), sand-blasting efficiency, residual soil moisture, and the erodible fraction of the soil;
(3) The data are taken from soil measurements which use a 'dry-sieving' technique (Chatenet et al., 1996) to measure the soil size distribution. Global soil data sets such as the FAO soil map of the World tend to use wet sieving techniques, which dis-aggregate the soil physically and by dissolving soluble minerals. This means that the observed size distribution will contain a higher fraction of smaller particles than would exist in the natural state. Within the Sahara, the IGBP soils contain a mean of 14.5% clay, whereas the LISA soils contain a mean of 1.0% clay.

3.3 Meteorological data

Meteorological data are required to drive the emissions and the transport models, using both wind and precipitation data. The Operational Analysis global data set (produced since 1994) from the European Centre for Medium-range Weather Forecasting (ECMWF) is used for this purpose. The data are gridded onto a reduced Gaussian grid format, with a resolution of $1.125\,^{\circ}\times1.125\,^{\circ}$. For calculating emissions, we require two parameters from ECMWF: the surface 10 m wind speed, and the daily rainfall. The wind speed is provided in two components: the 10 m zonal velocity (u), and the meridional velocity (v). The daily rainfall is provided by two properties: the large-scale precipitation (lsp) and the convective precipitation (cp). The cloud cover (cc) is also provided. The large-scale (frontal) and the convective precipitation are measured in $\mathrm{mm\,day^{-1}}$, and relate to two different types of rainfall, with the large-scale precipitation being less intense than the convective precipitation. The cloud cover is provided as a fraction of the sky covered by cloud, on height levels. Other properties which could be useful for calculating emissions include soil moisture, vegetation cover, and surface roughness length.

ECMWF is just one of the global meteorological data sets that could have been used to drive the dust emissions and transport model. The US National Centers for Environmental Prediction (NCEP) also produce a global meteorological data set. There are differences between the two data sets, and hence this could give rise to differences in the resultant modelled emissions between an ECMWF-driven model and a NCEP-driven model. According to Menut (2008), the ECMWF winds have much more spatial variability than the NCEP winds, suggesting that the ECMWF

winds could drive higher emission rates (since there would be a higher occurrence of high wind speed events). The focus in this thesis is on the soil properties and their effects on dust transport rather than on the analysed meteorology, so only the ECMWF data set is used.

The ECMWF model is produced in two main versions: the Operational Analysis model, which is the most up-to-date model version at the time, and the Re-Analysis model, which applies a standardised model version retrospectively, over a period of several years. ERA-40 re-analysis data, for example, is provided for a period of over four decades, from 1957 to 2002. Much more recently ERA-Interim, a new re-analysis data set, has been introduced, providing re-analysis data up to the present. Due to the changes in the model used to produce the Operational Analysis data set, this data set has the problem of inconsistency in the model over an extended multi-year period; its advantage is that it is the most state-of-the-art model produced by ECMWF at the time. Meanwhile re-analysis data has the advantage of consistency, although it may be produced by a less sophisticated model. For multi-year SHAMAL simulations of dust emission we may prefer to use re-analysis data (only recently available for 2006, however). On the other hand, Operational Analysis data may be preferable for shorter timescales, such as for March 2006, the specific period of interest for the data assimilation model (as described in chapter 7). Since this short period of time is our main focus in this thesis, it may be justified to use the Operational Analysis version throughout.

3.4 Dust emission parameterisation

3.4.1 Wind friction velocity

Within the layer of the atmosphere closest to the surface (the frictional boundary layer), the wind speed is reduced due to surface friction effects, reaching a minimum at the surface. The wind speed as a function of height $u(z)$ can be described by a logarithmic relationship (Prandtl, 1935):

$$u(z) = \frac{u^*}{\kappa} \ln\left(\frac{z}{z_0}\right). \tag{3.1}$$

The wind friction velocity, u^*, is dependent on the surface roughness, described by Almeida et al. (2006), for example, who define:

$$u^* = \frac{u(z)\kappa}{\ln(\frac{z}{z_0})}, \tag{3.2}$$

where κ is the von Karman constant ($\kappa = 0.4$), u^* is the wind friction velocity, and z_0 is described in more detail in section 3.4.4. Here, $u(z)$ is the 10 m wind speed, hence, $z = 10$ m.

3.4.2 Threshold friction velocity

The threshold friction velocity, u_t^*, defines the minimum wind friction velocity required to lift a particle of a certain size up from the surface into the saltation layer, or equivalently, the velocity at which the aerodynamic forces due to the air equal the particle weight and interparticle cohesion forces (Marticorena and Bergametti, 1995). Theoretically, if you consider spherical grains placed randomly on a surface, then each surface grain will be partially lodged in behind another grain. The equivalence of the moment of the weight of the grain around the contact point with the moment of the force exerted by the wind gives rise to a theoretical expression (Bagnold, 1941) for the threshold velocity:

$$u_t^*(D_p) = A\sqrt{\frac{\rho_p - \rho_a}{\rho_a} g D_p}, \tag{3.3}$$

where D_p is the particle diameter, ρ_p is the particle density, ρ_a is the air density, g is gravitational acceleration, and A is a dimensionless constant (discussed further below). Hence we would expect that the threshold velocity increases with particle size.

However, Bagnold (1941) also found (observationally) that the threshold velocity increased for the smallest particles. This is due to the interparticle cohesion forces, such as electrostatic and van der Waals forces (Iversen and White, 1982), as well as moisture. Using wind-tunnel measurements, Iversen and White (1982) produced empirical formulations to define the constant A in equation 3.3. Following this work, Marticorena and Bergametti (1995) use a semi-empirical equation to describe the threshold friction velocity:

$$u_t^*(D_p) = \frac{0.129}{\sqrt{1.928(1331 D_p^{1.56} + 0.38)^{0.092} - 1}} \times \sqrt{1 + \frac{6 \times 10^{-7}}{\rho_p g D_p^{2.5}}} \times \sqrt{\frac{\rho_p g D_p}{\rho_a}}. \tag{3.4}$$

The minimum threshold velocity occurs at 75 μm in diameter, where the threshold velocity is 0.2 $\mathrm{m\,s^{-1}}$. Above this diameter, the extra mass in the particle means that gravity holds it down, whereas below this diameter, interparticle cohesion forces bind the particles together more strongly, so that they are less free to move. Figure 3.2 shows how the threshold velocity increases for the smallest particles. These particles are the ones most likely to be suspended in the atmosphere after emission, so it is clear that wind alone cannot mobilise the smallest (sub-micron) particles, which are observed higher in the troposphere, since this requires excessively large surface wind velocities.

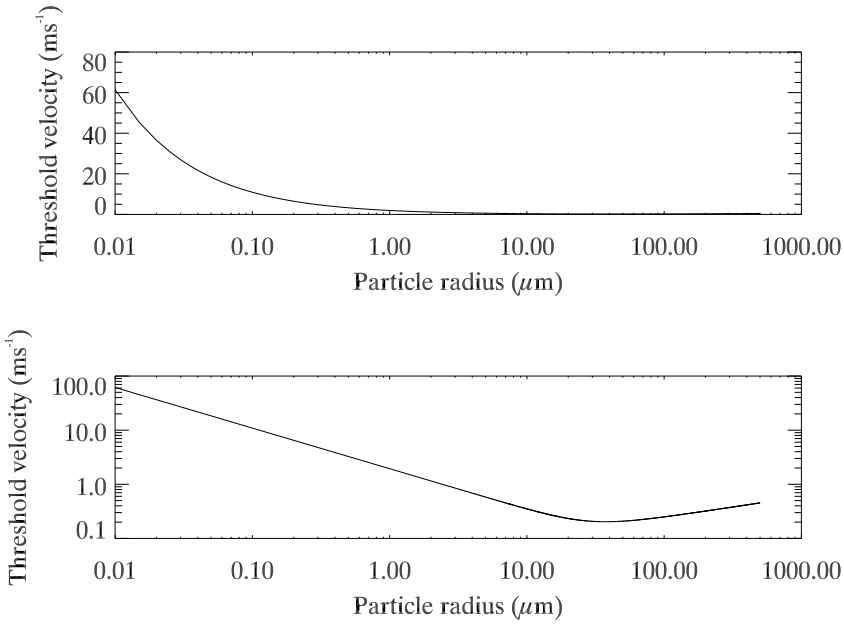

Figure 3.2: Threshold friction velocity as a function of particle radius. The threshold friction velocity is plotted on a linear scale (upper frame) and on a logarithmic scale (lower frame). Typical maximum surface wind speed is of the order of 10-20 $\mathrm{m\,s^{-1}}$. Particles with radii less than 100 nm are often only mobilised with difficulty.

When the larger particles strike the surface during saltation, they transfer momentum to the surface particles that they hit. This can break up some of the aggregates in the soil, and encourage the lifting of finer dust particles. Therefore, we can estimate the dust emission flux from the saltation flux: according to Mahowald et al. (2005), since emission requires saltation as an intermediate process, the emission flux is generally regarded as being directly proportional to the saltation flux.

3.4.3 Emission flux

To quantify the emission flux, two emission schemes have been tested within the model. The first is a power-law emission scheme which depends on wind speed, the threshold velocity, and the soil particle size distribution. The second is a 'saltation' emission scheme, based on the work by Marticorena and Bergametti (1995), of intermediate complexity, which first calculates the horizontal saltation flux explicitly, and uses this to predict the vertical emission flux.

Power-law schemes

Simple power-law schemes tend to be used in Global Climate Models (GCMs), since the resolution is coarse enough that it may not be useful to add extra sub-grid scale parameters. The power-law scheme considered here is the semi-empirical formulation of Ginoux et al. (2001), which considers emission to be a function of the surface wind speed ($u_{10\mathrm{m}}$), the threshold velocity (u_{t}), and the size distribution (which describes the normalised source fraction, $s(r)$). It is described by:

$$F(r) = \begin{cases} Cs(r)u_{10\mathrm{m}}^2(u_{10\mathrm{m}} - u_{\mathrm{t}}) & \text{if } u_{10\mathrm{m}} > u_{\mathrm{tp}} \\ 0 & \text{otherwise,} \end{cases} \tag{3.5}$$

where C is a dimensional factor, equal to 1 $\mu\mathrm{g\,s^2\,m^{-5}}$. Greater surface wind speed has two effects: firstly, it increases the mass from each size class which is lifted; secondly, it reduces the minimum particle size which can be lifted.

Sudden strong gusts of wind can have a significant effect on the quantity of dust emitted, since the emission is proportional to the cube of the surface wind speeds. Moreover, there may be a more significant correlation between wind gustiness and dust events than between average wind speed and dust events (Engelstaedter and Washington, 2007b). The method of Miller et al. (2006), also used by Menut (2008), enhances the formulation of Ginoux et al. (2001) to simulate wind gustiness, by imposing a Weibull distribution on the surface wind speeds. The shape factor (Grini and Zender, 2004) of the wind distribution is given by $k_{\mathrm{r}} = 0.94\sqrt{u_{10\mathrm{m}}}$. The scale factor of this distribution is given by $c_{\mathrm{r}} = u_{\mathrm{r}}/\Gamma(1 + \frac{1}{k_{\mathrm{r}}})$, and depends on the shape factor. The shape factor and the scale factor provide a distribution of wind speeds (w) around the ECMWF value of the wind speed (Justus et al., 1978):

$$p(w)\,dw = \frac{k_{\mathrm{r}}}{c_{\mathrm{r}}}\Big(\frac{w}{c_{\mathrm{r}}}\Big)^{k_{\mathrm{r}}-1} \exp\Big[-\Big(\frac{w}{c_{\mathrm{r}}}\Big)^{k_{\mathrm{r}}}\Big]\,dw. \tag{3.6}$$

The emission flux is then obtained by integrating the emission (based on equation 3.5) over this distribution of winds:

$$F(r) = Cs(r)\int_{u_{\mathrm{t}}}^{\infty} w^2(w - u_{\mathrm{t}})p(w)\,dw. \tag{3.7}$$

Results from the emission model using the power-law scheme are presented in section 3.9, but this method is not generally used in the SHAMAL model.

Emission from saltation flux: Marticorena and Bergametti (1995)

An alternative approach to calculating emission has been formulated by Marticorena and Bergametti (1995) (henceforth denoted as MB95). This approach explicitly calculates the horizontal saltation flux G (adapted from White (1979)):

$$G = E\frac{\rho_{\mathrm{a}}}{g}u^{*3}\int_{D_{\mathrm{p}}}^{\infty}\Big(1+\frac{u_{\mathrm{t}}^{*}(D_{\mathrm{p}})}{u^{*}}\Big)\Big(1-\frac{u_{\mathrm{t}}^{*2}(D_{\mathrm{p}})}{u^{*2}}\Big)\delta S_{\mathrm{rel}}(D_{\mathrm{p}})\,dD_{\mathrm{p}}, \tag{3.8}$$

where E is the fraction of erodible surface (section 3.4.4), and δS_{rel} is the fraction of the soil mass containing particles of each size D_{p}.

The vertical emission flux of fine particles (with a diameter less than 20 μm) F is linearly related to the saltation flux by the *sand-blasting efficiency*, α (typically in units of cm^{-1}):

$$F = \alpha G. \tag{3.9}$$

The sand-blasting efficiency is a surface property which defines how readily the surface emits fine aerosol particles, and is described in section 3.4.5. An example dust emission field from the MB95 scheme can be seen in figure 3.3.

More complex emission schemes, including aggregate disintegration

More complex emission schemes take into account more properties of the surface, and include processes such as *disaggregation* (Shao, 2001, 2004), wherein aggregates of soil are broken up, releasing finer particles. The method is broadly similar to the MB95 approach, since saltation is still required, and the flux is given by:

$$F(d_{\mathrm{i}},d_{\mathrm{s}}) = c_{\mathrm{y}}\eta_{\mathrm{fi}}[\Big(1-\exp(-(u^{*}-u_{\mathrm{t}}^{*})^{3})\Big)+\exp(-(u^{*}-u_{\mathrm{t}}^{*})^{3})\sigma_{\mathrm{p}}](1+\sigma_{\mathrm{m}})\frac{gG(d_{\mathrm{s}})}{u^{*2}}, \tag{3.10}$$

where d_{i} and d_{s} are the diameters of the emitted dust (denoted by i) under the influence of the saltators (denoted by s), c_{y} is a dimensionless coefficient, η_{fi} is the total dust fraction of free and aggregated dust, σ_{p} is the ratio of free to aggregated dust, σ_{m} is the ratio of the mass ejected to the mass of the impactor (bombardment efficiency), and G is the saltation flux. This method has not been used in the current model due to a paucity of information on ratios of aggregates, and on soil plastic pressure, used to find σ_{m}: excessive parameterisations may be required. The MB95 scheme

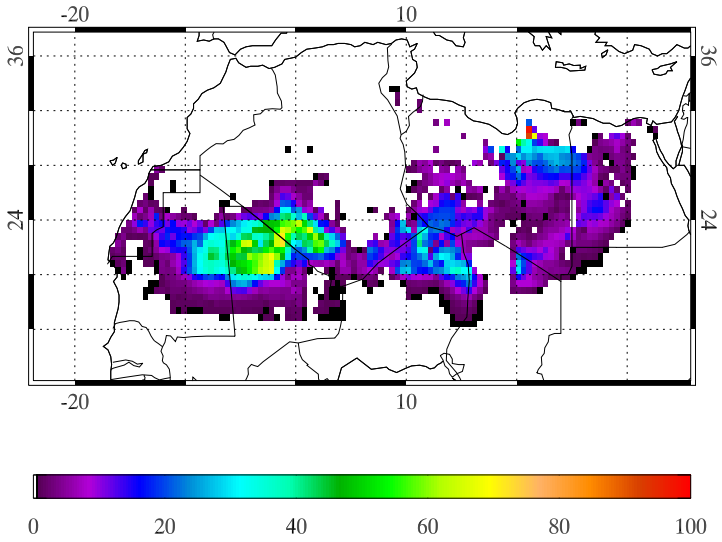

Figure 3.3: Daily dust emission ($\mathrm{g\,m^{-2}\,day^{-1}}$) computed over the Sahara for the 7th March 2006, using the MB95 emission scheme. Note the strong emission coming off southern Algeria and northern Mali, a region previously identified as an important source. This plot is from the period when a very strong dust event, observed by SEVIRI, swept south through West Africa and out into the Atlantic, originating from the lee of the Algerian Atlas mountains (Slingo et al., 2006). The total simulated emission for the day is 52.3 Tg.

has therefore been used, since it is more appropriate to use it than a simpler scheme, for a regional dust model. Tests comparing the two emission schemes (MB95 and power-law) are presented in section 3.9, and suggest that the MB95 scheme is preferable.

3.4.4 Roughness length

The roughness length, z_0, is a length scale which describes the roughness of the surface, and is the main surface property governing dust emissions within the Sahara desert, ahead of soil moisture (most important on the coasts and in the Sahel). Surface features associated with high roughness include mountains (i.e. sharp gradients in topography), stony deserts (such as hamadas), and areas of high vegetation. Vegetation suppresses emission (Tegen et al., 2002) both by providing extra roughness elements, and by binding the soil together due to roots, grass, and moisture. The presence of vegetation is included in the soil data set, with soil types 23 and 24 (table 3.1) relating to cultivated and irrigated land, both of which are considered a priori not to be source regions. Figure 3.4 maps the roughness length over North Africa used in this thesis, derived from satellite data from the POLDER instrument (Marticorena et al., 2004). Roughness length is derived using

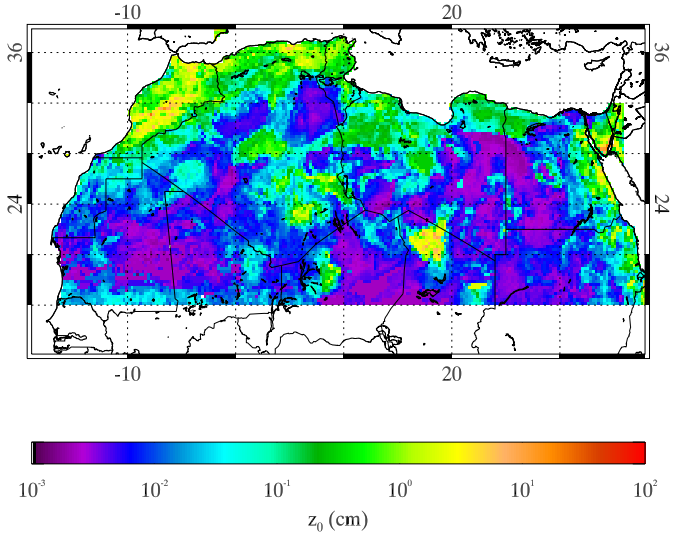

Figure 3.4: Map of the surface roughness length, z_0 (in cm), of soil class 1.

the bidirectional reflectance (BRDF) of the surface, from which a 'Protrusion Coefficient' (PC) can be estimated, which is a dimensionless parameter indicating the surface roughness. This relates to the roughness length by the empirically derived relationship (by comparing POLDER observations and site roughness lengths measured by a geomorphological approach):

$$PC = 0.052 \ln z_0 + 0.277. \tag{3.11}$$

The fraction of the erodible surface (Laurent et al., 2008), E, is a consequence of the roughness length. For particularly rough surfaces, the lower areas surrounded by the roughness elements (e.g. ripples, dunes, rocks, etc.) are sheltered from the wind, and so are not subject to wind stress forces. Figure 3.5 maps the erodible fraction over North Africa, while figure 3.6 shows the relationship between the roughness length (in cm) and E, and it is given by:

$$E(z_0) = \begin{cases} 1 & z_0 < 3 \times 10^{-3} \text{ cm} \\ 0.7304 - 0.0804 \log(z_0) & z_0 > 3 \times 10^{-3} \text{ cm}. \end{cases} \tag{3.12}$$

The drag partition function (Marticorena et al., 1997), f_{eff}, arises in a similar fashion to the fraction of erodible surface. Between the roughness elements an 'internal' boundary layer is formed, with a separate vertical wind profile to the overall profile. The 'smooth' roughness length $z_{0\text{s}}$ which

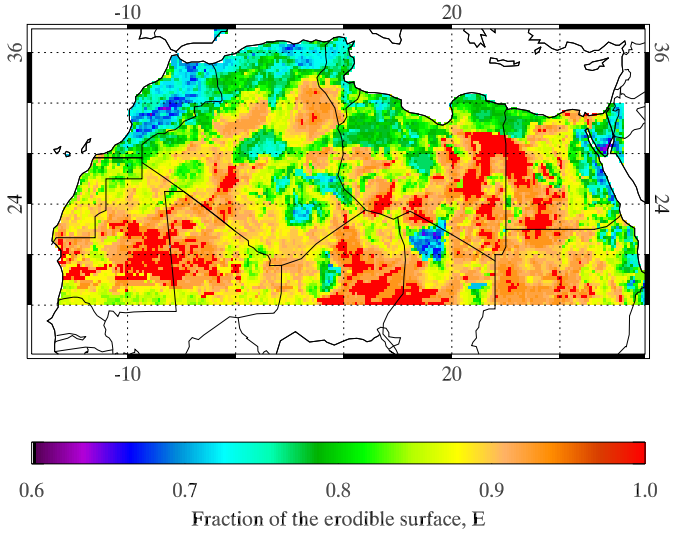

Figure 3.5: Map of the fraction of erodible surface, E, of soil class 1.

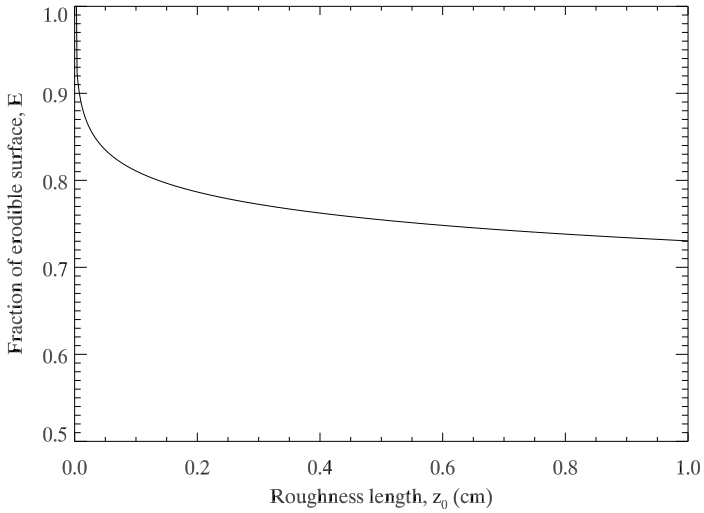

Figure 3.6: The relationship between the roughness length, z_0, and the fraction of erodible surface, E.

governs this internal region does not exceed 23 μm (in the LISA soil data set), which is always less than or equal to the total roughness length z_0. The presence of the larger roughness elements reduces the efficiency of the erosion of the erodible region, and the effect of this on the threshold friction velocity can be expressed as (Marticorena et al., 1997):

$$u_{\mathrm{t}}^{*}(D_{\mathrm{p}}, z_0, z_{0\mathrm{s}}) = \frac{u_{\mathrm{t}}^{*}(D_{\mathrm{p}})}{f_{\mathrm{eff}}(z_0, z_{0\mathrm{s}})}, \tag{3.13}$$

where

$$f_{\mathrm{eff}}(z_0, z_{0\mathrm{s}}) = 1 - \left\{ \ln\left(\frac{z_0}{z_{0\mathrm{s}}}\right) / \ln\left[0.35\left(\frac{10}{z_{0\mathrm{s}}}\right)^{0.8}\right]\right\}. \tag{3.14}$$

Figure 3.7 shows the relationship between z_0 and f_{eff}, and figure 3.8 maps the factor by which the threshold velocity increases in North Africa.

3.4.5 Sand-blasting efficiency, α

The sand-blasting efficiency, α (Marticorena et al., 1997), defines the ability of the soil to release the finer particles suitable for higher-altitude atmospheric transport, and is dependent on the quantity of these fine particles. It can be described by the empirical relation (Gillette, 1979):

$$\alpha = 10^{(0.134c-6)}, \tag{3.15}$$

where c is the percentage of clay, and α has units of cm^{-1}. Typically α is of the order of 10^{-6} cm^{-1} in the Sahara (since the Sahara has a low clay content, less than 6%), using data from the LISA soil data set and equation 3.15. It is mapped in figure 3.9. The sand-blasting efficiencies are derived from the list of soil types presented in table 3.1. The majority of the Sahara south of the Atlas mountains is composed of soils of types 2-4 (medium sand, coarse sand, and coarse medium sand), which have a low clay content and hence a low sand-blasting efficiency, of $\sim 1\times10^{-6}$ cm^{-1}. Further north, along the Mediterranean coast, the soils have a higher clay content (predominantly types 1 and 6, silty fine sand and silty medium sand), which corresponds to higher sand-blasting efficiencies of up to 6.15×10^{-6} cm^{-1}. As a consequence, the majority of the Sahara is comparatively inefficient at converting the horizontal saltation flux into a vertical flux of smaller particles to higher altitudes. While this might lead us to conclude that the central Sahara may not be an efficient dust source, the comparatively low sand-blasting efficiency must be balanced against the lower roughness lengths, and hence the lower threshold friction velocities and higher saltation fluxes, that will be found in the central Sahara, as opposed to those found on the coast and in the Atlas mountains.

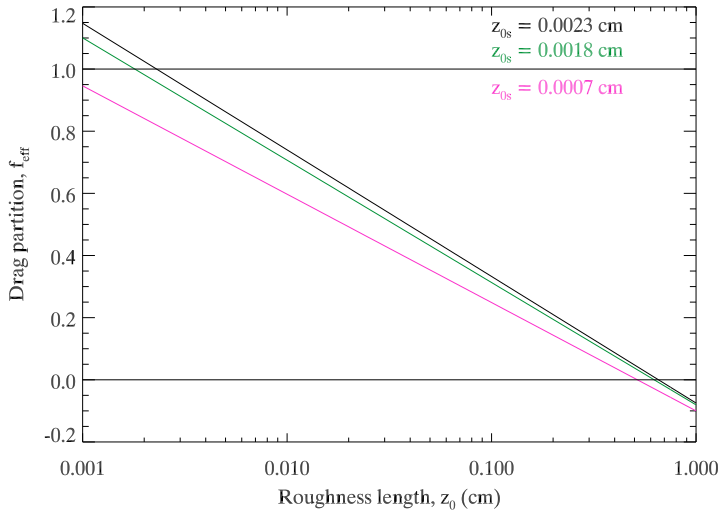

Figure 3.7: The relationship between roughness length z_0 and the drag partition f_{eff}, for typical values of $z_{0\text{s}}$. Above $f_{\text{eff}} = 1$, there is no drag partitioning (i.e. the threshold velocity does not increase), and below $f_{\text{eff}} = 0$, emission is completely suppressed.

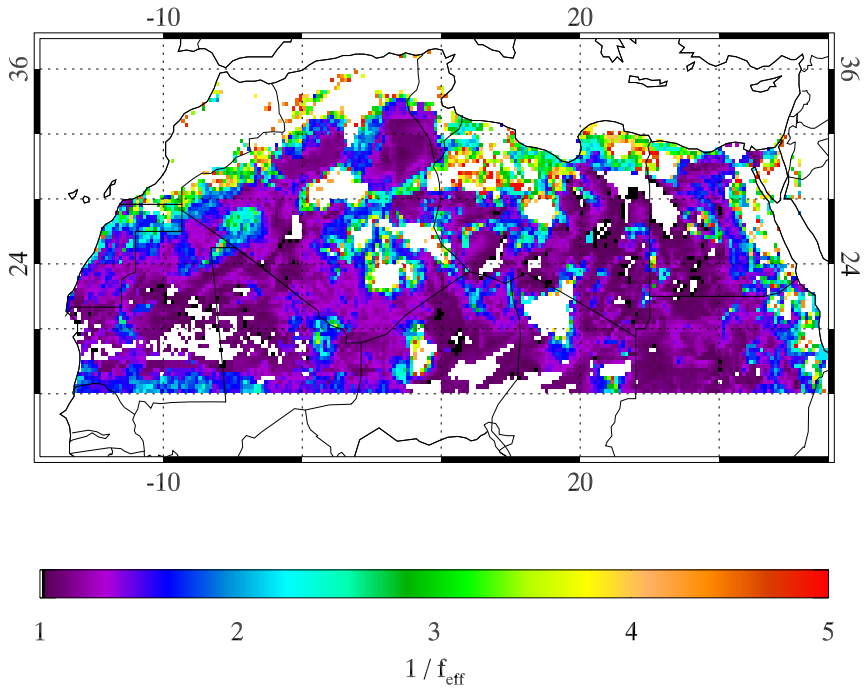

Figure 3.8: Map of the increase in threshold friction velocities due to the drag partitioning ratio 1 / f_{eff}. Regions in white areas are either non-emitting surfaces (e.g. seas, mountains), or are surfaces where the theshold friction velocity has increased by a factor of over 5, above which there is very rarely strong enough wind (> 20 m s^{-1}) to mobilise any particles.

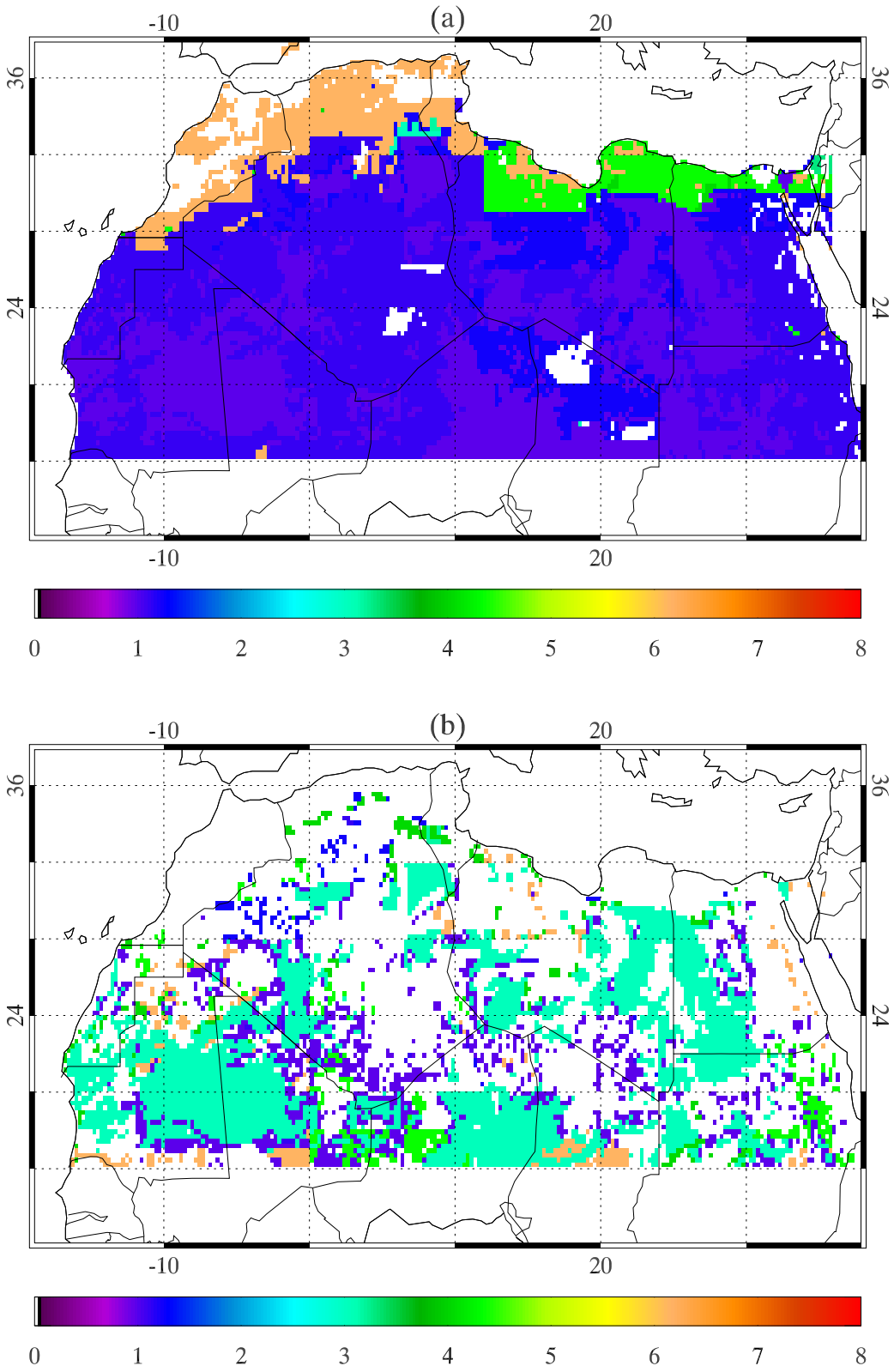

Figure 3.9: Maps of sand-blasting efficiencies ($\times 10^{-6}$ cm^{-1}) for (a) soil class 1, and (b) soil class 2.

3.4.6 Soil moisture

Soil moisture hinders dust emission by binding the soil together more tightly. The influence of soil moisture has been described by Fécan et al. (1999), who relates the fractional increase in the threshold friction velocity to the percentage gravimetric soil moisture w and the *residual soil moisture* w', a property of the soil dependent on the soil texture. Physically, the residual soil moisture is the moisture that is adsorbed by the soil particles: for larger particles the inter-molecular forces are weaker, so the residual soil moisture is reduced. It can therefore be described by reference to the clay percentage c of the soil:

$$w' = 0.0014c^2 + 0.17c. \tag{3.16}$$

The ratio of the wet threshold velocity to the dry threshold is of the form (Fécan et al., 1999):

$$\frac{u^*_{\mathrm{tw}}}{u^*_{\mathrm{td}}} = \begin{cases} 1 & \text{if } w < w' \\ \sqrt{1 + a(w - w')^b} & \text{if } w > w'. \end{cases} \tag{3.17}$$

Empirical estimates suggest that $a = 1.21$, and $b = 0.68$.

In the current model a simpler scheme has been used, following the approximations made by Grini et al. (2005), Myhre et al. (2003) and Claquin (1999). The reason for this approach is the unreliability of the ECMWF analysis soil data, which does not deal with evaporation from soil when the humidity is less than 0.171 $\mathrm{m}^3\,\mathrm{m}^{-3}$: hence the soil moisture of the arid desert is over-predicted. Grini et al. (2005) proposes to mask out emission during and after rainfall, on the basis that wet soils are not ready emitters of dust, and that the soils must have sufficient time to dry before emission can occur again: this time will be longer after heavier outbreaks of rainfall. Two conditions are imposed when there is a rainfall event: (1) if precipitation exceeds 0.5 mm, then emission is not permitted that day; (2) after a rainfall event, the soil takes as many days to dry as the amount of precipitation (in mm) that fell during the most recent rainfall event (up to a maximum of 5 days). Figure 3.10 shows a map of the annual frequency of rainfall events, when the precipitation exceeds 0.5 mm.

3.4.7 Summary of emission scheme

To summarise, the emission scheme used is the MB95 scheme, taking into account particle threshold velocities, wind friction velocity, surface roughness length, sand-blasting efficiencies, and modified

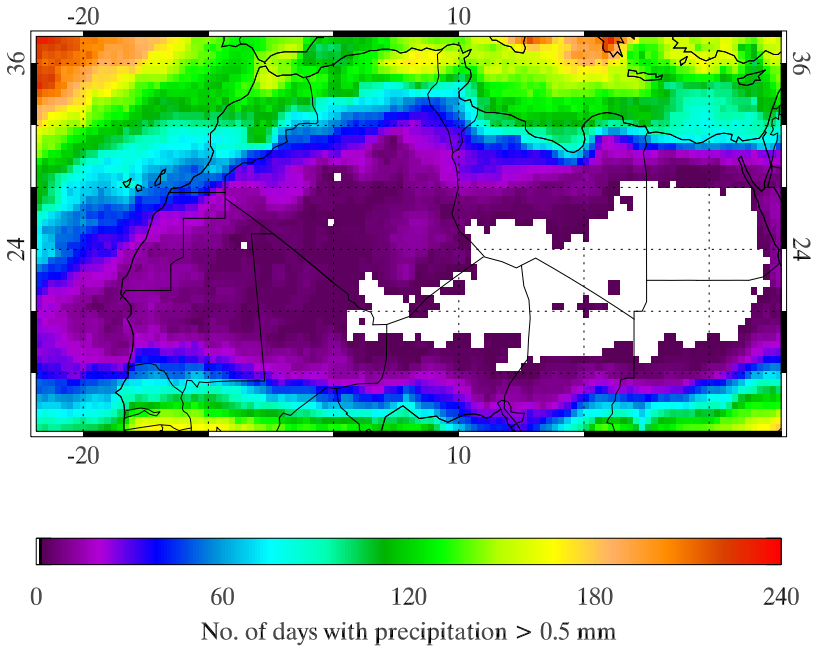

Figure 3.10: Map of the number of days during 2006 when precipitation exceeded 0.5 mm (the limit for emission). Areas in white had no such days.

to include the effects of precipitation on soil moisture. The LISA soil data set is used for the surface properties. By combining equations 3.8 and 3.9 the emission flux is given by:

$$F = \alpha E \frac{\rho_a}{g} u^{*3} \int_{D_p}^{\infty} \left(1 + \frac{u_t^*(D_p, z_0, z_{0s})}{u^*}\right)\left(1 - \frac{u_t^*(D_p, z_0, z_{0s})^2}{u^{*2}}\right) \delta S_{rel}(D_p)\, dD_p. \tag{3.18}$$

3.5 Soil size distribution

Two soil size distributions are used within the model: an example is displayed in figure 3.11. The first is the distribution for the saltation flux (which is most concerned with the saltation of sand and large silt particles, which require the lowest threshold velocities for them to mobilise), while the second is used in the aerosol transport model. The latter is the output of the emission and consists, by definition, of particles with a radius < 10 μm, i.e. clay and small silt. Computationally, the 3D atmospheric transport scheme is substantially more demanding than the 2D surface emission scheme, so it is possible to have a highly size-resolving distribution in the saltation flux without significant impact on the overall computational expense. This is important because the surface features of the desert source regions are much finer and more discrete in scale than is the

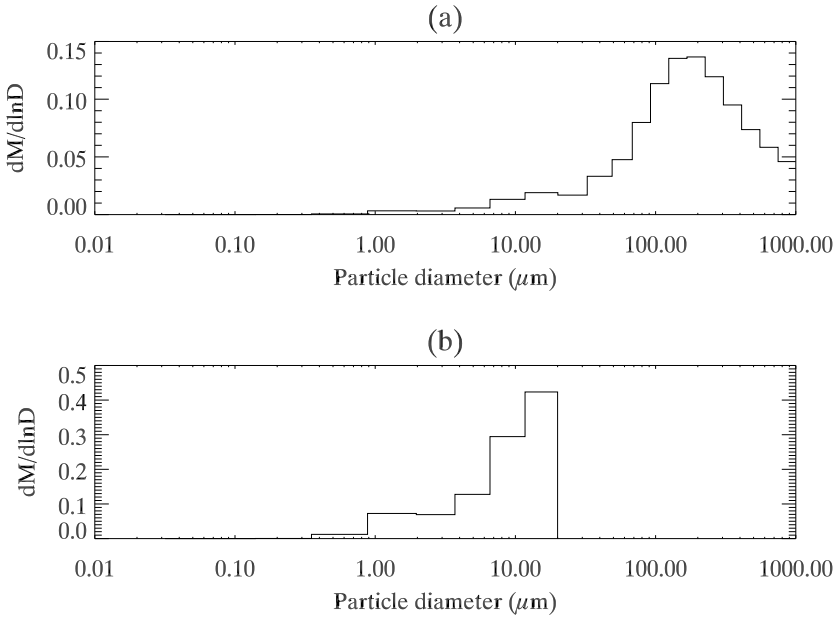

Figure 3.11: Normalised mass distributions of soil type 2 (medium sand) in the LISA soil data set, binned into the nine particle sizes. (a) Distribution of saltating particles. (b) Distribution of potential aerosol particles.

atmospheric dust transport, and hence it is preferable to have higher resolution for the surface processes than for the atmospheric processes.

To distribute the particle sizes, it is assumed that the dust aerosol follows a *lognormal* size distribution (Seinfeld and Pandis, 2006), whereby the logarithm of the particle sizes is normally distributed. The lognormal distribution is frequently used for aerosols since, empirically, it often gives a good approximation. If the mass is distributed lognormally, then the size distribution $dM/d\ln D$ as a function of particle diameter D is given by:

$$\frac{dM}{d\ln D} = \frac{M_0}{\sqrt{2\pi}} \frac{1}{\ln \sigma} \exp\left(- \frac{(\ln D - \ln \overline{D})^2}{2(\ln \sigma)^2} \right), \tag{3.19}$$

where M_0 is the total mass of aerosol, $\overline{D}$ is the mean diameter, and σ is the standard deviation. Figure 3.12 shows an example of a lognormal distribution.

A combination of four log-normal modes has been used for the four soil types: clay, silt, medium/fine sand, and coarse sand. Following Tegen et al. (2002), the properties of each mode are listed in table 3.2. There is substantial uncertainty in these distributions, and so in the SHAMAL model two possible values of the clay mean radius ($\bar{r}_{\text{clay}}$) are tested: the literature value of 1 μm,

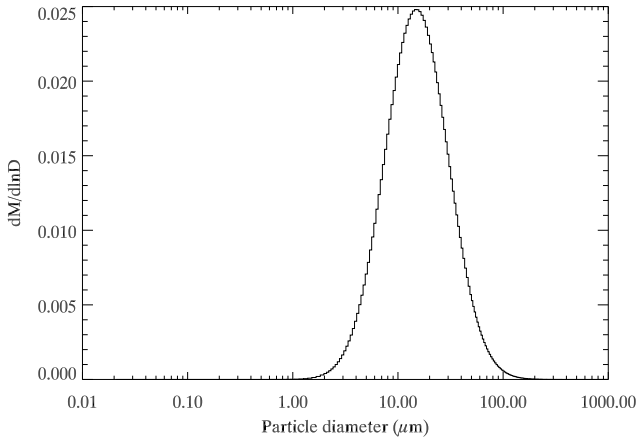

Figure 3.12: Normalised mass distribution of the silt component of figure 3.11, using a higher particle size resolution.

Type	Radius range, μm	Mean radius, μm	σ	Particle density, $\mathrm{g\,cm^{-3}}$
Coarse sand	500-1000	355	2	2.65
Medium/fine sand	25-500	80	2	2.65
Silt	1-25	7.5	2	2.65
Clay	0-1	1	2	2.5

Table 3.2: Distribution parameters of the four soil types, based on Tegen et al. (2002), table 1.

and a value of 0.5 μm to test the effect of having a size distribution which is more weighted towards the smaller particles.

3.6 Emission at constant wind speed

To understand which of the surfaces of North Africa are particularly susceptible to emitting dust, it is useful to compare the emissions at constant wind speeds. The study of these emissions at constant wind speed is independent of weather conditions, so there is no influence of precipitation or moisture.

The total dust emissions increase as a cubic function of wind speed (as expected from the MB95 equation) and these are presented in figure 3.13. There are no emissions at any wind speeds below 7 $\mathrm{m\,s^{-1}}$, hence the minimum threshold wind velocity (at 10 m) in the Sahara is between 6 and 7 $\mathrm{m\,s^{-1}}$. This agrees well with Tegen and Fung (1994), who chose a threshold wind velocity of 6.5 $\mathrm{m\,s^{-1}}$.

Maps of emissions at constant wind speeds are presented in figure 3.14. At lower wind speeds, areas which emit are quite sporadic (mainly areas in Mauritania, eastern Niger, and the south-western end of the Bodélé Depression). That there are emissions at wind speeds of 7 and 8 $\mathrm{m\,s^{-1}}$ contrasts with the work of Todd et al. (2007), who estimate a dust emission threshold of 10 $\mathrm{m\,s^{-1}}$ at 2 m height for the Bodélé. These areas which do emit some dust at the lowest wind speeds are the areas with the shortest roughness lengths: comparing figure 3.14(a) with figure 3.4, we see that the emissions occur where the roughness lengths are of the order of 10^{-3}-10^{-2} cm, the shortest roughness lengths found in the Sahara. At higher wind speeds, most of the potentially erodible surfaces do emit, while the peaks of emission have shifted to the north. The northern areas tend to have a higher increase in threshold velocities due to drag partitioning, so it is obvious that they will not emit at low wind speeds. The area in coastal north-eastern Libya, at the south-eastern most extent of the Gulf of Sidra, is particularly noticeable as an emitting region. This area is to the south of the Akhdar mountains: it is marked by chotts and wadis, and so has a relatively high clay content which means that this area has a higher sand-blasting efficiency than central Saharan sources, and will tend to emit more when the winds exceed the threshold velocity. This suggests that at the highest wind speeds it is areas which have the highest sand-blasting efficiencies (as shown in figure 3.9) which have the highest emissions, compensating for their longer roughness lengths. These areas have the soil types (figure 3.1) which have the highest clay contents, so there are larger quantities of available dust for long-range transport. Hence at low wind speeds areas with the shortest roughness lengths are the only areas which can emit, while at the highest wind speeds the α term in equation 3.18 dominates, favouring the more northerly areas, which have finer soils.

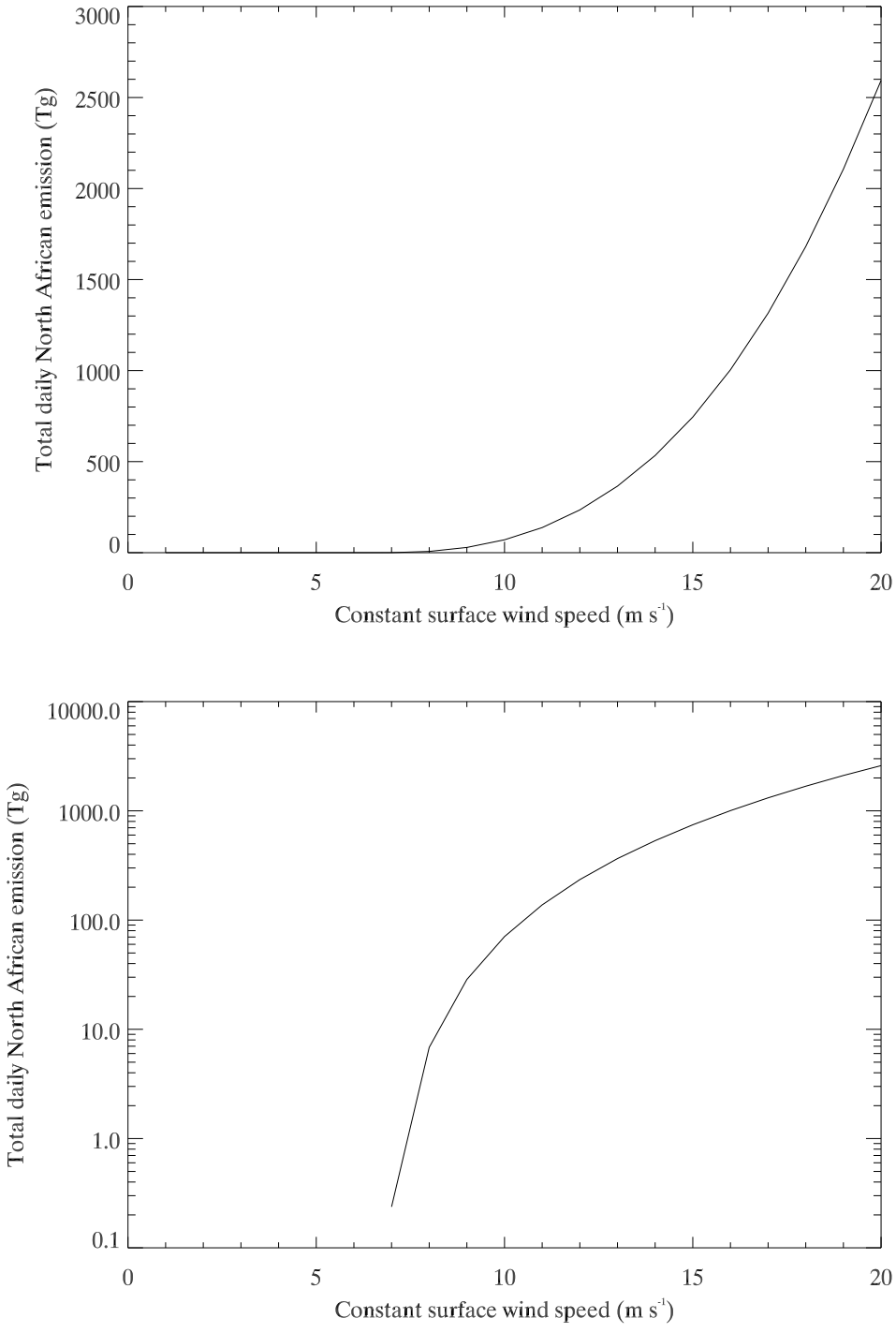

Figure 3.13: Total daily emissions ($\mathrm{g\,m^{-2}\,day^{-1}}$) as a function of constant wind speed.

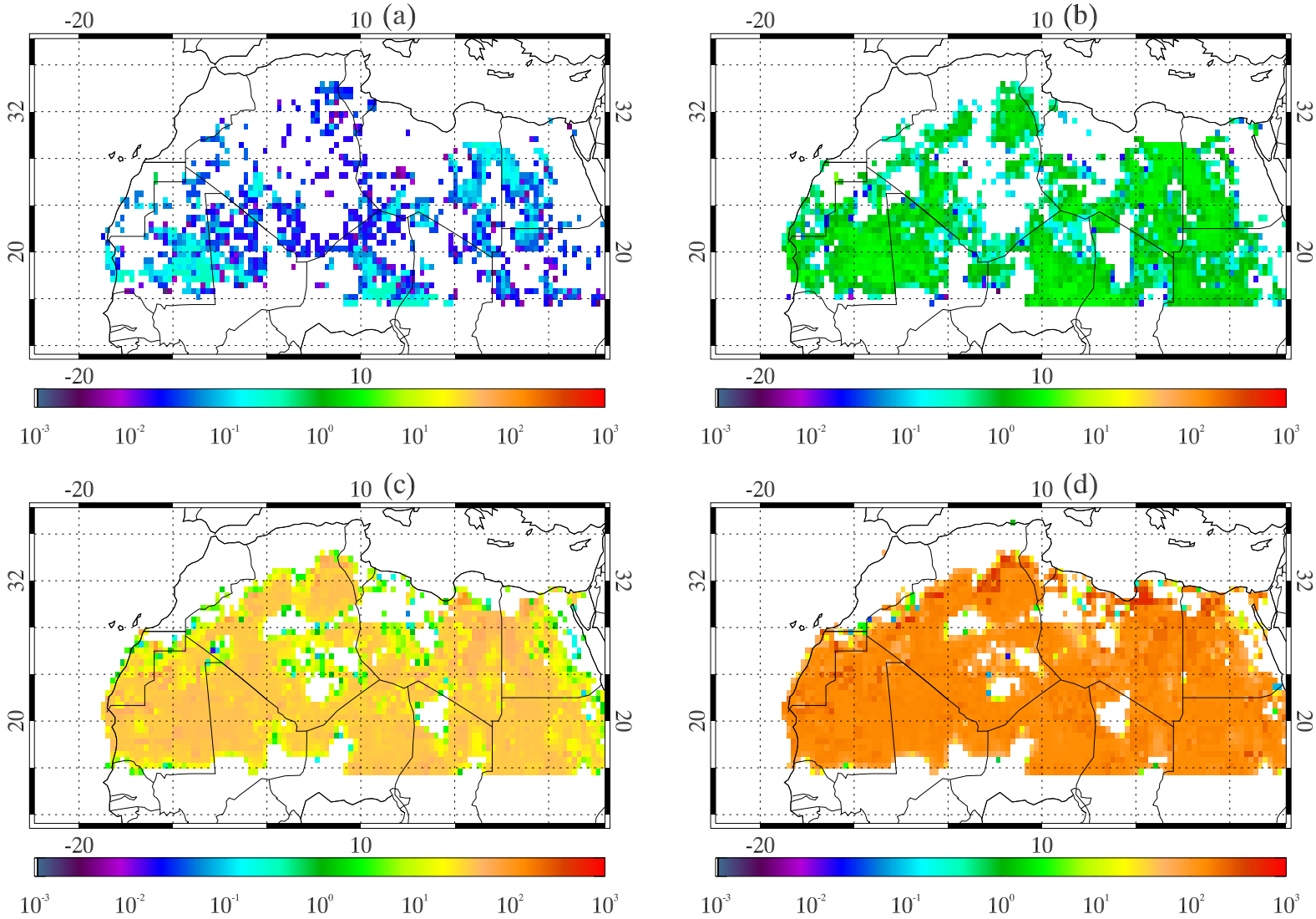

Figure 3.14: Maps of the emissions ($\mathrm{g\,m^{-2}\,day^{-1}}$) at constant wind speeds, at a resolution of 0.5 °. Below 7 $\mathrm{m\,s^{-1}}$ there is no emission anywhere. At 7 $\mathrm{m\,s^{-1}}$ (a) the total emission is 0.23 $\mathrm{Tg\,day^{-1}}$, at 8 $\mathrm{m\,s^{-1}}$ (b) it is 6.83 $\mathrm{Tg\,day^{-1}}$, at 12 $\mathrm{m\,s^{-1}}$ (c) it is 234.7 $\mathrm{Tg\,day^{-1}}$, and at 16 $\mathrm{m\,s^{-1}}$ (d) it is 1004 $\mathrm{Tg\,day^{-1}}$.

Year	Low resolution	High resolution
2004	1364	1393
2005	1389	1417
2006	1225	1251
2007	510	532
2008	529	553

Table 3.3: Yearly totals for North African emission (Tg) for the years 2004-2008. Comparison between the low resolution (0.5 °), and the high resolution (0.25 °).

3.7 Sensitivity to model resolution

In order to test the sensitivity of the emission model to the surface resolution, the model has also been tested at the higher resolution of 0.25 °, for the period of 2004-2008. A table of these yearly emissions is presented in table 3.3. Further discussion on the climatologies will be presented in section 3.8, here we will only consider the differences between the two resolutions. There is broad agreement between the two resolutions for most years: the maximum difference is 29 Tg, in 2004, a percentage increase from low to high resolution of 2.1%. This suggests that the uncertainty caused by the resolution is quite small compared to the inter-annual variability in the meteorology (especially between 2006 and 2007). For the requirements of the transport model, the sensitivity due to the resolution is sufficiently small that the lower resolution can be used, particularly for yearly time-scales.

Spatially, there are again few differences between the high and the low resolution versions, as shown in figure 3.15. The strongest changes are on the Western African coast, where some of the grid cells vary their emissions by up to 1.8 Tg, in 2006 (there is a focus on 2006 since it will be studied in further detail in chapters 5 and 7). Here the emissions are reduced slightly in the high resolution model (from 57.9 $\mathrm{Tg\,year^{-1}}$ to 56.7 $\mathrm{Tg\,year^{-1}}$ in a 2.5×2.5 ° area). This is because the low resolution model was using a particularly erodible region for entire grid cells, where there should have been sea, or other less erodible surfaces, present within the grid cell. Locally on some parts of the same coast the emissions are increased: this relates to erodible areas which have been misidentified as sea in the low resolution model. In the other main source areas (northern Mauritania, the Bodélé Depression, the Libyan coast) the emissions are increased.

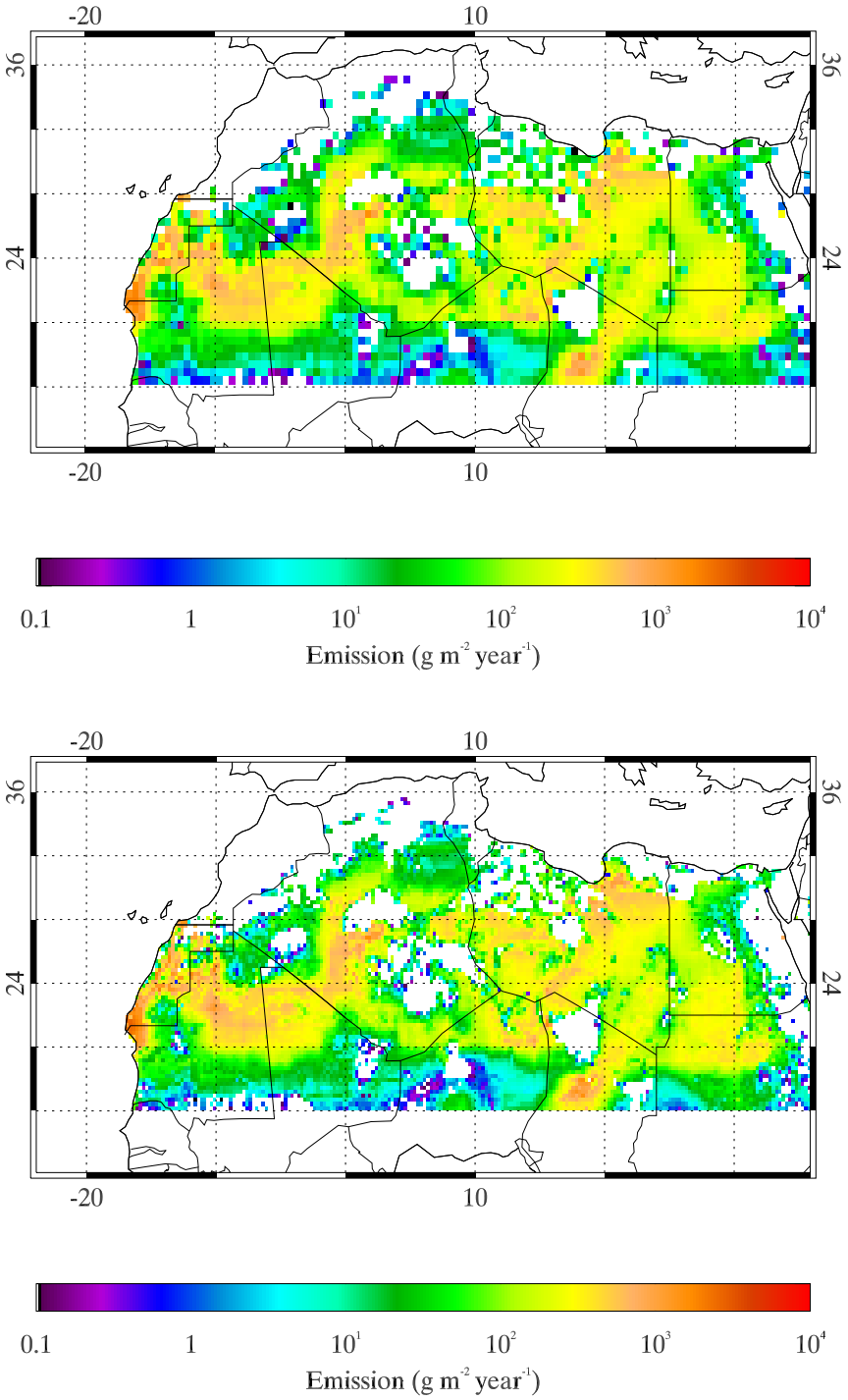

Figure 3.15: Maps of the total emissions for 2006. Above, at the low resolution of 0.5 °, the total is 1225 Tg; below, at the high resolution of 0.25 °, the total is 1251 Tg.

3.8 Emission climatology

To understand the inter-annual variability of emissions, and to predict dust sources, emissions have been calculated from 2004-2008, using wind and precipitation data from ECMWF. In sections 3.8.1 and 3.8.2 the focus is on 2006, for a more detailed study of the seasonality of dust storms.

3.8.1 2006 emissions and meteorological conditions

On a yearly basis, the two most important varying conditions which have a bearing on dust emission are the winds and the precipitation. A priori, we can expect that persistent source regions will have reliably strong winds, and will be particularly arid. The geographical distribution of emissions for 2006 is shown in figure 3.15. The distribution is not uniform: particularly strong source regions emit in the range of 1-10 $\mathrm{kg\,m^{-2}\,year^{-1}}$, whereas much of the desert emits rather less, below 0.1 $\mathrm{kg\,m^{-2}\,year^{-1}}$. Areas of mountains, regs, and hamadas (where the drag partitioning is high: see figure 3.8) are clearly visible as regions which do not emit. The Atlas mountains in north-west Africa, the Hoggar massif in southern Algeria, the Tibesti massif in northern Chad, and the hamadas of north-western Libya are clearly visible as non-source regions.

After the surface conditions, the winds are responsible for most of the variability in emissions. Looking at the winds (figure 3.16), it can be seen that particularly strong source regions are marked by strong winds. This can be seen in the mean wind speeds, but it becomes more obvious when the higher end of the probability density function (pdf) of the winds is studied. The highest standard deviation on the winds is observed in areas such as the coastline between Mauritania and Western Sahara (the West African coast source), with an arc through Western Sahara, Mauritania, northern Mali and central Algeria (the West African sources), and other regions including northern Niger, northern Sudan, the Bodélé Depression, and the coast in north-eastern Libya (the Libyan coast source). In these areas the winds more regularly exceed 10 $\mathrm{m\,s^{-1}}$, permitting dust events. The West African coast is particularly buffeted by high winds from the Atlantic, situated as it is on a cape jutting out into the Atlantic. Similarly, the Libyan coast is subject to high winds coming in from the Mediterranean.

Precipitation is required to moderate particular dust sources, especially on the Libyan coast. In this area, high winds are often associated with cold fronts coming in from the Mediterranean. These can channel in very strong winds, but if they also bring in rain then the precipitation will suppress emissions. As a sensitivity study, the emissions model has also been run for 2006 with the precipitation scheme disabled. In total, the emissions are increased to 1278 Tg, 53 Tg more than

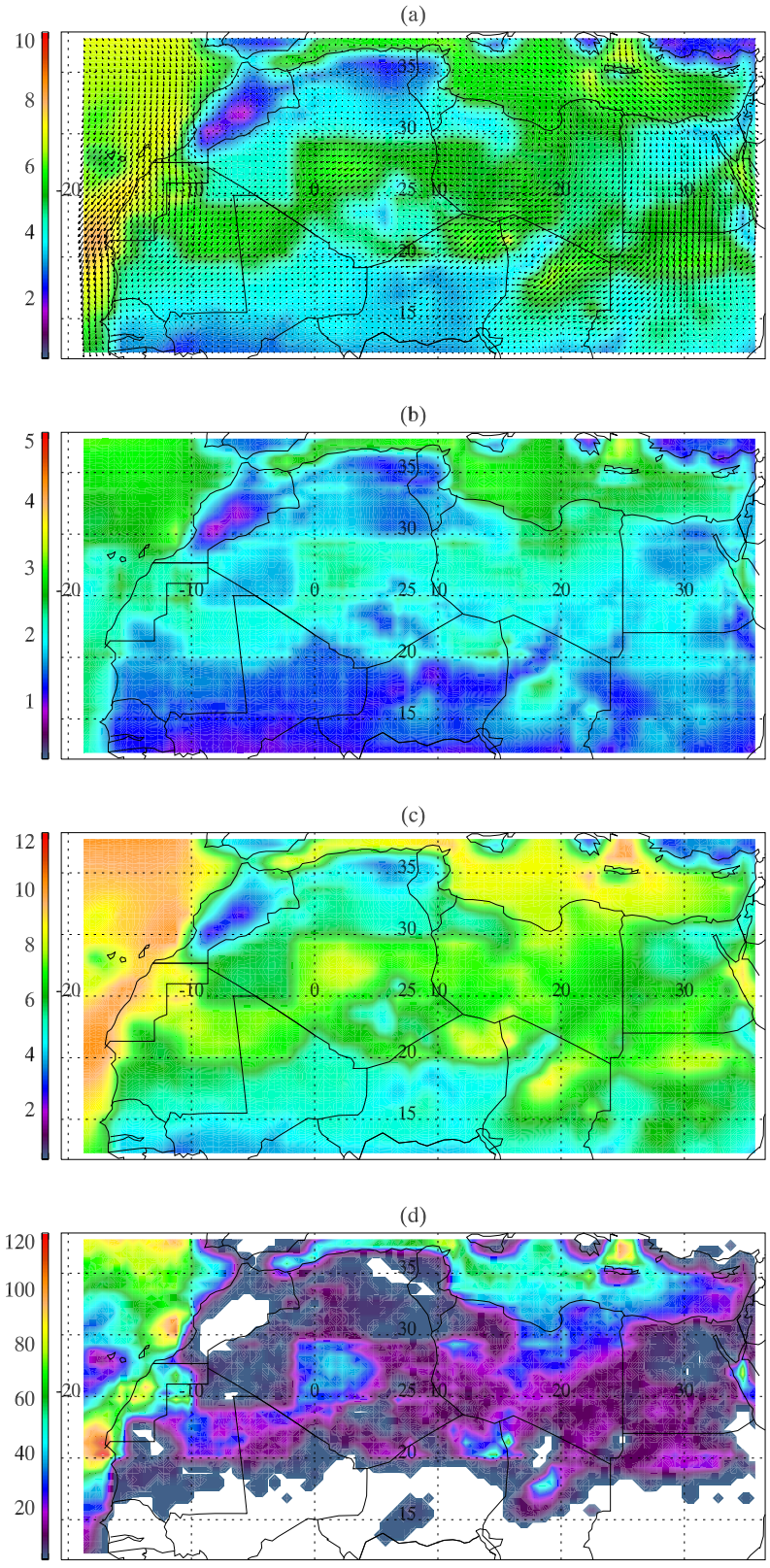

Figure 3.16: Wind conditions for 2006. (a) Mean wind speed ($\mathrm{m\,s^{-1}}$). (b) Standard deviation on wind speed ($\mathrm{m\,s^{-1}}$). (c) Mean + standard deviation on wind speed ($\mathrm{m\,s^{-1}}$). (d) Frequency of days when wind speed exceeds 10 $\mathrm{m\,s^{-1}}$.

Area	With precipitation	Without precipitation
Bodélé Depression (17.75 °N, 18.25 °E)	34.75	34.79
West coast (21.25 °N, 16.25 °W)	57.86	58.35
Northern Mauritania (24.75 °N, 10.25 °W)	24.56	24.99
NE Libya (30.75 °N, 21.25 °E)	21.92	31.67
Total for North Africa	1225	1278

Table 3.4: The effect of precipitation on the annual emissions (in Tg) for the four most concentrated source areas.

in the case in which precipitation is included. On a regional level the effect is more pronounced, as in table 3.4. For source regions which can be particularly wet, such as north-eastern Libya, the effect of including precipitation is to decrease emissions by up to 30%, while in other areas the effect is negligible.

3.8.2 Seasonal emissions and meteorological conditions

There is strong seasonal variability in dust emission, with emissions from different regions peaking at different times of the year. This is shown in figure 3.17. The total emissions across the Sahara per month are plotted in figure 3.18.

Emissions peak in the early summer, in June, with a second peak earlier in the year in March; the latter third of the year, from September on, shows much less dust activity. Apart from the Bodélé, everywhere is quiet September-November, since the winds are particularly weak at this time (figure 3.19). March-May is reasonably strong everywhere, but this time (and February) is when the Libyan coast source is particularly strong. At this time, the cold fronts in the Mediterranean are active, bringing in strong winds, and behind it, rain (figure 3.20), along the Libyan coast. The fronts run west-east: they often start in the Atlantic, passing the Atlas mountains, then are channelled through the Gulf of Sidra into eastern inland Libya, south of the Akhdar mountains. Ahead of the rain, intense dust lifting is possible.

From April onwards, and through the summer until the autumn, there is very little rainfall anywhere in the Saharan source regions. This is the peak season for Saharan dust emissions, especially for the West African coast sources, the rest of the West African sources, and for the far-eastern region in northern Sudan and southern Egypt. Emissions are particularly intense on the West African coast and in Western Sahara, where there are frequent strong wind events. The rest of West Africa is only quite strong at this time, but since they cover a much greater area, the total emissions are much more than for the more localised intense sources. Meanwhile, the Bodélé

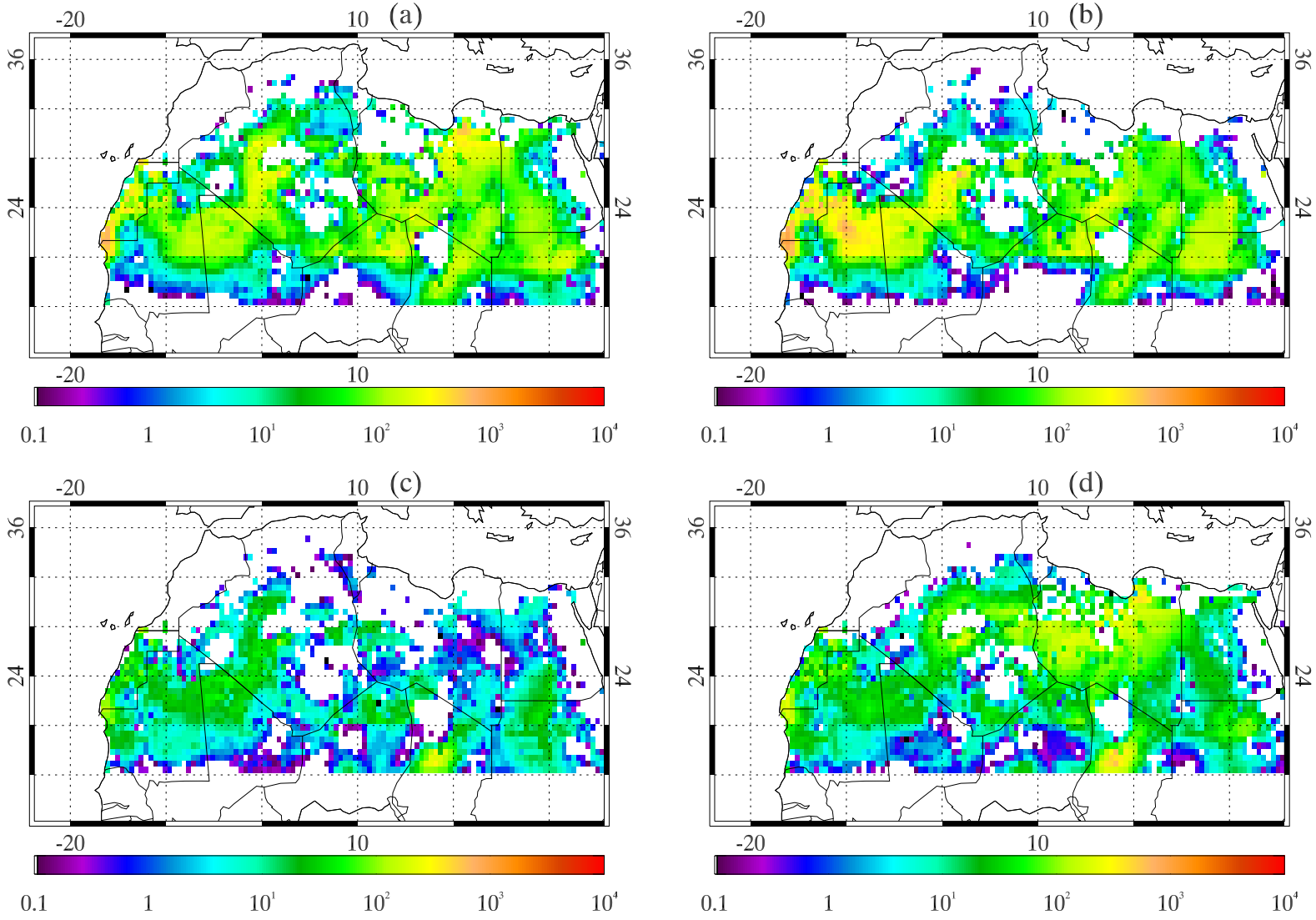

Figure 3.17: Emission ($\mathrm{g\,m^{-2}\,season^{-1}}$), per season, for 2006. (a) MAM. (b) JJA. (c) SON. (d) DJF.

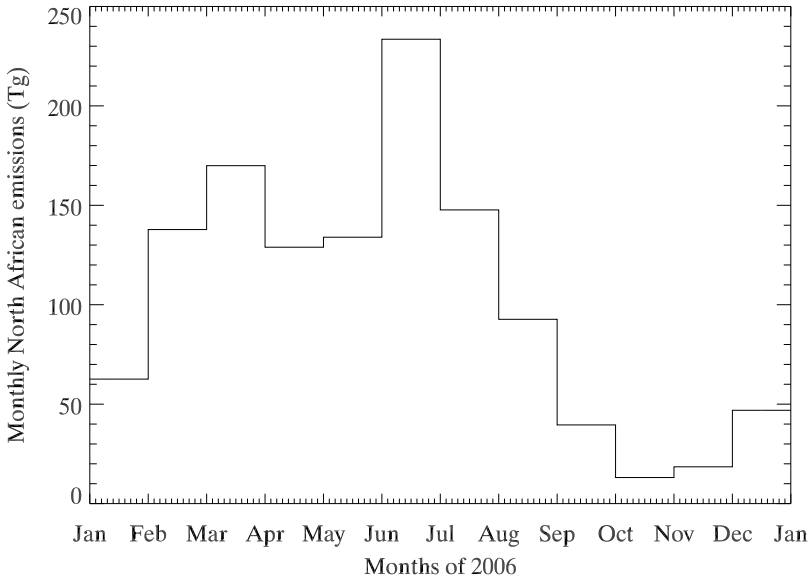

Figure 3.18: Monthly North African emissions.

Depression is a strong emitter during two periods of the year: from October to December, and in June. At these times the ECMWF winds are strongest; precipitation very rarely affects this region.

Figure 3.21 shows the emissions for three of the most intense source regions, on the West African coast, the Libyan coast, and in the Bodélé. The seasonal occurrences of these dust sources, as described above, is shown by the shift in activity between the three peak source regions. This plot also indicates that dust emission occurs in discrete packets, as dust 'events', occurring when winds are stronger than average. This is perhaps not surprising, since emission is a cubic function of the wind speed. Moreover, since there is a threshold velocity term (a minimum of $\sim$6.5 m s^{-1}, as in section 3.6), during much of the year no emission may occur. Hence, the 'background' emission may only be as much as a few tenths of a teragram, yet most of the yearly emissions will be from just a handful of dust events, when the daily emissions will be of order a few teragrams. This is particularly true of the Libyan coast, where there are very few but very strong events in February and March, and then it is quiet for most of the rest of the year.

That the simulated emissions from the Bodélé peak in winter is in agreement with AOT observations from TOMS, as well as with our understanding of the seasonal cycle of the Bodélé LLJ (Washington and Todd, 2005), which peaks when a high-pressure system over Libya is at its

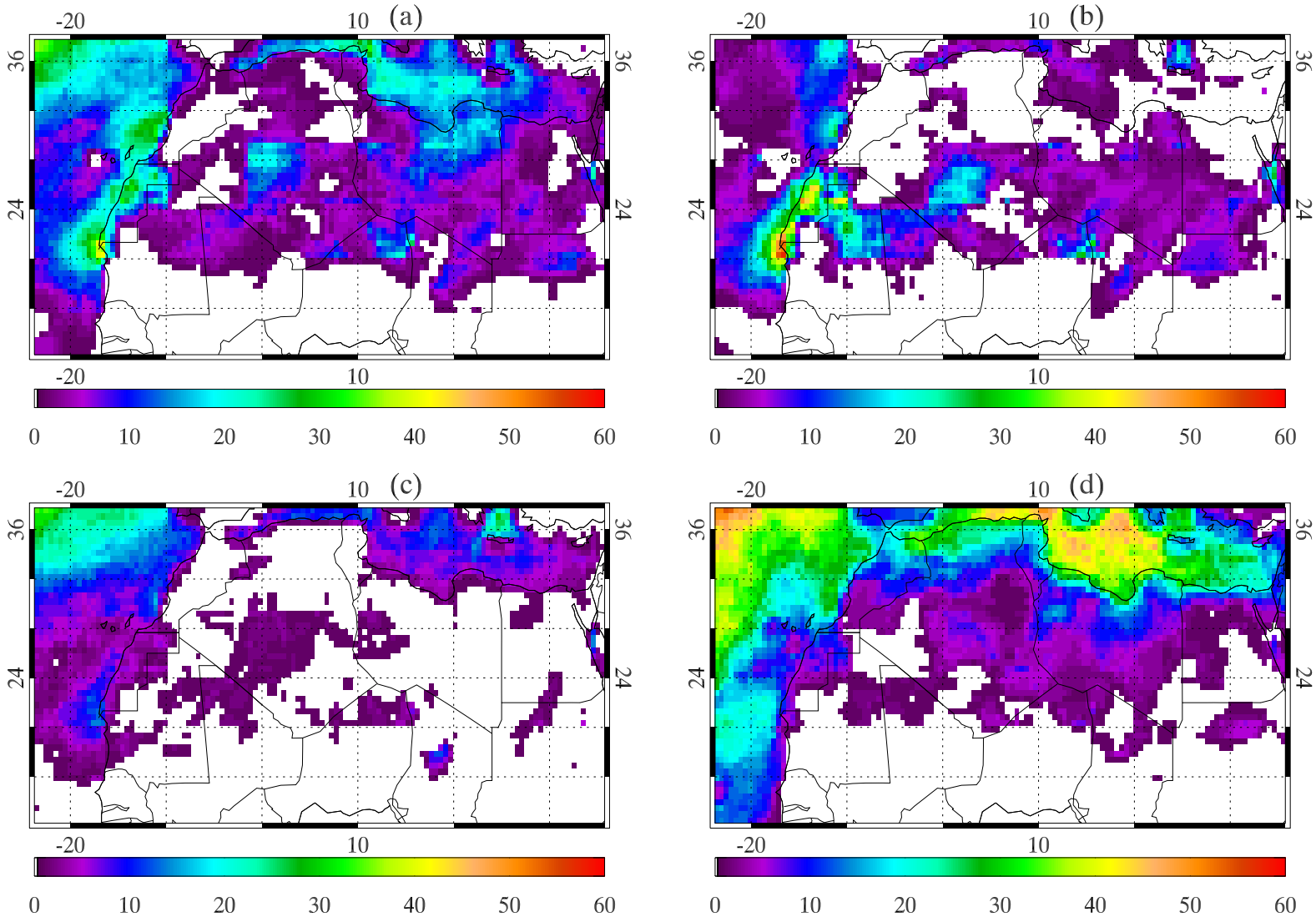

Figure 3.19: Number of days of high winds (when surface wind speed exceeds 10 $\mathrm{m\,s^{-1}}$), per season, for 2006. (a) MAM. (b) JJA. (c) SON. (d) DJF.

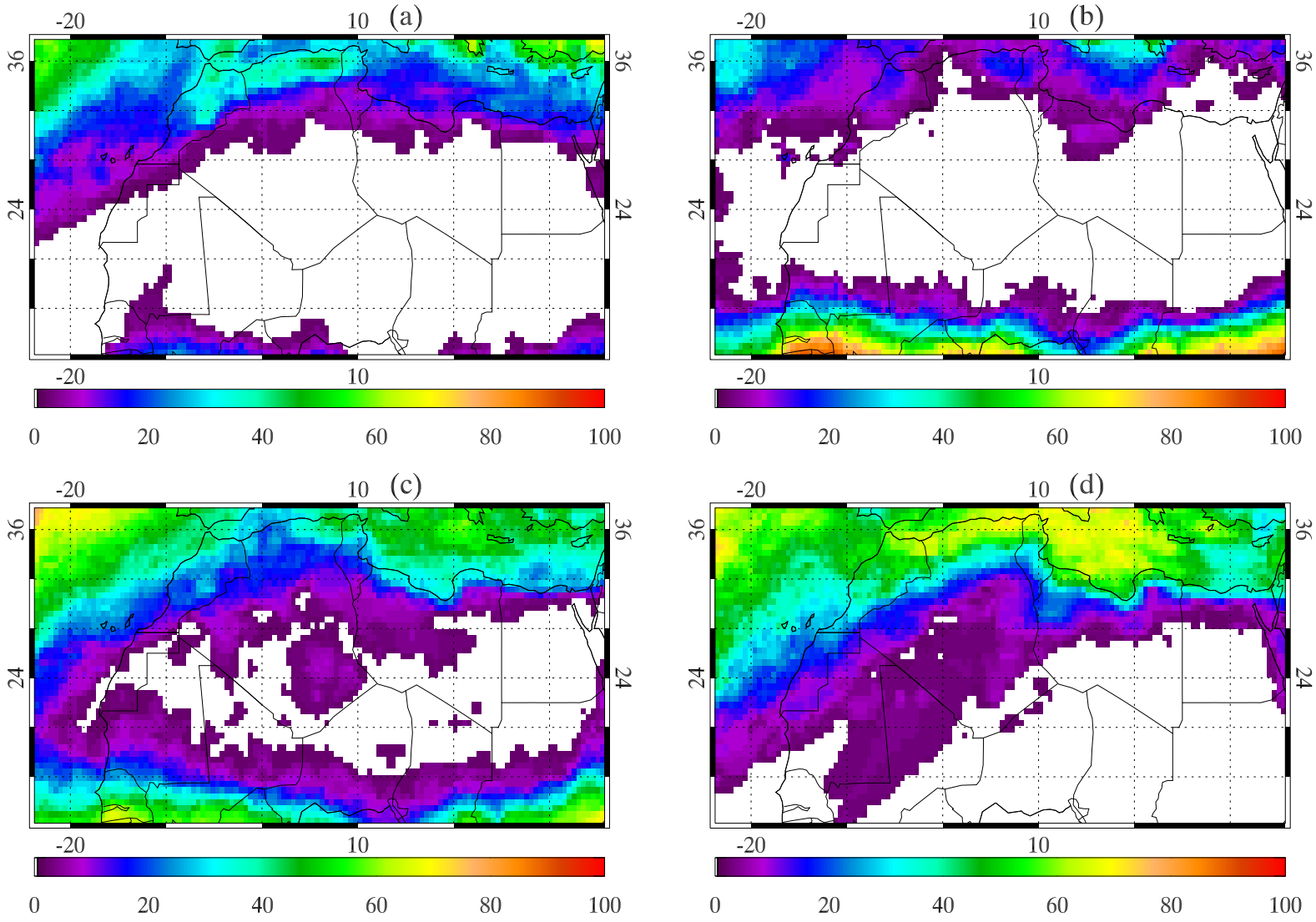

Figure 3.20: Number of days of precipitation (when precipitation exceeds 0.5 mm), per season, for 2006. (a) MAM. (b) JJA. (c) SON. (d) DJF.

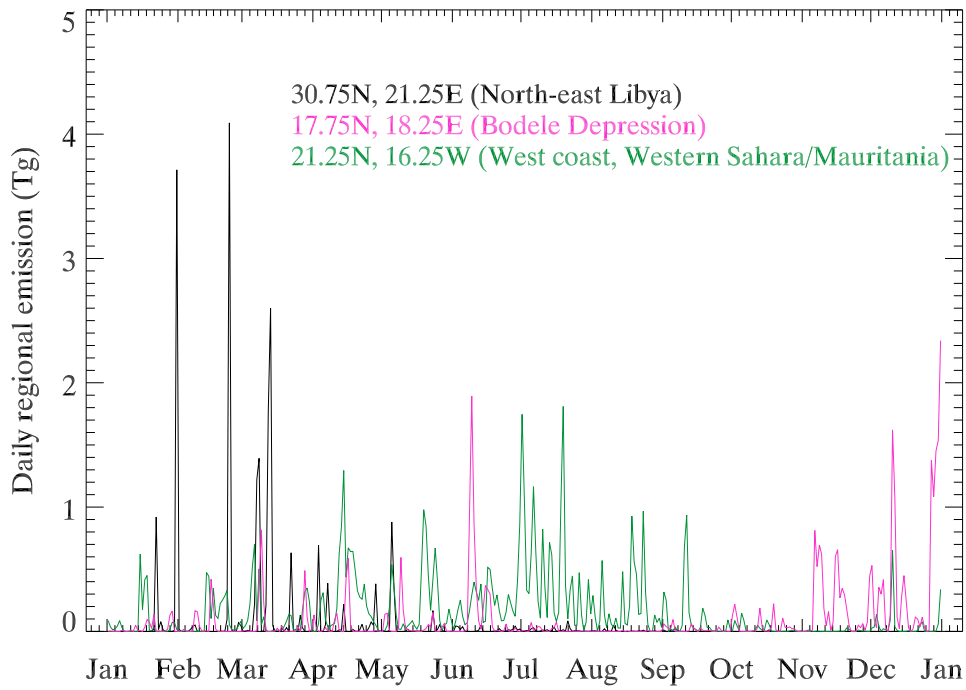

Figure 3.21: Time-series of emissions from various regional dust sources, for 2006. Emissions data are taken from the 2.5×2.5° square around the peak source region. The total from the north-eastern Libyan region is 21.9 Tg, from the Mauritanian coast is 57.9 Tg, and from the Bodélé is 34.8 Tg.

strongest (feeding winds into the Bodélé). However, the LLJ is at its weakest during the summer, whereas SHAMAL does predict a subsidiary peak in activity in June. This is a consequence of just one or two events triggered by high ECMWF winds during the month, which could be regarded as anomalous events. Meanwhile, TOMS AI observations do indicate the presence of dust aerosol over the Bodélé at this time (Engelstaedter and Washington, 2007a). In the case of TOMS AI, caution is required though, since TOMS AI retrieves low altitude ($< \sim$1.5 km) dust quite poorly: this may overestimate its observations of dust emissions during the summer (when vertical transport is at its strongest) relative to the winter season. Hence we would not expect substantial dust emissions from the Bodélé in June, which may indicate an anomaly in SHAMAL and the ECMWF winds used to drive it.

3.8.3 Inter-annual variability

The results from 2006 are reproducible for other years, especially for 2004 and 2005. The emissions for 2004-2007 are shown in figure 3.22, and the relevant wind fields for these years are shown in figure 3.23. 2004-2006 show a very similar pattern, with sources across West Africa and through the central areas all being significant. There is inter-annual variability between these years: in 2004 the total emissions are 1364 Tg, in 2005 they are 1389 Tg, and in 2006 they are 1225 Tg. The West African sources are particularly active in 2005. The inter-annual variability of the monthly emissions and the monthly frequency of high wind speed events are shown in figure 3.24. As in figure 3.18, it is persistently the case that the first half of each year is more active than the second, though the peak month may vary from year to year.

The results from 2007 and 2008 are quite different to those in 2004-2006. Much of the central Sahara has substantially lower emissions, as do the West African and Libyan coasts. All of these areas have a significantly reduced occurrence of high winds. Only the Bodélé and an area of northern Algeria (south of the Atlas mountains) have increased high winds, and increased emissions. In total, however, North African emissions are substantially reduced, from ∼1300 Tg to ∼500 Tg (2007 has 510 Tg, and 2008 has 529 Tg). This is due to the change in the analysis model used by ECMWF to produce the operational analysis data set: on the 12th September 2006, 'Cycle 31r1' was begun in the operational analysis, which included changes in the parameterisation of turbulent orographic drag, and of gusts due to orography. Over the Sahara this has had a substantial effect on the surface winds, as revealed by the change in the emissions.

Figure 3.25 shows the interannual variability in the seasonal emissions of the four major source regions. The West African source regions are consistently stronger in the summer than in the winter, though 2007 and 2008 are much weaker than 2004-2008. The Libyan source region is only active in winter and spring, and 2006, especially March, is a particularly active time for this region. The Bodélé Depression also only tends to be active in winter and spring (until as late as June). After the version change in the ECMWF model, the emissions from the Bodélé increased substantially, with the winter of 2006 and the winters/springs of 2007 and 2008 being much more active than in previous years (a result of the increase in the frequency of high winds as shown in figure 3.24).

In order to resolve this disagreement in the emissions produced by the two analysis cycles, it is necessary to look at an independent source of information as to the inter-annual variability. Figure 3.26 maps the annual mean AOD and AI values from OMI, for 2005-2008 (when OMI

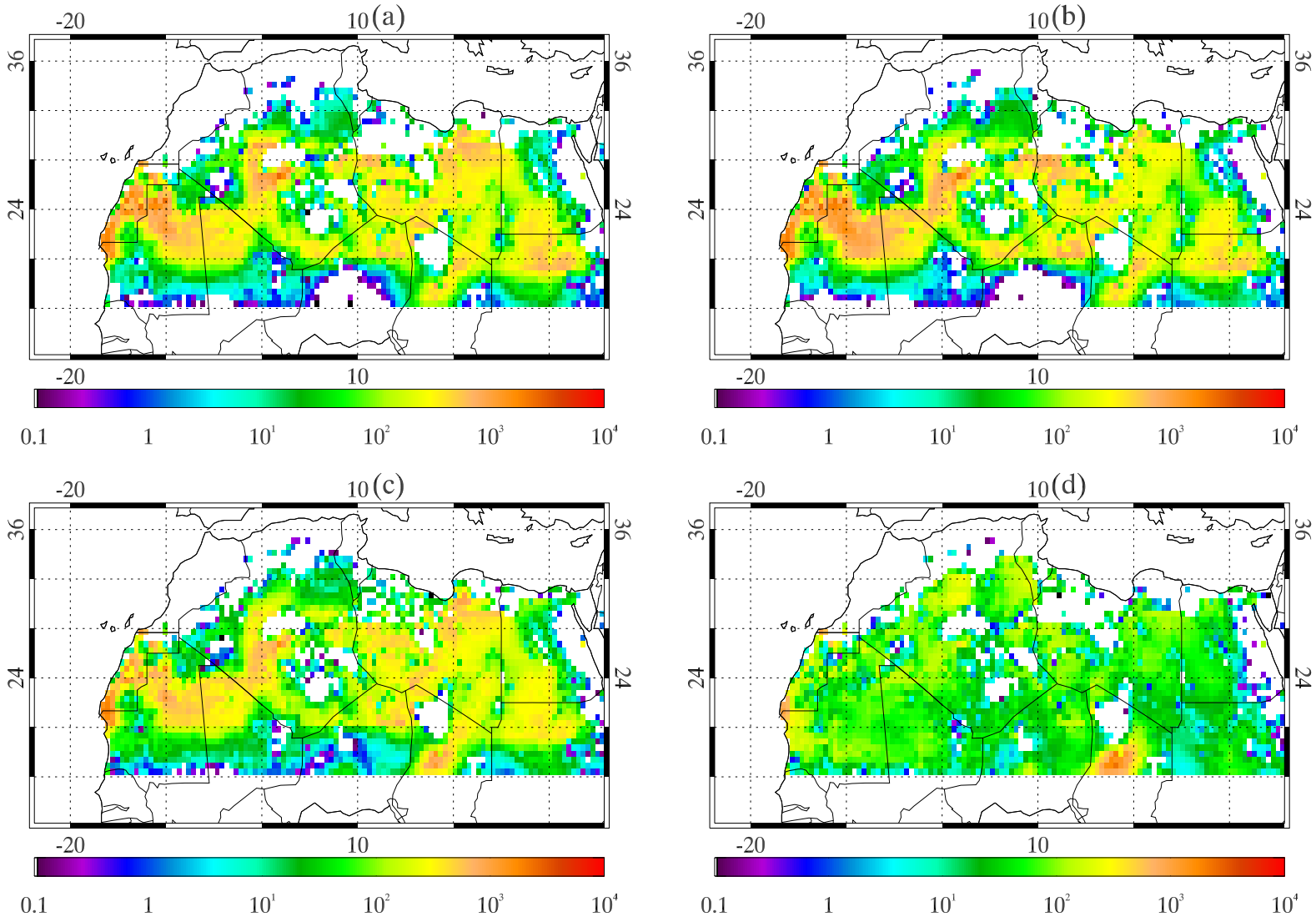

Figure 3.22: Annual emissions ($\mathrm{g\,m^{-2}\,year^{-1}}$). (a) 2004. (b) 2005. (c) 2006. (d) 2007.

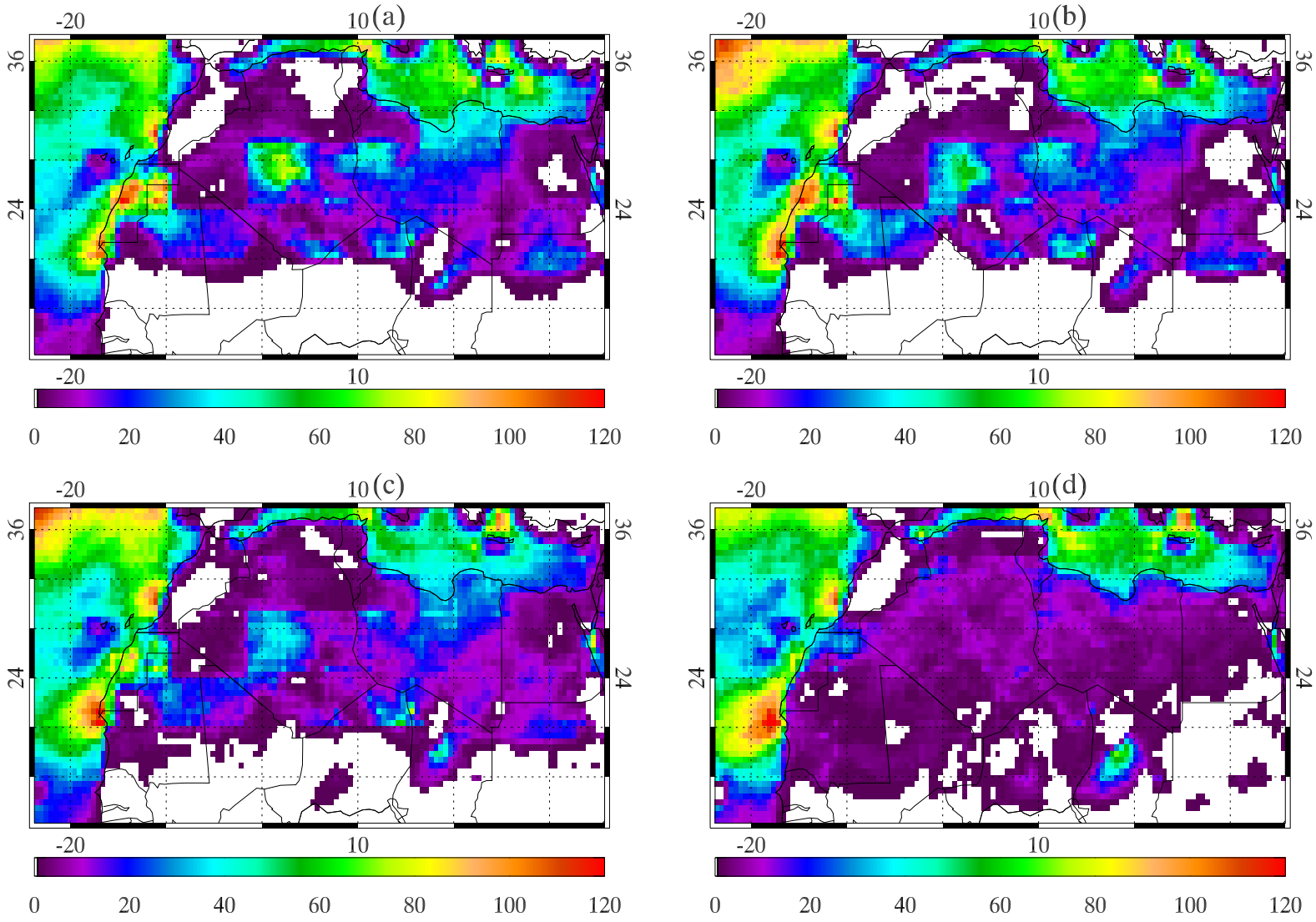

Figure 3.23: Number of days of high winds ($> 10\ \mathrm{m\,s^{-1}}$), per year. (a) 2004. (b) 2005. (c) 2006. (d) 2007.

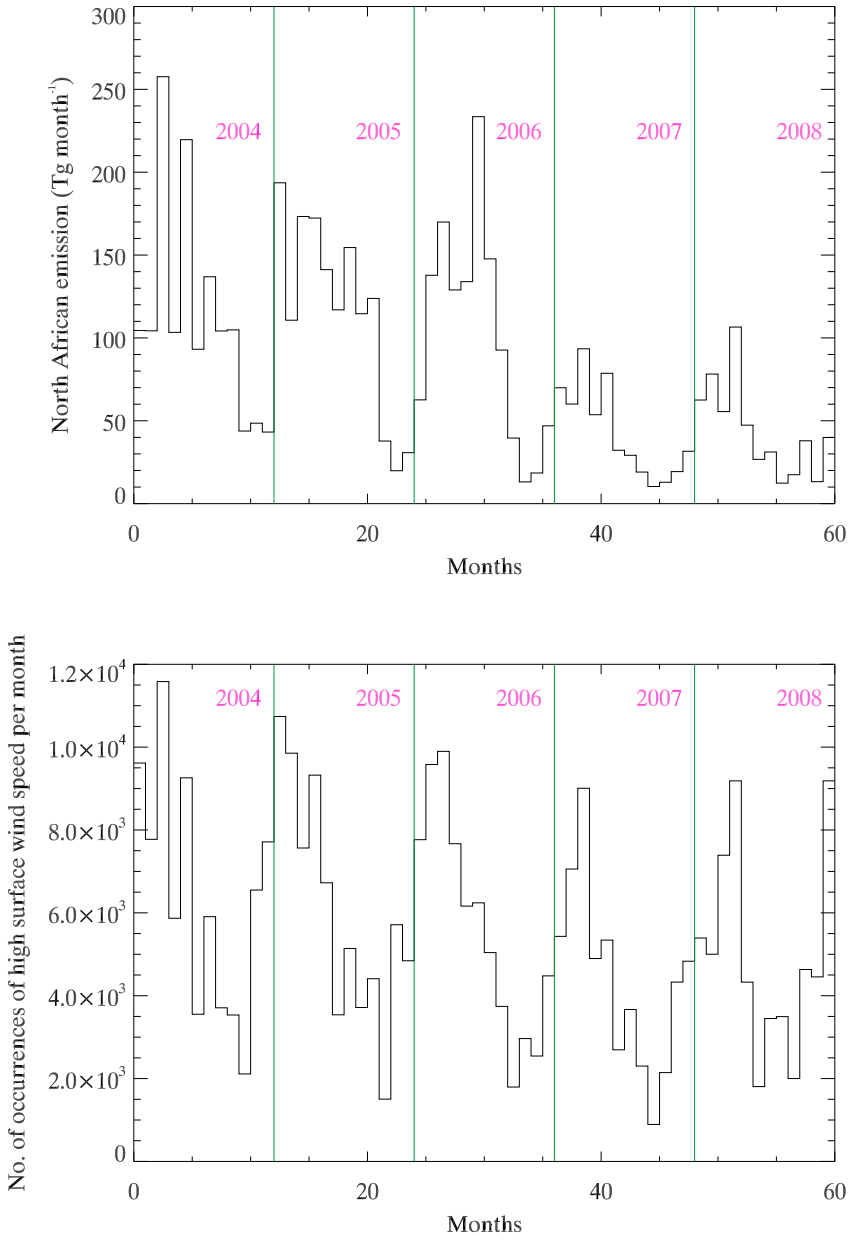

Figure 3.24: Total monthly emissions (top) and the monthly frequency of high wind speed events (bottom), when surface wind speeds exceed 10 $\mathrm{m\,s^{-1}}$, 2004-2008. Wind speeds are taken from the region of 16-35.5 °N and -17-36 °E, which bounds the source regions.

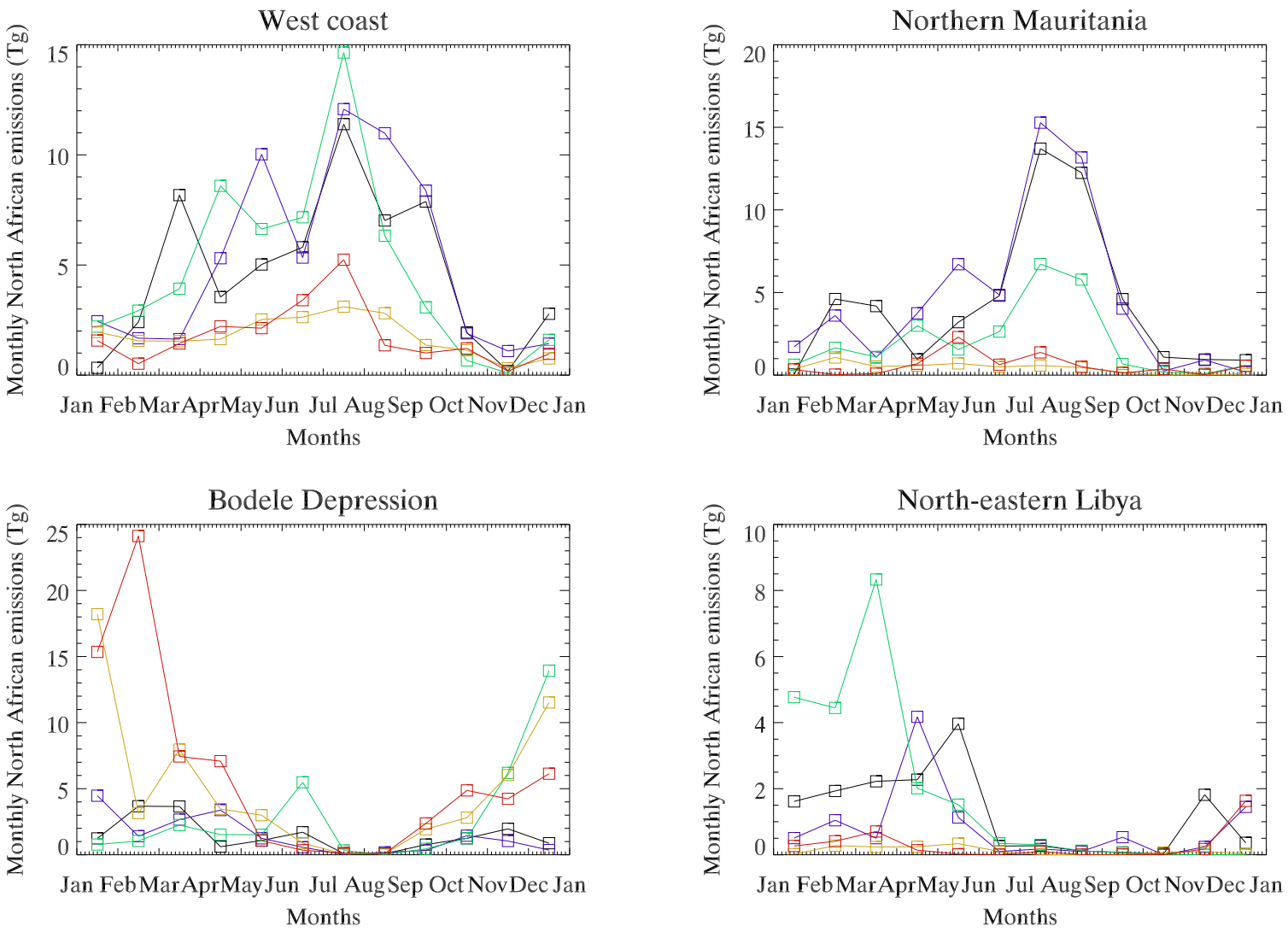

Figure 3.25: Inter-annual variability of monthly emissions, for each source region. Black- 2004, blue- 2005, green- 2006, yellow- 2007, red- 2008.

data is available for complete years), as a proxy for dust emission. The first thing to note is that there is very little difference between 2005-2006 and 2007-2008, confirming that the marked change in simulated emissions is a result of a change in the analysis model, rather than reflecting the differences in observed dust emissions for these years. In both the OMI AOD and AI, the Bodélé Depression and the various West African sources (especially in Mali and Mauritania) tend to dominate, while there is also activity in southern Algeria, Niger, and Libya. This is a broadly similar picture to that provided by the emissions model, at least in 2004-2006. In terms of the dominance of the Bodélé, OMI agrees more with the later analysis cycle (2007-2008) than with the earlier cycle (2004-2006), in which the Bodélé was relatively weak, and subordinate to the stronger and much more extensive West African sources. Given the dominance of the Bodélé in the OMI observations, it is reasonable to prefer the later cycle for this region. However, the later cycle appears to smear out most of the other sources across the Sahara, and to unduly diminish the importance of the Malian and Mauritanian sources (which are still significant in the OMI observations). Other source regions are given excessive prominence in the later cycle, such as the Western Saharan coast (present in both cycles) and the Grand Erg Occidental in north-western Algeria, not identified as a significant source by OMI. Hence neither cycle is completely satisfactory: the earlier cycle preserves the spatial pattern of the dust sources (to some agreement with OMI), whereas the later cycle is required to give the Bodélé the prominence that OMI suggests it should have.

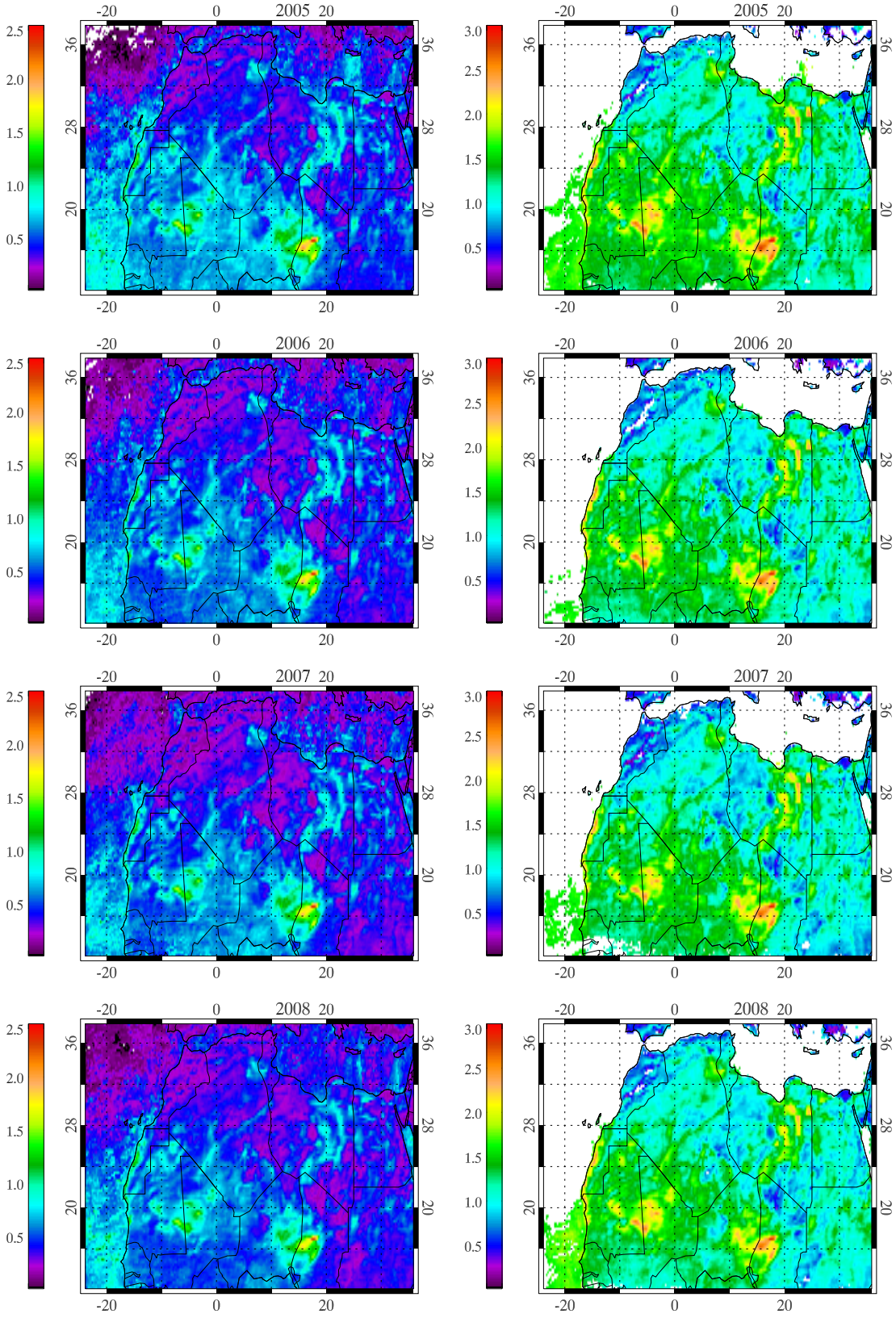

Figure 3.26: Annual mean OMI optical depths at 500 nm (left) and AI (right), for 2005-2008.

3.8.4 The relationship between emission and wind speed

In order to learn more about the nature of the meteorology that creates dust storms, it is instructive to determine the relationship between dust emissions and the wind speeds which give rise to them. Figure 3.27 plots the yearly (for 2006) and mean daily emissions as a function of wind speed, along with the frequencies of these wind speeds. The emission and wind distributions show some similarity in nature to Boltzmann distributions, since there is a long tail of high wind speed events; however, this similarity breaks down for lower wind speeds, where there are zero emissions. Hence it would not be accurate to fit a Boltzmann distribution to the emission distribution. The winds are the cause of this distribution, since they are driven by the energy of the air particles.

Emission does not occur anywhere at wind speeds of less than 6.5 $\mathrm{m\,s^{-1}}$, which is a result of the particle threshold velocities: even where the surface is most favourable for emission, no dust can be lifted when the winds are weaker than this. This compares well with previous work (Kalma et al., 1988; Tegen and Fung, 1994), which identifies this threshold velocity from measurements. This means that the emission and wind distributions are offset from each other: while the peak in wind activity is between 2 and 5 $\mathrm{m\,s^{-1}}$, this is simply not strong enough to lift any particles from the surface. As the wind speeds increase, the frequency of their occurrence drops off exponentially.

The peak of emissions occurs at 10 $\mathrm{m\,s^{-1}}$, which validates the choice of this value as the threshold wind speed above which we may expect a significant dust event to occur (over source regions). Winds of between 6.5 and 10 $\mathrm{m\,s^{-1}}$ occur much more frequently than do higher wind speed events, and are indicative of widespread and frequent low-intensity dust emissions. However, these winds do not lift the majority of dust: 516 Tg (42%) of dust is lifted by winds $< 10\ \mathrm{m\,s^{-1}}$, while 710 Tg (58%) of dust is lifted by winds $> 10\ \mathrm{m\,s^{-1}}$. The tail of the distribution forms due to the occurrence of just a handful of high-wind speed events, which can emit substantial quantities of dust (from the source regions only) due to the fact that the saltation flux is a cubic function of wind speed.

Per day, the peak of the emission distribution also occurs at 10 $\mathrm{m\,s^{-1}}$. One thing to note is how the ratio between the standard deviation and the mean of the daily emissions increases with increasing wind speed, which is a result of the larger impact that higher wind speed events have on sources. Consider two regions covered by the same winds, but with different soil properties (e.g. roughness length): when the winds are strong, then the absolute magnitude of the difference between the two regions will be very large, whereas at lower wind speeds the emissions will be weaker, and there will be a smaller difference. This pattern is most pronounced at the highest

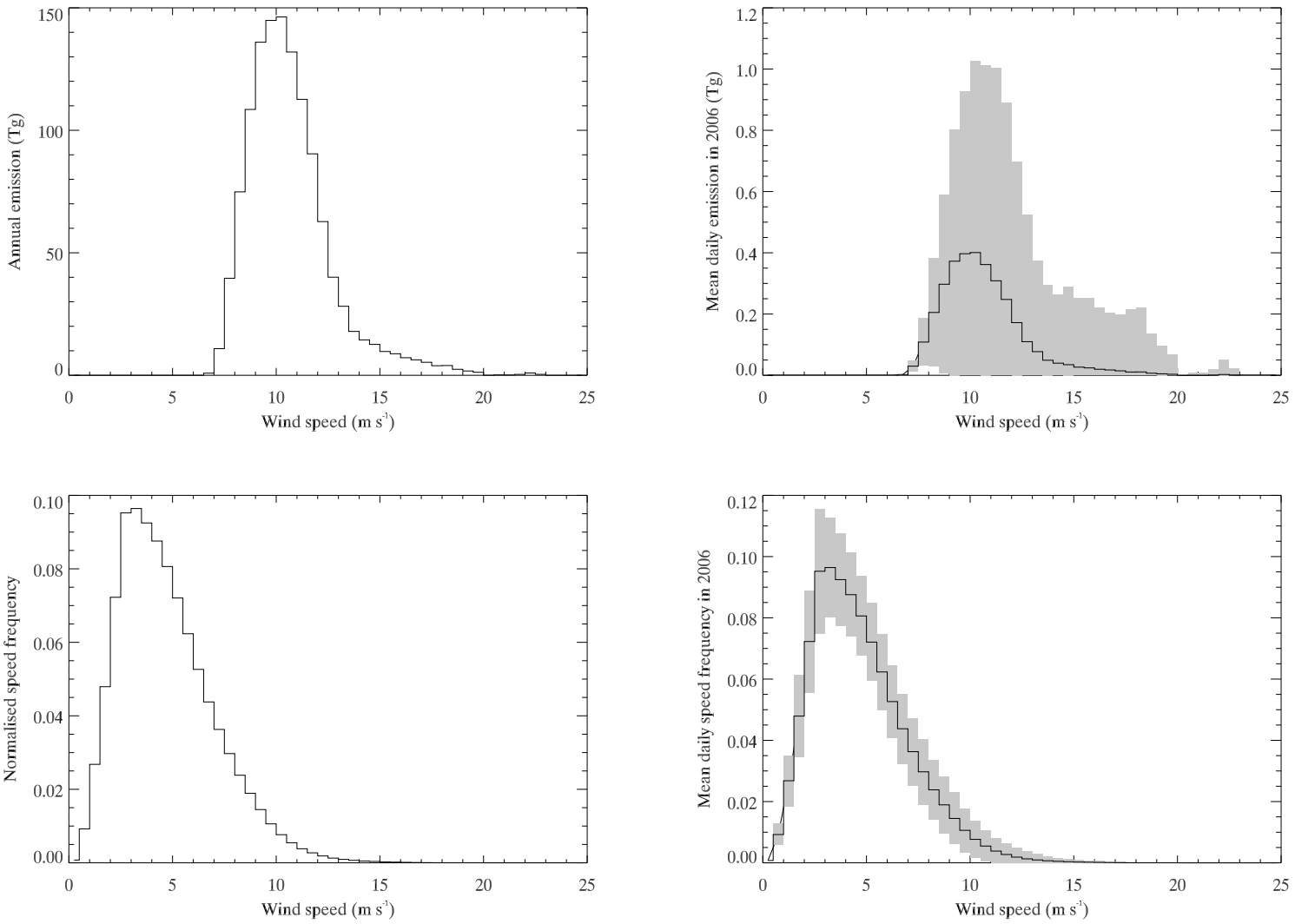

Figure 3.27: Plots of emissions as a function of wind speed. Top left: total yearly emissions. Top right: mean daily emissions, with standard deviations. Bottom left: normalised frequency of occurrence of wind speeds. Bottom right: mean daily normalised frequency of wind speeds, with standard deviations.

	MB95		Power-law	
Area	IGBP-DIS	LISA	IGBP-DIS	LISA
Bodélé Depression (17.75 °N, 18.25 °E)	21.9	34.8	95.9	22.6
West coast (21.25 °N, 16.25 °W)	48.8	57.9	150.6	25.6
Northern Mauritania (24.75 °N, 10.25 °W)	51.0	24.6	130.3	18.4
NE Libya (30.75 °N, 21.25 °E)	19.8	21.9	66.6	18.5
Total for North Africa	779.9	1225.2	6195.4	1241.1

Table 3.5: Total yearly emissions (in Tg) for the two different soil data sets, and the two different emissions schemes.

possible wind speeds (22-23 $\mathrm{m\,s^{-1}}$), at which a very low number of events can produce short-lived, intense dust events.

3.9 Comparisons between emission schemes, and between soil data sets

The chosen emissions scheme is the MB95 scheme, and the LISA soil data set has been chosen for the soil properties. There are several other valid possibilities for the emissions, that involve either the MB95 or the power-law (with and without wind gustiness) emission schemes, and either the LISA or the IGBP-DIS soils. Table 3.5 and figure 3.28 present comparisons of the simulated emissions for 2006 from four of the possible emissions scenarios. Here, the power-law emission scheme does not include the wind gustiness parameterisation. The parameterisations of drag partitioning and of the erodible fraction E are made using the roughness length data from the LISA data set, and these are used in both emissions schemes and both soil types.

Within the context of the MB95 emissions, the emissions from the LISA soils are noticeably stronger than those from the IGBP-DIS soils (reduced from a total of 1225 $\mathrm{Tg\,year^{-1}}$ to 780 $\mathrm{Tg\,year^{-1}}$), except in the northern Mauritanian source region and a few other areas, such as on the Algerian/Nigerien border. The west coast and the Bodélé remain major source regions in the IGBP-DIS version. Broadly the pattern remains the same, though there is a greater difference between the baseline emissions from most of the desert and the peak source regions. Hence the uncertainty in the MB95 emissions due to the soils is very similar to the uncertainty due to the meteorology.

The power-law emission schemes predict substantially larger annual emissions than the MB95 schemes, and are extrememly sensitive to the choice of soil properties. The power-law emissions are rather less constrained by the threshold velocity than are the MB95 emissions, because the scheme

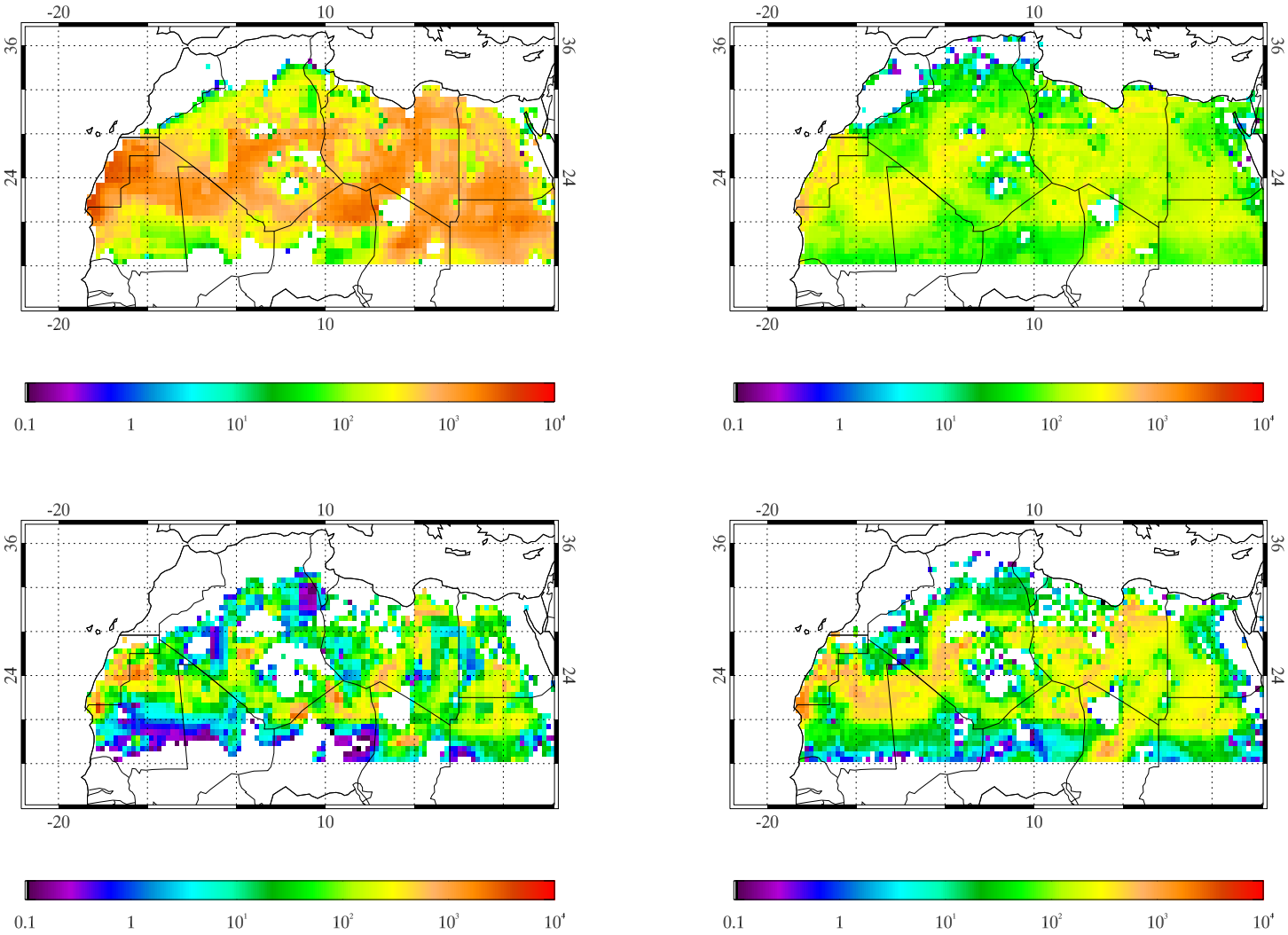

Figure 3.28: Maps of 2006 emissions ($\mathrm{g\,m^{-2}\,year^{-1}}$) for: top left, power-law emission from IGBP-DIS soils; top right, power-law emission from LISA soils; bottom left, MB95 emission from IGBP-DIS soils; MB95 emission from LISA soils.

uses the 10 m winds instead of the friction velocity (the 10 m winds are typically of the order of several $\mathrm{m\,s^{-1}}$, while the friction velocities are typically of the order of tenths of a $\mathrm{m\,s^{-1}}$). This permits smaller particles to be directly entrained by the winds, rather than explicitly requiring a formulation for saltation. However, this does mean that larger areas of North Africa are permitted to emit, and so larger quantities of dust are emitted. The LISA power-law emissions are much more similar to the MB95 emissions than are the IGBP-DIS emissions, which may reflect the higher precision of the LISA soils, and their more physical clay and silt fractions: in the IGBP-DIS soils there are much more fine particles which can be directly mobilised by the wind. This explains why these soils emit such an unrealistic quantity in the power-law scheme, but not in the MB95 scheme, which requires sufficient quantities of sand for the saltation flux. Since the two soil data sets agree much better in the MB95 scheme, this is chosen as the model emission scheme.

3.10 Emission comparison

Other models have made estimates of dust emissions from North Africa. Since regional emissions cannot be measured directly, we require models to provide substantive comparisons. Emissions can be validated within the model context by comparing the transported dust against observations (satellite or AERONET). The work of Laurent et al. (2008) is perhaps the most relevant to this study, since the same soil data set has been used in both models. A comparison of the resultant emission maps is displayed in figure 3.29. The current model reproduces well the spatial distribution of dust sources, such as the West coast source, the arc of West African sources, the Bodélé, and the far eastern Egyptian/Sudanese source region. However, the magnitudes are slightly different: in Laurent et al. (2008), the average yearly dust emission (using ECMWF ERA-40 data) for 1996-2001 is 669±62 $\mathrm{Tg\,year^{-1}}$, whereas in the current model it is 1340±81 $\mathrm{Tg\,year^{-1}}$ for 2004-2006 (using both resolutions) and 531±18 $\mathrm{Tg\,year^{-1}}$ for 2007-2008.

GCMs meanwhile, predict rather higher emissions. Ginoux et al. (2004), using a simple emission scheme, predict dust emissions of 1430±66 $\mathrm{Tg\,year^{-1}}$, while Zender et al. (2003), using the MB95 scheme, predict emissions of 980 $\mathrm{Tg\,year^{-1}}$ for Africa (globally, 1490±160 $\mathrm{Tg\,year^{-1}}$). The majority of simulated African emissions come from North Africa, though there are smaller source regions in southern Africa (in the Kalahari and the Namib) and in Ethiopia, which are of the order of <10% of the African emissions. The emissions predicted by the current model are at the same order of magnitude as the other models, giving quite similar results.

Since there are no direct measurements of emission (though saltation can be measured by surface

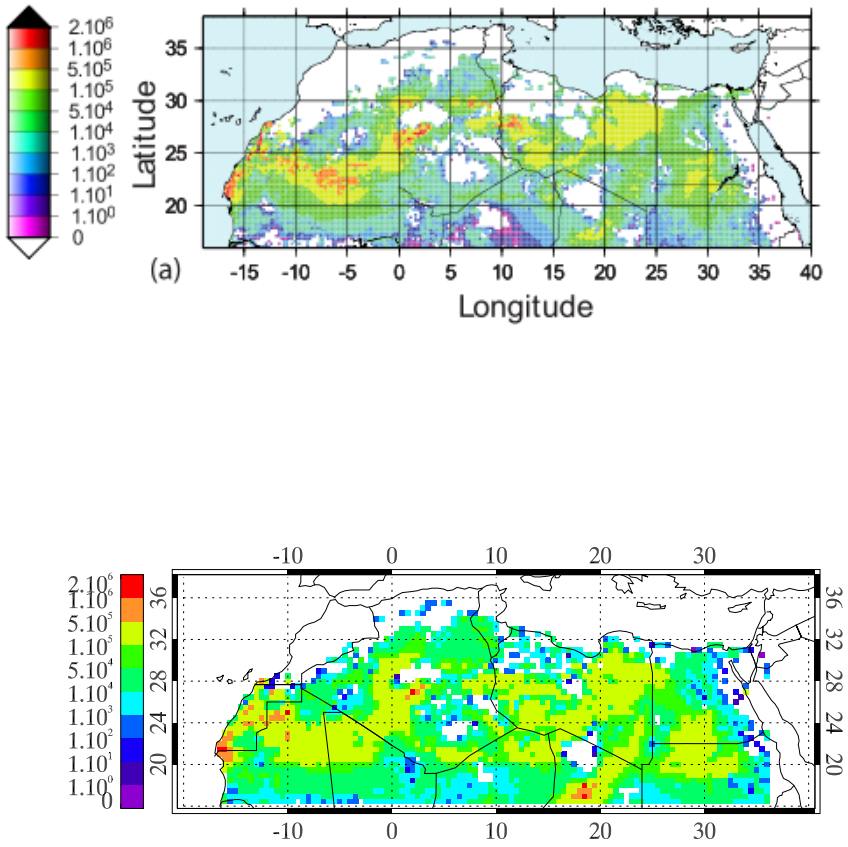

Figure 3.29: (a) Yearly dust emissions, in Mg grid cell^{-1}, for 1996-2001, adapted from figure 3 (Laurent et al., 2008). (b) SHAMAL model yearly dust emission, in Mg grid cell^{-1}, for 2004-2008.

instruments, e.g. Rajot et al. (2008)), for further validation, we require the use of transport models. The advantage that transport models have is that they can be used to link the modelled emissions to modelled optical depths (by calculating the transport and atmospheric dust loading), which *can* be validated against measurements (e.g. from satellites, or from AERONET sites). Chapter 4 will explain the structure of the SHAMAL dust transport model, and chapter 5 will present and validate the results from this model.

Chapter 4

The Dust Transport Model

A three-dimensional regional dust transport model has been created to simulate the atmospheric transport of desert dust. In this chapter the model is described, with details of the model input data, the atmospheric processes included in the model, the method used to predict dust optical depth, and an evaluation of the model uncertainty.

4.1 Dust and Aerosol Transport Models

Previous work has been carried out with dust transport models, on varying scales, from the regional to the global. Table 4.1 shows several examples of dust/aerosol transport models. This section will describe a few of these (with the most relevant dust components) in more detail.

Model	Reference	Model type	Domain	Horizontal resolution
CHIMERE	Bessagnet et al. (2004)	Aerosol	Regional	0.5 °
DEAD	Zender et al. (2003)	Dust	Global	2.8125 °
DREAM	Nickovic et al. (2001)	Dust	Regional	4-100 km
GOCART	Ginoux et al. (2001)	Aerosol	Global	2 ° lat., 2.5 ° lon.
LM-MUSCAT-DES	Heinold et al. (2007)	Dust	Regional	0.125 ° (14 km)
MesoNH	Grini et al. (2006)	Aerosol	Regional	Variable
MOCAGE	Bousserez et al. (2007)	Aerosol	Regional	Variable- 0.5 °, 2 °
ModelE	Miller et al. (2006)	Aerosol	Global	4 ° lat., 5 ° lon.
RegCM3	Zakey et al. (2006)	Dust	Regional	20-80 km
SHAMAL		Dust	Regional	0.25 °/0.5 °

Table 4.1: Some examples of aerosol/mineral dust transport models from recent literature. Aerosol models tend to have a dust component, while dust models specifically focus on dust processes.

4.1.1 DEAD

The Dust Entrainment And Deposition (DEAD) model (Zender et al., 2003), of the University of California, is a global dust emission and transport model. It is embedded within the Model for Atmospheric Chemistry and Transport (MATCH), which has a resolution of 2.8125 ° (Rasch et al., 1997) and uses NCEP meteorology to drive it. The IGBP-DIS soil texture data set is used, as described in section 3.2. As with the SHAMAL model, DEAD uses the MB95 emission scheme to simulate emissions produced by the process of saltation. Deposition processes included are gravitational settling, turbulent mix-out, and wet scavenging.

Results from the model predict (Zender et al., 2003) an average annual emission during the 1990s of 1490±160 Tg, less than the GOCART prediction. Africa provides 980 Tg yr^{-1} of this total, while Asia provides 415. Globally, the simulated annual oceanic deposition is 314 Tg, of which 178 Tg is to the North Atlantic, 29 Tg is to the South Atlantic, 39 Tg is to the Pacific, and 48 Tg is to the Indian Ocean. Total simulated annual deposition to the land and sea is 866 Tg for dry deposition and 607 Tg for wet deposition. Dust dry deposition is centred over the dry belt across North Africa through the Middle East to Central and East Asia, with a 'tongue' extending off the coast of West Africa to the Caribbean. Wet deposition is much more diffuse, extending over a much wider area, including all of Europe, most of Asia, Africa, Australia and the North Atlantic, and much of the Americas. The average annual mean optical depth due to dust at 630 nm is 0.030±0.004.

4.1.2 DREAM/SKIRON

The Dust REgional Atmospheric Modeling (DREAM) system (Nickovic et al., 2001; Kallos et al., 2006; Haustein et al., 2009) has been developed primarily at the University of Athens, in the framework of the SKIRON/Eta forcasting system. It is a multiscale model that can be used for a domain covering much of Africa, reaching out to Europe and across the Atlantic to North America, but it can also be used on a smaller scale, covering only North Africa. Soil information from the FAO/UNESCO soil data set is used (Zobler, 1986), and vegetation from the USGS. Emission is proportional to $u_*^2[1-(u_{*_t}/u_*)^2]$, following the work of Shao et al. (1993) and is part of the family of emission schemes which explicitly calculate the saltation flux in order to calculate the emission flux (described in section 3.4.3).

The DREAM model has been used to calculate dust concentrations in transatlantic dust episodes (Kallos et al., 2006), with a peak concentration of Saharan dust of 20 $\mu g\,m^{-3}$ over the

southern United States during a summer 1993 dust event. More recent work compares model output size distributions during May 2006 (Haustein et al., 2009) against observations from the SAMUM (Saharan mineral dust experiment) project which measured dust size distributions and particle characteristics in southern Morocco during May and June 2006 (Heintzenberg, 2009). Of particular interest was a dust plume which stretched along Morocco to the Iberian coast: the simulations suggested it had an optical depth of up to 0.75, with a plume extending as high as 4 km (which compared favourably with aircraft measurements carried out during SAMUM).

4.1.3 GOCART

The Global Ozone Chemistry Aerosol Radiation and Transport (GOCART) model (Ginoux et al., 2001, 2004) has been produced at the NASA Goddard Space Flight Center. It is a global model, and is used to predict the transport of mineral dust and other aerosols and trace gases such as sulphates (Chin et al., 2000) and carbon monoxide (Allen et al., 1996).

The GOCART model uses assimilated meteorological data from the Goddard Earth Observing System Data Assimilation System on a 2 ° latitude by 2.5 ° longitude grid, with 20-40 height layers. It calculates seven aerosol processes: emission (using the power-law emission scheme described in section 3.4.3); chemistry (aerosol microphysics, such as aerosol-cloud interactions); advection, using a flux-form semi-Lagrangian transport scheme (Lin and Rood, 1996); diffusion; convection; dry deposition; wet deposition. Emission is carried out by pre-defining a constant soil size distribution (Ginoux et al., 2001), and using a 'source function' S which is calculated from the elevation difference surrounding a grid cell (over bare soils only, as observed by AVHRR). These processes are calculated for four size bins: 0.1-1 (0.75), 1-2 (1.5), 2-3 (2.5), and 3-6 (4.5) μm radius, with the numbers in brackets representing the average radius. Within each bin the size distribution $dM/d\ln r$ is constant. Particles larger than this fall out quickly and so are ignored. The time step is 20 minutes, and the wind fields are linearly interpolated to every time step, from the instantaneous values at every six hours. The model is initialised with near-zero aerosol mass, and is spun-up for 1 month (Ginoux et al., 2001).

The GOCART model was run using data from 1981-1996, and predicts a maximum annual global emission of airborne dust of 2400 Tg (Ginoux et al., 2004), calculated for 1988, and a minimum of 1950 Tg in 1996. Sixty-five percent of these emissions are from North Africa, with the Bodélé Depression being the major dust source in winter. Ninety percent of the global dust deposition occurs due to dry deposition (as opposed to wet deposition), which has significant

regional variations. Over North Africa the annual deposition is 1119±54 Tg, of which 60±11 Tg is wet deposition (and 53±9 Tg of this are in the Sahel, defined as being south of 21.25 °N). Over the North Atlantic, the simulated annual dry deposition is 128±12 Tg, while the wet deposition is 33±6 Tg. The majority of this deposited dust is North African in origin.

4.1.4 Deficiency of current models: motivation for SHAMAL

The differences between the various models show that there is more work that needs to be done to constrain predictions of dust loading, emissions, and transport. Consider emission: GOCART (Ginoux et al., 2004) predicts that North Africa emits 1430±66 Tg of dust per year, whereas Laurent et al. (2008) predicts that North Africa emits 669±62 Tg of dust per year, which is a difference of a factor of two. The reasons for this discrepancy include the use of different soil data sets, dust emission schemes, and spatial resolution (SHAMAL is closer in configuration to the model used by Laurent et al. (2008), but uses a different version of the ECMWF meteorological data set). Similarly, predictions of dust deposition are also variable: GOCART and DEAD predict quite similar values of deposition into the Atlantic of 161±33 and 178 $\mathrm{Tg\,year^{-1}}$, but observations from MODIS (Kaufman et al., 2005) suggest a lower value of 140±40 $\mathrm{Tg\,year^{-1}}$. Deposition has rarely been explicitly calculated by regional models, only by GCMs such as DEAD and GOCART. It would therefore be instructive to use a higher resolution regional model such as SHAMAL, which uses more highly resolved (and less parameterised) surface characteristics, to make predictions of dust transport features such as deposition.

The SHAMAL model has been designed to include the technique of *data assimilation*, which takes advantage of observations to produce a more accurate representation of dust transport. Other models can be used to predict dust transport, but SHAMAL can also use data from various satellite instruments, such as SEVIRI, AATSR, and MISR, to come to a better understanding of various transport processes, as well as sources (using two soil size distributions, so as best to test their effectiveness) and sinks.

4.2 Model structure

The SHAMAL model is run using wind and soil data, which are used to predict the influence of atmospheric processes on the dust spatial distribution. Firstly, the model considers surface dust emission, i.e. the *source* of the dust, which was described in chapter 3. Once the dust has been

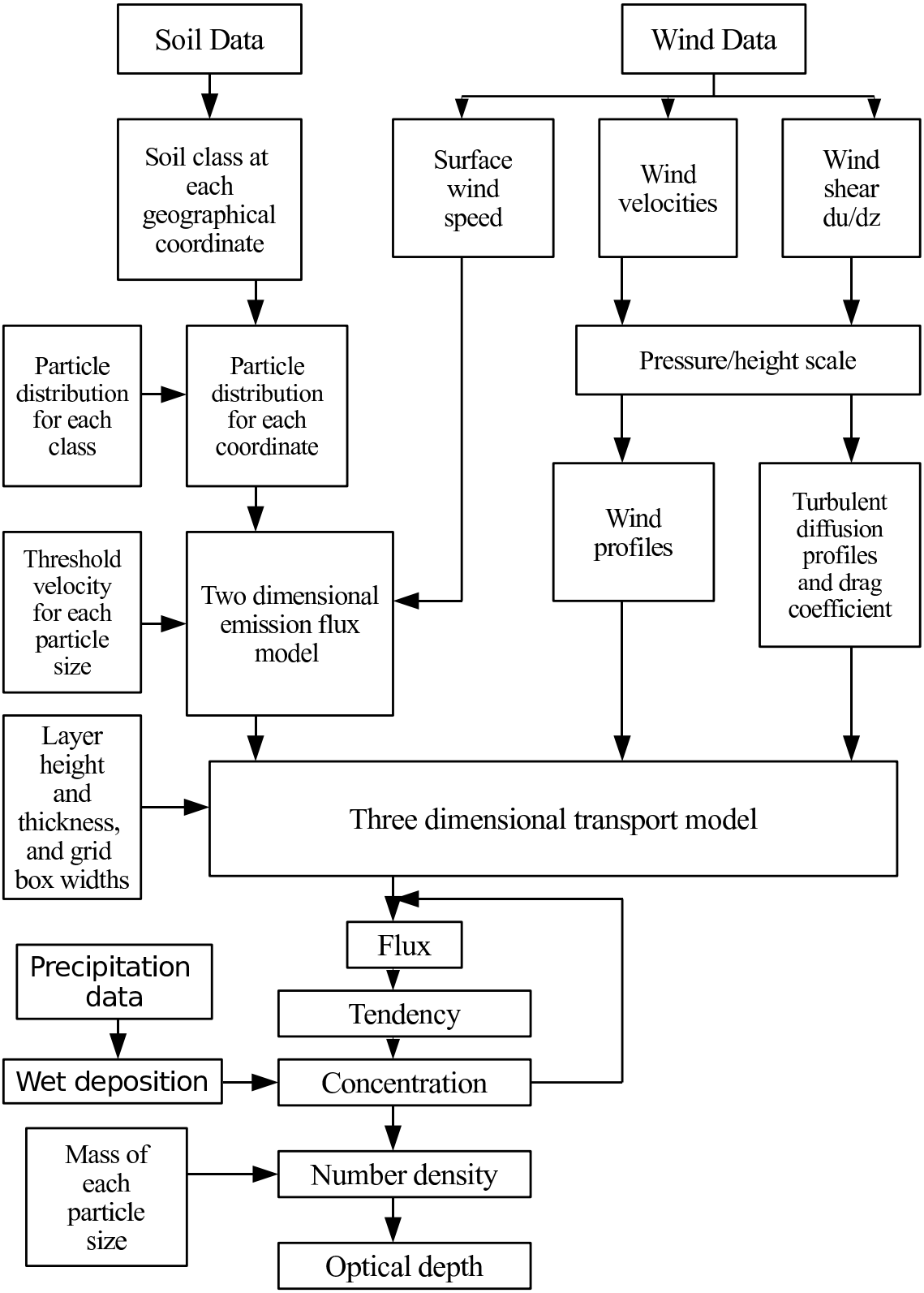

Figure 4.1: Flow chart showing the modules and processes included in the 3D dust transport model. Fluxes, tendencies, concentrations, and particle sizes are calculated for each particle size and each grid box, for each time step. Wet deposition adjusts the concentration at each time step, where there is precipitation.

lifted from the surface, then the other atmospheric processes can transport the dust. These processes include winds (zonal, meridional, and vertical), diffusion (in all three space dimensions), gravitational fall velocities, turbulent (dry) deposition, and wet deposition by precipitation scavenging. These processes move the dust concentrations between grid boxes, and can deposit dust back to the surface.

The code is structured into several parts (figure 4.1): the model setup, the transport model, and the calculations of optical depth (and other properties such as plume height, etc., which are calculable from the dust concentration).

The model setup defines the domain of the model, the numbers of grid boxes and particle sizes, and determines the conditions present within the model. These conditions include the emissions, wind speeds, diffusion coefficients, settling and deposition velocities, and precipitation rates, all bilinearly interpolated to the model grid and interpolated to a model time period of 20 minutes (model time steps within these time periods use the same atmospheric conditions). The winds are linearly interpolated from the ECMWF temporal resolution of 6 hours (at 0000, 0600, 1200 and 1800) to this higher resolution of 20 minutes: hence the winds are updated every 20 minutes. With a time-step of 80 seconds, the winds are updated after every 15 time-steps. These are pre-computed before running the transport model.

The transport model uses these boundary conditions to calculate the fluxes between each grid box, and from which the *tendency* in each grid box can be calculated. This grid scheme is an *Eulerian* approach, and uses finite-difference calculations to calculate the fluxes between each grid box, and therefore the grid box concentrations. Each time step is calculated sequentially, and the time step is 80 seconds. The tendency is the measure of the change in concentration χ in a grid box per unit time, and (in the vertical direction) is defined as

$$\frac{d\chi_i}{dt} = \frac{F_{i-1:i} - F_{i:i+1}}{\delta z}, \tag{4.1}$$

where $F_{\text{i-1:i}}$ is the flux between layers $i-1$ and i, and δz is the layer thickness. The tendency is then integrated over the time step to find the concentration at the end of the time step. Every 20 minutes the concentration is saved. Using the concentration data, particle number densities $n(r)$ can be extrapolated from the particle mass $m(r)$:

$$n(r) = \frac{\chi(r)}{m(r)}. \tag{4.2}$$

From this we can find the optical depths at the various wavelengths of interest.

The method used to calculate the fluxes and the concentrations is the standard Runge-Kutta scheme, a fourth-order numerical method (e.g. Selvam (2007)) which computes fluxes and concentrations at intermediate points within the model time-step. Given certain initial conditions, the method is self-starting, and has been chosen for this simplicity. If the system is 'stiff' (Brasseur and Madronich, 1992), such that the various processes occur too strongly within the model time-step and grid-box width, then this method can be unstable and inaccurate: the choice of time-step has been chosen to minimise this problem. Other methods, such as the second-order Lax-Wendroff scheme (Haltiner and Williams, 1980), could also have been used, and would have been valid methods.

The time-step is small enough that errors in mass conservation are minimal. A test run over the North African domain using the transport model with emissions from the 1st March 2006 only, and run for the subsequent 10 days, showed a slight amount of spurious extra mass. Emissions (i.e. the gains) for 1/3/2006 were 1.714 Tg, whereas the cumulative losses (from dry and wet deposition and from transport out of the domain, to the west, south, east, and north) up to the end of 11/3/2006 were 1.728 Tg: this is an increase of 0.82% over 11 days. Losses exceeded the gains only after 5 days, at 2100 on 6/3/2006. This indicates that there will be very small errors in the model due to mass conservation.

4.2.1 ECMWF meteorological data

Beyond the data used in the emission scheme (section 3.3), the extra ECMWF data set used is the regular $1.125\,^{\circ}\times1.125\,^{\circ}$ gridded data. These are extended up into the atmosphere on 91 hybrid levels, since 0600 on 1/2/2006, before which they were on 60 levels. Measurements are made and processed every six hours, at 0000, 0600, 1200, and 1800. There are wind speeds in three directions: zonal (u), meridional (v), and vertical omega velocity (ω). As with the wind speeds, there are temperature (T) data on all hybrid levels. Log surface pressure ($lnsp$) is plotted on the two-dimensional grid, and is used to define the pressure on the hybrid levels. The British Atmospheric Data Centre (BADC), based at the Rutherford Appleton Laboratory in Oxfordshire, UK, provides a text file which defines parameters $A(i)$ and $B(i)$ for each hybrid level i, which define the pressure at the edges of each hybrid layer, using (Bouttier and Courtier, 1999):

$$p_{\mathrm{half}}(i) = A(i) + B(i)\exp(lnsp). \tag{4.3}$$

The pressure on each hybrid level (on which u, v, ω and T are defined) can then be found using:

$$p(i) = \frac{p_{\text{half}}(i) + p_{\text{half}}(i+1)}{2}. \tag{4.4}$$

The altitude (z) at each pressure level is defined by reference to T.

Zonal and meridional wind speeds are measured in units of $\mathrm{m\,s^{-1}}$. The vertical omega wind velocity is measured in units of $\mathrm{Pa\,s^{-1}}$, which must be converted into units of $\mathrm{m\,s^{-1}}$ by multiplying by the change in height with respect to pressure:

$$w = \omega \frac{dz}{dp}. \tag{4.5}$$

The vertical wind velocity w is in $\mathrm{m\,s^{-1}}$, ω is in $\mathrm{Pa\,s^{-1}}$. For use in the model, the hybrid level velocities are interpolated to obtain wind velocity profiles against altitude, in metres.

4.3 Processes

Several processes are included in the transport model, including advection, diffusion, and deposition. Emission is also included, and is described in detail in chapter 3. Here, we only consider processes which affect atmospheric aerosols, rather than surface dust particles.

4.3.1 Advection: wind velocities and the gravitational settling velocity

Vertical wind velocity w is derived from the ECMWF omega velocity, as described above. This is dependent on the height of the level. Physically, w arises from atmospheric *convection*. Horizontal (zonal and meridional) wind velocities are also obtained from the ECMWF data: mean wind profiles are shown in figure 4.2.

The other vertical velocity to account for is the particle fall velocity, which is dependent on particle size and density. This is governed to a good approximation by Stokes' settling, where the settling velocity (Kasten, 1968), v_{settling}, is given by:

$$v_{\text{settling}} = \frac{2r^2 g\rho}{9\eta} C_{\text{Cunn}}, \tag{4.6}$$

where r is the particle radius, g is gravitational acceleration, ρ is the particle density, and η is the viscosity of air (or, generally, the viscosity of the fluid through which the particle is falling). The

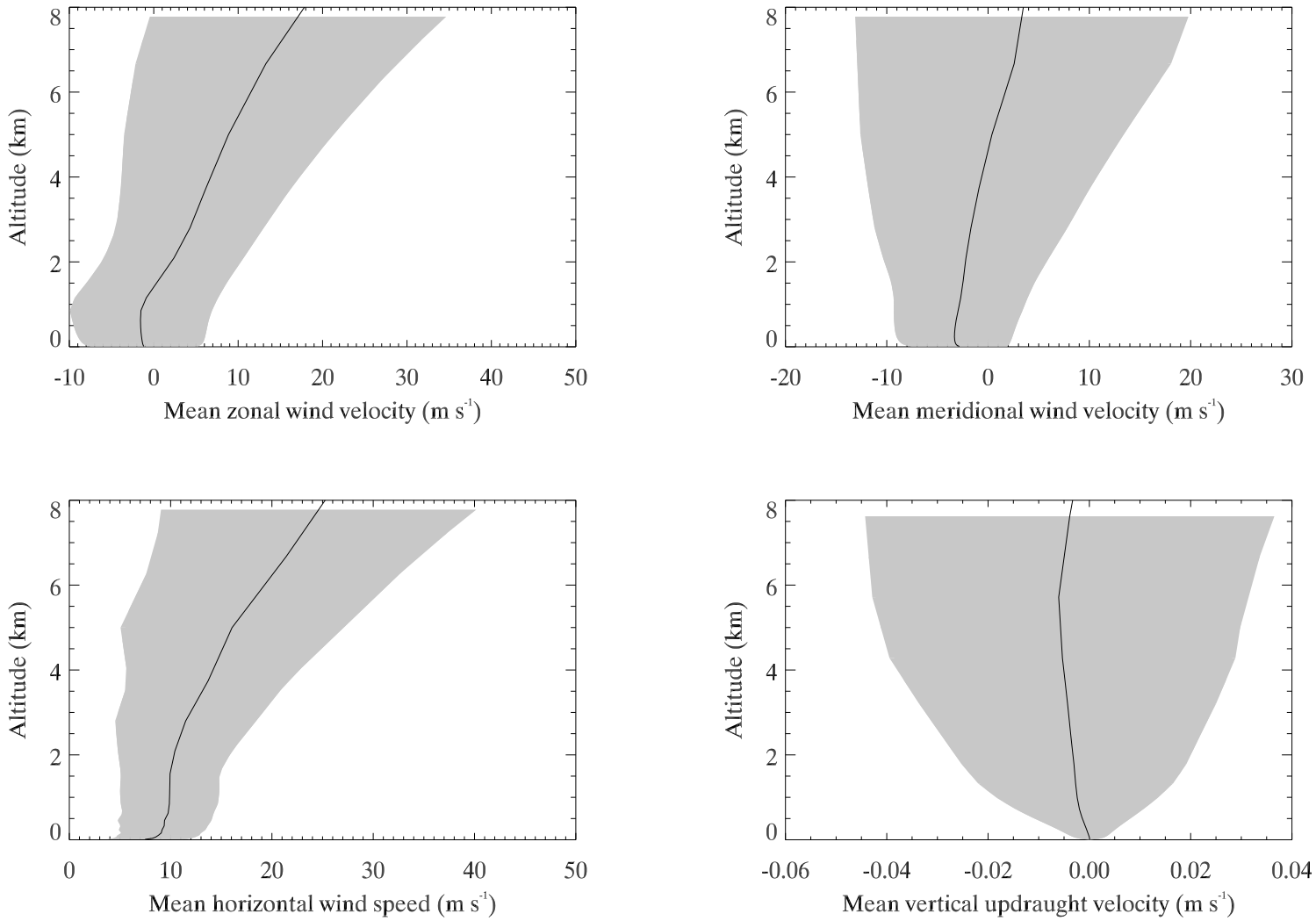

Figure 4.2: Mean wind profiles over North Africa, at 1200 on 7/3/2006: (a) zonal, (b) meridional, (c) speed, (d), vertical. The grey shading represents the standard deviation.

Cunningham correction factor, C_{Cunn}, is given by:

$$C_{\mathrm{Cunn}} = 1 + \frac{\lambda}{r}\left(1.249 + 0.418\exp\left(\frac{-0.847r}{\lambda}\right)\right), \tag{4.7}$$

where λ is the mean free path of the air molecules, and is small at low altitudes, i.e. in the troposphere. Therefore, C_{Cunn} can be taken to equal 1 for tropospheric dust transport.

The vertical wind velocities contribute the first term in the vertical flux equation. The flux is dependent on the concentration of particles between the layers, such that:

$$F_{\mathrm{i:i+1}} = \frac{1}{2}(w - w_{\mathrm{fall}})(\chi_{\mathrm{i}} + \chi_{\mathrm{i+1}}), \tag{4.8}$$

where w is the vertical wind velocity, w_{fall} is the particle fall velocity (settling velocity), and χ_{i} and $\chi_{\mathrm{i+1}}$ are the concentrations in layers i and $i+1$. An 'upstream' approximation is used so that if the particles are falling ($w_{\mathrm{fall}} > w$) then the concentration is χ_{i}, and vice versa.

4.3.2 Turbulent diffusion

Turbulent diffusion is controlled by the turbulent diffusion coefficient, K_{zz}, which controls the rate of diffusion of dust in the atmosphere. The other conditions which control the rate are the thickness of the grid box, and the difference in concentrations between adjacent grid boxes. K_{zz} varies with height within the planetary boundary layer (PBL), above which it is assumed to be negligible. Used here is the scheme described by Troen and Mahrt (1986) and Holtslag and Boville (1993), whereby K_{zz} varies as a quadratic function within the PBL:

$$K_{zz} = \kappa u^* z\left(1 - \frac{z}{h}\right)^2. \tag{4.9}$$

A mean diffusion profile is shown in figure 4.3. K_{zz} cannot be negative, because it is a measure of how strongly particles diffuse away from each other, to areas of lower concentration; negative diffusion coefficients imply that the particles are 'diffusing' towards each other, which is unphysical.

In equation 4.9, the height of the PBL is h, of the order of $u^*/4f$ (Blackadar and Tennekes, 1968) where u^* is the friction velocity and f is the Coriolis parameter ($f(\phi) = 2\Omega\sin\phi$ where Ω is the angular velocity of the Earth's rotation and ϕ is the latitude). The ECMWF operational analysis model outputs values of the PBL at 1200 and 0000 each day. North Africa has an extremely

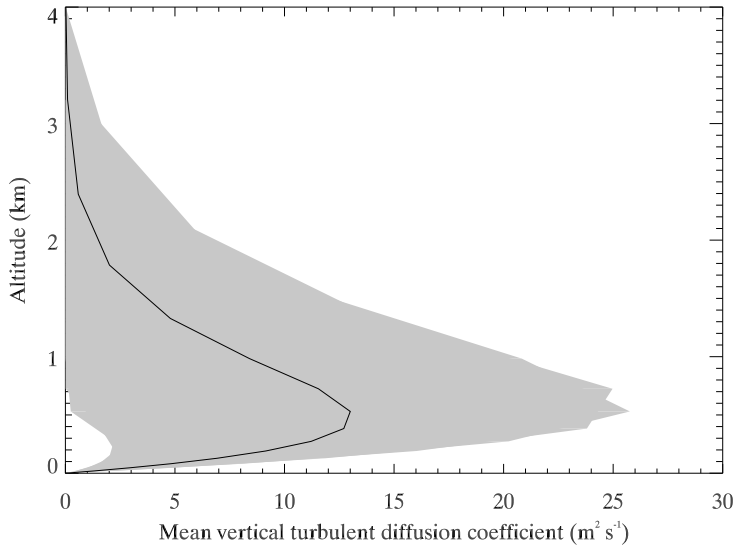

Figure 4.3: The mean vertical turbulent diffusion coefficient (K_{zz}) profile over the Sahara, at 1200 on 7/3/2006. The grey shading represents the standard deviation.

large diurnal variation in the height of the PBL, due to the large temperature variations (figure 4.4). Since the atmosphere cools so much at night there is much less buoyant energy available for turbulent mixing (Warner, 2004), and so the depth of the boundary layer shrinks. Since vertical transport is dominated by diffusion, vertical uplift is often suppressed at night.

The diffusion term in the vertical flux equation is as follows:

$$F_{i:i+1} = -\frac{K_{zz}}{\delta z}(\chi_i - \chi_{i+1}). \tag{4.10}$$

The thickness of the layer is δz. Following Nickovic et al. (2001), the same value of the diffusion term (K_{zz}) is used for lateral diffusion.

4.3.3 Deposition

Dry deposition

Dry deposition is mainly the result of gravitational settling, though there can also be downdrafts in the vertical wind velocity. Another component of dry deposition is turbulent mixing from the first, or lowest, layer of the atmosphere, down to the surface. Dry deposition is the main mechanism of deposition near the source areas, since the source areas are almost always arid, and forms the bulk

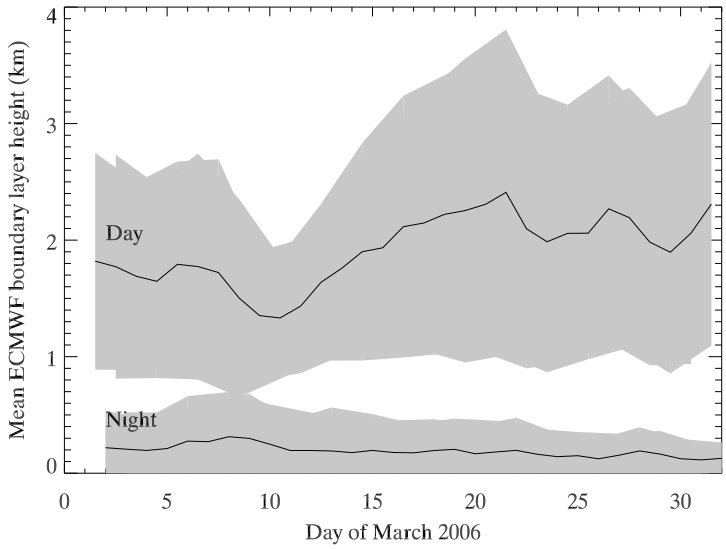

Figure 4.4: The mean PBL height over the Sahara, during March 2006. The standard deviation is marked in grey.

of the vertical transport scheme in the model.

Turbulent mixing from the lowest layer to the surface cannot be described using the turbulent diffusion coefficient scheme outlined above, since the surface is not an atmospheric layer, and cannot have a concentration of particles within it. Instead we consider the effect of drag on the lowest layer. Bagnold (1941), in his seminal work, defines the drag (stress), τ ($\mathrm{kg\,m^{-1}\,s^{-2}}$), which is dependent on the friction velocity u^* and the air density ρ:

$$\tau = \rho u^{*2}. \tag{4.11}$$

The drag coefficient (Brown, 1974, p.50), C_D, is defined as the ratio of the drag stress τ and the pressure exerted by the wind velocity:

$$C_\mathrm{D} = \frac{\tau}{\rho u^2}. \tag{4.12}$$

In the dry case, we can take the turbulent mixing velocity, v_d (Tegen and Fung, 1994), out of the first layer to the surface to be:

$$v_\mathrm{d} = u C_\mathrm{D}. \tag{4.13}$$

We then multiply this by the concentration in the lowest layer to find the flux to the surface due to turbulent settling.

Wet deposition

Wet deposition is a rare process over desert regions, but becomes more relevant for dust plumes that pass over seas and oceans, and other less arid regions, such as Europe. When rain falls through a dust cloud the process of *scavenging* (Zender et al., 2003) occurs, whereby dust particles are collected within the raindrops and dropped to the surface. This can be an important deposition process for small particles because dry deposition processes are very inefficient for $D < 2\mu$m, due to very slow particle settling velocities. The larger particles are more likely to have been already removed from the plume by the time the plume reaches an area where precipitation occurs (since source regions are generally arid), so wet deposition is most important for smaller particles, and will occur some distance from the source.

Wet deposition is parameterised simply in the model, due to the fact that precipitation is sporadic in desert regions, and localised in extent. Only on the peripheries of the Sahara region, along the Mediterranean and Atlantic coasts and over the Sahel, is precipitation of any significance to dust transport. A similar approach is followed as for the suppression of emission due to soil moisture (section 3.4.6): all dust aerosol is washed out of the atmosphere underneath the top of the cloud layer if there is greater than 1 mm of rain during that day.

4.4 Optical depth

In order to compare the simulated model to reality and to test its validity, it is necessary to extrapolate a property which can be detected. One such property is the aerosol optical depth, which is detected principally by satellites, though there are ground sites (e.g. AERONET) which can be used as well. Models such as GOCART and DEAD also calculate optical depth, since the aerosol optical depth is often retrieved by satellite instruments, and is indicative of the aerosol loading (Chin et al., 2002). Indeed, one of the main methods for comparing model output to satellite observations is by comparing the predicted and the observed optical depths.

The optical depth caused by a column of aerosol is dependent on four factors:

(1) The effective refractive index of the mineral (i.e. dependent on the dust composition);

(2) The size distribution of the aerosol particles;

(3) The depth of the aerosol layer;

(4) The wavelength of the light used to retrieve the aerosol properties.

(2) and (3) are output by the model, while (1) and (4) must be parameterised. The optical depth

can be found using Mie scattering theory (Mie, 1908; Van de Hulst, 1957), which assumes that the dust particles are spherical.

We first define the size (Mie) parameter, dependent on the radius of the particle, r, and the wavelength of the radiation, λ:

$$\alpha = \frac{2\pi r}{\lambda}. \tag{4.14}$$

The extinction efficiency, $Q^{\text{ext}}(r)$, is related to the extinction coefficient, $\sigma^{\text{ext}}(r)$, by the cross-sectional area of the particle:

$$\sigma^{\text{ext}}(r) = \pi r^2 Q^{\text{ext}}(r). \tag{4.15}$$

The scattering efficiency is dependent on α, the effective refractive index n, and the coefficients a_{n} and b_{n}, which are the amplitudes of the scattered partial waves:

$$Q^{\text{ext}}(r) = \frac{2}{\alpha^2}\sum_{n=1}^{\infty}(2n+1)Re(a_n^2 + b_n^2). \tag{4.16}$$

For a number size distribution, $n(r)$, the extinction coefficient β^{ext} is given by:

$$\beta^{ext} = \sum \sigma^{\text{ext}}(r)n(r). \tag{4.17}$$

The optical depth, τ, is the integral of the extinction coefficient with the variation in height:

$$\tau = \int_0^{\infty} \beta^{\text{ext}} dz. \tag{4.18}$$

The transport model outputs $\chi(r)$ for each particle size r (and hence $n(r)$), spatial grid box, and time, and dz for each height layer. Hence optical depths and optical thicknesses for each grid box can be predicted from the model.

Following Munoz et al. (2007), the effective refractive index for Saharan dust is assumed to be $n = 1.5 + 0.004i$.

4.5 Resolution/domain size

The SHAMAL model has a domain extending from 24 °W to 36 °E, and from 12 to 38 °N. This domain stretches from the Atlantic (off the coast of West Africa, west of Cape Verde) in the west, to the Red Sea and Israel in the east. In the south-north direction it stretches from the Sahel region (e.g. northern Nigeria, Burkina Faso) in the south to the Mediterranean in the north, cutting across

the southernmost reaches of Spain, Greece, and Turkey.

The horizontal resolution of the model is 0.5 °, twice the width of a 0.25×0.25 ° grid cell (the LISA soil resolution). The meridional width is a constant 55.5 km, whereas the zonal width varies with latitude: at 12.25 °N the width is 54.2 km, while at 37.75 ° the width is 43.9 km. Vertically, there is an 18 layer atmosphere, extending to an altitude of about 10 km, near the height of the tropopause. The vertical layer thickness increases linearly with height: the lowest layer has a thickness of 20 m, while the top layer has a thickness of over 2000 m. The time step of the model is 80 s, though the output data are only saved every 20 minutes.

The particle sizes used in the model are distributed in a sectional bin scheme, in log-space, whereby each bin has a discrete particle size associated with it. The bins must be distributed among the clay and silt components of the soil, and must have a radius of less than 10 μm, since these are the aerosol particles which can be lifted to higher altitudes after the sand-blasting process. Clay and silt are the dominant components of the aerosol burden at higher altitudes and longer distances (and the optical depth). Sand only tends to be present within the saltation layer. There are 9 particle sizes in the model, so the clay fractions are at 0.016 μm ($logr$ = -1.8), 0.040 μm ($logr$ = -1.4), 0.1 μm ($logr$ = -1), 0.251 μm ($logr$ = -0.6), and 0.631 μm ($logr$ = -0.2), and the silt fractions are at 1.33 μm ($logr$ = 0.125), 2.37 μm ($logr$ = 0.375), 4.22 μm ($logr$ = 0.625), and 7.50 μm ($logr$ = 0.875).

4.6 Sensitivity analysis

Sensitivity analysis is the method by which the numbers of layers, the numbers of particle sizes, grid box width, etc., are determined. For greatest model accuracy we may prefer the model resolution to be as large as possible, but computational expense imposes limits on this. In terms of model run-time, we prefer as low a resolution as possible. To reconcile these we need to find a resolution that is high enough to agree with the most accurate resolution (within a certain tolerance), while still running at an acceptable efficiency.

Figure 4.5 shows the results of a sensitivity analysis study on varying the number of atmospheric layers, using a 1D column model. The 'true' values should converge for the smallest bin sizes (the largest number of layers), so here we compare against 401 layers. The chosen number of layers is 18, corresponding to a $\delta z_{\max}$ of over 2 km at the top of the troposphere, so that the top of the atmosphere is just over 10 km in altitude. The optical depth is 9.73 (the optical depth is particularly large because there is no horizontal advection in the 1D model) for 401 layers, and

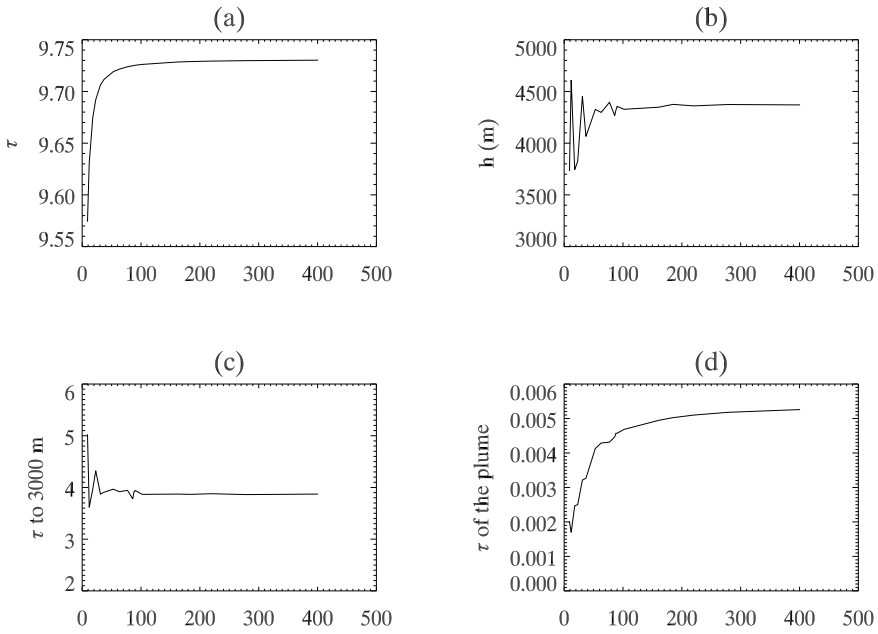

Figure 4.5: Variation of optical/dynamic properties of the aerosol distibution with the number of layers. Values taken from the steady state model from 12.00 on 16/5/2006 at 38.25 °E, 28.25 °N, after 27 hours. (a) Total optical depth, at 550 nm. (b) Height of the plume, the layer of maximum number density (above the surface layer). (c) Optical depth down to 3000 m. (d) Optical depth per metre within the plume.

9.67 for 18 layers: these agree to within 1%. The average height of the plume is 4370 m for 401 layers, 3740 m for 18 layers: this is 15% less than the 'true' value. The optical depth down to 3 km is 3.87 for 401 layers, 3.97 for 18 layers: a 2.5% difference.

Figure 4.6 displays the effect of varying the resolution, for a 36 hour run of the model to 1200 on the 8/3/2006, during which time an extreme dust event is simulated. A resolution of 0.25 ° can be considered to be the maximum resolution of the model since this is the resolution of the soil data. The chosen resolution is 0.5 °, so this must be compared against the 0.25 ° resolution. The same area is covered in each plot, but the number of grid boxes depends on the resolution. The mean optical depth in the low resolution version is 0.648, while in the high resolution version it is 0.649 (a 0.23% difference). The domain mass is similarly insensitive to the resolution change: in the low resolution version it is 17.56 Tg, while in the high resolution version it is 17.62 Tg, a 0.35% difference. Similarly, the emissions and deposition agree to with 0.5%. The peak in the optical depth is higher at the higher resolution (25.70 at high resolution, and 21.07 at low resolution): this is because there is more variability in mass between the columns (hence some columns can have

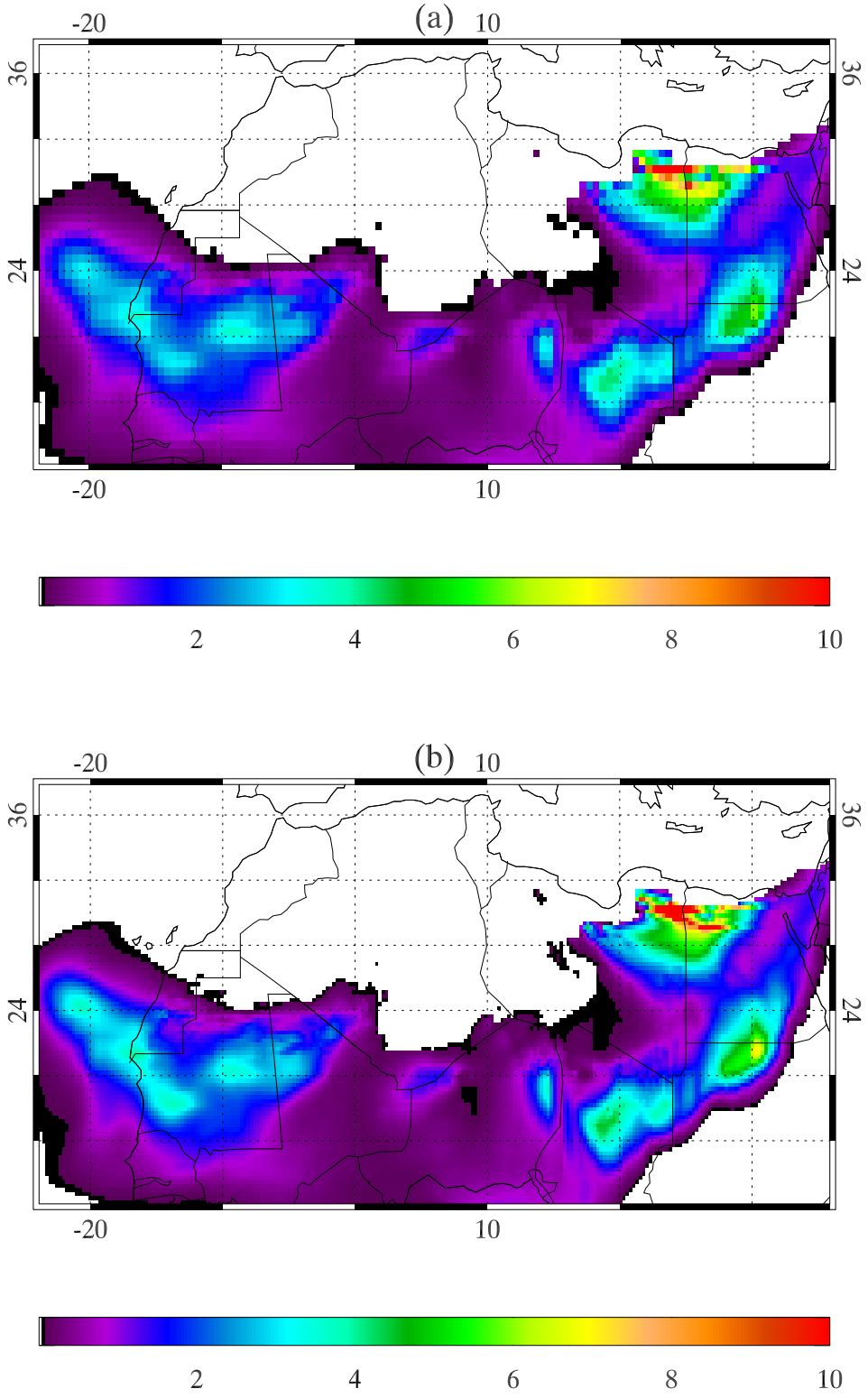

Figure 4.6: Effect of variation of resolution on optical depth (at 550 nm), after 36 hours to 8/3/2006, without model spin-up. (a) Resolution = 0.5 ° (δxy ∼55 km, 120×52 grid cells). (b) Resolution = 0.25 ° (δxy ∼28 km, 240×104 grid cells).

higher concentrations of dust), even though the total over the whole domain remains much the same. On the large-scale, the low resolution version is sufficient, since there is negligible change in the large-scale quantities. The only problem with the low resolution version that could occur is when studying local grid cells, especially when comparing against AERONET, for example. At this time, the greatest fractional increase from high resolution to low resolution AOD (over all the AERONET sites) is 2.08. The greatest difference between the two resolutions tends to be along the edges of dust storms. Even during an extreme dust event, both resolutions agree to within a factor of about two even on the local scale.

Since both resolutions will be used in this study, for different purposes, we shall refer to the low resolution version as SHAMAL-low and the high resolution version as SHAMAL-high. Results from SHAMAL-low will be presented in chapter 5, and the results from SHAMAL-high will be presented in chapter 7.

Chapter 5

A year of dust storm activity

In order to understand the impacts and the significance of dust storms, it is necessary to study their activity over an extended period, of months or years. Dust storms occur in discrete pulses, and studying just one such event without knowing about the synoptic dust conditions will not provide much understanding as to the spatial and temporal extent and variability of Saharan dust storms. This chapter will study Saharan dust activity over the course of a year, in order to understand the seasonal and geographical distribution of dust sources and dust storm activity.

There are several aspects of dust storm activity that are of interest. Firstly we are interested in dust sources (as described in chapter 3). Having estimated these, it is important to know about the *transport* of the emitted dust. Once emitted, where does the dust travel to? For example, what are the patterns of dust loading and deposition, and how do they compare to the pattern of emission? Of particular interest is the pattern of dust transport (and deposition) into the Atlantic: this may be important both for Atlantic biogeochemistry, e.g. Mahowald et al. (2005), and for transport to the Americas, e.g. Koren et al. (2006). Similarly for the European climate, it is of interest to understand the transport to Europe and the deposition into the Mediterranean, e.g. Guerzoni et al. (1997).

The advantage of using a model to study dust transport (compared to observations) is that a complete three-dimensional picture of dust activity over an entire region can be built up. For example, one of the main methods of estimating the quantities of dust being transported in the troposphere above North Africa is by using a transport model (satellites can also be used for this purpose, e.g. Kaufman et al. (2005); Koren et al. (2006)). Producing a statistically useful description of dust properties can be of great help in producing atmospheric radiative transfer

models for the purposes of remote sensing, for example. Dust altitude is also a feature of dust activity (which can only be studied otherwise by localised observations from individual lidars, aircraft campaigns, and from satellites such as CALIPSO) which can help us understand the extent of a dust storm: where dust reaches higher altitudes, the dust storm tends to be strong enough to transport the dust hundreds (if not thousands) of kilometres and to have a duration of days. There is also a size dependence on dust that reaches high altitudes, since only the smallest particles tend to be lifted to an altitude over 1 km. Hence studies of the dust aerosol size distribution will indicate the nature of the particles being transported.

Across North Africa, dust can have a significant impact on the local weather conditions, and on human health and activity; understanding where the surface (in the lowest 20 m of the atmosphere) dust concentrations are strongest will indicate where the physical impacts of Saharan dust are strongest. The North African climate may also be affected by the radiative effects of dust, and estimates of dust optical depth will give an indication of where dust has its greatest effect on the atmosphere. Moreover, the optical depth is one of the most heavily observed features of aerosols (from ground instruments and from satellite instruments), so this dust property can be used to extensively compare the model predictions to observations. Without comparing against observations it is impossible to validate the model, and so observations of dust optical depth (along with in-situ measurements of dust size distributions, etc.) are essential to understanding the usefulness of the model.

The transport model has been run from February 2006 to March 2007, a period of over a year, to simulate such quantities as dust transport, deposition, dust storm optical depths, plume heights, and dust size distributions. The results described in this model are from the 0.5° resolution model, SHAMAL-low, since these large scale quantities vary very little with resolution, as described in section 4.6. 'Yearly' results correspond to the period from March 2006 to February 2007; February 2006 is regarded as the model spin-up period (the model was initialised with zero aerosol mass at the beginning of February 2006), while model simulations from March 2007 were carried out for comparison with March 2006.

5.1 Sources and sinks

Deposition comes in two main types: *dry* and *wet* deposition. Over the entire North African domain, dry deposition dominates, since there is so little rainfall over the Sahara; however, wet deposition can be more significant around the edges of the domain, and at more local scales. We

are also interested in understanding how deposition varies between *source* and *remote* regions. Examples of remote regions include the Atlantic, the Mediterranean, the Atlas mountains, and the southern Sahel.

The net surface flux defines whether a region (or a whole domain) is a net source or a net sink of dust. It is the difference between the emission and the deposition (net sources are positive). Some source regions are actually net sinks, if they are downwind of stronger dust sources. If dust can be suspended in the atmosphere for a substantial period of time, or if the dust is allowed to move beyond the edges of the domain, then we can say a priori that the North African domain is a net source of dust aerosols, since all the dust aerosol sources are within the domain; hence, the total net surface flux will be positive.

5.1.1 Deposition over North Africa

Deposition is highly correlated with emissions (the yearly spatial correlation in SHAMAL-low is 0.94), so most Saharan dust depostion is over North Africa. Deposition estimates are presented in table 5.1. Dry deposition (the dominant deposition process over North Africa) tends to be largest near the source since the dry deposition processes (gravitational settling and turbulent deposition) can only deposit particles when they are in the lowest layer of the atmosphere. This is most efficiently done above source regions, where dust particles are emitted into the lowest atmospheric layer and which can then be quickly deposited (hence the mode of transport is between saltation and suspension, in terms of atmospheric residence lifetime).

In order to characterise the geographical distribution of source and sink regions, it is first necessary to define the source regions (figure 5.1). Sink regions are also mapped in figure 5.1, in terms of the two modes, dry and wet deposition. The areas of greatest dry deposition correspond to the source regions, as described above. However, the geographical distribution of dry deposition is much smoother than that of the emissions, which are confined to discrete source regions: dry deposition can occur over any surface, as long as there is dust suspended in the atmosphere. Atmospheric transport spreads dust to remote regions, so 'smearing out' the dry deposition.

Wet deposition does not tend to take place over source regions (the correlation between emission and wet deposition is -0.17), because dust emission requires dry soils; instead, it occurs on the coasts, over the sea, and over the seasonally wet region of the Sahel and the Sudanian Savanna to the south. Wet deposition is a more discrete process than dry deposition, since it requires the presence of precipitation, a rare process over North Africa (and is not continuous over wetter

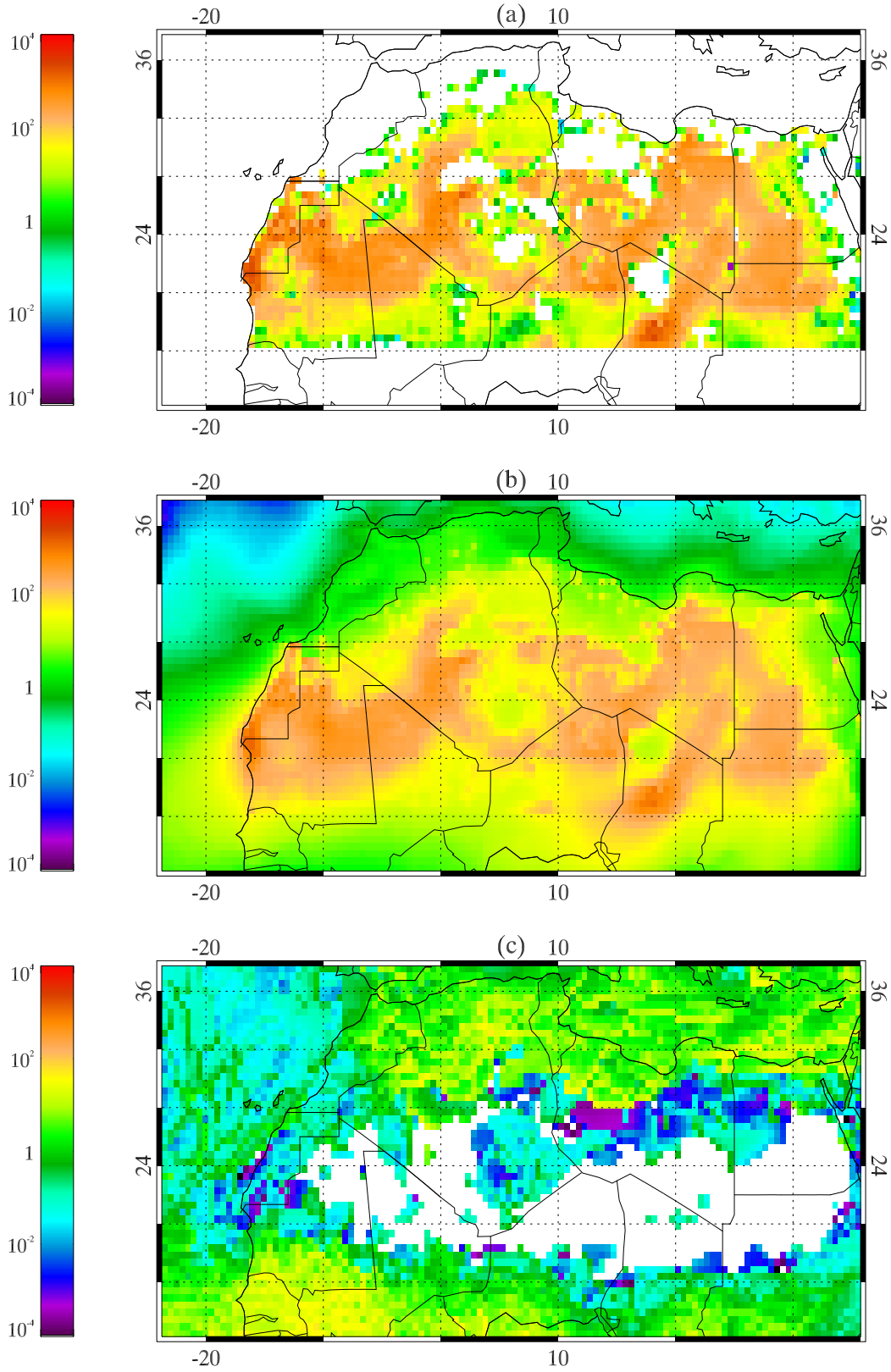

Figure 5.1: Total yearly emission and deposition (in $\mathrm{g\,m^{-2}\,year^{-1}}$), March 2006 to February 2007. (a) Emission. (b) Dry deposition. (c) Wet deposition. White areas correspond to areas with emission and deposition less than 10^{-4} $\mathrm{g\,m^{-2}\,year^{-1}}$.

			Domain deposition			North African deposition			
Year	Month	Emission	Dry	Wet	Total	Dry	Wet	Total	Net surface flux
2006	Mar	170.1	151.6	5.1	156.7	147.6	1.4	149.0	13.4
	Apr	129.1	113.3	4.4	117.8	110.3	2.1	112.4	11.3
	May	134.0	116.0	4.7	120.7	113.2	4.1	117.3	13.4
	Jun	233.6	201.1	7.2	208.3	198.9	6.5	205.4	25.3
	Jul	147.8	121.5	6.0	127.5	116.4	5.1	121.6	20.3
	Aug	92.7	74.2	8.0	82.2	71.8	6.2	77.9	10.6
	Sep	40.8	33.8	4.9	38.7	32.5	4.1	36.6	2.0
	Oct	13.2	11.1	0.9	12.0	10.5	0.8	11.3	1.1
	Nov	18.5	16.4	0.3	16.7	16.2	0.09	16.3	1.8
	Dec	47.0	41.3	0.8	42.1	40.0	0.7	40.7	4.9
2007	Jan	70.0	67.2	0.2	67.4	64.8	0.1	64.9	2.6
	Feb	60.4	53.9	2.8	56.7	52.5	2.0	54.5	3.7
	Mar	93.9	83.3	4.3	87.6	81.8	2.2	84.0	6.3
Yearly total		1157.1	1001.4	45.3	1046.7	974.8	33.2	1008.0	110.3

Table 5.1: Table of monthly emissions, depositions (dry, wet, and total) over the domain and over the North African landmass, and net surface fluxes, in $\mathrm{Tg\,month^{-1}}$. For comparison with March 2006, the emission and deposition in March 2007 is also included.

areas either). Moreover, wet deposition is strongest at the leading edge of rain-bearing clouds, where dust plumes first interact with precipitation. Some examples of this can be seen in the wet depositions (figure 5.1(c)) over the North Atlantic and the Mediterranean. Behind the leading edge, despite sufficient rainfall, there will be very little wet deposition because most of the dust has already been deposited at the leading edge; in this region wet deposition can only occur when particles which had passed over the top of the clouds, at the leading edge, subsequently descend into the cloud layer by gravitational settling.

Monthly depositions are mapped in figure 5.2. These plots indicate the strength of the dust activity over the summer months (JJA), especially over West Africa, compared to the autumn and winter months.

Figure 5.3 clarifies where the two modes of deposition dominate, on the yearly basis. While the central Sahara is dominated by dry deposition, there are some areas of northern Libya where wet deposition is important: the hamadas of north-western Libya are not source regions, nor are they frequent transport pathways for airborne dust, so even if there are only a few rainfall events per year coinciding with dust in this region, then wet deposition may become important. Dry deposition remains significant even at quite low latitudes, into southern Chad and northern Nigeria, and only to the south-west (in Burkina Faso, southern Mali and Senegal) does wet deposition dominate. On the yearly timescale, most of the dust deposited to this south-western region is during the summer months of June and July, during the monsoon season, and when the nearby West African source

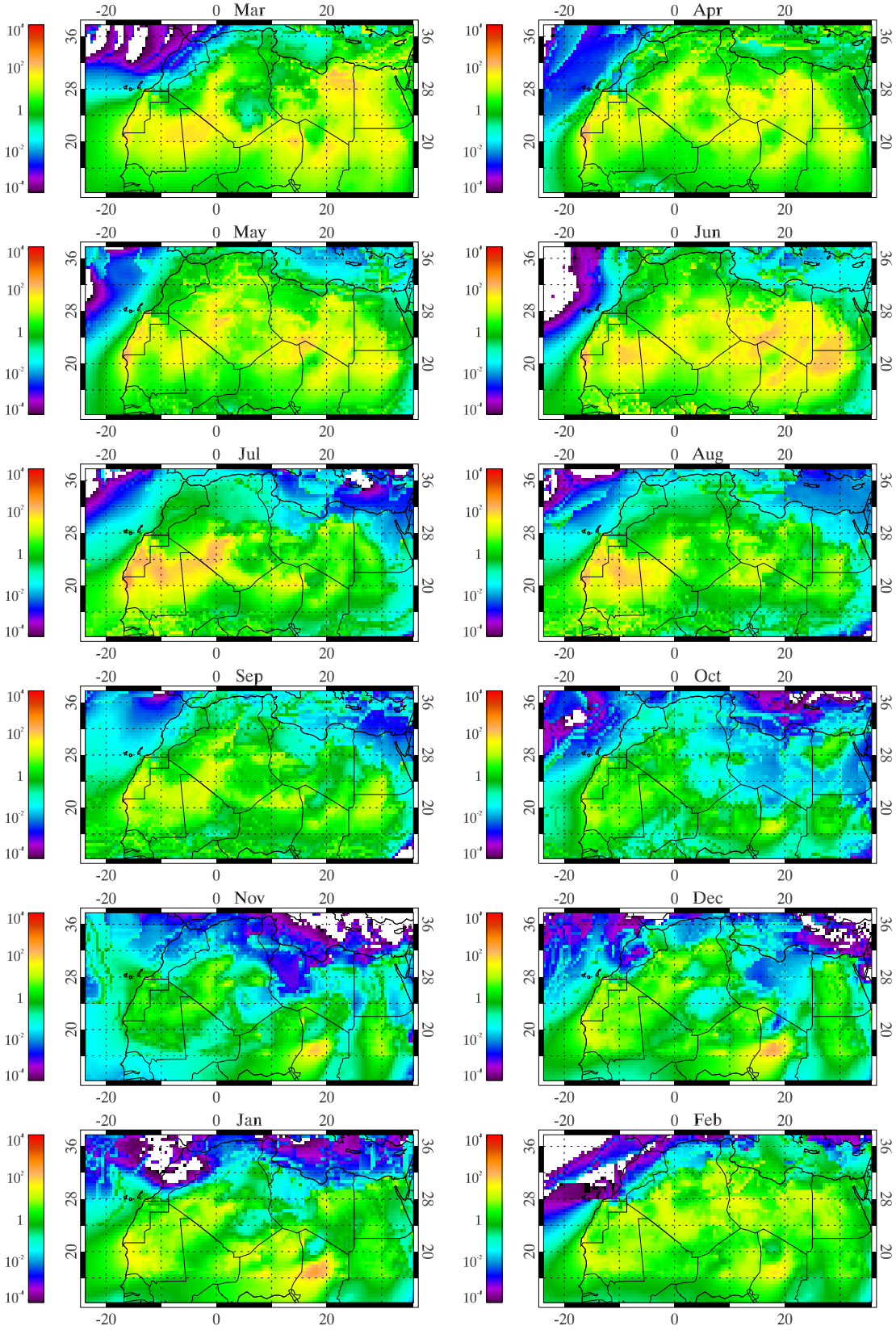

Figure 5.2: Total monthly deposition ($\mathrm{g\,m^{-2}\,month^{-1}}$), March 2006 to February 2007.

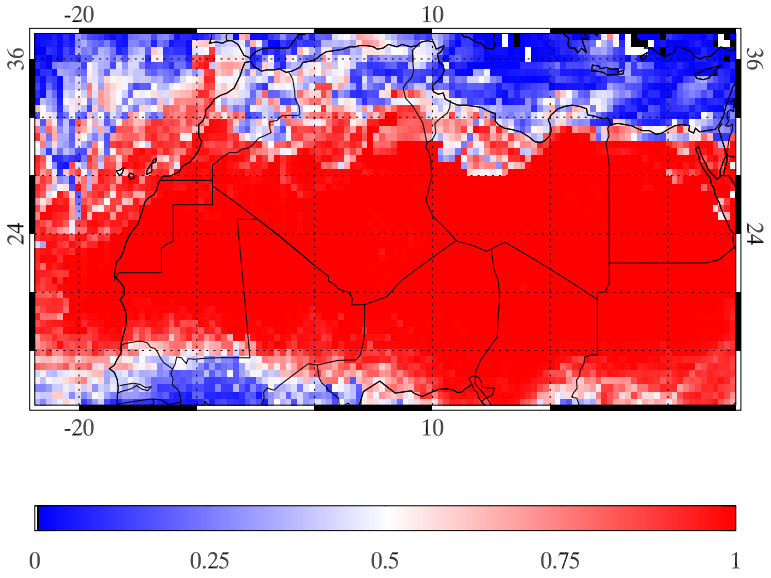

Figure 5.3: Fraction of yearly deposition carried out by dry deposition (as opposed to wet deposition) processes, March 2006 to February 2007. Red indicates where dry deposition is dominant, and blue indicates where wet deposition is dominant.

regions are at their most active.

Most of the North African domain is a net sink of dust (figure 5.4), since the only net sources are the particularly strong emitting regions (with a yearly emission greater than of order 100 $\mathrm{g\,m^{-2}}$). Many source regions are actually net sinks, situated as they are next to strong net sources of dust, which is also where the dry deposition is strongest.

A comparison of deposition over the Sahara and the Sahel (table 5.2) shows that while there is more dust deposition over the Sahara, the wet deposition over the Sahel is greater. The boundary between the Sahara and the Sahel is delineated as the line of 21 °N (following the method of Ginoux et al. (2004)), which cuts through central Mauritania and the far south of Algeria, for example. The Saharan wet deposition is concentrated along the Mediterranean coast, and mainly occurs during the spring wet season (but also occurs year-round), from February to May, when emissions are also greatest. Meanwhile the wet deposition over the Sahel is only significant during the summer (June-September) monsoon season, when wet deposition is substantial.

For comparison with previous model results, Saharan emissions and deposition agree very well with model output from GOCART (Ginoux et al., 2004), with slightly less emissions but more deposition: this suggests that both the deposition processes are stronger in the SHAMAL model.

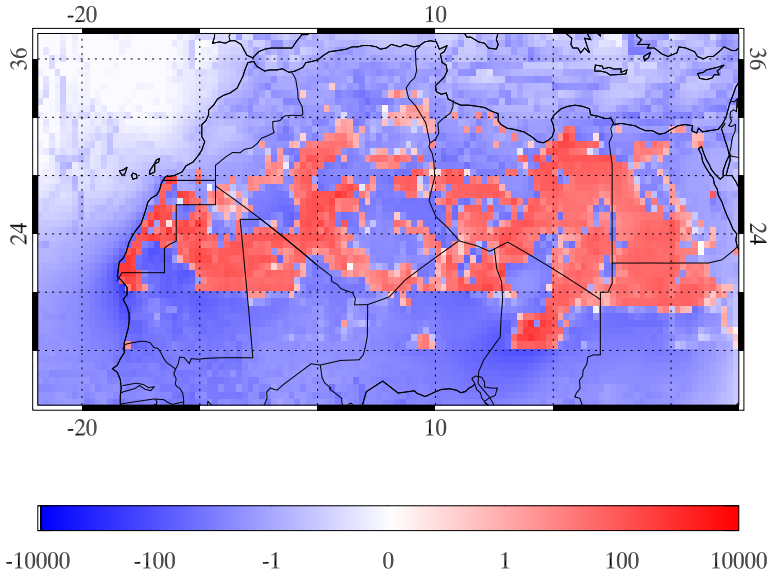

Figure 5.4: Total yearly surface flux ($g\,m^{-2}\,year^{-1}$), March 2006 to February 2007. Net sources are positive, while net sinks are negative. The maximum (i.e. net source) is 1185 $g\,m^{-2}\,year^{-1}$, while the minimum is -502 $g\,m^{-2}\,year^{-1}$.

SHAMAL has less emission in the Sahel than does GOCART (with two-thirds the GOCART emission), perhaps because GOCART is a global model, with soil data from larger areas: hence areas like Senegal, southern Mali, northern Burkina Faso, southern Niger, Chad and Sudan, and Ethiopia, may also be emitters in GOCART. Considering these emissions, the SHAMAL Sahelian deposition is relatively strong, perhaps due to the influence of transported Saharan dust.

Deposition measurements made at several ground sites (~4.25 °W, 14.75 °N) in the Niger Inland Delta in Mali (McTainsh et al., 1997) during dust events in 1990 appear to show that deposition ranges from 2.5 to 28.6 $g\,m^{-2}\,day^{-1}$, with an average of 11.5 $g\,m^{-2}\,day^{-1}$. Within SHAMAL at the same location in 2006-2007, the maximum daily dust deposition is 2.4 $g\,m^{-2}\,day^{-1}$, at the lowest end of the observations, and a total yearly deposition of 12.6 $g\,m^{-2}$. Hence the SHAMAL predictions are lower than the observations, though they are of the same order of magnitude. This may be due to the fact that the site is over a degree to the south of the modelled source region (>16 °N), whereas it is known that areas further to the south can also be source regions, especially during the drier winter months; these January dust outbreaks could be more local.

		Sahara				Sahel			
Year	Month	Emission	Dry	Wet	Total	Emission	Dry	Wet	Total
2006	Mar	121.3	84.8	1.4	86.2	48.7	62.8	0.0008	62.8
	Apr	106.8	79.1	2.0	81.1	22.3	31.2	0.2	31.4
	May	104.4	78.4	3.2	81.6	29.6	34.7	0.9	35.7
	Jun	169.0	124.0	1.6	125.6	64.6	74.9	4.9	79.8
	Jul	124.5	86.2	0.03	86.3	23.3	30.2	5.1	35.3
	Aug	73.2	50.3	0.1	50.5	19.5	21.4	6.0	27.5
	Sep	29.3	21.0	1.2	22.2	11.5	11.5	2.9	14.4
	Oct	5.9	4.4	0.3	4.8	7.3	6.1	0.4	6.5
	Nov	5.7	4.5	0.09	4.6	12.9	11.7	0.002	11.7
	Dec	15.2	11.4	0.7	12.1	31.7	28.6	0.0	28.6
2007	Jan	18.3	15.5	0.1	15.6	51.7	49.3	0.007	49.3
	Feb	41.3	33.4	2.0	35.4	19.0	19.1	0.0003	19.1
	Mar	68.5	54.6	2.1	56.8	25.4	27.2	0.05	27.2
Yearly total		814.8	593.2	12.7	605.9	342.2	381.6	20.5	402.1
Ginoux et al. (2004)		897	591	7	598	531	468	53	521

Table 5.2: Table of emissions and monthly depositions (dry, wet, and total) over the Sahara and the Sahel, in $\mathrm{Tg\,month^{-1}}$. The 'Sahara' region has an area of 6.66 million $\mathrm{km^2}$, while the 'Sahel' region has an area of 5.57 million $\mathrm{km^2}$. Included are the results from table 4 of Ginoux et al. (2004).

5.1.2 Oceanic deposition

Dust deposition to the oceans is of interest, since the minerals that dust carries can act as a fertiliser (Jickells et al., 2005; Mahowald et al., 2005; Solmon et al., 2009) by providing iron, which can increase phytoplankton production. This effect on the ocean biogeochemistry may consequently have an effect on ocean CO_2 uptake. There are two major bodies of water within the model domain: the Atlantic Ocean and the Mediterranean Sea (a small section of the northern Red Sea is also present). The domain Atlantic region has an area of 2.63 million $\mathrm{km^2}$, compared to the Mediterranean region area of 1.78 million $\mathrm{km^2}$ (i.e. the Atlantic region is 1.48 times larger than the Mediterranean region). Note that explicit measurements of dust deposition into the Atlantic will be an understimate, since the domain only contains a fraction of the Atlantic, and there will also be atmospheric dust transport out through the western, north-western and south-western edges of the domain: much of this dust will also be deposited into the Atlantic. Hence we can make two estimates of Atlantic dust deposition: explicitly over the domain, and by adding the western transport.

SHAMAL-low simulations (table 5.3) suggest that Saharan dust deposition to the Atlantic is greater than deposition to the Mediterranean, except in March. However, there are significant differences in the mode of deposition: over the smaller area of the Mediterranean there is over

		Atlantic deposition				Mediterranean deposition		
Year	Month	Dry	Wet	Total	Total+transport	Dry	Wet	Total
2006	Mar	3.26	0.001	3.26	5.84	0.39	3.53	3.92
	Apr	2.52	0.12	2.65	2.94	0.34	2.13	2.48
	May	2.52	0.02	2.53	3.57	0.09	0.59	0.68
	Jun	1.96	0.09	2.05	7.14	0.11	0.59	0.70
	Jul	4.83	0.85	5.68	24.62	0.01	0.03	0.04
	Aug	2.28	1.62	3.90	13.37	0.03	0.16	0.19
	Sep	1.24	0.66	1.90	5.44	0.01	0.13	0.14
	Oct	0.53	0.12	0.65	1.43	0.003	0.03	0.03
	Nov	0.22	0.15	0.37	0.51	0.0002	0.004	0.005
	Dec	1.22	0.03	1.25	2.02	0.002	0.04	0.04
2007	Jan	2.34	0.06	2.40	4.22	0.005	0.02	0.02
	Feb	1.26	0.003	1.26	1.82	0.04	0.72	0.76
	Mar	1.19	0.11	1.30	2.27	0.22	1.96	2.18
Yearly total		24.17	3.72	27.89	72.91	1.04	7.96	9.00

Table 5.3: Table of monthly depositions to the Atlantic and the Mediterranean, in $\mathrm{Tg\,month^{-1}}$. Included in the last column of the Atlantic deposition is the addition of the western transport from table 5.4.

twice as much wet deposition as over the Atlantic. There are two reasons for this: firstly, there is more precipitation closer to the Mediterranean coast than the Atlantic coast (figure 3.10); and secondly, the specific source regions for Mediterranean dust are closer to the coast (the West African sources extend much further inland across Mauritania to Mali). During the year 70% of Mediterranean deposition occurs in March and April, when the winds are strongest in northern Libya (and hence the emissions are stongest from this region at that time), but when there is also plenty of precipitation over the Mediterranean coast. The Mediterranean deposition predictions broadly agree with measurements (Guerzoni et al., 1997) which suggest that 2-46 $\mathrm{g\,m^{-2}\,year^{-1}}$ of dust are deposited over various regions of the Mediterranean; this compares well with a maximum Mediterranean deposition in SHAMAL of 40.7 $\mathrm{g\,m^{-2}\,year^{-1}}$. Maps of deposition into the Atlantic and the Mediterranean are presented in figures 5.5 and 5.6.

Dust deposition into the Atlantic (figure 5.7) is divided into two main zones: the North Atlantic, and the subtropical north Atlantic, defined for the purposes of this work as being divided by the line of 24 °N. In the North Atlantic, deposition is generally weaker, though wet deposition occurs more persistently than in the area south of the tropics. In the subtropical north Atlantic, there is much more dust deposition, due to the presence immediately to the east of the substantial West African (Western Saharan, Mauritanian and Malian) source regions, and this is where the bulk of the dry deposition occurs. This is also where the largest wet deposition episodes take place, from July to September when the West African source peaks coincide with the monsoon season in the

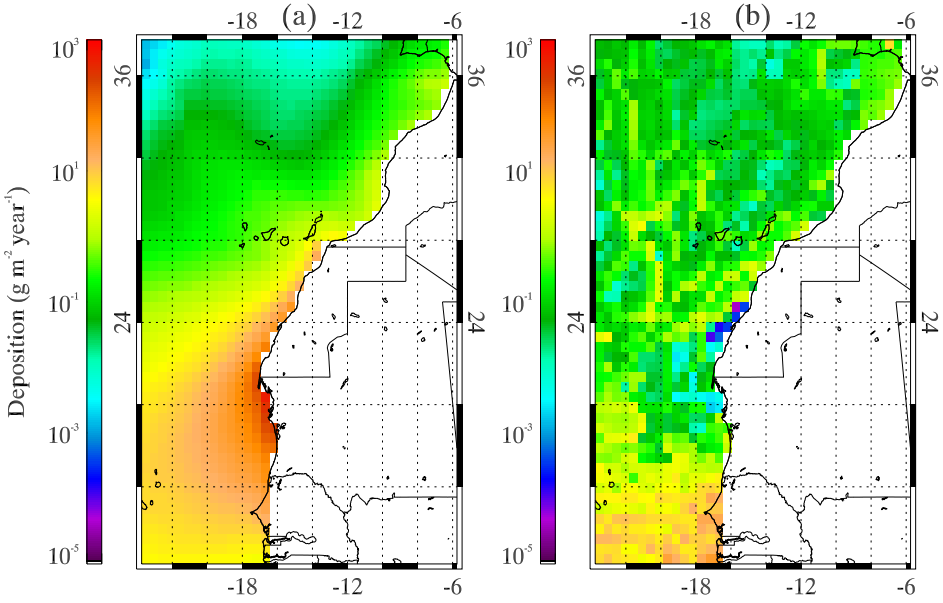

Figure 5.5: Total yearly deposition into the Atlantic, March 2006 to February 2007. (a) Dry deposition, (b) wet deposition.

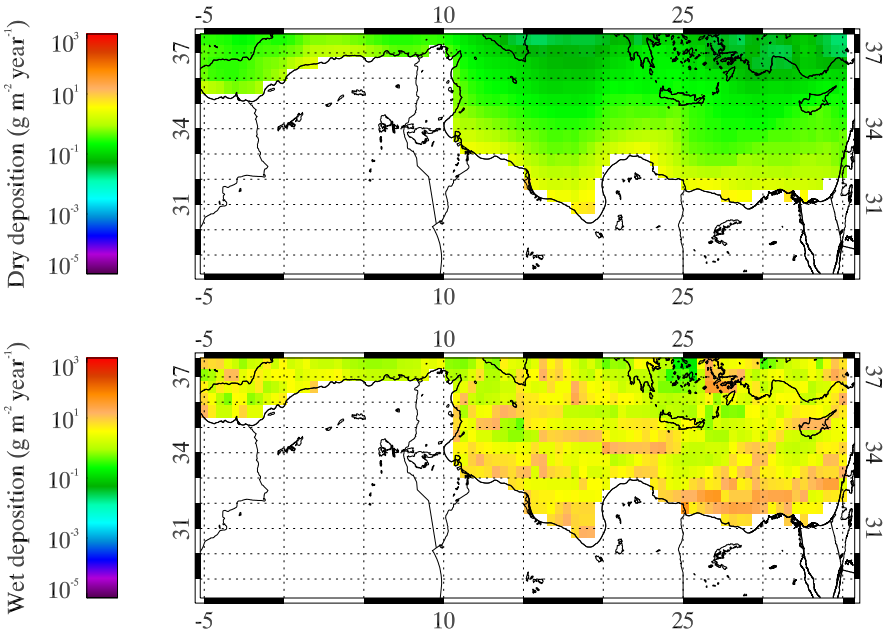

Figure 5.6: Total yearly deposition into the Mediterranean (dry and wet), March 2006 to February 2007.

south.

For the 2006-2007 test period, therefore, SHAMAL-low predicts up to 72.91 Tg of deposition

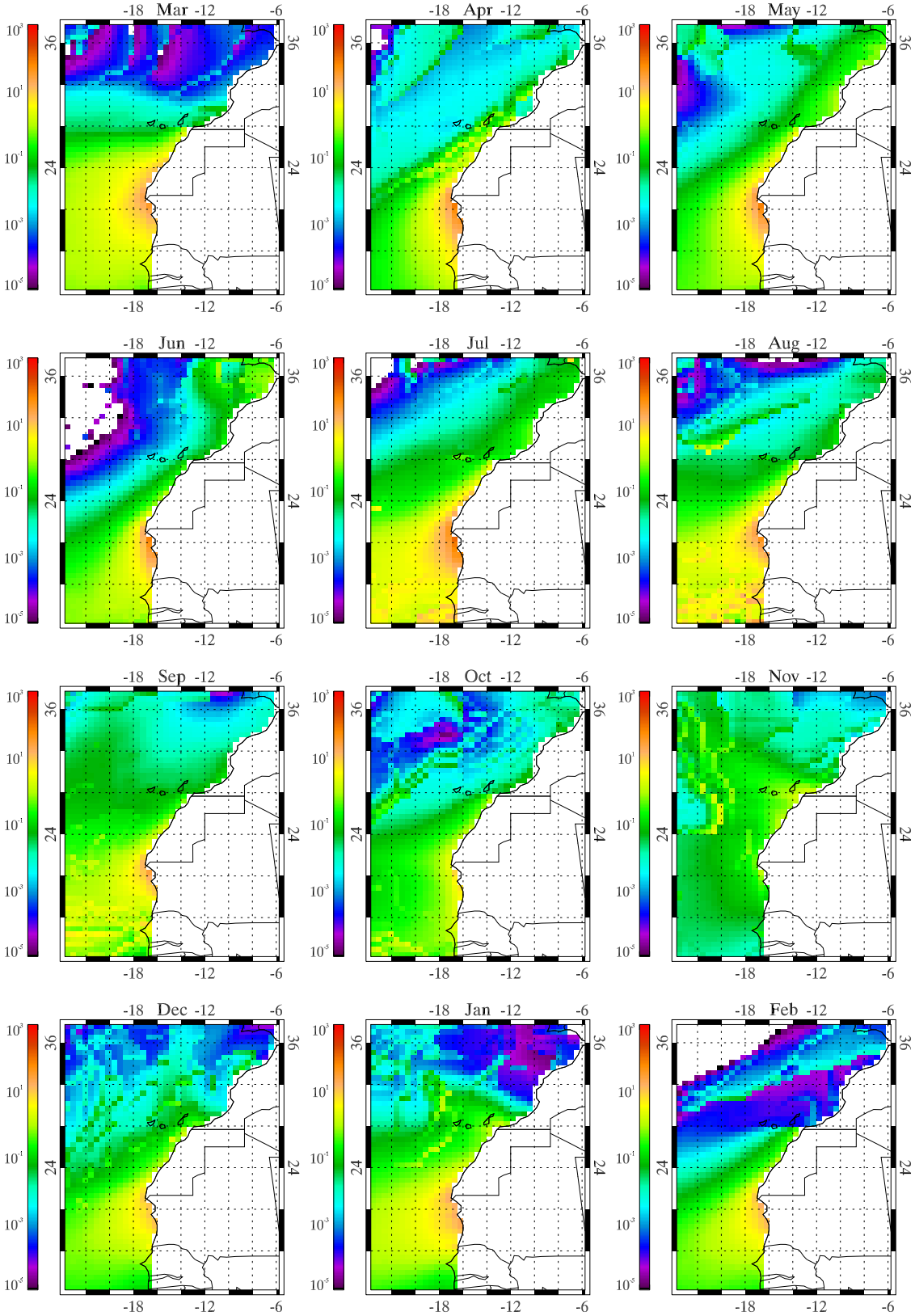

Figure 5.7: Total monthly deposition ($\mathrm{g\,m^{-2}\,month^{-1}}$) into the Atlantic, March 2006 to February 2007.

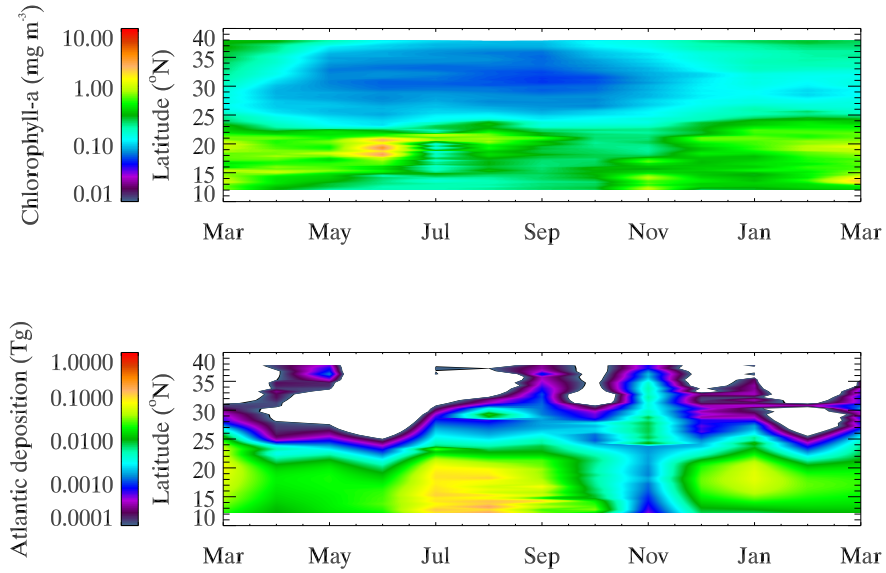

Figure 5.8: Zonal mean Atlantic chlorophyll-a concentration (mg m^{-3}) and zonal total monthly deposition (Tg) into the Atlantic, March 2006 to March 2007.

into the Atlantic, assuming that all the dust that is transported to the west of the domain is also deposited into the Atlantic. There may also be other other transport pathways to the Atlantic from North Africa, perhaps to the north via Europe and to the south via the Sahel. Predictions made from MODIS measurements (Kaufman et al., 2005) suggest that for the Atlantic region of 0-40 °N, there is 144±40 Tg of deposition (for 2001). Meanwhile, the GOCART model (Ginoux et al., 2004) predicts deposition into the North Atlantic of 161±18 Tg, while the DEAD model (Zender et al., 2003) predicts North Atlantic deposition of 178 Tg. All three estimates are for larger areas of the Atlantic than is covered by the SHAMAL Atlantic region, of order 10-20 times greater than the SHAMAL domain. In this context the SHAMAL prediction is reasonable: per unit area the explicitly calculated SHAMAL depositions are greater than previous estimates, which we would expect since deposition is greatest closer to the source region (i.e. off the coast of West Africa).

Comparisons between simulated dust deposition and satellite observations of ocean colour (figure 5.8) can be made, using a weighted average of satellite observations from MERIS, MODIS, and SeaWiFs (the merged product was produced within the framework of the ESA project GlobColour, described in Barrot (2010)). Comparisons are made over the region 19-24 °W (this region does not touch the coast, because there may be contamination from river outflow, etc.) and 12-38 °N,

within the model domain. On the latitudinal basis, there is a very strong correlation (of 0.90) between the yearly zonal mean concentration of chlorophyll-a and the total dust deposition for each latitude band. This does not necessarily imply that dust input to the ocean causes chlorophyll production: temperature and solar irradiance may also stimulate chlorophyll production at lower latitudes. Temporally however, these comparisons do not appear to provide a significant correlation between chlorophyll-a and dust deposition, at least not on the monthly time-scale. In fact, the mean concentration (over the domain) of chlorophyll is anti-correlated to the total dust deposition, with a correlation of -0.25 (since peaks in chlorophyll seem to be ahead of the peaks in deposition): this is too weak to draw any meaningful conclusion, so we can suggest that the timing of chlorophyll growth is dependent on other factors, though dust presence may be significant (since there is a good spatial correlation). Hence the nutrient content would be more likely to reflect the seasonal or annual deposition of dust.

5.1.3 Surface concentrations

The surface concentration of dust (i.e. the concentration of dust in the lowest layer of the atmosphere) is the interface between the surface and the atmosphere, and hence the atmospheric composition of this layer is strongly dependent on the local emission. Figure 5.9 maps the yearly mean surface concentrations, segregated by size. The geographical distribution of surface concentrations is very similar to that of deposition, with the highest concentrations being over source regions, while the dust is allowed to spread across the Sahel, the Atlantic, and the Mediterranean. The smallest aerosol sizes have the weakest concentrations (since there is very little of these sizes lifted or available to be lifted). Meanwhile, over the source regions the largest silt particles dominate over the smaller size ranges (since the soil size distributions tend to favour larger particles), yet can be substantially weaker over remote areas such as the North Atlantic (due to the effect of gravitational settling depositing larger sizes closer to the sources).

Measurements of surface dust concentrations have been made as part of the AMMA project at the Banizoumbou supersite (Rajot et al., 2008; Sow et al., 2009) in south-western Niger (∼60 km to the east of Niamey), which also contains an AERONET station. This is in the Sahel region, and is south of the modelled emitting regions. For comparison, figure 5.10 plots the SHAMAL-low maximum daily surface concentration over Banizoumbou over the course of the year. Surface concentrations are very weak during the summer monsoon months, when heavy rainfall prevents the spread of Saharan dust into the Sahel, and are strongest in the dry months (December-June).

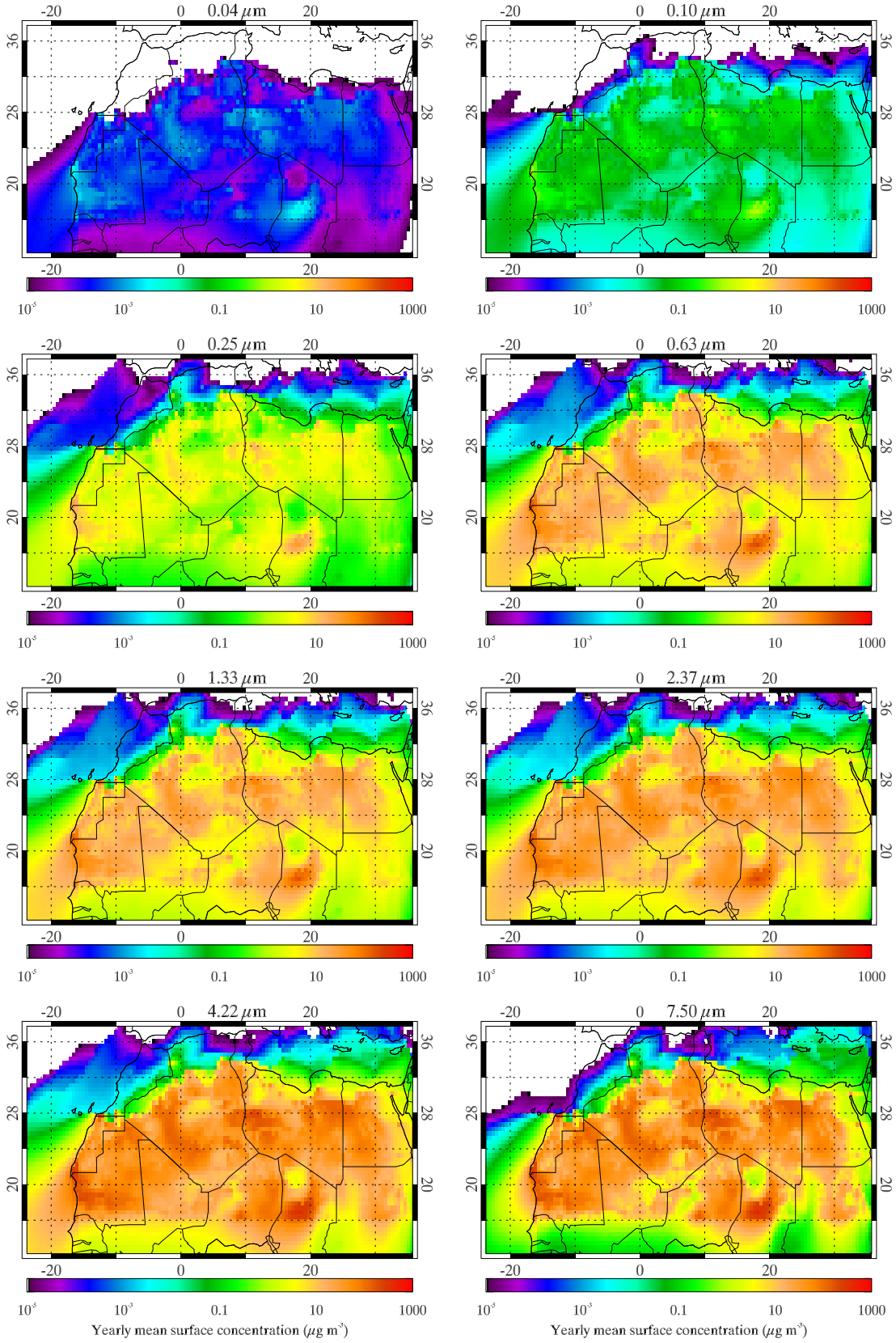

Figure 5.9: Map of yearly mean surface concentrations ($\mu g\,m^{-3}$) for each particle size, March 2006 to February 2007.

As with other properties of dust storms (e.g. emission, optical depth, etc.) the variability in surface concentration is dominated by a discrete handful of dust outbreaks.

The maximum model-predicted concentration is 394 $\mu g\,m^{-3}$, for the 2nd January 2007. Direct measurements made at Banizoumbou during January and early February 2006 (Rajot et al., 2008), at a height of 2.7 m, show that the maximum dust mass concentration per dust event during this period was $494\pm138\,\mu g\,m^{-3}$, peaking at 691 $\mu g\,m^{-3}$ on the 15th January 2006 (though the modelled and observed concentrations are at different times, comparisons can be made, especially with the January 2007 model output). The observed background aerosol concentration is $\sim$100 $\mu g\,m^{-3}$, whereas SHAMAL-low predicts a rather lower value, $\sim$10 $\mu g\,m^{-3}$. Hence it can be seen that the modelled concentrations are rather lower than the observed values; one reason for this could be because the observations may also include locally emitted dust or biomass burning aerosols, neither of which are present in SHAMAL-low. Another possible explanation is that the observations are taken at a height of 2.7 m, whereas the modelled concentrations are the mean for the bottom layer, at a mean height of 10 m; the dust concentrations should be higher at 2.7 m than at 10 m. However, as will be described in section 5.4.2, the scale height of dust aerosol in the atmosphere is sufficiently large ($\sim$1 km) that there should be very little variability in the concentration over such a small height difference. Saltation is also unlikely to have a significant effect on the observations either, since the saltation layer typically has a height of order of centimetres, at most 1 or 2 metres (Bagnold, 1941). Inter-annual variability may also account for some discrepancies, as may excessively strong deposition processes in the model.

5.2 Dust transport

5.2.1 Dust transport across North Africa

Figure 5.11 maps the intensity and direction of Saharan dust transport totalled over the year. Within the context of an Eulerian grid cell scheme, fluxes are measured along the sides of each grid cell: in order to get a flux intensity including both zonal and meridional fluxes, these fluxes are re-gridded onto the same grid (and summed over the entire column). Hence the presented fluxes (in Tg km^{-1}) represent the flux through two crossed surfaces whose centres are at the same point (consider the fluxes through the two lines of a '+' sign). Note these dust fluxes do not include possible in-flow from the Arabian deserts to the east, since these are outside the model domain.

The strongest dust fluxes are near the source regions, and show even more similarity to the

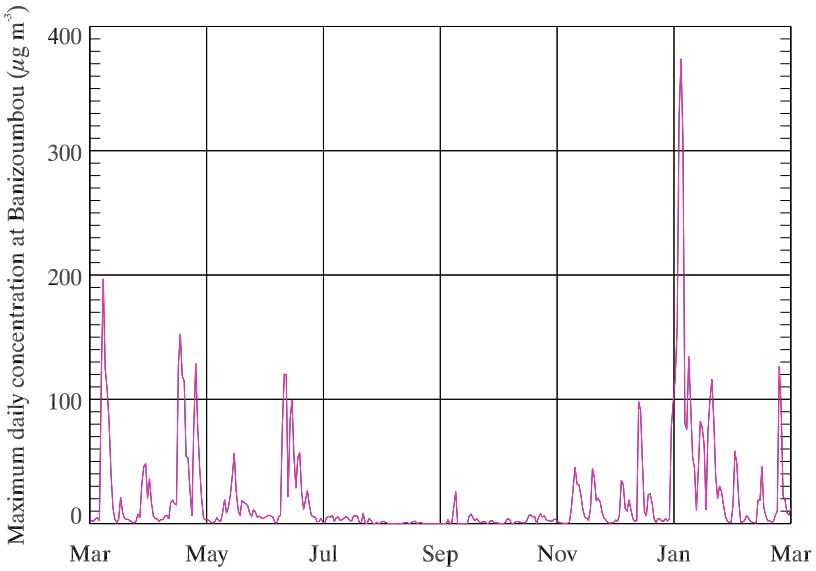

Figure 5.10: Time-series of modelled daily maximum dust surface concentration over Banizoumbou (13.54 °N, 2.67 °E), March 2006 to March 2007.

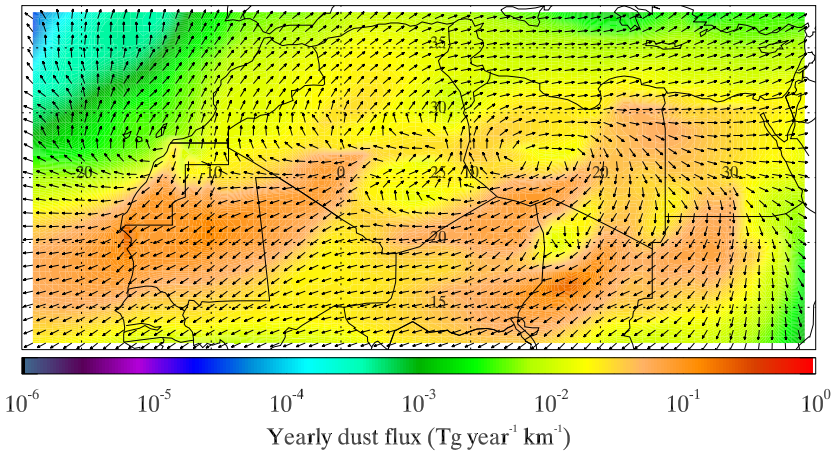

Figure 5.11: Total yearly Saharan dust fluxes across North Africa, along with prevailing directions of transport, March 2006 to February 2007.

spatial distribution of dry deposition. Seasonally (figure 5.12), the geographical distribution of fluxes follows a similar distribution to that of deposition (figure 5.2). However, the drop-off in flux

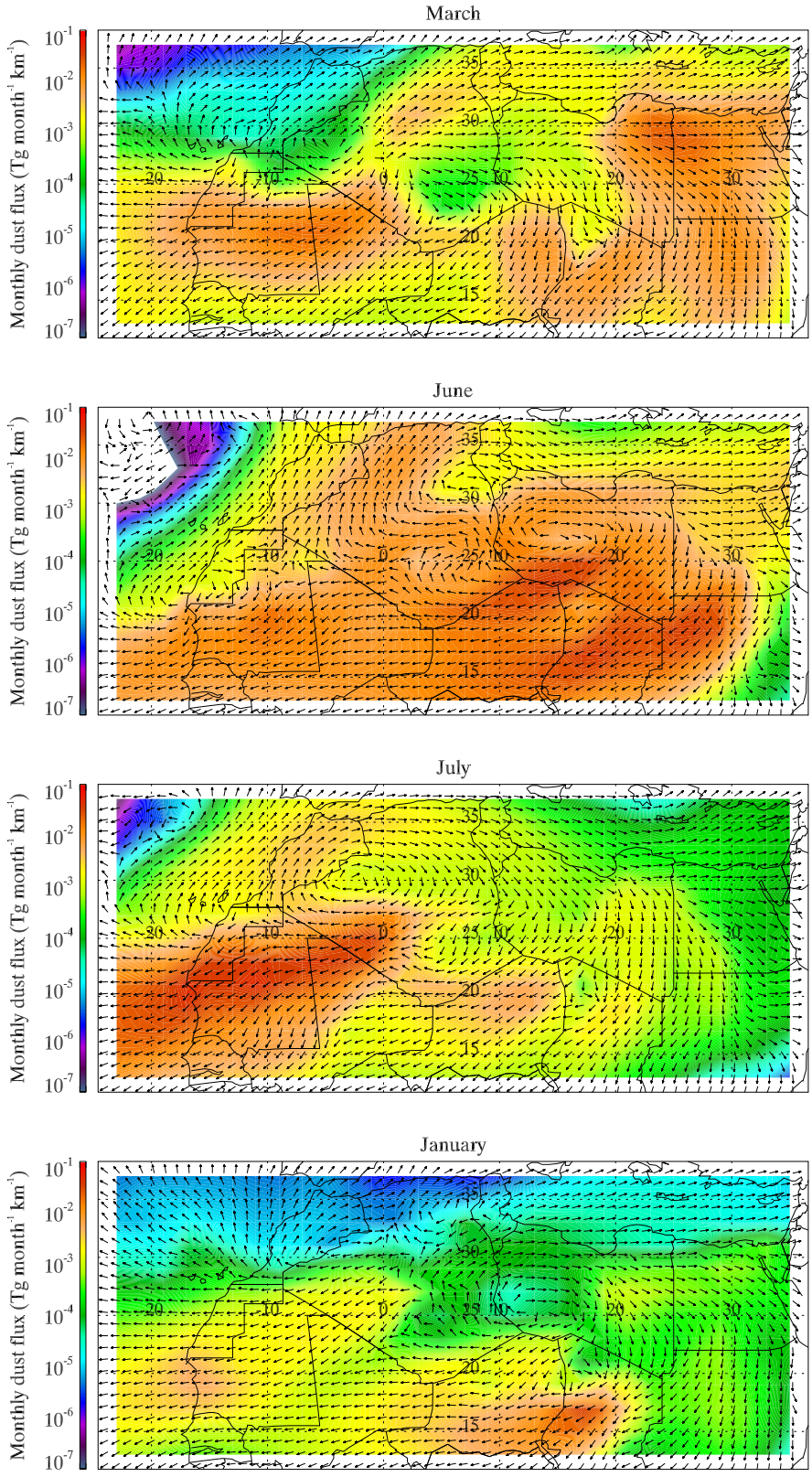

Figure 5.12: Total monthly Saharan dust fluxes across North Africa, along with prevailing directions of transport, for four months in 2006-2007.

intensity with distance from the source is much less than the drop-off in deposition. This may be due to the fact that most deposition at the source is of larger dust particles which may never have lifted beyond the bottom layer of the atmosphere, nor have travelled out of the source grid cell. Hence any transported dust is dust that is already able to travel some distance, and hence there is a bias towards particles that can travel large distances.

Within the central and eastern Sahara, the general trend is for the dust transport to circulate anti-cyclonically: from northern Libya the dust flows eastwards, into Egypt (and north to the Mediterranean and east to Israel and Saudi Arabia) and veering to the south, through south-eastern Libya, Sudan, and Chad. In Chad the flow starts to head in the south-westerly direction, especially strongly through the Bodélé Depression. From here the flow heads in one of two directions: east through Niger, Mali, Mauritania, Senegal, and into the Atlantic; or north-west, through Niger into southern Algeria, and back to northern Libya. In general, the prevailing flow across the Mediterranean (in the north of the domain) is to the east, while across the Sahel (in the south) it is to the west.

In West Africa, there are two dominant and opposite modes of transported dust, which diverge in western Algeria. To the south-west are the intense West African sources in Mali and Mauritania, from where the dust is transported in the south-westerly direction into the Atlantic; to the north is a transport corridor heading north and east across Algeria towards the Atlas mountains and the Mediterranean. Over the Atlantic the dominant transport is to the south (in the south-westerly direction), but some dust veers northwards as it leaves the coast of Mauritania and Western Sahara. From here there is also a transport corridor north-eastwards through Morocco and along the Moroccan coast.

5.2.2 Dust transport into the Atlantic, and to other regions

Significant quantities of dust from North Africa can be transported to remote regions. Saharan dust can be found in, for example, Barbados (Ellis and Merrill, 1995). As well as measuring deposition, it is also useful to measure the dust fluxes through transects in the domain. Described here are the dust fluxes through the four edges of the domain (West, South, East, and North) and a transect ('Atlantic') along a line at 18 °W, chosen because it lies just offshore from the westernmost tip of Africa (west of which there are no sources), and so it can be used to estimate the quantity of dust that is being transported out from the coast of West Africa across into the Atlantic. Estimates of dust fluxes are presented in table 5.4.

Year	Month	Atlantic (18 °W)	West	South	East	North	Total out
2006	Mar	4.90	2.58	0.86	4.32	7.59	15.34
	Apr	1.42	0.29	1.57	4.39	4.67	10.92
	May	2.34	1.04	1.64	4.16	6.03	12.86
	Jun	7.22	5.09	4.30	2.69	13.46	25.54
	Jul	22.24	18.94	0.95	0.26	3.16	23.31
	Aug	11.82	9.47	0.48	0.16	0.98	11.09
	Sep	4.49	3.54	0.40	0.14	0.72	4.79
	Oct	1.11	0.78	0.05	0.06	0.45	1.34
	Nov	0.36	0.14	0.01	0.02	1.47	1.64
	Dec	1.71	0.77	0.006	0.02	1.95	2.74
2007	Jan	2.96	1.82	0.02	0.12	3.65	5.61
	Feb	1.41	0.56	0.09	0.75	1.82	3.22
	Mar	1.84	0.97	0.37	2.12	3.97	7.43
Yearly total		61.98	45.02	10.38	17.07	45.94	118.41

Table 5.4: Table of monthly dust transport, off the coast of West Africa ('Atlantic'), and through the four edges of the domain, in Tg month^{-1}. The domain extends from 24 °W to 36 °E, and from 12-38 °N.

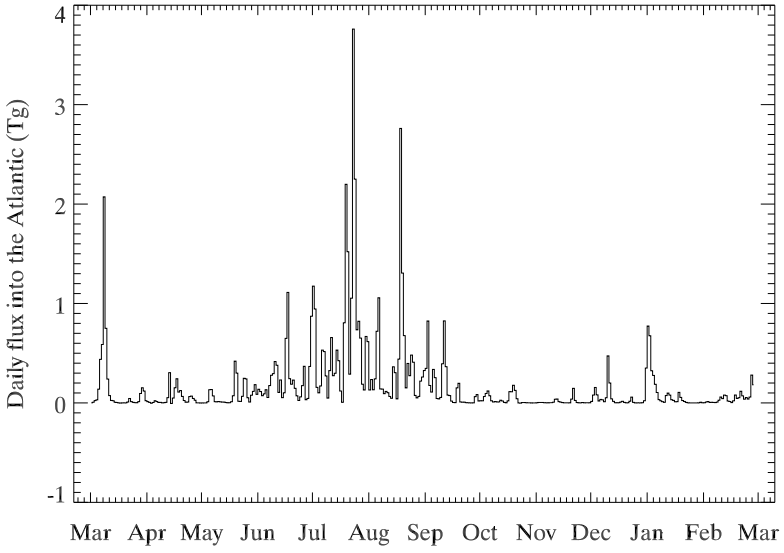

Figure 5.13: Time-series of dust transport into the Atlantic, for 2006-2007.

On the yearly basis (figure 5.13), we see that most dust transport into the Atlantic occurs in pulses, during dust emission outbreaks from West Africa. The strongest outbreaks occur during June-August, during the peak season for emission from the West African sources.

Figure 5.14 compares the West African emissions and the flux into the Atlantic during March 2006. There are some days (such as the 18th March) when there is a dust emission event, but

there is no subsequent dust outbreak into the Atlantic: either the dust is transported inland (e.g. to the Sahel) or it is quickly deposited. The time-series plot shows that the peak in the Atlantic flux, on the 8th March, follows shortly after the peak in the emissions, on the 7th March. Hence the observed dust event on the 8th March is actually caused by a large-scale dust emission event on the 7th March. From this we can suggest the hypothesis that the flux into the Atlantic will be most highly correlated with emissions some time before the observed flux.

Figure 5.15 supports this hypothesis that the correlation between the flux and the emissions is stronger when the emissions are measured on the day *before* the flux, as compared to simultaneous measurements of the two quantities. The more westerly emission transects have a shorter lag time before heading out into the Atlantic. Furthermore, the more easterly transects generally show a poorer correlation, since they tend to be less responsible for dust travelling into the Atlantic. Perhaps unusually, the 12-6 °W transect has a higher correlation than the 18-12 °W transect, despite being further from the Atlantic coast: this may be due to the more easterly region being a larger emitter of transportable dust, while more locally emitted dust gets deposited over the West African coast. After two days the comparison starts to deteriorate (although the correlation is still strong), while after three or four days the life cycle of a dust event has been exceeded. Hence we can argue that a typical dust outbreak into the Atlantic is created by dust lifting activity over West Africa 12-36 hours before it passes out into the Atlantic.

An unusual feature in figure 5.15 is the second (subsidiary) peak in correlation, which occurs between 4.5 and 6.5 days before the measured flux. This peak occurs at days 4.5, 5.5, 6.5, and 6.5, for the four respective emissions transects. This compares well with periods of the easterly waves over the emissions transects (calculated by taking the mean zonal wind velocities over transects from 12-25 °N at longitudes 15 °W, 9 °W, 3 °W, and 3 °E, then calculating the periods between successive peaks in the easterly winds, and taking the mean of these periods), which comes to 4.5±2.0 days. This suggests that while the dust transport into the Atlantic is dominated by just a few events (as shown by the strength of the correlation in the first 12-36 hours), there are also second-order dust events which correspond to the cycle of easterly waves across the southern Sahara and the Sahel (over northern Mali and Mauritania).

Observations of dust events over Cape Verde (Middleton and Goudie, 2001) suggest that on 20-29% of the days during 1999, the TOMS AI exceeded 1.9. TOMS AI is not directly comparable to aerosol optical depth, but a qualitative comparison can be made, if we take a simple metric of dust AOD exceeding 0.2 to be a dust event. Figure 5.16 plots the peak daily AOD over Cape Verde

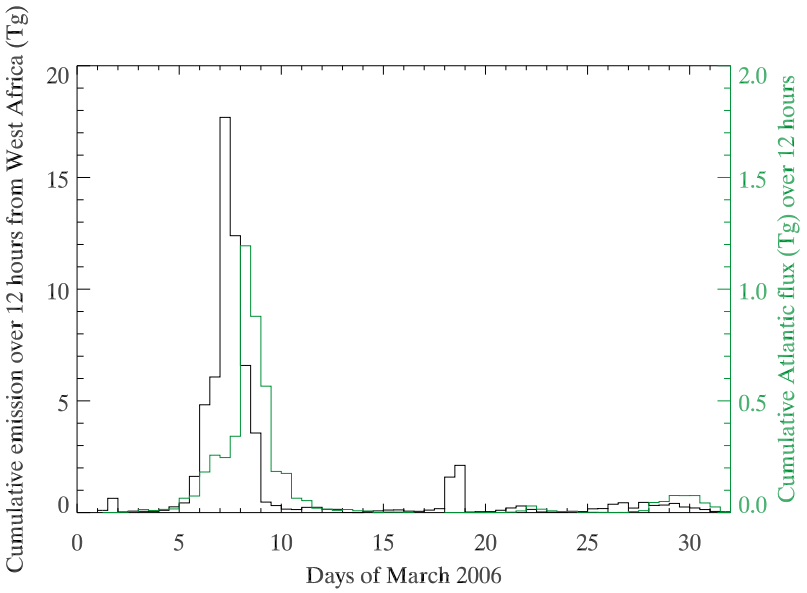

Figure 5.14: Comparison between 12-hourly dust emissions from West Africa (west of 6 °E) and 12-hourly fluxes into the Atlantic.

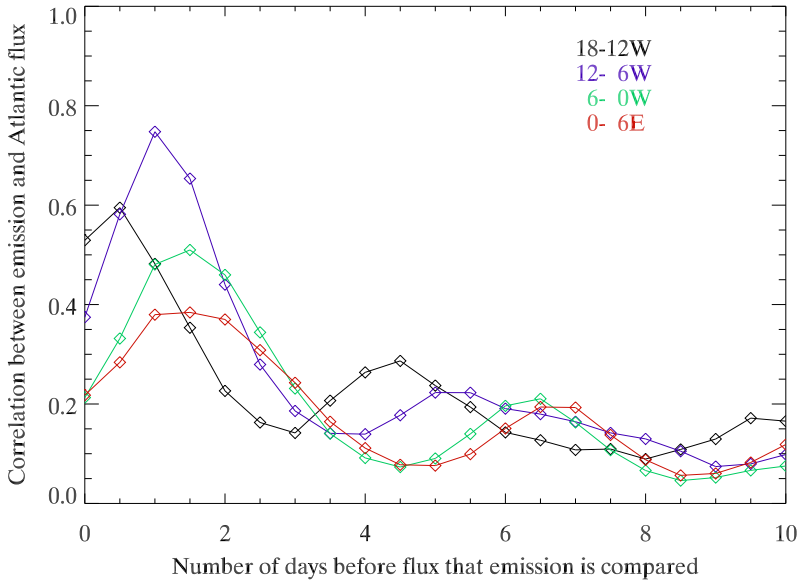

Figure 5.15: Lagged correlations between the emission from longitude transects over West Africa and the flux into the Atlantic, from the yearly simulations. The horizontal axis indicates the temporal discontinuity between the measurements: when the value is *nday*, the comparison is between the flux on day x and the emission on day x-*nday*.

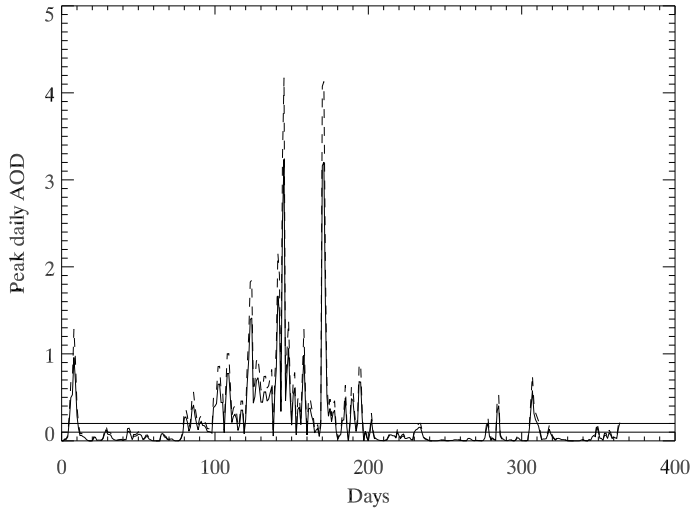

Figure 5.16: Peak daily AOD over Cape Verde, March 2006 to February 2007. The dashed line uses a clay mean radius of 0.5 μm.

during the course of the model year, and shows that the AOD exceeds 0.2 on 62-70 (27.1-31.0%) of the days, which is marginally more than, but still comparable to, the number observed/predicted by TOMS. The majority of these cases take place during the summer, when the West African sources which feed the Cape Verde region with dust are the most active.

5.3 Dust storm activity

5.3.1 Optical depth of dust storms

On a yearly basis, the highest optical depths (figure 5.17) are concentrated over West Africa, extending south-west into the Atlantic, and over the central Sahara. This pattern is similar to the maps of deposition shown in figure 5.1, with the difference that the maps of optical depth indicate the presence of dust aerosol in the atmosphere. A comparison with OMI is also presented in figure 5.17. An important difference is that OMI often observes a higher background AOD than is predicted by SHAMAL, especially over the oceans, where other aerosols may also be present. This may reflect a bias in the instrument, but this does suggest that SHAMAL does under-predict the general dust loading. There is general agreement that the areas of highest aerosol loading are over the Bodélé Depression and over West Africa. However, the observed peaks over West Africa appear to be further east over Mali than the peaks over Mauritania that SHAMAL predicts. A

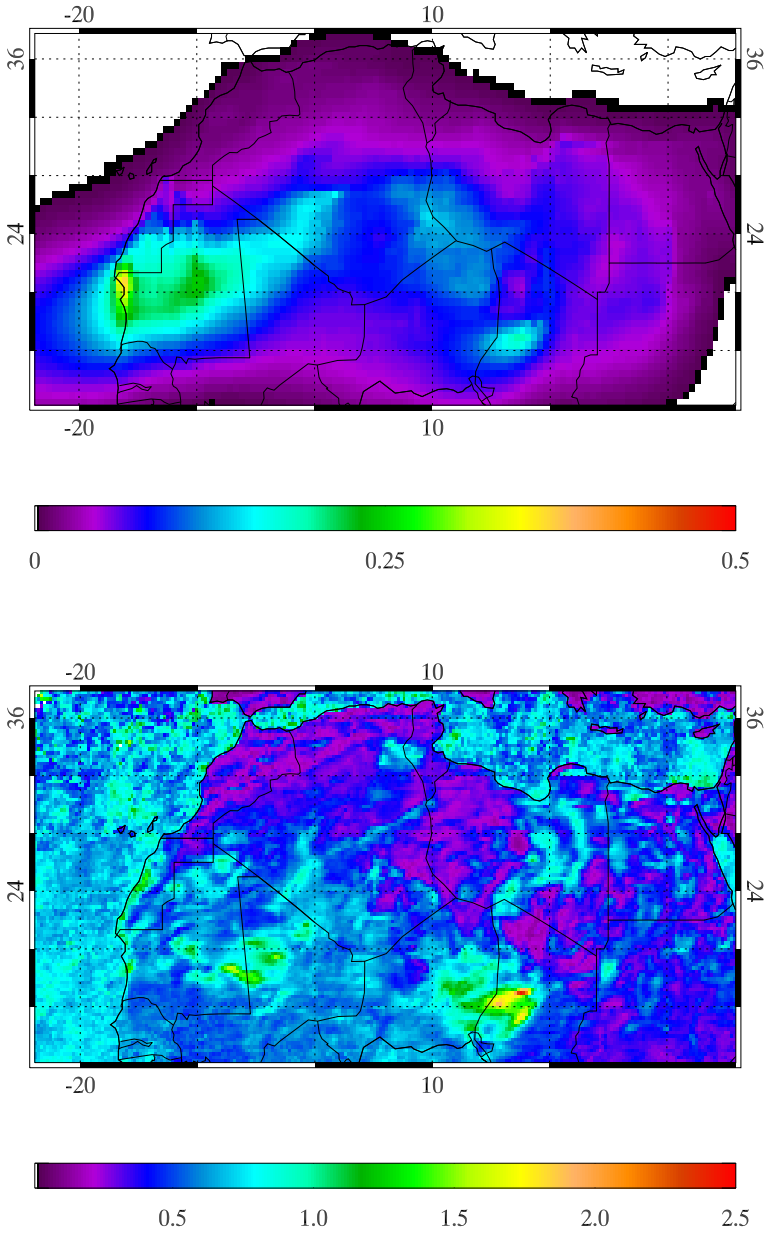

Figure 5.17: Yearly mean dust optical depth, March 2006 to February 2007. White areas correspond to areas with a mean optical depth of less than 0.01. The upper frame maps the simulated SHAMAL AOD, while the lower frame maps the yearly average AOD from OMI, at 500 nm.

significant difference is the SHAMAL predicted source on the Western Saharan and Mauritanian coasts, which is not observed by OMI as being particularly significant. In SHAMAL, this is a result of soils conducive to dust lifting and winds cutting across the headland from the Atlantic (as shown in figure 3.16). The OMI observations therefore suggest that over this region either the

soils have been inaccurately represented, or that the ECMWF winds cut too fast and too deep inland in this small area.

The variation across the year is readily apparent in figure 5.18, which shows the monthly mean optical depths at 550 nm. From March to September, there is widespread dust storm activity, reaching its greatest extent in June, when large areas of the western and central Sahara have significant dust storms. In July the dust storms are at their most intense, very strong over large areas of Western Sahara and Mauritania, and into the subtropical north Atlantic. There is much less activity later in the year, but in October-February the influence of the Bodélé Depression becomes apparent, with noticeable dust plumes extending from it and heading to the south-west, the characteristic direction of dust from the Bodélé. Meanwhile, the north-eastern Libyan source region is only significant in March.

For comparison, figure 5.19 plots the monthly mean AOD observed by OMI, over the same period of time as the SHAMAL simulations. There are substantial similarities and differences, varying from month to month. Year-round, OMI observes the Bodélé Depression to be a substantial hotspot of aerosol loading, especially over the winter months, when the LLJ is at its most active (at which time there are more frequent and strong high-pressure systems over Libya (Washington and Todd, 2005), which feed the north-easterly winds that form the LLJ). SHAMAL emphasises the Bodélé in October-February, agreeing with OMI, but sees much less activity than does OMI earlier in the year, except in June.

There is broad agreement as to the seasonal cycle of the West African sources (though OMI observes the peaks in AOD to be further east than does SHAMAL), with these areas being dominant during the summer months, especially in June and July. At this time the subsolar point has moved up from the equator and across the Sahel into the Sahara, reaching as far north as northern Mali and southern Algeria. This heating causes a temperature gradient between the hot and dry Sahara, and the cooler and moister Sahel during the West African monsoon, as well as an increase in dry convection (Engelstaedter and Washington, 2007a), such that there is an increase in high wind speed events during the summer. Density currents (Knippertz et al., 2007) can also form more frequently at this time, when convective systems pass over the southern Sahara bringing rainfall (from the Sahel, for example), which evaporates as it falls, creating a *cold pool* of high winds and hence high dust uplift. African easterly waves (Knippertz and Todd, 2010) can help to trigger this, by pulling moist air north from the Sahel; this may explain why the OMI observations predict more activity further east than does SHAMAL, since African easterly waves tend to originate further

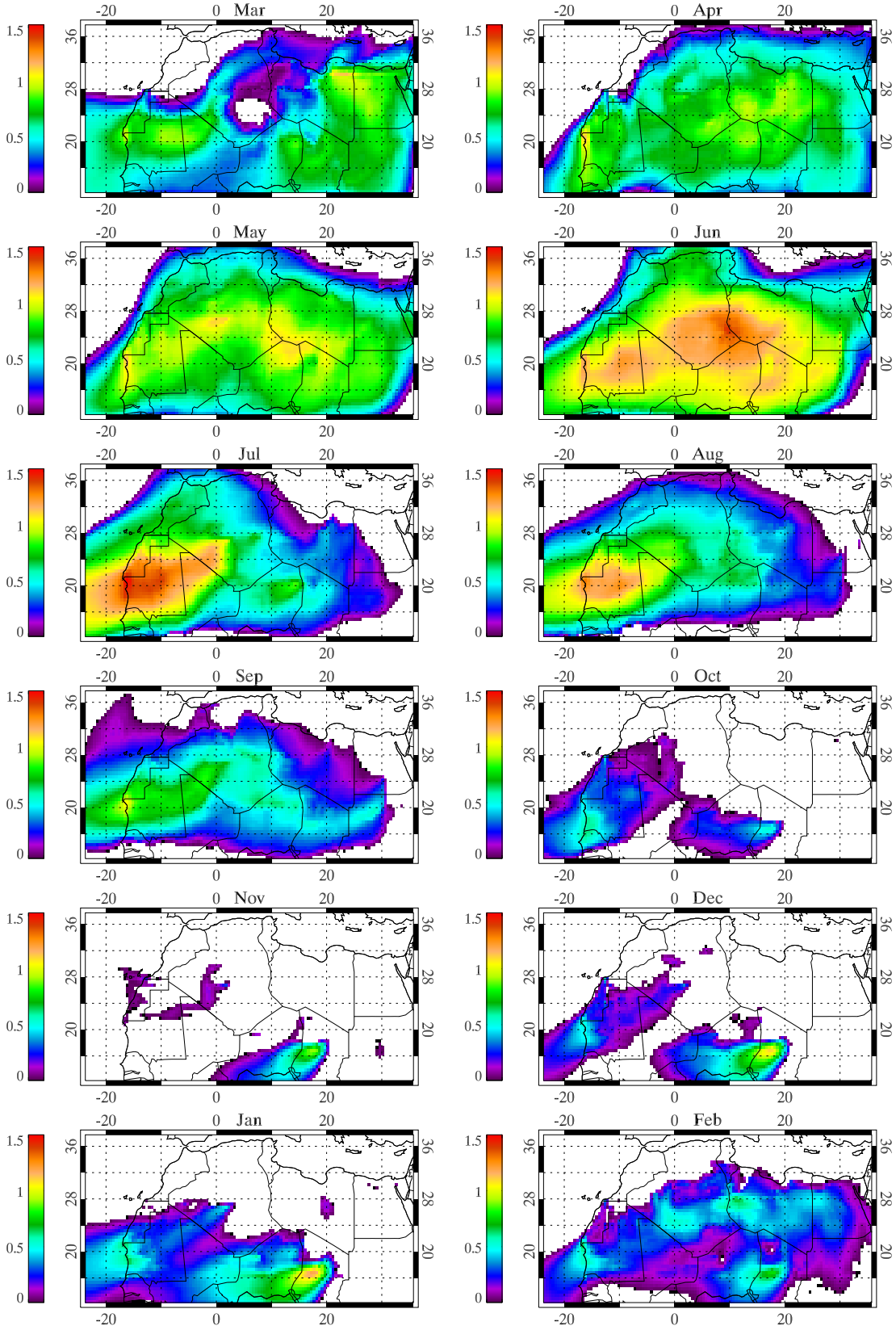

Figure 5.18: Mean monthly dust optical depth, March 2006 to February 2007.

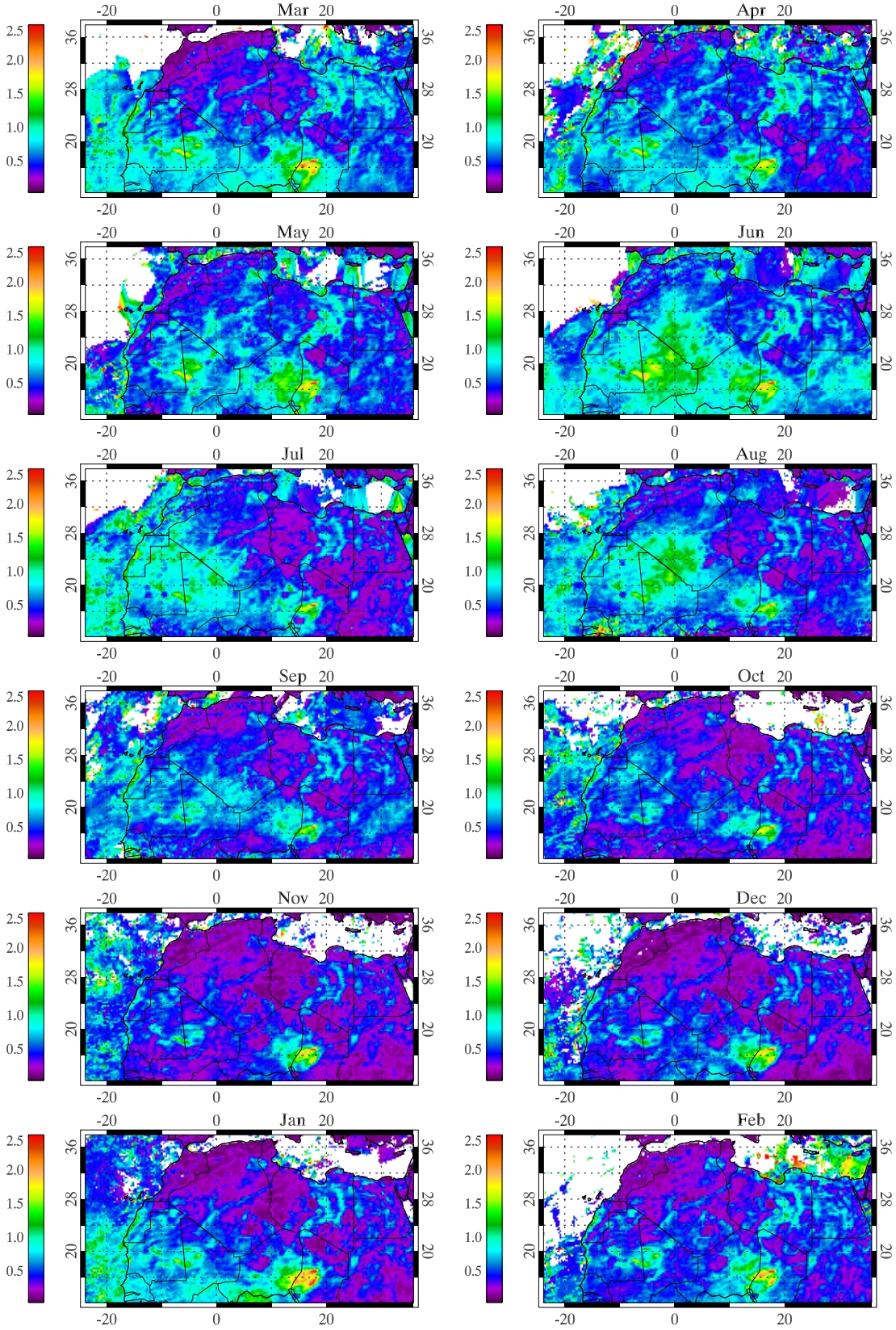

Figure 5.19: OMI monthly mean dust optical depth at 500 nm, March 2006 to February 2007.

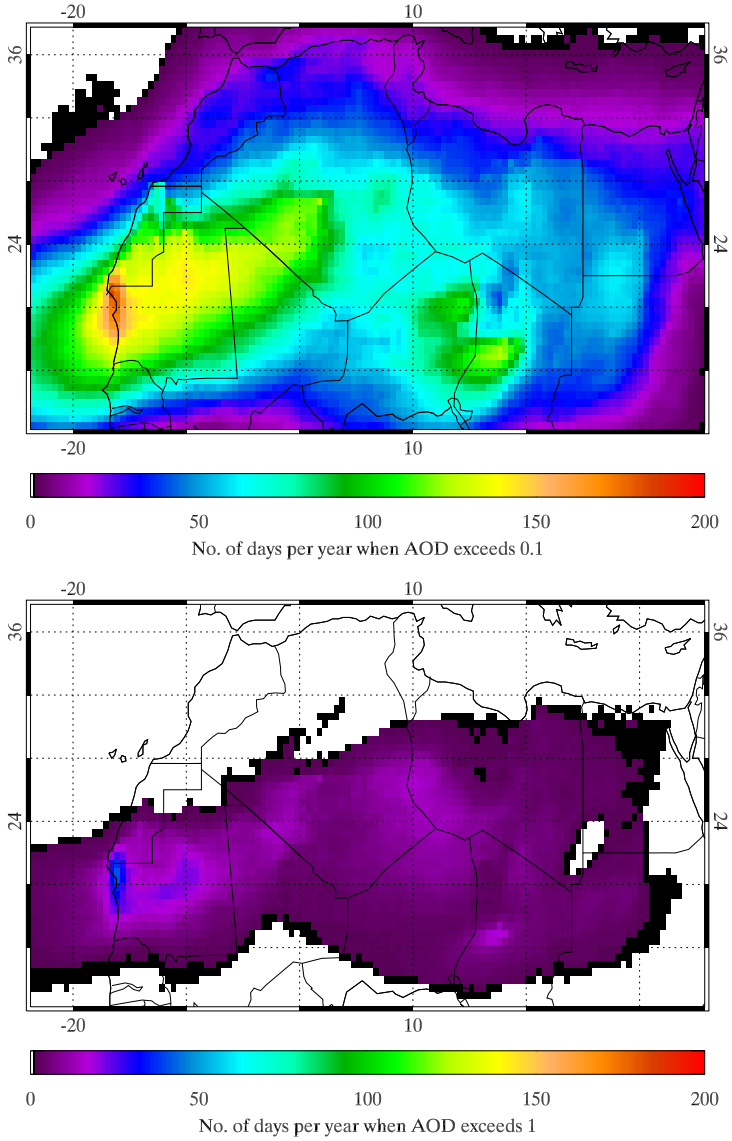

Figure 5.20: Number of days per year when optical depth exceeds 0.1 (upper) and 1 (lower), March 2006 to February 2007. White areas correspond to areas where the number of days is zero.

east, over Niger for example. These are not explicitly accounted for in SHAMAL.

Figure 5.20 is a map which uses the number of days per year when the optical depth exceeds 0.1 as a metric for dust activity, and the number when the optical depth exceeds 1 as a metric for particularly intense dust storms. Again, the West African region has substantially the most dust storms, with the Bodélé also being reasonably strong. Large areas of Mauritania are particularly susceptible to dust storms. Such large optical depths can cause the visibility on the ground to be decreased substantially: an example of this can be seen in figure 5.21.

Figure 5.21: Photo of a sand storm in northern Chad (Giles, 2005).

The optical depth is positively correlated to both the emission and the deposition, reflecting the high near surface dust concentrations that high emissions and depositions imply. The correlation with deposition is quite strong, at 0.71, but the correlation with emission is relatively weak, at only 0.53. The weakness of the correlation with emission compared to that with deposition may be due to atmospheric transport: source regions are very discrete, whereas both deposition and optical depth show much more homogeneous fields. Hence some caution is required in trying to identify dust sources using optical depth information (i.e. from model output and satellites), since the peak in optical depth is often downwind of the source, and the spatial distribution is much less distinct than the source distribution.

The results from July 2006 compare well with observations of dust storm frequency and OMI AI, an example of which is shown in figure 5.22 (from figure 2 in Schepanski et al. (2007)), which shows the dust storm frequency and mean aerosol indices (defined in section 1.3.1) as derived from SEVIRI measurements, for July 2006. Here, dust source activation is found by tracing plume patterns back to their origins, from the SEVIRI images. SHAMAL and the OMI observations agree well, with a broad swathe of West Africa, including most of northern Mali, Mauritania, Western Sahara, and into the Atlantic having consistently high AI values as measured by OMI. There is a difference in emission however: SEVIRI suggests that the sources are further to the east, around the border of Mali, Algeria and Niger, whereas SHAMAL suggests that it is Mauritania and Western Sahara which are the major sources. There is particular disagreement over north-western Niger, a region pinned in between the Hoggar massif in southern Algeria and the Aïr mountains in central Niger: while SHAMAL does not predict much emission here, due to weak winds, it is identified by

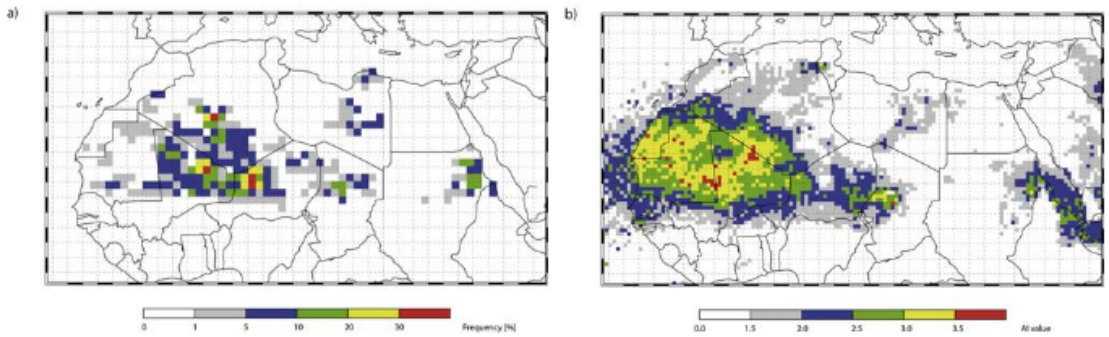

Figure 5.22: Maps of (a) frequency of dust activation, and (b) averaged OMI aerosol index (AI), July 2006, from figure 2 in Schepanski et al. (2007).

Prospero et al. (2002) as a distinct source region. It may be that on a seasonal basis this region is more susceptible to wind erosion than is predicted by SHAMAL, or it may be that the frequency of dust activation is not a reliable metric of dust sources (since there is only a moderate correlation between emission and optical depth).

Year	Month	Atlantic	Mediterranean	Domain
2006	Mar	0.86	2.87	1.17
	Apr	1.22	3.73	2.28
	May	1.66	4.22	2.76
	Jun	3.00	4.13	3.24
	Jul	2.95	5.40	2.71
	Aug	3.01	3.80	2.69
	Sep	2.72	2.86	2.42
	Oct	1.53	-	1.23
	Nov	1.03	-	0.59
	Dec	0.57	1.11	0.48
2007	Jan	0.50	0.47	0.49
	Feb	0.59	3.10	0.93
	Mar	1.10	2.25	1.11
Yearly mean		2.13	4.33	2.85

Table 5.5: Table of monthly mean plume heights (defined by the mass weighted average height) over various regions, in km. The Atlantic region is 18-24 °W and 12-38 °N, the Mediterranean region is 5.5 °W-36 °E and 33-38 °N, and 'domain' represents the entire model region.

5.3.2 Dust plume heights

Long-range dust transport requires dust to be lifted to higher altitudes, where dust particles are less susceptible to dry deposition processes (and also wet deposition processes, if a dust plume ascends above rainfall-bearing clouds).

The method used to measure dust plume heights is a weighted average technique, calculating the mass in each height layer, and weighting the average height by the distribution of mass. In order to filter out areas where there is only a very thin haze of ambient dust, plume heights are only calculated when the dust optical depth is greater than 0.1. Another possible method is to look at the height at which the dust concentration is greatest: this has the problem that typically near source regions the thickest layer of dust is near the surface, so the measured plume height would not take into account possible plumes being formed at higher altitudes, possibly from other source regions. Plume heights could also be estimated by using optical depth, but these have the problem of using a secondary product, derived from the mass and dependent on particle properties. Estimates of plume heights are presented in table 5.5.

On a yearly average (figure 5.23), the plume heights are lowest nearest the source regions, and greatest in remote regions. Plumes heights are negatively correlated with optical depth, emission, and dry deposition, with correlations of -0.60, -0.37, and -0.47 respectively (by contrast, there is a weak positive correlation between plume height and wet deposition, at +0.18). Plumes are particularly high over the Mediterranean, due to the effect of rainfall washing out low-level dust

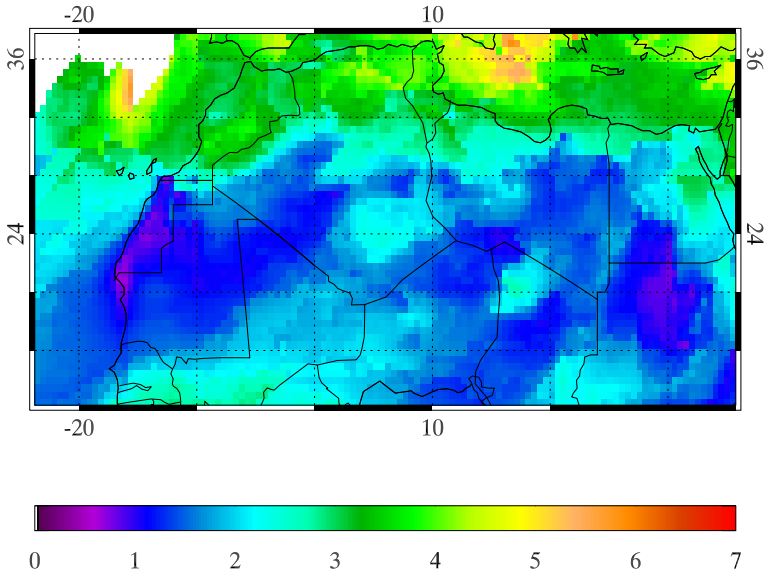

Figure 5.23: Yearly mean plume heights (km), weighted by mass, March 2006 to February 2007. White indicates where the dust loading is too thin (optical depth of less than 0.1) for a meaningful plume to be measured.

plumes, and hence the dust loading is weighted more towards high altitude background dust aerosol. The highest plumes are found over Sicily, in the north of the domain; there are also surprisingly high plumes over Cyrenaica on the north-eastern Libyan coast, an important location for wet deposition during March 2006, when large dust outbreaks can encounter cold fronts passing along the Mediterranean coast. Meanwhile the main pathway of West African dust over the Atlantic (the south-west trajectory off the coast of Mauritania) shows a particularly low oceanic plume height, reflecting its proximity to the source and the dryness of the atmosphere (low altitude dust is most affected by precipitation scavenging).

Observations of dust plumes from CALIPSO are presented in figure 5.24. Representative swaths for four different seasons (from June, September, December, and March) of the year are shown, for the region over the Atlantic just off the West African coast. Each swath has a relatively constant longitude, of ∼18 °W (with a slight drift from east to west as the satellite heads north), and an overpass time of ∼14.15. The modelled plume heights are generally lower than the observed aerosol plumes over the Atlantic. From SHAMAL the mean plume heights are simulated to be: 3.00 km in June 2006; 2.72 km in September; 0.57 km in December; and 1.10 km in March 2007. By comparison, sample dust plumes are observed at about: 3-5 km from June 2006; 2-5 km from

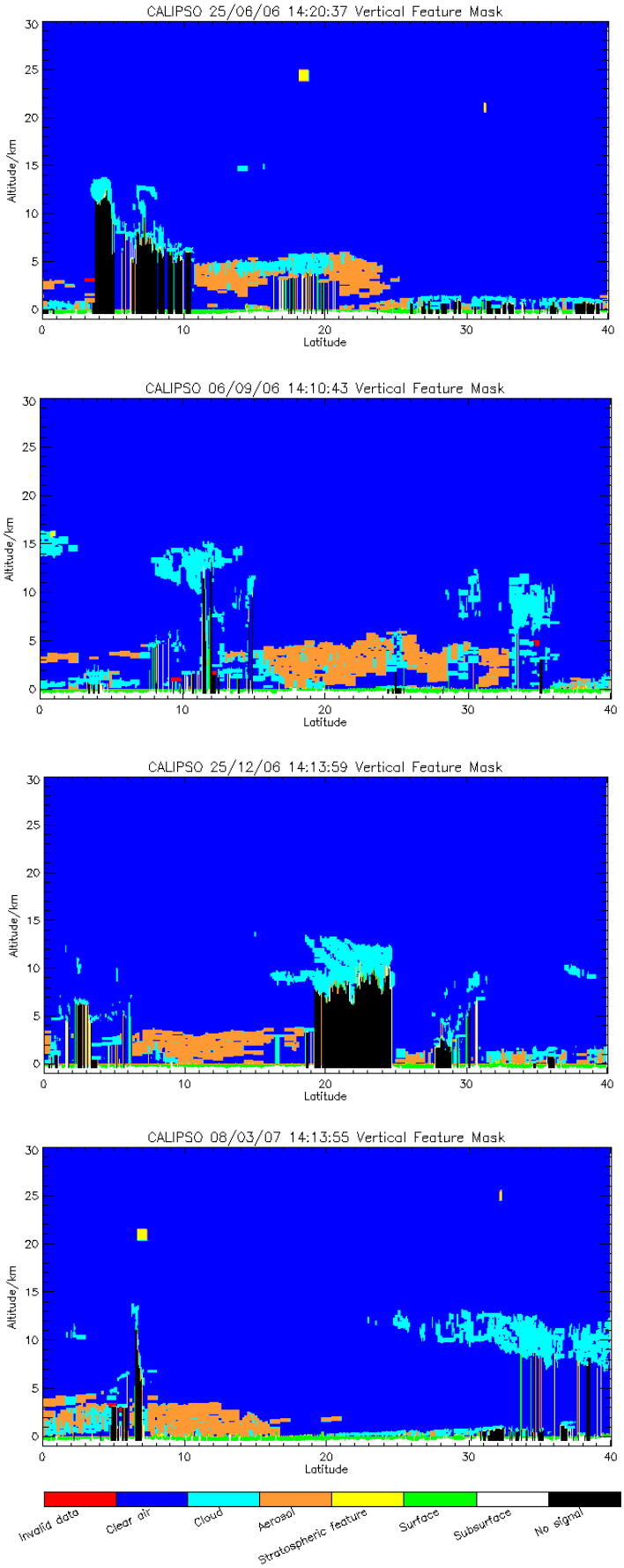

Figure 5.24: CALIPSO observations of the vertical profiles of aerosols and clouds. Aerosol plumes are orange.

September; 1-3 km from December; and 0-3 km from March 2007. From these examples it is clear that SHAMAL under-predicts the plume heights of dust heading out over the Atlantic, by a factor as low as a half (although the agreement is rather better with the example from March 2007).

The presence of the Saharan Air Layer (SAL) suggests that dust over the Atlantic should be travelling at the heights observed by CALIPSO. The SAL (Engelstaedter and Washington, 2007a) is a region of warm, dry and stable air that forms over the Atlantic off the coast of West Africa at an altitude of 1.5 km to as much as 6 km. This layer is highest and deepest during the summer months, caused as it is by the dry convection of air (and dust) over the West African Sahara, which enables a fast vertical flow of air, and which is then transported outwards over the Atlantic, where vertical transport diminishes (since the engine of dry convection is weakened). This caps the cooler and moister air which is closer to the surface of the ocean. Due to the intensity of this vertical uplift, we would expect that Saharan dust from West Africa would mostly be transported within the SAL, within the prevailing flow, with much less transport closer to the ocean surface. This will be strongest during the summer when the heating over the Sahara is greatest (and which also helps to drive emission), such that the SAL will be highest during summer, and lowest during winter. This seasonal pattern of the probable dust plume height is simulated by SHAMAL, with maximum plume heights reaching 3.01 km in August, and just 0.50 km in January. While the temporal cycle is in good agreement with this understanding of the dynamics of the SAL, the simulated altitude is rather lower (for example, plume heights are simulated to be $\sim$3 km in summer, while we would expect the SAL to be at an altitude of $\sim$4.5 km), which points out a weakness in the transport model. This suggests that the simulated vertical transport of dust is too weak over West Africa, for example, the turbulent diffusion may be too inefficient in the simulations, or that too much dust is dropped at night, when the PBL drops and convection diminishes.

5.4 Dust size

5.4.1 Dust effective radius

The effective radius r_{eff} of a distribution is defined by (e.g. Levy (2009)):

$$r_{\text{eff}} = \frac{\int_0^\infty r^3 n(r) dr}{\int_0^\infty r^2 n(r) dr}, \tag{5.1}$$

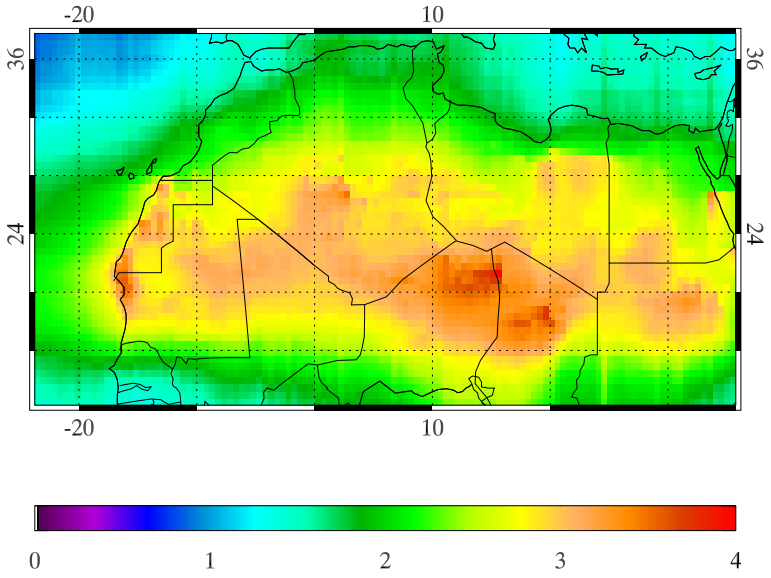

Figure 5.25: Yearly mean effective radius (μm), March 2006 to February 2007.

where $n(r)$ is the aerosol number concentration, and r is the particle radius. Hence the effective radius is a weighted average radius by particle area of a particle size distribution, and can be used as a measure of the typical radius of a size distribution.

The yearly mean effective radii are mapped in figure 5.25; the yearly mean effective radius across the domain is 2.33 μm. The effective radius is greatest nearest the source regions (the correlation between effective radius and emissions is 0.49), where the largest particles have not dropped out yet: the maximum is 4.08 μm. Dust over remote regions, such as the North Atlantic, have the smallest effective radii, as low as 0.85 μm. Since larger particles have stronger gravitational settling, we expect that effective radius should be negatively correlated with dust plume height: this is the case, with a correlation of -0.58.

5.4.2 Dust aerosol size distributions

Figure 5.26 shows typical size distributions. The number of particles emitted from the surface is centred at $r \sim 0.25$ μm, and this is the strongest influence on the mean atmospheric particle number, which follows the same distribution. However, the mass is weighted towards larger particles, to $r \sim 4.2$ μm, within the silt particle range. These three distributions are mono-modal, as we might expect. Since the area covered by each size range is proportional to the radius, the surface area

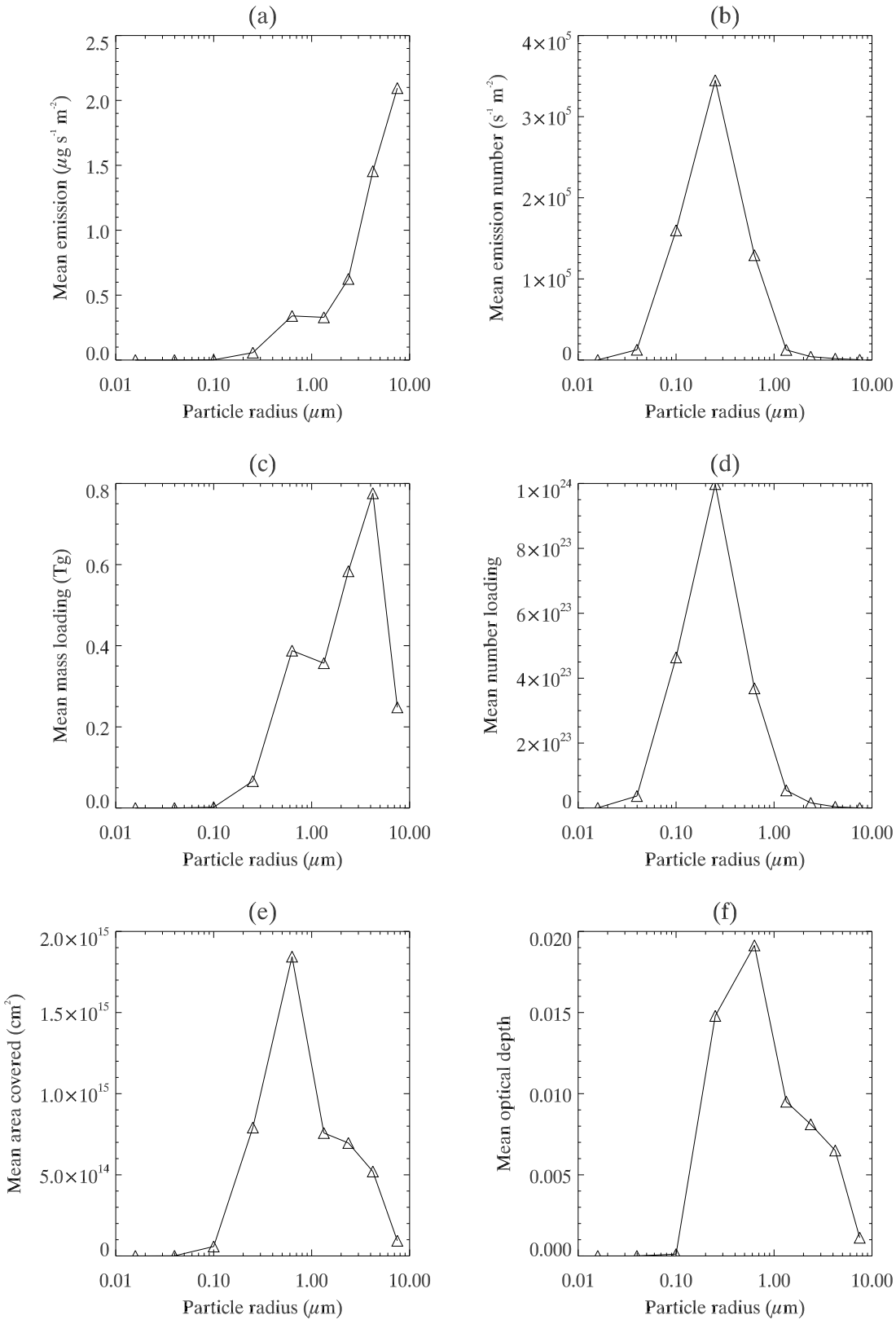

Figure 5.26: Plots of size distribution, averaged over the course of the year. (a) Mass surface emission flux. (b) Number surface emission flux. (c) The mass loading. (d) The number loading. (e) Mean surface area covered by all particles. (f) Optical depth, at 550 nm.

distribution is shifted more towards the larger clay particles (centred at $r \sim 0.63$ μm). Hence the optical depth, which follows the particle area, peaks at larger particle sizes compared to the number distribution (and is very insensitive to the smallest particles, below 0.1 μm).

Figure 5.27 depicts the yearly mean size distributions, differentiated by height layers. The peak of the number size distribution is at 0.25 μm (between 0.16 and 0.4 μm). To a good approximation the concentrations drop off exponentially with height: on the yearly mean, the mass concentration $\chi_{\mathrm{i}}(z)$ (for particle size i) can be approximated by an expression of the form:

$$\chi_i(z) = \chi_{(z=0)} \exp(-z/H_i), \tag{5.2}$$

where H_{i} is the scale height, which represents the height by which the concentration has fallen by a factor of exp. Figure 5.28 plots the predicted scale heights as a function of particle size and of gravitational settling velocity. For clay particles there is almost no variation in scale height ($\sim$2.5 km), since the settling velocity is so low; for silt however, since the settling velocity increases so much (as the square of the radius) the scale height decreases dramatically. These values for the scale height are in good agreement with the estimate of a scale height of 2 km for desert dust aerosol used by Jaenicke (1993), from global model simulations. The scale height as a function of r can also be approximated by an exponential decrease:

$$H(r) = 2.65 \exp(-0.101r), \tag{5.3}$$

where $H(r)$ is in km, and r is in μm. For the scale height to be the top of the bottom layer (at 20 m), the particle radius would be 48.3 μm. Particles larger than 100 μm are unlikely to ascend higher than 10 cm. Hence for atmospheric aerosols there is very little variability in concentration in the bottom layer (so it can be regarded as homogeneous), whereas for saltating particles there will be a sharp gradient between the concentrations at the surface and at the top of the lowest layer.

For comparison, figure 5.29 shows a typical mineral dust aerosol number size distribution (plotted in pink), adapted from figure 6 of D'Almeida and Schütz (1983), compared with the mean number size distribution from SHAMAL (in black) in the lowest kilometre of the atmosphere and across the domain. The peak of the observations occurs at $r = 0.1$ μm, and drops off with increasing particle radius: hence this distribution appears to be shifted towards smaller particles compared to the SHAMAL predictions. This suggests both that the SHAMAL particles are too large, and that

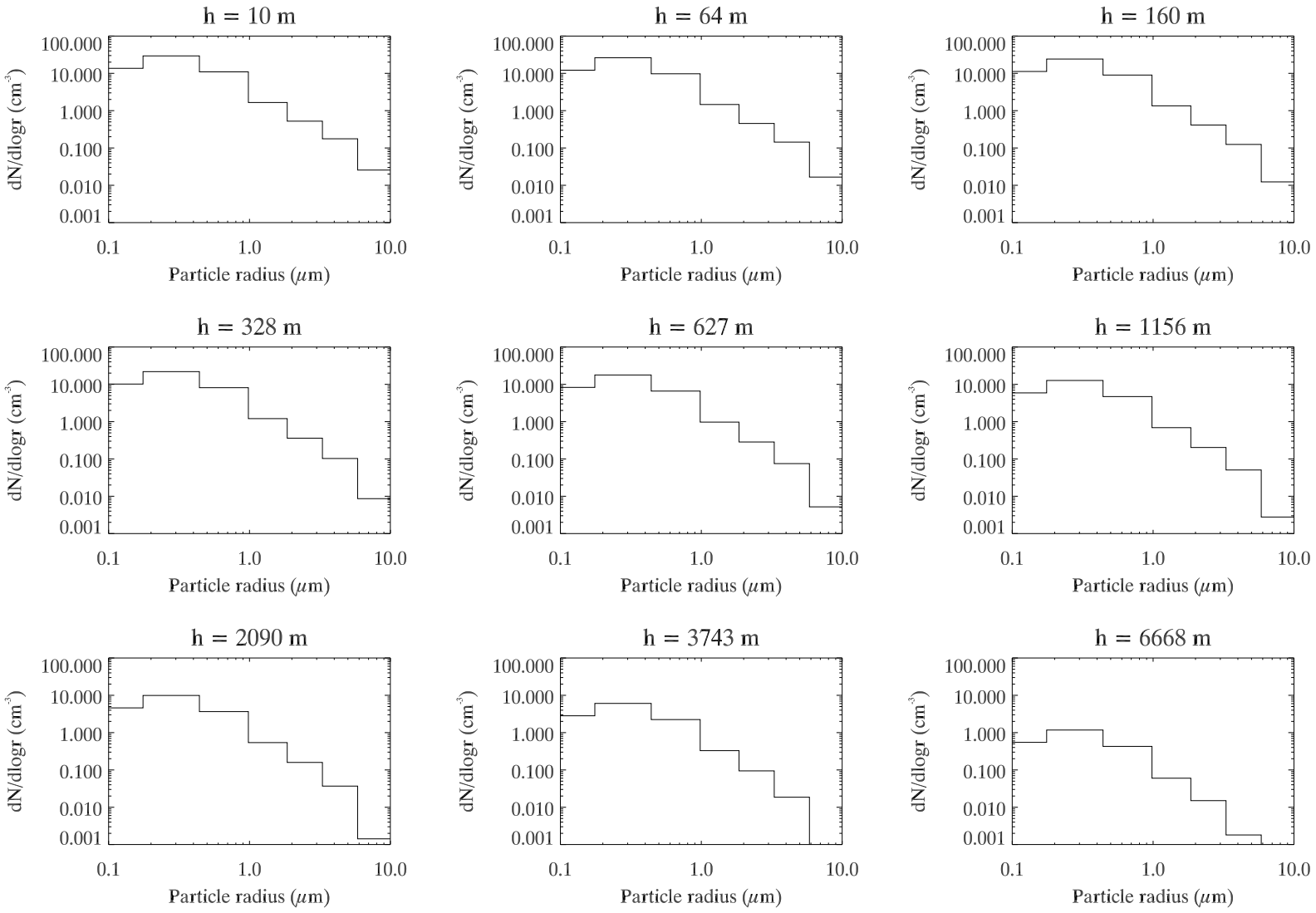

Figure 5.27: Plots of the number size distribution, $dN/d\log r$, for 9 height layers.

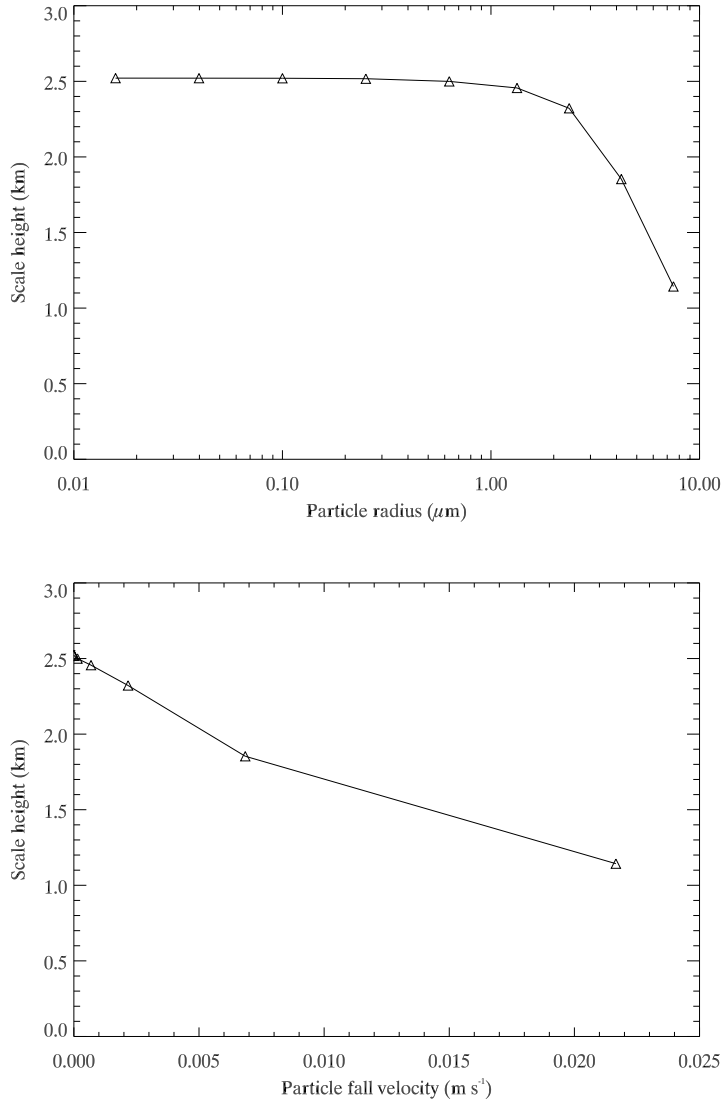

Figure 5.28: Plots of the relationship of the scale height of dust in the atmosphere to particle size and to gravitational settling velocity, from SHAMAL modelled mean concentrations.

SHAMAL under-predicts the number loading. However, the observations were made using a wet-sieving technique, which may cause disaggregation and artificially shift the observed distribution towards a greater proportion of smaller particles. The size of the particles will be studied further in section 5.6, while the SHAMAL under-prediction can partially be attributed to the usage of dust loading across the entire domain.

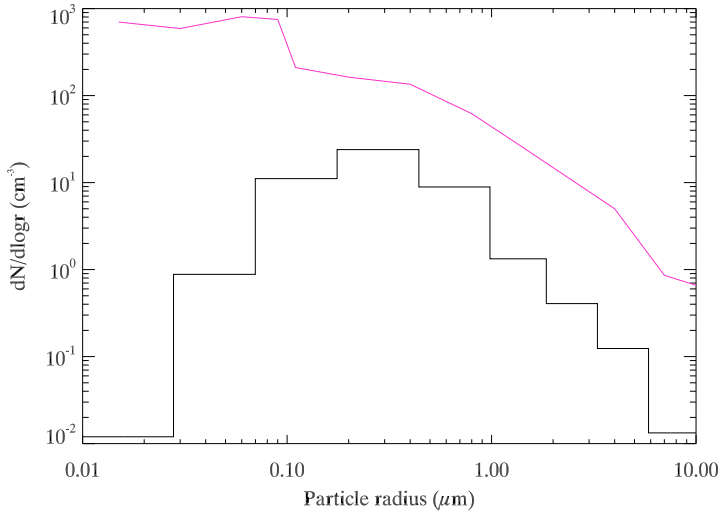

Figure 5.29: Plot of typical number size distribution of atmospheric mineral dust aerosol. In black is the mean number distribution for SHAMAL in the lowest kilometre across the domain. In pink is mean observational data produced by D'Almeida and Schütz (1983), taken from ground sites in Mali, Senegal, and Libya.

5.5 AERONET comparisons

In order to validate the model output, it is helpful to use AERONET data, which are available as a long time-series of data for the 21 sites across the North African domain. This is a more extensive data set than the other types of data, e.g. deposition measurements. Figures 5.30 and 5.31 show time-series comparisons between AERONET and SHAMAL-low during the course of the year. Agreement for various sites is mixed, though generally the model under-predicts the optical depth relative to the AERONET observations. Particularly good agreement exists for sites such as Capo Verde, Dakar, Ouarzazate, and Tamanrasset.

Over the Sahel especially the model under-predicts the observed optical depths; one possible reason for this is that the Sahel sites (Agoufou, Banizoumbou, DMN Maine Soroa, IER Cinzana, Niamey and Ouagadougou) are all remote regions as defined by the model, i.e. they are not in source regions. In reality, these areas can be sources (especially during the dry season, over the winter), and so it is highly likely that there is rather more dust aerosol over the Sahel than is predicted by SHAMAL-low. However, since there is a such variability in soil erodibility over the Sahel from season to season (during the wet season the Sahel can be covered in low vegetation cover, such as grass) this can make a parameterisation of the soil properties and roughness length rather more complicated, and so this is left out of the model emission scheme.

Table 5.6 shows the yearly root mean square (RMS) differences and correlations between the optical depth measurements (at 870 nm) of the various AERONET sites and the results from SHAMAL-low. Comparisons are only made when there are AERONET data available, so there are never any comparisons at night. To remove any bias from local aerosol plumes (which can cause AERONET to observe higher optical depths over very short timescales), the AERONET observations are averaged over each model time step. Generally the evolution of the model optical depths shows a smoother and more continous trend than the AERONET observations, which can have sharp spikes in the data, due to the fact that the AERONET observations are more localised over both space and time.

The correlations are generally positive, with a minimum of 0.44 over Dakar and Tamanrasset, and a maximum of 0.82 over Niamey. The weighted mean is 0.58 ± 0.10; this compares to the mean correlation of 0.70 that the GOCART global aerosol model has with AERONET (Chin et al., 2002). On the monthly basis, the Capo Verde site exhibits the largest variation in correlations, with a maximum correlation of 0.97, and a minimum of -0.31: this suggests that the magnitudes of the dust storms are generally in good agreement with the AERONET observations, but on some

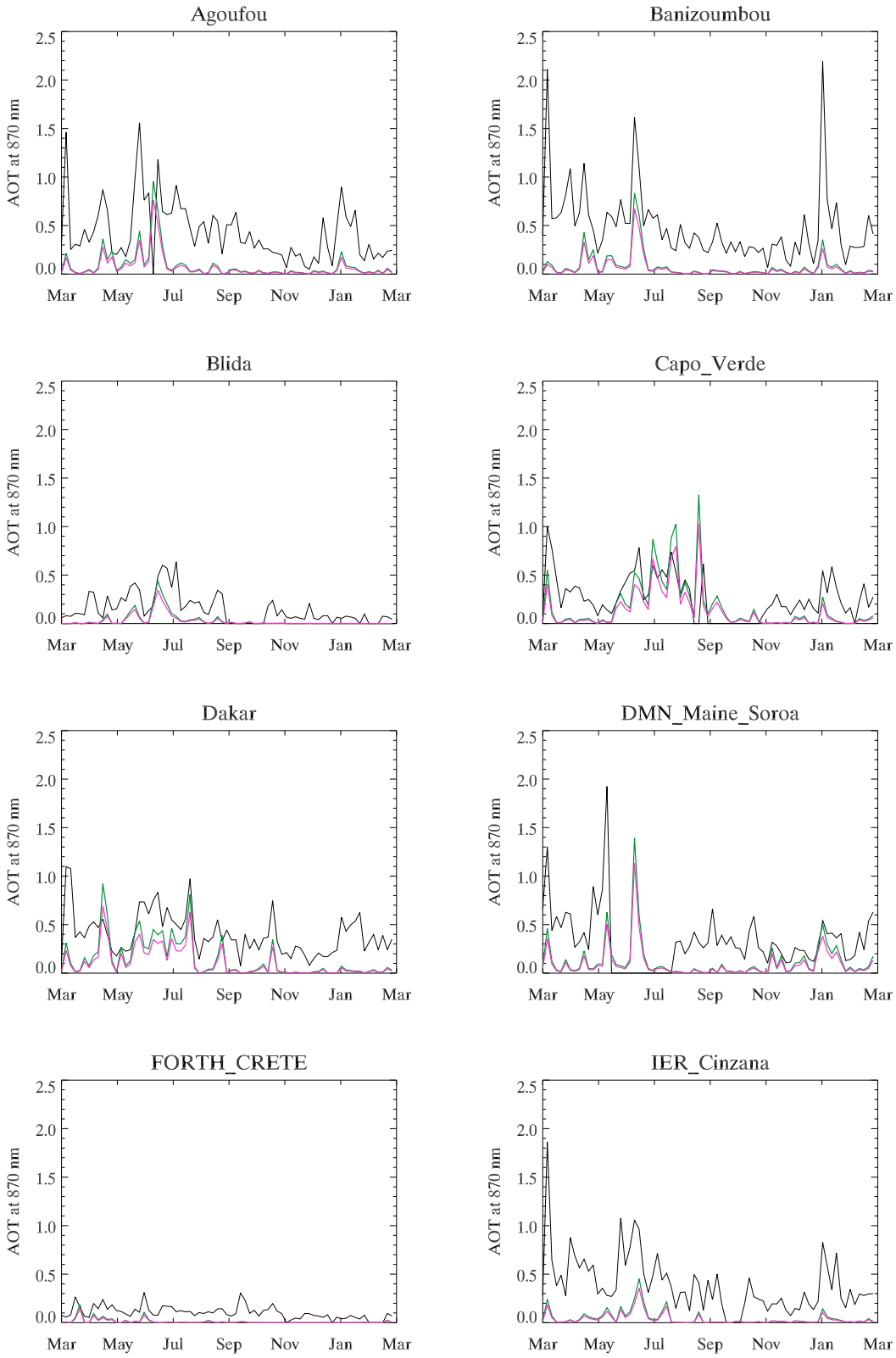

Figure 5.30: Time-series plots of AERONET and SHAMAL-low optical depths (at 870 nm) over each AERONET site, March 2006 to February 2007. The data are averaged over a 5-day period. AERONET data are in black, SHAMAL-r1 are in pink, and SHAMAL-r0.5 are in green. Times without AERONET data are indicated when the black line joins the x-axis. Excluded are Cairo EMA, El Arenosillo and IMS-Metu-Erdemli (due to a paucity of data), Lampedusa (again due to a paucity of data and since similar results are shown by Forth Crete), and Nes Ziona (similar to Sede Boker). Missing months: Blida (September); Capo Verde (September); DMN Maine Soroa (June).

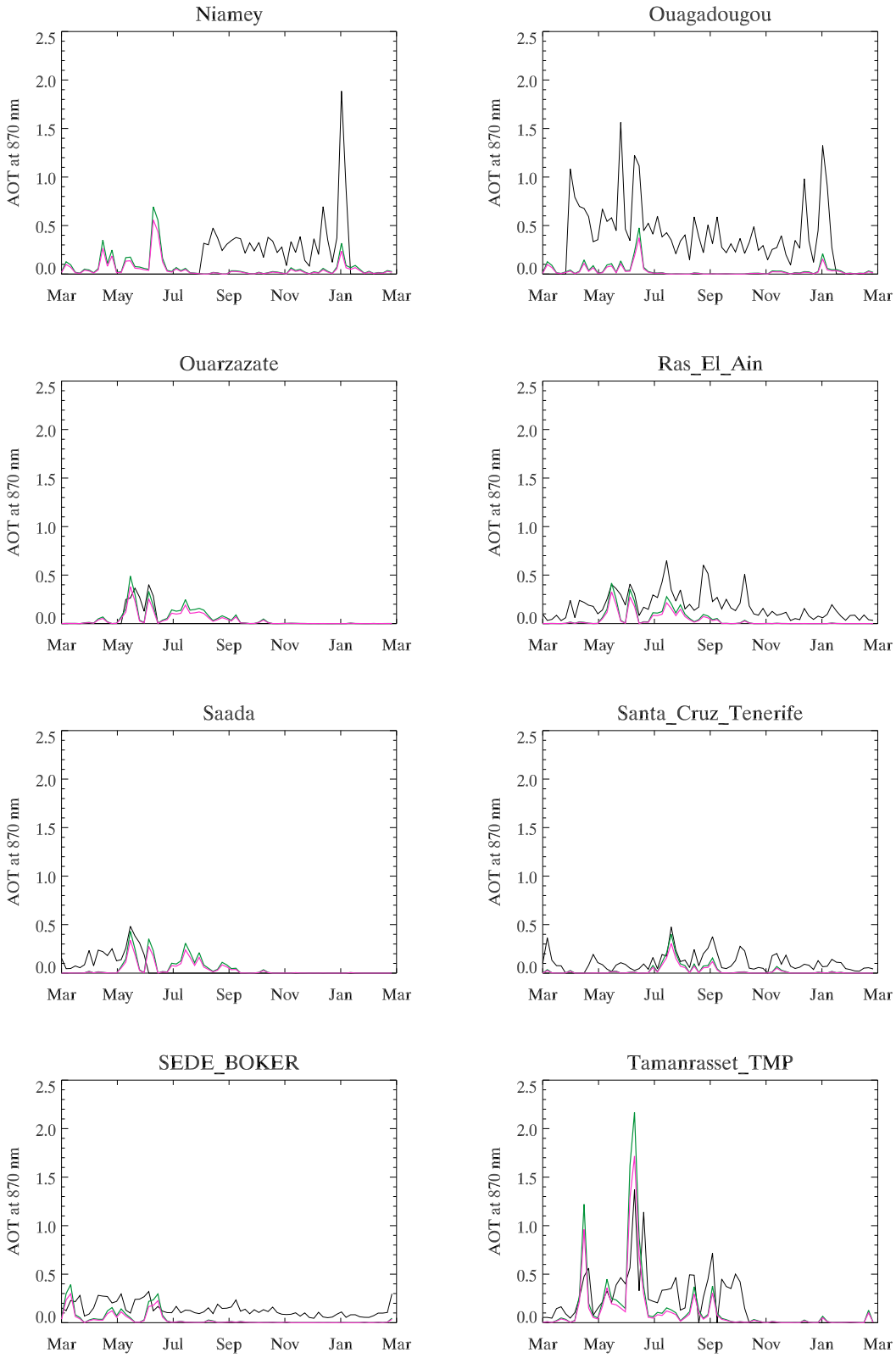

Figure 5.31: As with figure 5.30. Numerous missing months for Niamey, Ouagadougou, Ouarzazate, Saada, and Tamanrasset TMP.

Site	Months of data	No. of data points	RMS difference	Correlation
Agoufou	12	6966	0.479	0.62
Banizoumbou	12	6962	0.558	0.59
Blida	11	2460	0.193	0.72
Cairo EMA	1	346	0.332	0.80
Capo Verde	11	3167	0.300	0.58
Dakar	12	6775	0.400	0.44
DMN Maine Soroa	11	4318	0.455	0.57
El Arenosillo	1	211	0.125	0.56
Forth Crete	12	5293	0.145	0.61
IER Cinzana	12	5979	0.482	0.50
IMS-Metu-Erdemli	5	914	0.175	0.51
Lampedusa	4	1139	0.115	0.77
Nes Ziona	9	3988	0.179	0.74
Niamey	6	2733	0.428	0.82
Ouagadougou	10	4734	0.593	0.53
Ouarzazate	2	428	0.213	0.49
Ras El Ain	12	5821	0.215	0.58
Saada	4	1616	0.187	0.73
Santa Cruz Tenerife	12	3958	0.140	0.71
Sede Boker	12	7070	0.162	0.46
Tamanrasset TMP	8	3556	0.391	0.44
Weighted Mean	-	-	0.342	0.58

Table 5.6: Comparison of AERONET and SHAMAL-low, per site (included are the number of months during the year when AERONET data are available). The mean is weighted by the number of available AERONET data points.

months the modelled dust storms are out of phase with the observed dust storms. With such a large number of coincident data points (on the yearly time-scale), it is safe to assume that these calculated correlations are significant (the weakest t value is 9.9 at El Arenosillo, with 211 counts: there is less than a probability of 0.01 that this is random).

The RMS differences and the correlations are both presented because in some areas the RMS differences may be small due to small observed and modelled optical depths. Comparing only the RMS differences may not be useful, since areas with large dust storms will have large optical depths, and hence greater scope for larger RMS differences even if the correlation is good. Meanwhile, areas which do not get significant dust storms will have small RMS differences, but this does not necessarily mean that there is good agreement between AERONET and SHAMAL-low.

Figure 5.32 shows the pdf of the optical depth values for AERONET and SHAMAL, and the normalised cumulative frequencies of the optical depth. Both of these plots show that SHAMAL has a much higher frequency of the smallest optical depths (< 0.1) than does AERONET, which has a more log-normal distribution peaking at an AOD of 0.22. The background dust/aerosol

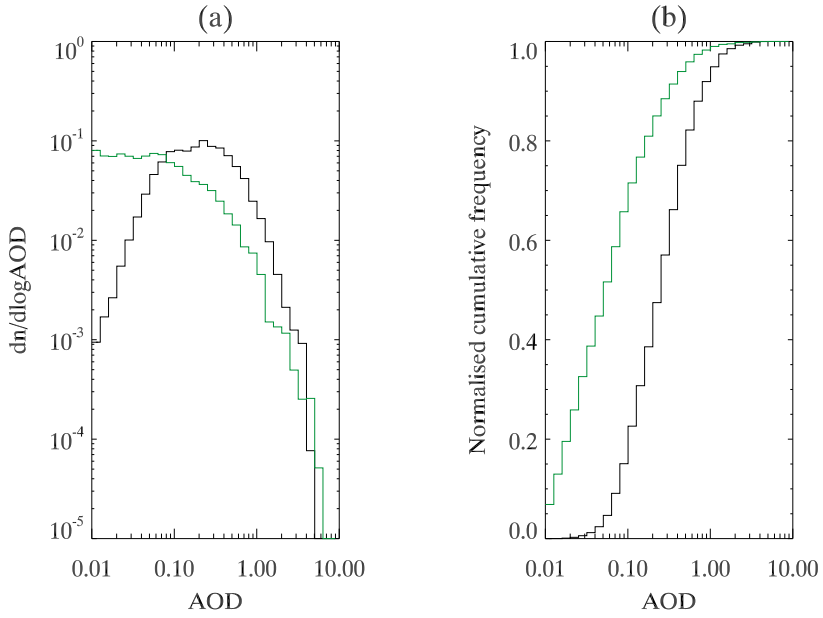

Figure 5.32: (a) Normalised AOD distribution (n refers to the fraction of occurrences) for AERONET (black), and for SHAMAL (green), for all sites and times. (b) Normalised cumulative frequency distribution.

loading in SHAMAL is therefore much lower than is observed by the AERONET sites. Possible reasons for this include the absence of Sahelian and Arabian dust, other aerosols, or excessively strong deposition rates. Meanwhile SHAMAL has rather lower frequencies of higher optical depths between 0.1 and 1, which dominate the AERONET observations. There is closer agreement for the largest optical depths, though these are much rarer events (hence SHAMAL is better at identifying the major dust events than it is at identifying the background dust).

5.6 Ensemble of model schemes

Two versions of the model have been run, to test the sensitivity of the model to the initial size distribution. One parameter has been modified; this is the clay mean radius in the soil size distribution (as described in section 3.5). Throughout this chapter the mean radius has been set as 1 μm, whereas the test case sets it at 0.5 μm. In this section, the version with the mean radius of 1 μm will be denoted SHAMAL-r1, and that with 0.5 μm will be denoted SHAMAL-r0.5. Table 5.7 compares the model results from the two versions.

There is very little difference between the two versions of the model in terms of the bulk proper-

	SHAMAL-r1	SHAMAL-r0.5
Emission (Tg)	1157.1	1156.5
Dry deposition (Tg)	1001.4	995.0
Wet deposition (Tg)	45.3	46.4
Total deposition (Tg)	1046.7	1041.5
Net surface flux (Tg)	110.3	115.0
Atlantic deposition (Tg)	27.9	27.6
Mediterranean deposition (Tg)	9.0	9.2
Atlantic flux (Tg)	62.0	64.2
Western flux (Tg)	45.0	47.1
Southern flux (Tg)	10.4	10.8
Eastern flux (Tg)	17.1	17.9
Northern flux (Tg)	45.9	47.5
Mean domain dust mass (Tg)	2.42	2.48
Mean effective radius (μm)	1.29	0.86
Mean dust optical depth	0.059	0.109
Mean plume height (km)	2.32	2.39

Table 5.7: Table of yearly properties, for SHAMAL-r1 and SHAMAL-r0.5.

ties (e.g. emission, deposition, mass fluxes, etc.) and indeed between the AERONET comparisons. For example, the total yearly emissions are 1156.5 and 1157.1 Tg year^{-1}: there is such a small difference because saltation is so heavily dependent on the larger particles, and large clay particles contribute very little to the saltation flux. Hence the total emission (which is dependent only on the saltation flux and the sand-blasting efficiency) is very insensitive to the clay distribution. Meanwhile diffusion and wet deposition are the dominant processes in the vertical transport of clay particles (since the settling velocity is so low), so there is also very little difference in the atmospheric transport. SHAMAL-r1 predicts total deposition of 1046.7 Tg year^{-1} and a flux into the Atlantic of 62.0 Tg year^{-1}, while SHAMAL-r0.5 predicts deposition of 1041.5 Tg year^{-1} and a flux of 64.2 Tg year^{-1}. There is a drop in the dry deposition of 6 Tg for SHAMAL-r0.5, due to the reduced settling velocity: hence there is more chance for the dust to linger in the atmosphere, and consequently the wet deposition, the fluxes, the domain mass, and the plume heights are all slightly higher.

There is more of a difference, however, in terms of the optical depth and the size distribution of the lofted aerosol. During the course of the year, the mean optical depth in SHAMAL-r1 is 0.059, whereas in SHAMAL-r0.5 it is 0.109, a difference of a factor of two. This is because the smaller particles (with a radius of 500 nm) are much closer to the 550 nm wavelength: hence the lofted dust in SHAMAL-r0.5 is much more optically active. Meanwhile the size distribution is shifted more towards the smaller particles, since the source particles are smaller as well. The mean effective

radius is not halved, because there is also the unchanged silt distribution, larger dust particles which can also linger in the atmosphere.

Figure 5.33 compares the ensemble schemes to AERONET retrievals of size distribution. The magnitudes of the number size distribution from the model and from the AERONET retrievals tend to be very similar (especially for SHAMAL-r1), though for some of the more remote sites (e.g. IMS-Metu-Erdemli, El Arenosillo, both of which have very little data) the modelled magnitudes are rather lower than the AERONET, due perhaps to the dominance of more local sources of aerosol (unaccounted for in SHAMAL). For example, some of the city sites, such as Ouagadougou and Niamey, may be strongly affected by urban pollution (e.g. Liousse et al. (2009)). Some of the sites in SHAMAL-r0.5 have much larger magnitudes (e.g. Agoufou, Capo Verde, etc.) because the number density of smaller particles, at the same mass, is much greater than that for larger particles. Hence in terms of magnitude, SHAMAL-r1 agrees better with AERONET. The distribution is shifted towards lower particles in SHAMAL-r0.5, with the peak in the distribution occuring at 0.1 μm, compared to the typical peak in the AERONET retrievals at 0.86 μm. Hence in terms of the position of the distribution, SHAMAL-r0.5 agrees better with AERONET.

This comparison of the effects of two different initial size distributions on the transported dust indicates the uncertainty on the transport due to the uncertainty on the source size distribution. The results of this analysis suggest that while there may not be much difference in the quantities of transported dust, there may be a difference of a factor of two in the optical depth, the property which is required for comparison with satellites and with AERONET, as well as a difference in the predicted aerosol size distribution. Hence the choice of initial size distribution can have an important effect on model-observation comparison and validation. Interestingly, the comparison of the two versions against AERONET (at 870 nm) shows that the two versions have remarkably similar comparisons: the correlations are both 0.58, while the rms differences are 0.335 in SHAMAL-r0.5 and 0.342 in SHAMAL-r1.

5.7 Summary

The aims of this chapter were to study the yearly North African dust activity, and to provide quantitative statistics of dust storm features such as deposition, transport into the Atlantic, optical depth, typical dust heights, and dust aerosol size distributions, as well as validation of the model output by comparison with observations.

Estimates of dust transport into the Atlantic have been made, suggesting that dust outbreaks

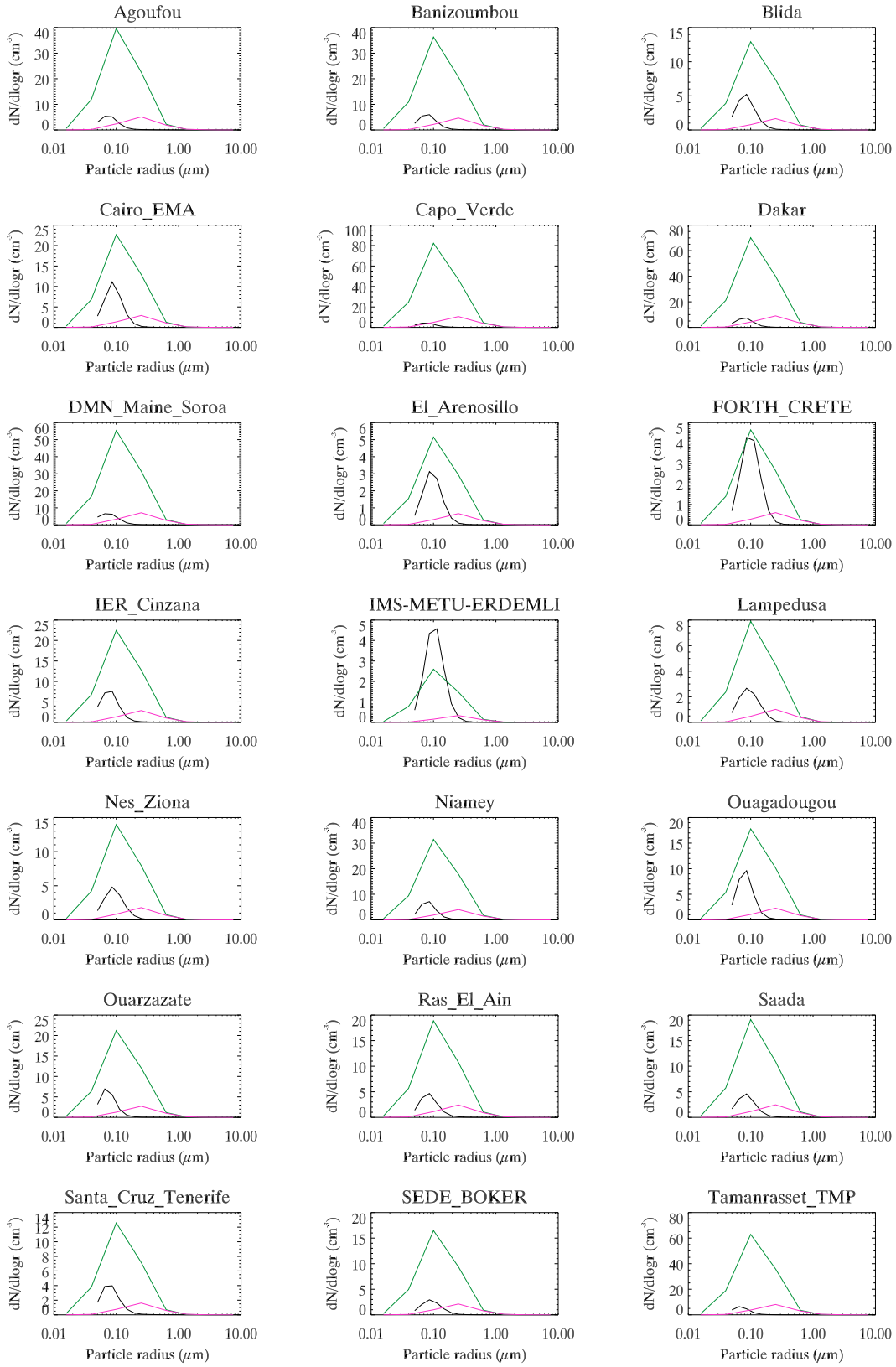

Figure 5.33: Plots comparing AERONET mean number size distributions (black line), averaged over the period 1992-2008, and SHAMAL mean number size distributions (pink line: $\bar{r}_{\text{clay}} = 1$ μm; green line: $\bar{r}_{\text{clay}} = 0.5$ μm), averaged over March 2006 to February 2007.

occur most frequently and intensely during the summer, when the West African source regions are most active. Dust takes time to travel from the source regions to the coast, hence there is a lag in the peaks of the correlations between the emissions and the fluxes into the Atlantic: typically, most dust travelling into the Atlantic is emitted from 6-18 °W and takes ∼24 hours to leave the coast of West Africa (where the peak in correlation is 0.75). Total yearly dust transport into the Atlantic is calculated to be 62.0-64.2 Tg, ∼5.5% of the yearly emissions. Yearly deposition into the East Atlantic is calculated to be 27.6-27.9 Tg.

On the annual mean, it has been shown that the dust concentration drops off exponentially with height (for specific events, discrete, elevated dust plumes may form). The scale height is ∼2.5 km for sub-micron particles (for which gravitational settling is a weak process), but is reduced for larger silt particles, descending to just under 1 km for particles with radii of 10 μm. This is evidence that the typical altitude that dust particles reach is determined by their size.

The yearly study indicates that it may be inaccurate to use optical depth as a metric to determine the location of source regions. While properties such as deposition are very highly correlated with emission (correlation of 0.94), the correlation between AOD and emission is quite poor (correlation of 0.53), since the AOD refers to the spatial extent of *atmospheric* dust, which is dependent on the winds to transport the dust typically hundreds (sometimes thousands) of kilometres from the source. This means that the geographical spread of AOD is much more diffuse than that of the emissions, and so it is not possible to locate precisely the source regions using optical depth (e.g. from satellites). This indicates the advantage that modelling has over satellites in determining the dust sources.

There are still a number of uncertainties in the model, as shown by the fact that the correlations between the modelled AOD and the AERONET AOD, while positive, are quite weak (with a weighted mean correlation of 0.58). There is a particular source of uncertainty in defining the initital soil (clay) size distribution: though properties such as total emission and transport may be quite insensitive to the difference in size distribution, the optical depth and the lofted size distributions are sensitive to it, and these differences do not favour either defined distribution. Hence, using AERONET data, there is not enough evidence to decide which soil size distribution is most accurate. Such uncertainties indicate the need for an improved model system, and this is what the next two chapters will address, using the technique of data assimilation.

Chapter 6

Data Assimilation

Introduced in this chapter is the data assimilation scheme used in the SHAMAL model (theory, and its usage in the model structure), included specifically to get a better understanding of dust transport during the March 2006 test period.

6.1 Theory of Data Assimilation

Data assimilation is a method of finding a model result which most closely resembles the true state of a system (e.g. dust in the atmosphere). It does this by taking the model predicted output (which requires an understanding of the physics of the system) and compares this prediction with the observations of the system, e.g. from satellites. Due to observational errors, the observations cannot be regarded as the true state, but nor can the model be regarded in this way, since the true state can never be modelled exactly, due to insufficient parameterisations and the chaotic nature of the system. Data assimilation uses both the model and the observational data, along with an estimate of their associated errors, to find a closer match to the 'true' state.

6.1.1 Least Squares fitting

The least squares fitting method (Kalnay, 2003) aims to fit a linear relationship between two sets of data, so as to produce a best estimate of the true state. If we consider two observations x_1 and x_2 (e.g. satellites/model observations), then their associated errors with respect to the 'true' state

x_t are denoted by ϵ_1 and ϵ_2, respectively. This relationship is described by:

$$x_1 = x_\mathrm{t} + \epsilon_1, x_2 = x_\mathrm{t} + \epsilon_2. \tag{6.1}$$

The expected values $E()$ represent the average that one would expect to obtain if numerous observations are made. Assuming that the observations are unbiased, then the results should converge on the true state, and so the expected error would be zero:

$$E(x_1 - x_\mathrm{t}) = E(x_2 - x_\mathrm{t}) = 0 = E(\epsilon_1) = E(\epsilon_2). \tag{6.2}$$

The expected values of the squared errors are equal to the variances (which are assumed to be known), hence $E(\epsilon_\mathrm{i}^2) = \sigma_\mathrm{i}^2$. The errors on the observations and the model should be uncorrelated, so $E(\epsilon_1\epsilon_2) = 0$. In order to find the analysis state x_a we use a linear combination of the two observations, governed by two parameters a_1 and a_2:

$$x_\mathrm{a} = a_1 x_1 + a_2 x_2. \tag{6.3}$$

If the analysis is unbiased (i.e. $E(x_\mathrm{a}) = E(x_\mathrm{t})$), then by substituting equation 6.1 into equation 6.3 we find that

$$x_\mathrm{a} = (a_1 + a_2)x_\mathrm{t} + a_1\epsilon_1 + a_2\epsilon_2, \tag{6.4}$$

and hence this implies that (since $E(\epsilon_\mathrm{i}) = 0$):

$$a_1 + a_2 = 1. \tag{6.5}$$

Minimising the mean squared error of the analysis state allows us to set the analysis as the best estimate of x_t, where the mean squared error is given by:

$$\sigma_\mathrm{a}^2 = E[(x_\mathrm{a} - x_\mathrm{t})^2] = E[(a_1(x_1 - x_2) + a_2(x_2 - x_\mathrm{t}))^2]. \tag{6.6}$$

Differentiating and minimising the variance with respect to the parameter a_1,

$$\frac{\partial \sigma_\mathrm{a}^2}{\partial a_1} = E[2a_1(\epsilon_1 - \epsilon_2)^2 + 2\epsilon_2(\epsilon_1 - \epsilon_2)] = 0, \tag{6.7}$$

we find that a_1 and a_2 can be specified as functions of the variance:

$$a_1 = \frac{\sigma_2^2}{\sigma_1^2 + \sigma_2^2}, a_2 = \frac{\sigma_1^2}{\sigma_1^2 + \sigma_2^2}. \tag{6.8}$$

Substituting these values of a_1 and a_2 into equation 6.3, we find the relation:

$$x_\mathrm{a} = \frac{x_1\sigma_2^2 + x_2\sigma_1^2}{\sigma_1^2 + \sigma_2^2}. \tag{6.9}$$

If we have a pair of observations x_1 and x_2, with associated variances σ_1^2 and σ_2^2, then we can use equation 6.9 to find the analysis state x_a, the best estimate of the true state x_t.

6.1.2 The Cost Function

The cost function (Kalnay, 2003; Niu et al., 2008), $J(x)$ (where x is the state of the system) is a measure of the agreement between the model (background) state, x_b, the observation y_o, and the state of the system. The variances of the background state and the observation, respectively, are σ_b and σ_o.

$$J(x) = \frac{1}{2}\left(\frac{(x - x_\mathrm{b})^2}{\sigma_\mathrm{b}^2} + \frac{(x - y_\mathrm{o})^2}{\sigma_\mathrm{o}^2}\right) \tag{6.10}$$

In order to find the optimum value $\hat{x}$, we need to minimise the cost function, and find the value of x at which the derivative of J with respect to x is 0:

$$\frac{dJ}{dx} = \frac{x - x_\mathrm{b}}{\sigma_\mathrm{b}^2} + \frac{x - y_\mathrm{o}}{\sigma_\mathrm{o}^2} = 0, \tag{6.11}$$

and, rearranging, we find the optimum value:

$$\hat{x} = \frac{x_\mathrm{b}\sigma_\mathrm{o}^2 + y_\mathrm{o}\sigma_\mathrm{b}^2}{\sigma_\mathrm{b}^2 + \sigma_\mathrm{o}^2} \tag{6.12}$$

This result is identical to equation 6.9. The drawback to this system for finding the optimal value of the optical depth is that it is only valid over the entirety of an atmospheric column, which means that it neglects the information that is provided by the 3D model about the vertical structure of the dust column. In practice, the cost function is used to find the optimal value of the optical depth over a column (or the optimal thickness, for each grid box); the model value is compared against this optimal value to produce a scaling factor, by which the concentrations of the dust particles within the grid box are scaled. The assimilation method scales these concentrations to

the expected optical thickness.

6.1.3 Cressman Analysis

Cressman analysis (Bouttier and Courtier, 1999) is a method of repeatedly constraining the model results to the observations. We have three state variables: x_{b}, the model (background) state; y_{o}, the observed state; x_{a}, the *analysis* state, which is the state predicted by the assimilation method as being the closest approximation to the true state. The method requires that a continuous, unaltered model state is produced (which shall be referred to as the *background*), which is not influenced by the observations. Meanwhile the observation state is taken at discrete time intervals, depending on the frequency of observations. The analysis state is put through the model, so that after an observation adjusts the analysis state, the model uses the updated state to predict what the future state will be.

$$x_{\mathrm{a}}(j) = x_{\mathrm{b}}(j) + \frac{\sum_{\mathrm{i=1}}^{\mathrm{n}} w(i,j)[y(i) - x_{\mathrm{b}}(i)]}{\sum_{\mathrm{i=1}}^{\mathrm{n}} w(i,j)} \tag{6.13}$$

The weight function $w(i,j)$ represents the influence of the observations on the prediction of the analysis state, and it generally decreases with distance from the observation. An example of the form of the weight function is given by:

$$w(i,j) = max\left(0, \frac{R^2 - d_{\mathrm{i,j}}^2}{R^2 + d_{\mathrm{i,j}}^2}\right), \tag{6.14}$$

where R is the 'influence radius' of the observation and $d_{\mathrm{i,j}}$ is the distance between the observations $y(i)$ and the model grid points $x_{\mathrm{b}}(j)$. Where the observations and the model grid points are at the same locations, then the weight function reduces to 1. In the case of the DRI data, there are observations for every grid point covered by the model, so assimilation with DRI data can use this simpified weight function. For instruments such as AATSR and MISR, the weight function holds rather more importance.

The problem with this method is that, if the prediction and the observations are at the same location, the analysis value will simply replace the model prediction with the observation. This is acceptable if we place high confidence in the observation, but it is known that the observations are not perfect, and it is not desirable to throw away potentially useful information from the model. An updated version of the Cressman scheme replaces the observation term $y(i)$ with the optimal value of the optical depth found using the cost function, and this is the method used in the SHAMAL

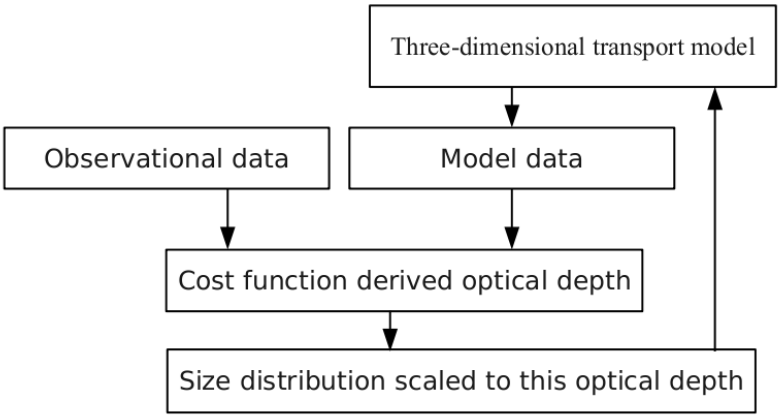

Figure 6.1: Flow chart showing the modules and processes included in the SHAMAL assimilation model.

model. A flow chart of the scheme is presented in figure 6.1.

6.1.4 Adjoint schemes

Adjoint schemes (Errico, 1997) compute the inverse of the model to produce a better estimate of the initial conditions, e.g. sources, wind speeds, diffusion parameterisation, etc. This is achieved by running the model *backwards* in time, to find some initial state. In the context of the current model, it is straightforward to reverse the advection terms, and to model the emission as a sink rather than as a source. The adjoint model becomes slightly more complicated when gravitational settling to the surface is taken into account, since this is an 'emission' whose magnitude is only known after the calculation can be made. Diffusion is the other major problem since this requires an anti-diffusion term which is difficult to characterise, and which can be very unstable. The adjoint method is not currently used within the assimilation scheme because of this instability, and the difficulty in finding an exact inverse model.

6.2 Assimilation with data from the Dust Retrieval Intercomparison (DRI) project

In the SHAMAL model, assimilation is carried out using data from the DRI project (described in section 2.2.7). In order to assimilate using satellite data, the satellite data must be put into

the same format as the model data, i.e. on the same model grid, at the same model time. The DRI data are on a 0.5×0.5 ° grid, a grid which exactly matches the grid used in SHAMAL-low (hence there is no need for a weighting function on the observations). SHAMAL-high has double the resolution of DRI and SHAMAL-low, so four SHAMAL-high grid cells fit exactly into a DRI grid cell. However, there are no DRI data north of 35 °N, so from 35-38 °N no assimilation is calculated (assimilation will still have an effect though, since advected dust from over the Sahara will be affected by the assimilation). Temporally, the components of the DRI data range from 10.00 to 16.00 on each day: the composite is formed of a daily average. Hence the assumption that can be made is that the DRI data can only be representative of the dust field in the middle of the day: for simplicity, within SHAMAL the DRI composite data are assumed to be from 12.00 on each day. The analysis model is constrained by the observations on a daily basis, at the assumed DRI data time of 12.00. The observational errors are assumed to be the standard deviation on the measurements taken by the suite of satellite instruments within the DRI data set; hence the error on the DRI data is a measure of the agreement between the instruments/retrieval algorithms.

6.3 Model uncertainty

Comparisons of the model results against AERONET observations can be used to make predictions of the model uncertainty (necessary for predicting the optimum value of the optical depth). The number and quality of the AERONET observations varies from site to site, and they are not necessarily made at regular time intervals, though they can easily be compared with the equivalent SHAMAL prediction in model time.

AERONET has advantages and disadvantages in evaluating the model and estimating uncertainties. The main advantage relates to the accuracy of the sun-photometers, since they take in-situ measurements, so the uncertainties are small (peaking at ∼0.4, with a mean less than 0.04, and with a maximum relative uncertainty of ∼0.1). The disadvantage of AERONET is the spatial distribution of the sites: the sites are rarely located in the dust source regions. The simple explanation for this is that the photometers require maintenance, which makes remote sites in the centre of the desert expensive. Of the twenty-one AERONET sites within the model domain, only the Tamanrasset site is in the central Sahara, the rest are on the periphery: there are seven on the Atlantic coast, six in the Sahel, and the rest are in the Mediterranean region.

To quantify the model uncertainty, the root mean square (rms) difference between each of the AERONET measurements and the associated model prediction is calculated. The same procedure

can be carried out on the background or assimilated field for the purposes of validation. Hence an estimate of the model uncertainty (and hence the variance, σ) can be given by:

$$\sigma^2 = \frac{\sum_{i=1}^{n}(x_{\mathrm{b,i}} - x_{\mathrm{o,i}})^2}{n}, \tag{6.15}$$

where $x_{\mathrm{b,i}}$ is the model optical depth at site and time i, $x_{\mathrm{o,i}}$ is the AERONET optical depth at site and time i, and n is the number of observations. The number of observations will vary depending on the number of AERONET sites used, and the time period chosen.

Within the SHAMAL assimilation scheme, estimates of model uncertainty are made from the previous 12 hours (over all the available AERONET sites) before the analysis field is constrained by the observations. The AERONET observations are only made during daylight, so in truth the comparison is between observations from ∼05.00 to 12.00. A trade-off needs to be made between making an instantaneous measurement of the model uncertainty (needed because the assimilation process takes place at a discrete time) and having enough data to produce a meaningful estimate. Since the DRI data are drawn from a period of ∼6 hours, it is reasonable to compare them against model data from a comparable time period. The result of this analysis is a model uncertainty on the optical depth (at 870 nm), which can be used as an absolute uncertainty on the model, across the domain.

This method of imposing one instantaneous value of the uncertainty across the domain has the drawback that it assumes that the model works equally well over all areas of the domain. This does not take into account the fact that the model may perform better for specific processes, and in specific areas. It also does not take into account the magnitude of the dust event: thicker dust plumes will have a stronger signal, and hence they may have a lower absolute uncertainty; whereas for a weak dust haze, the predicted uncertainty could be much greater than the original signal. Ideally we may prefer to have a relative uncertainty on the model, defined uniquely for each grid cell. However, there is not enough AERONET data to justify doing this, because this would require having an AERONET site at every grid cell (or distributed in a regular pattern across the model domain, whereas the available AERONET sites are distributed too randomly). A possible alternative is to divide up the model domain into sectors, in which the dust conditions are assumed to be broadly similar, and which include sufficient AERONET stations (and data) to produce acceptable estimates of the uncertainty. The uncertainty is constant within each sector. The proposed sectors over North Africa are mapped in figure 6.2, and while they may appear to be arbitrary, there is a qualitative reason for their geographical distribution. The subtropical

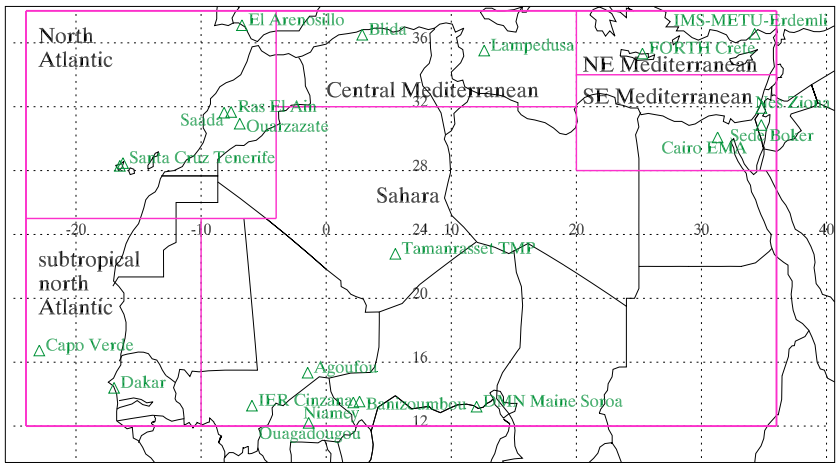

Figure 6.2: Map of the North African domain showing the six assimilation regions, and the AERONET sites contained within them.

north Atlantic region is chosen because this is the main pathway for dust from West Africa; the North Atlantic is chosen because this is another distinct pathway for West African dust (and has numerous AERONET stations); Central Mediterranean dust is transported from northern Algeria; the two eastern Mediterranean sites are chosen due to the sources in north-western Libya, and are divided up on the basis of precipitation effects (which are more substantial for the north-eastern Mediterranean). Meanwhile the 'Sahara' sector is chosen due to the lack of AERONET sites in the central Sahara (none in Chad, Sudan, or Libya, nor in northern Niger or northern Mali); such a large area is poorly served by AERONET, so the six Sahel sites and Tamanrasset are used to measure the continental uncertainty. Hence this method produces six measures of the model uncertainty for any given day.

6.4 Summary

In the SHAMAL assimilation scheme (SHAMAL-assim), equation 6.9 is used to find the optimum value of the optical depth, and the concentrations are scaled accordingly. This assimilation scaling is carried out using DRI data every day in March 2006 at 12.00. Two versions of the model uncertainty are tested: the first uses one value of the model uncertainty per day, over the entire domain; the second uses six values of the model uncertainty per day, over six defined sectors. In

so doing, an analysis model that is more consistent with the observational data can be produced, adding to the ensemble of SHAMAL models to get a better fix on dust transport in March 2006.

Chapter 7

Dust storms in March 2006

The high resolution model SHAMAL-high and its assimilation schemes are designed to study specific case studies: presented here is the case study of March 2006. There are two main reasons for the choice of time period for this study:
(a) on the days around the 8th March 2006 there was a spectacularly intense dust storm emanating originally from Algeria which spread across large swathes of the Sahara, and into the Atlantic. Outside of summer, March saw the most dust transported into the Atlantic, due mostly to this one event. March 2006 also has some other interesting events, such as dust storms caused by the Khamaseen winds along the Mediterranean coast;
(b) the DRI project has collated many satellite data sets and retrieval algorithms, so that there is excellent coverage over North Africa during March 2006.
This combination of interesting dust activity and an abundance of data makes the March 2006 period an excellent case study of North African dust storms.

As well as studying the dust weather during March 2006 (to understand the dust processes involved), it is also instructive to assess the differences between various members of the model ensemble (i.e. background or assimilation, clay size distribution, and method of assimilation). The assimilation schemes will emphasise some elements of dust activity over others: in some geographical regions the assimilation schemes will have much more effect than in other areas, depending on the uncertainties in the model and in the observations. How will the dust plumes change, and will the size distributions be altered? We are interested in knowing where this happens, and why.

This chapter is split into two main parts:

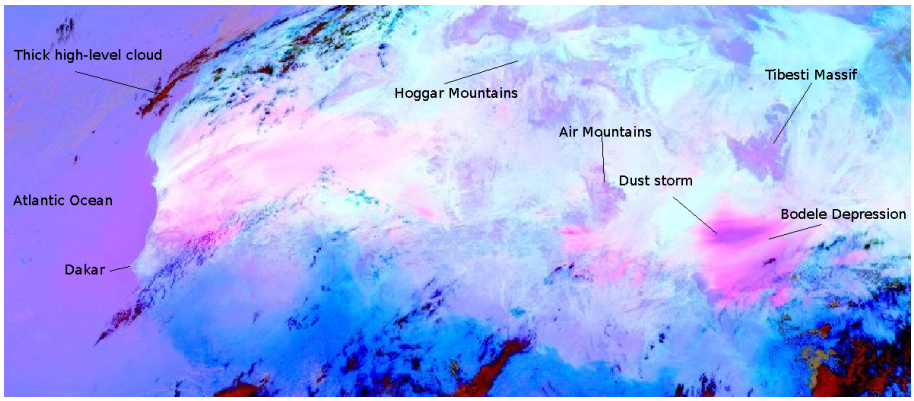

Figure 7.1: MSG-SEVIRI false-colour image of North Africa, from 1200 on 28/3/2006. Colours correspond to various types of surfaces, clouds, and dust storms. Pink denotes dust, while red denotes thick high-level cloud, and brown and green denote mid-level clouds. Light blue indicates warm desert surfaces, while light purple indicates other warm land surfaces. Image courtesy of the RADAGAST project [http://radagast.nerc-essc.ac.uk/Home.htm., last accessed 11/1/2010].

(1) a study of the March 2006 dust weather, and the consequences of using the data assimilation schemes on the model predictions of dust transport, deposition, and optical depth (and their comparisons with AERONET, to assess the advantages of using the assimilation schemes);
(2) a detailed focus on the 8th March dust event, from its inception on the 5th, through the height of the event on the 7th and the 8th, to its dissipation on the 9th. Estimates will be made of the dust emissions, transport, deposition, and the altitude of the dust layer, to explain why this event was so significant.

7.1 Overview of March 2006 North African dust weather

By far the most prominent dust event in March 2006 took place during the five day period of the 6th-10th, centred on the 8th. This is the dominant event of the month, due both to its intensity and its spatial extent.

There were also a number of small dust outbreaks from the Bodélé Depression, the biggest of which was emitted on the 28th, and dust was transported to the west across Niger over the following day. Figure 7.1 shows a SEVIRI false-colour image of West Africa from noon of the 28th showing the intensity of the Bodélé dust source (the Tibesti massif is shown in light purple, just to the north of the Bodélé source region).

The March 2006 period also sees the onset of the Khamaseen wind (Abed et al., 2009), a cyclone system across the Mediterranean and North Africa which travels from west to east. The

name refers to the Arabic word for fifty, and is named for the fifty day period during March to May when Saharan dust is most strongly blown towards the eastern Mediterranean, especially across Egypt, Israel, and Jordan. During the spring, Mediterranean cyclones can descend deeper into the Sahara (and hence expand the dust-lifting capabilities of the northern Sahara), because the Saharan temperatures have started to rise, reducing the Saharan air pressure. During March 2006, this manifests itself in the intense dust emissions from the Great Sand Sea spanning the border between Libya and Egypt, and especially the area to the south of the Jebel Akhdar (mountains) in north-eastern Libya.

7.2 Comparison between background model results from SHAMAL-high and SHAMAL-low

Before taking a closer look at the results of SHAMAL-high and the assimilation scheme, it is instructive first to compare the performance of the background model in SHAMAL-low and SHAMAL-high, for March 2006. Comparisons of various monthly properties of the North African dust environment are presented in table 7.1, for both resolutions, and for both of the possible size distributions. Generally, the domain emissions are slightly higher (by a factor of about $\sim$1.015) in SHAMAL-high then in SHAMAL-low: hence most of the resultant depositions and fluxes are correspondingly higher in SHAMAL-high. There are regional variations however, since only the Atlantic/western flux is increased, while the northern, eastern, and southern fluxes are reduced. This may be because certain discrete sources (such as the north-eastern Libyan source) which are strong contributors to the flux in certain directions, are weakened in the higher resolution analysis.

This analysis shows the differences between the two resolutions, which are small, and not particularly significant. The maximum variation is in the southern flux, where SHAMAL-low predicts the flux to be $\sim$1.25 times greater than by SHAMAL-high. The importance of doing this test is to quantify the differences between the two resolutions, and to show that the use of the low resolution version is justified since the degradation in the quality of the model with decreased resolution is not substantial. A reason that the two resolutions are so coherent with each other is that the 'low' resolution version actually uses intermediate resolution emission: the emission for each 0.5 $^\circ$ grid cell is actually an average of the emissions for each of the four 0.25 $^\circ$ soil data grid cells within the model grid cell. The only reason that there is any difference at all in the total emissions is that low resolution surface winds are used.

	$\bar{r}_{\text{clay}} = 1$ μm		$\bar{r}_{\text{clay}} = 0.5$ μm	
	SHAMAL-low	SHAMAL-high	SHAMAL-low	SHAMAL-high
Emission (Tg)	170.1	172.7	170.0	172.6
Dry deposition (Tg)	151.6	153.3	150.8	153.1
Wet deposition (Tg)	5.1	5.5	5.2	5.7
Total deposition (Tg)	156.6	158.8	156.0	158.8
Net surface flux (Tg)	13.4	13.9	14.0	13.9
Atlantic deposition (Tg)	3.26	3.64	3.21	3.58
Mediterranean deposition (Tg)	3.91	4.66	3.99	4.79
Atlantic flux (Tg)	4.90	4.96	5.13	5.21
Western flux (Tg)	2.58	2.60	2.80	2.84
Southern flux (Tg)	0.86	0.69	0.88	0.71
Eastern flux (Tg)	4.32	4.17	4.49	4.54
Northern flux (Tg)	7.59	7.24	7.86	7.73
Mean domain dust mass (Tg)	2.32	2.28	2.38	2.41
Mean effective radius (μm)	2.50	2.54	2.30	2.22
Mean dust optical depth	0.057	0.055	0.105	0.106
Maximum dust optical depth	16.7	20.0	33.0	39.4
Mean plume height (km)	1.17	1.16	1.31	1.32

Table 7.1: Table of properties for March 2006, for SHAMAL-low and SHAMAL-high, and for $\bar{r}_{\text{clay}}$ = 1 μm and $\bar{r}_{\text{clay}}$ = 0.5 μm.

As noted in section 5.6, there is very little difference in the bulk properties between the two possible size distributions, though there is a more substantial difference in properties such as the optical depth, the effective radius, and the plume height. Over the course of March 2006, the $\bar{r}_{\text{clay}}$ = 1 μm size distribution model (SHAMAL-r1) only emits ∼1.0006 times as much dust as the $\bar{r}_{\text{clay}}$ = 0.5 μm model (SHAMAL-r0.5). With larger particles there is a larger saltation flux, but since clay and silt add very little to the saltation flux, there is very little impact. Figure 7.2 maps the ratio of the two emissions models for March 2006. Note that the largest difference occurs in the far north and far south, where there are the largest clay fractions, but it is still less than 0.25%. The ratio of the optical depths is also mapped, which shows that the mean AOD in SHAMAL-r0.5 is between 1.6 and 3.1 times larger than the mean AOD in SHAMAL-r1. This is a more substantial difference, which indicates the increase in the more optically active smaller particles.

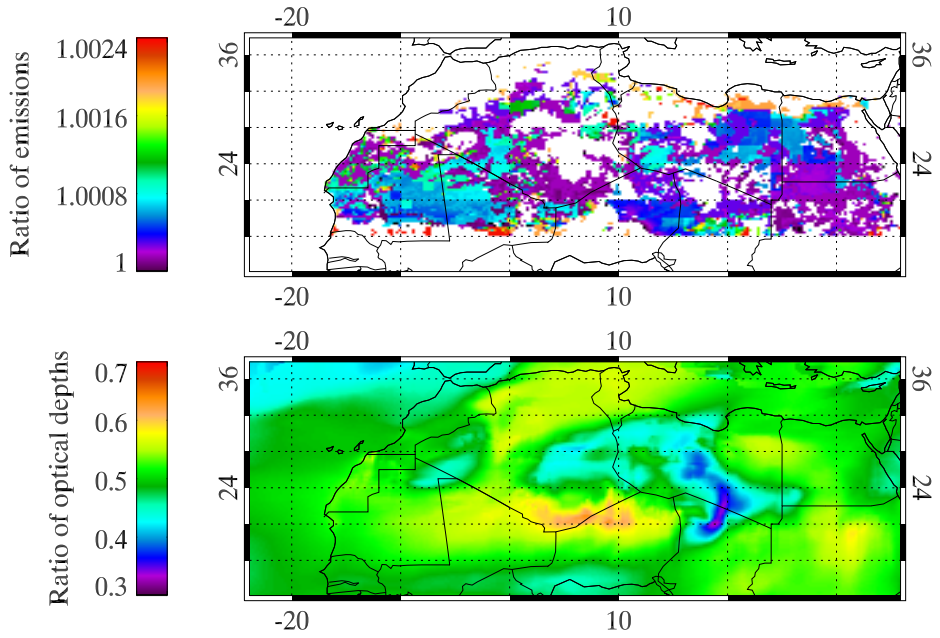

Figure 7.2: Ratio of model output from SHAMAL-r1 and from SHAMAL-r0.5, for March 2006, for emission and mean AOD. The emissions ratio is always greater than or equal to 1 (i.e. SHAMAL-r1 > SHAMAL-r0.5), except where there are no emissions. SHAMAL-r0.5 has the higher AOD across the domain.

7.3 Overview of modelled results from March 2006

To put the events of the 8th March in context, it is instructive to outline the dust activity during the whole month of March 2006. Table 7.2 summarises the dust activity for March as predicted by the six members of the background and assimilation model ensemble.

Note that emissions are unaltered by the assimilation schemes since the emissions are computed offline, and it is only the atmospheric dust aerosol that is influenced by the satellite observations. Across the domain, the bulk pattern is that the assimilation increases the quantity of dust that is in the atmosphere: hence bulk quantities such as domain dust mass, dust transport, dust deposition, and mean optical depth are increased. Assimilation also tends to increase the proportion of smaller particles in the atmosphere (effective radii are reduced and plume heights are increased) because the largest increases in dust presence are over remote areas, e.g. the North Atlantic and Morocco, where the DRI data suggest that there is a semi-permanent haze of dust, while the background model only sees significant quantities of dust in these regions on the rare occasions when a dust storm passes through. Assimilation can have a moderating effect on modelled major dust storms, hence the maximum optical depth is slightly reduced in the assimilation models.

	$\bar{r}_{\text{clay}} = 1$ μm			$\bar{r}_{\text{clay}} = 0.5$ μm		
	SHAMAL-high	SHAMAL-assim1	SHAMAL-assim6	SHAMAL-high	SHAMAL-assim1	SHAMAL-assim6
Emission (Tg)	172.7	172.7	172.7	172.6	172.6	172.6
Dry deposition (Tg)	153.3	172.2	168.3	153.1	155.5	155.8
Wet deposition (Tg)	5.5	9.0	7.8	5.7	6.9	6.7
Total deposition (Tg)	158.8	181.1	176.1	158.8	162.3	162.5
Net surface flux (Tg)	13.9	-8.4	-3.4	13.9	10.3	10.1
Atlantic deposition (Tg)	3.64	5.88	5.21	3.58	4.26	4.07
Mediterranean deposition (Tg)	4.66	7.18	6.28	4.79	5.48	5.44
Atlantic flux (Tg)	4.96	8.18	7.77	5.21	6.12	5.99
Western flux (Tg)	2.60	7.26	6.36	2.84	4.38	4.19
Southern flux (Tg)	0.69	1.90	1.54	0.71	1.33	1.15
Eastern flux (Tg)	4.17	11.30	11.30	4.54	6.84	7.38
Northern flux (Tg)	7.24	21.78	24.60	7.73	12.72	13.60
Mean domain dust mass (Tg)	2.28	5.54	5.27	2.41	3.80	3.61
Mean effective radius (μm)	2.54	1.87	1.99	2.22	1.60	1.69
Mean dust optical depth	0.055	0.198	0.163	0.106	0.241	0.209
Maximum dust optical depth	20.0	18.4	19.8	39.4	34.6	39.1
Mean plume height (km)	1.16	2.09	2.36	1.32	1.99	2.19

Table 7.2: Table of properties for March 2006, for the background and assimilation models, and for $\bar{r}_{\text{clay}} = 1$ μm and $\bar{r}_{\text{clay}} = 0.5$ μm.

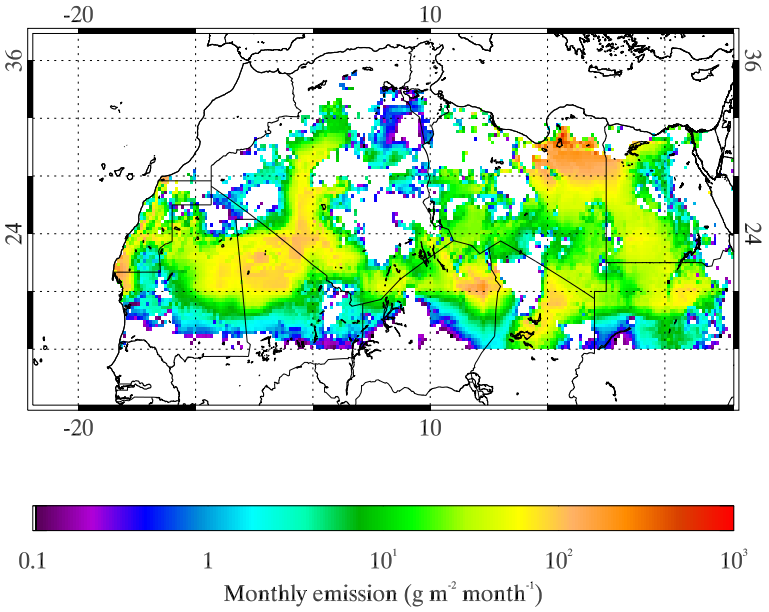

Figure 7.3: North African emissions for March 2006, SHAMAL-high-r1.

7.3.1 Sources and sinks

As shown in figure 3.18, March is the second strongest month for emission during 2006 (after June). Figure 7.3 maps the total emissions for March 2006. There are four major source areas to consider: north-eastern Libya, West Africa, the Bodélé Depression, and the Grand Erg de Bilma (north-estern Niger) in the south central Sahara.

These sources activate during different events, and so figures 7.4 and 7.5 map the daily emissions for the 1st-30th March, indicating the extent of the dust weather during the month (this also puts the emissions during the 8th March event into perspective). On most days dust source activation is sporadic and weak: these days do not contribute much to the monthly/yearly dust burden. There are ∼10 particularly noteworthy days for dust events, including the 6th-9th (across the Sahara), the 12th-13th (in north-eastern Libya), the 18th (in western Algeria), the 22nd (north-eastern Libya), and the 27th-28th (the Bodélé Depression, Grand Erg de Bilma, and eastern Libya). Figure 7.6 gives a clearer picture of the importance of each region per day: there is a low baseline of emission of under 1 $\mathrm{Tg\,day^{-1}}$ so days with > 2 Tg of emission can be regarded as significant. This plot also clearly shows the importance of the 8th March event: the days of the 7th and the 8th are the strongest days of emission for all three regions of the Sahara, greater than double the emissions of the next highest day in the south, and as much as eight times the next highest day of emissions in

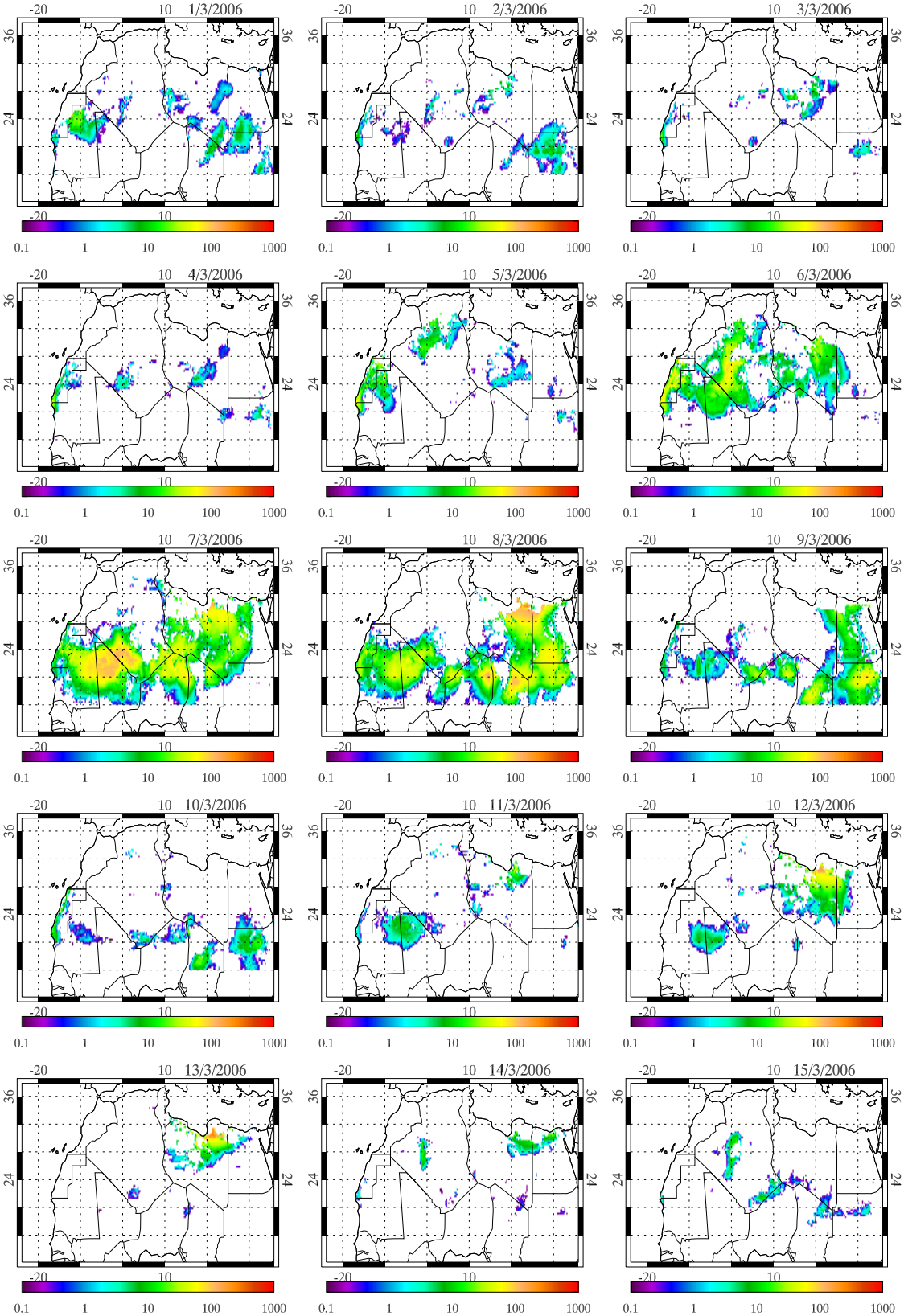

Figure 7.4: Daily emission ($\mathrm{g\,m^{-2}\,day^{-1}}$), 1-15/3/2006, using SHAMAL-high-r1.

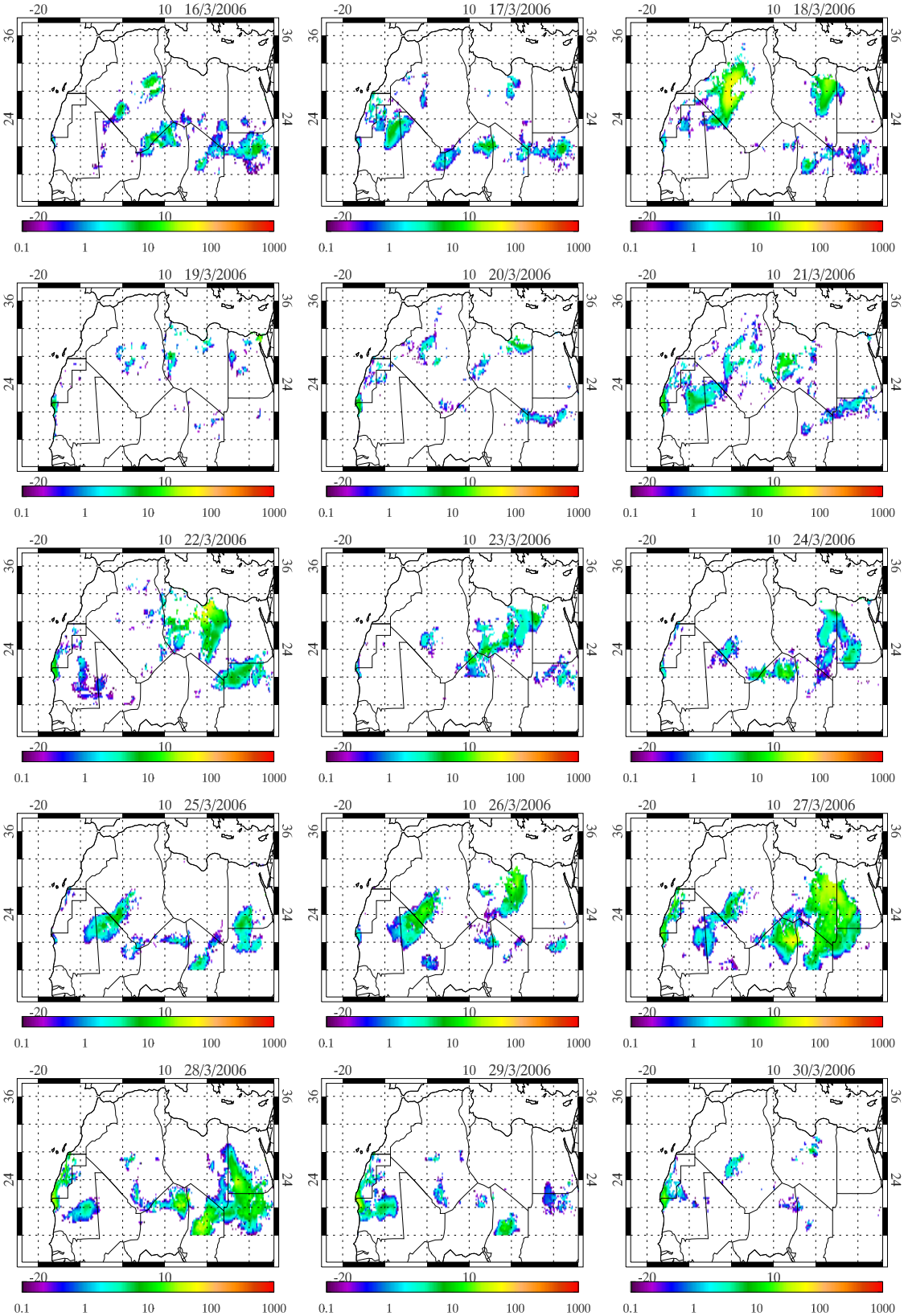

Figure 7.5: As figure 7.4, 16-30/3/2006.

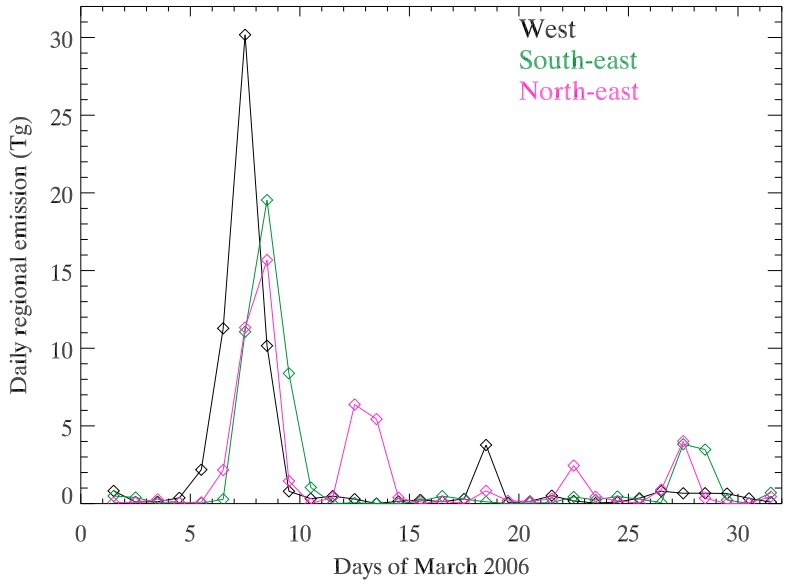

Figure 7.6: North African regional emissions (Tg) for March 2006. West: 12-38 °N, -24-6 °E. South: 12-24 °N, 6-36 °E. North: 24-38 °N, 6-36 °E.

the west.

Deposition in March 2006 is greatest over the three major source regions, as described above. For the six members of the model ensemble, the total dust deposition is mapped in figure 7.7. Generally, dust deposition is greatest over the source regions and over the transport pathways leading off from the sources. An interesting feature of these plots are the 'tendrils' of dust deposition over the eastern Mediterranean, emanating from the Libyan/Egyptian coast, most often tracking north-eastwards towards Cyprus and Turkey, but there is also a weak tendril curving back towards the west, towards Sicily. These are associated with fronts of precipitation, which initiate wet deposition along the leading edge of the front; such sharp lines of deposition are not seen in plots of dry deposition (e.g. figure 5.1), but are a feature of wet deposition.

The magnitude of the deposition is increased by the assimilation schemes, and as shown by table 7.2, the net surface flux is reduced in all cases: for SHAMAL-assim-r1, the net surface fluxes are actually negative (i.e. net sinks). Hence it appears that the deposition in SHAMAL-r1 is more sensitive to the assimilation than in SHAMAL-r0.5 (similarly with the mean domain dust aerosol mass, which appears to be more sensitive to the assimilation in SHAMAL-r1). The increase in deposition rates is most obvious over non-source regions, such as the North Atlantic and the Mediterranean.

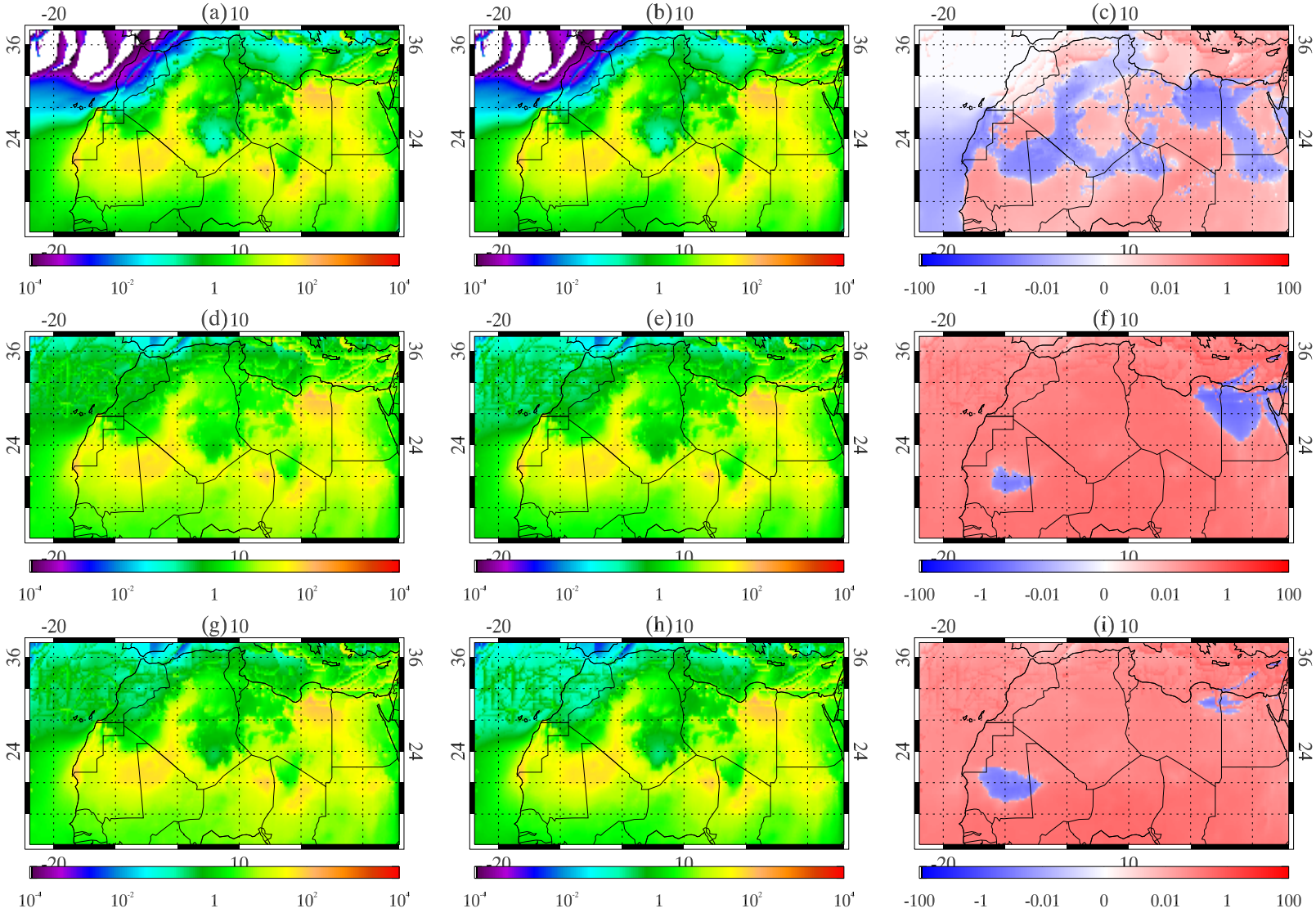

Figure 7.7: Total deposition for March 2006 ($\mathrm{g\,m^{-2}\,month^{-1}}$), for the background model and the two assimilation schemes. (a), (d), (g): $\bar{r}_{\mathrm{clay}} = 1$ μm. (b), (e), (h): $\bar{r}_{\mathrm{clay}} = 0.5$ μm. (c) SHAMAL-high-r0.5 - SHAMAL-high-r1 ((b)-(a)). (f) SHAMAL-assim1-r1 - SHAMAL-high-r1 ((d)-(a)). (i) SHAMAL-assim6-r1 - SHAMAL-high-r1 ((g)-(a)).

Difference plots between three versions (SHAMAL-high-r0.5, SHAMAL-assim1-r1, and SHAMAL-assim6-r1) and SHAMAL-high-r1 are mapped in the third column of figure 7.7. In terms of size, the decreases in deposition take place primarily over the (dry) source regions, where the particles are closest to the surface and hence most susceptible to deposition by gravitational settling; interestingly this is also the case over the subtropical north Atlantic, suggesting that this is a particularly low transport pathway. Meanwhile deposition is increased in the assimilation versions everywhere except over West Africa and in the north-east (where the most intense dust storms are located, and where the assimilation actually *decreases* the dust loading). SHAMAL-assim1 moderates the north-eastern dust storm more than does SHAMAL-assim6 (since the model uncertainties are defined as being larger).

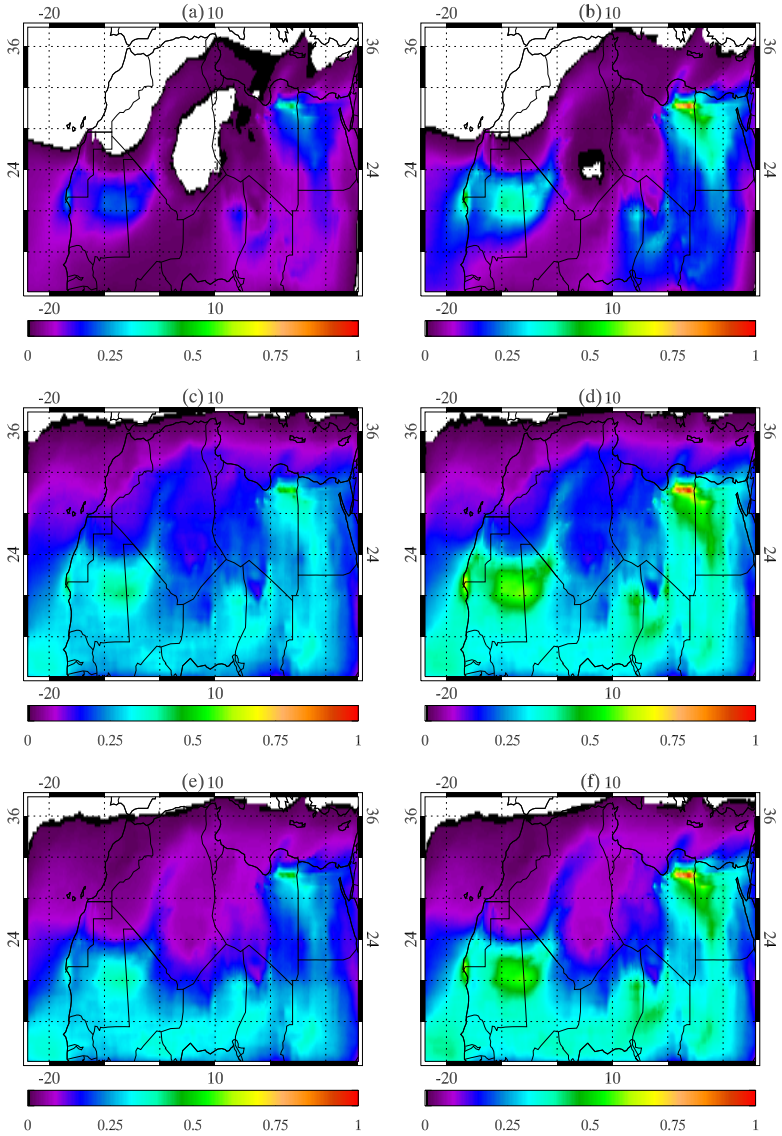

Figure 7.8: Mean monthly optical depth, March 2006, for the background model and the two assimilation schemes, and the two size distributions. On the left, $\bar{r}_{\text{clay}} = 1$ μm, and on the right, $\bar{r}_{\text{clay}} = 0.5$ μm.(a), (b): SHAMAL-high. (c), (d): SHAMAL-assim1. (e), (f): SHAMAL-assim6. White indicate areas where the mean optical depth is less than 0.01.

7.3.2 Optical depth

The monthly mean optical depths for the six high resolution versions of the model ensemble (background and assimilation) are mapped in figure 7.8. All of the members of the ensemble agree on the pre-eminence of four major source regions: the swathe of West Africa across Mauritania and Mali; the north-estern Libyan source; the Bodélé; and the Grand Erg de Bilma. The assimilated dust fields indicate that dust is much more widely spread than in the background versions: for

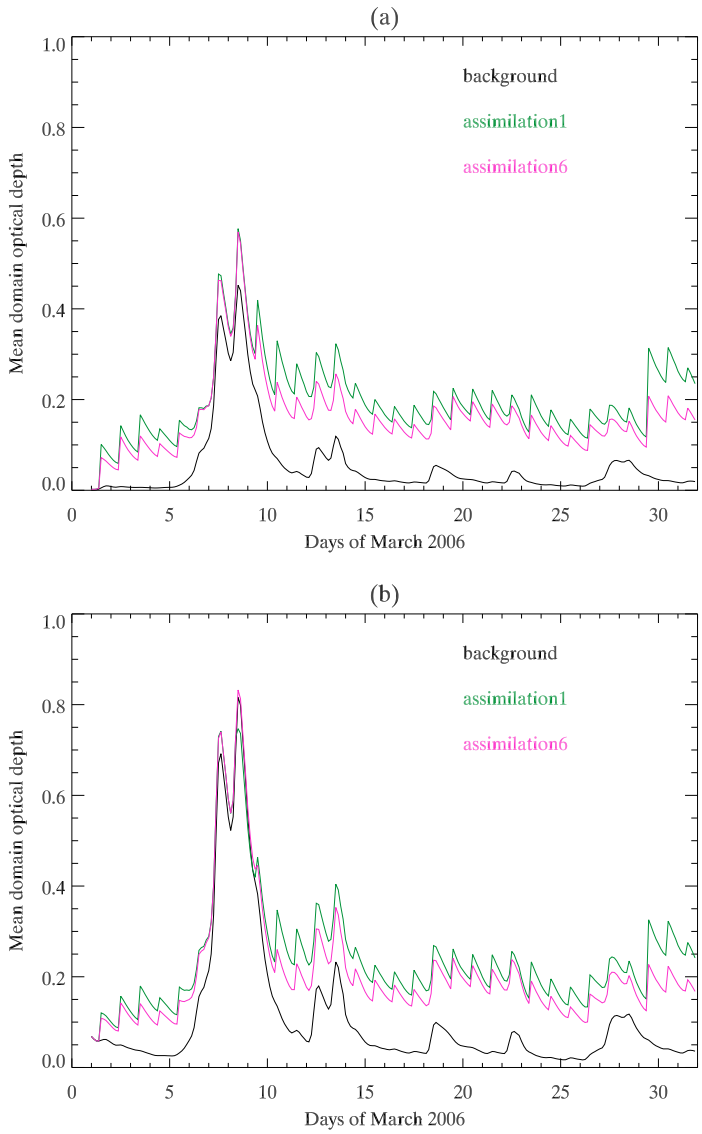

Figure 7.9: Mean domain optical depth, during March 2006, for the background model and the two assimilation schemes. (a) $\bar{r}_{\text{clay}} = 1$ μm. (b) $\bar{r}_{\text{clay}} = 0.5$ μm.

example, over Morocco the mean optical depth is less than 0.01 for the background models, while for the assimilation models the mean is of order 0.1 (there is a similar picture over south-western Algeria, particularly over the Hoggar massif). This stems from the DRI observations suggesting that there is a much higher ambient dust loading than is predicted by the model.

A time-series of the ensemble model mean domain optical depth is presented in figure 7.9. The first point to note is that the background model optical depths are generally rather lower than those of the assimilation schemes, except on the 8th. At least on the 8th, this suggests that the model

reproduces well the bulk of the dust storm activity as observed by the DRI instruments. This may indicate that SHAMAL is better at simulating the strength and timing of the strong emission events. Generally, however, the background model underpredicts the optical depth with respect to DRI, which suggests that there is more ambient dust (or aerosol) in the real atmosphere than in the model atmosphere. There are three possible reasons for this: firstly, the model emissions may be too low; secondly, there may not have been enough time for model spin-up; and thirdly, the deposition processes may be too strong. The latter seems to be the most plausible, as evidenced by the 'saw-tooth' pattern of the output of the assimilation schemes: on every day (except the 6th, the onset of the 8th March event), the assimilation process causes a jump in the optical depth at 1200, and then the model optical depth relaxes by $\sim$0.05. This indicates first that there is more dust in the observations than in the model, and that there is a model bias, in that the model is trying to remove more dust from the atmosphere than occurs in reality. It may also be possible that the ECMWF updraught velocities are too weak, or cause a net descent of dust. Temporally, there is broad agreement on the main dust events, especially on the events around the 8th, the 13th, and the 18th.

The most likely cause of this saw-tooth pattern is that either the wet deposition or the turbulent dry deposition (or both) are parameterised to be too strong (the smaller aerosol particles which are responsible for the bulk of the optical depth are insensitive to gravitational settling, making this an unlikely cause). For example, the turbulent deposition which is responsible for much of the dry deposition may be too strong, such that dust is quickly removed from the lower atmosphere before it can travel to higher altitudes and longer distances. Wet deposition may also be excessively parameterised, since a simple method of removing all dust in an atmospheric column (when rainfall is greater than a certain threshold) is used. Across the domain this is not a significant problem, since wet deposition is much less than dry deposition, but it may be a particular problem over the remote ocean, where the thin concentrations of dust present there can easily be wiped out by precipitation. Moreover, the remote ocean is consistently a region where the model under-predicts the dust loading compared to the observations by DRI and OMI, so it may be that wet deposition is too efficient at scavenging dust over the ocean, and it may be that the dust particles are not travelling high enough to ascend above the cloud layer. Hence this could be a consequence of the low plume heights (compared to CALIPSO observations, and our understanding of the height of the SAL) over the Atlantic, as described in section 5.3.2.

The ocean is also the region which is most affected by the assimilation process, since the DRI

optical depths are often substantially larger than the modelled AODs. This contrasts with the desert, where the model generates AODs which are more equivalent to the DRI observations. With such thin background dust loadings, the assimilation scaling process may be more unreliable than over desert regions, from which more distinct plumes are formed. Over the ocean the dust will be diffuse, and quite possibly aged, and so it will be harder to accurately determine a sensible height profile and spatial distribution. This means that the assimilation process could be more erratic over the ocean than over land.

Figures 7.10 and 7.11 map the daily average optical depth for the 1st-30th March (output from SHAMAL-high-r1), putting the dust extent and intensity during the 8th March event into perspective (as well as highlighting the occasional strength of the north-eastern Libyan source). Note that not all emitting regions provide a noticeable signal in the optical depth, and that the optical depth fields are much more homogeneously spread out than the emitting regions.

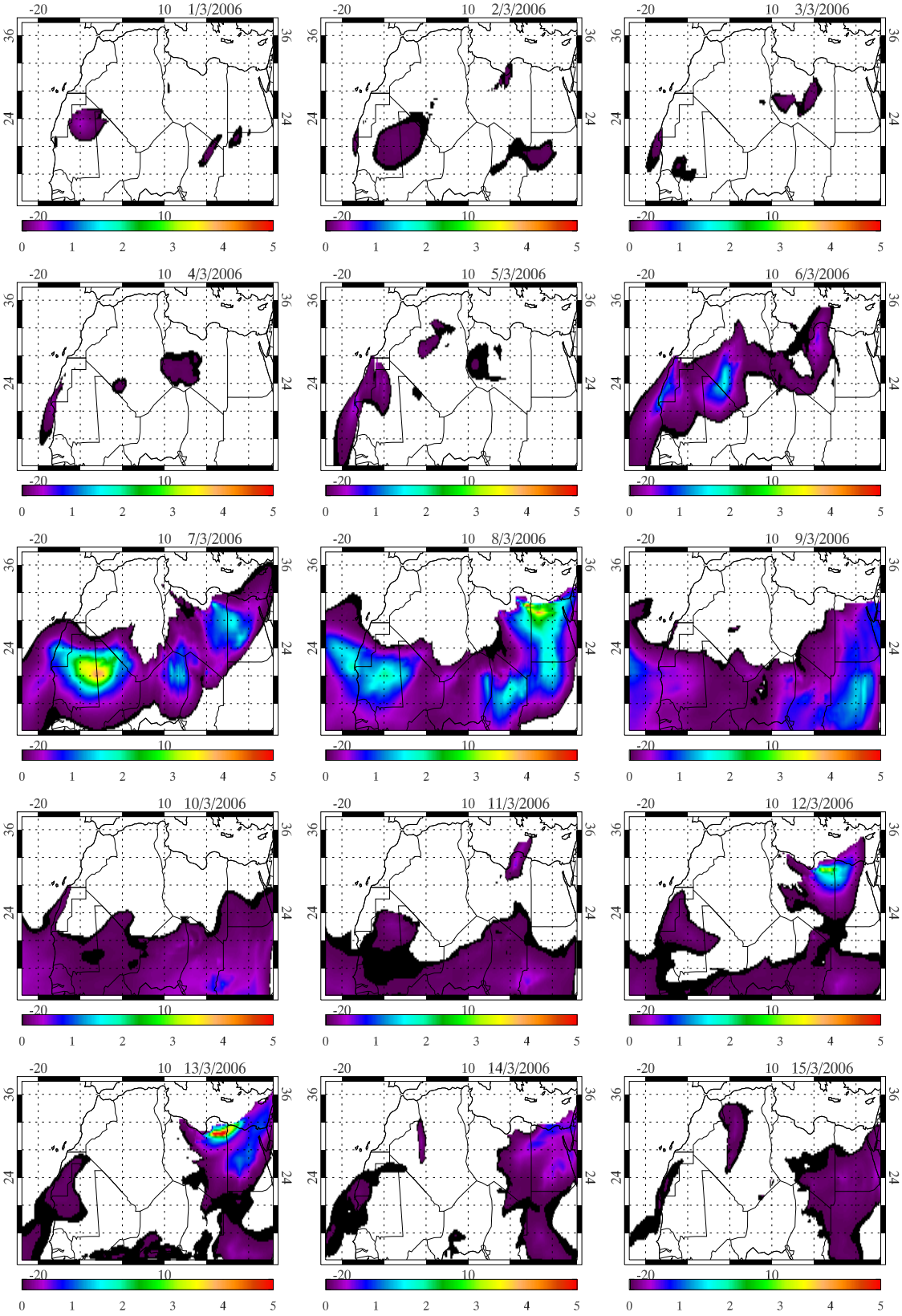

Figure 7.10: Daily average optical depth (at 550 nm), 1-15/3/2006, using SHAMAL-high-r1.

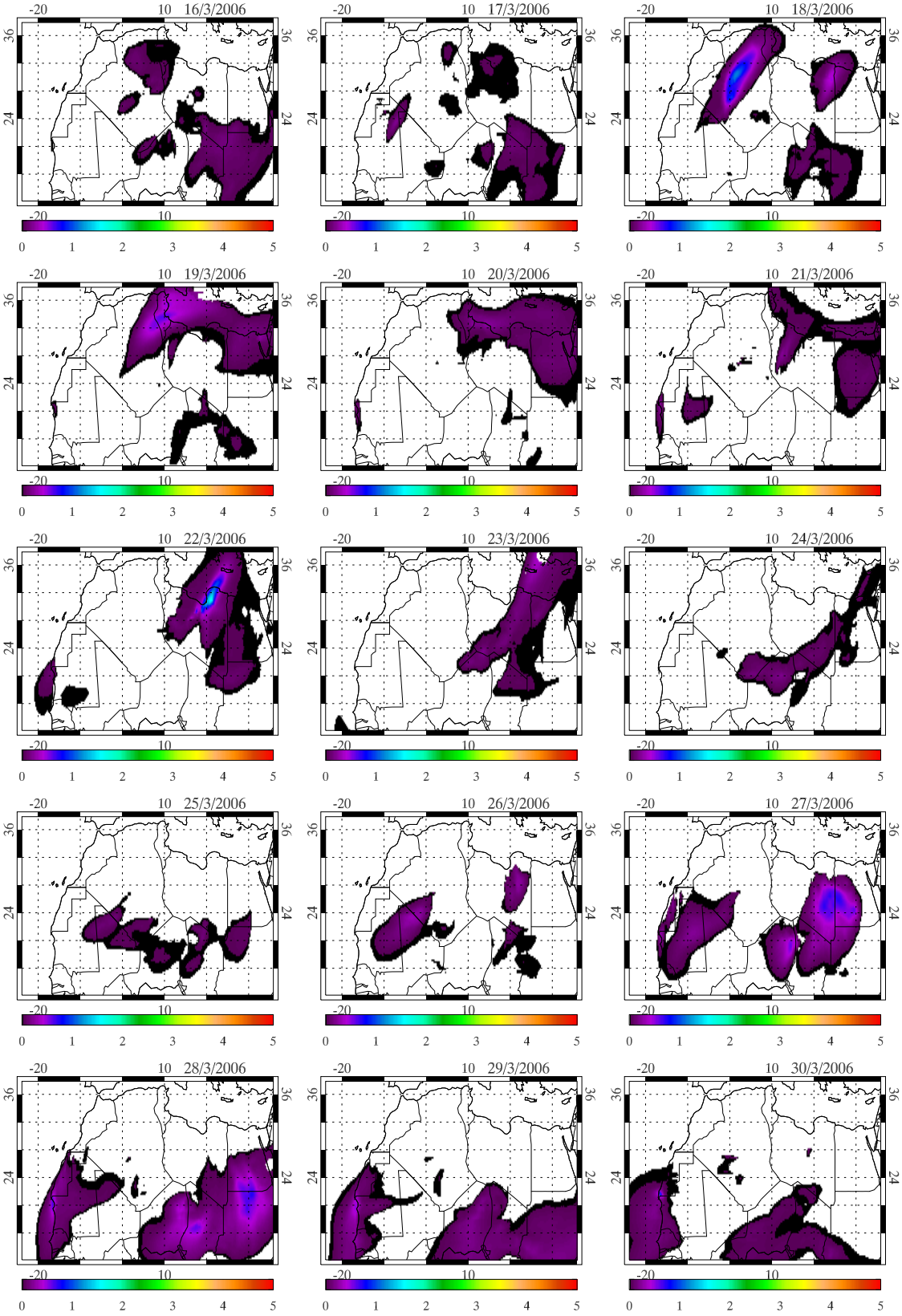

Figure 7.11: As figure 7.10, 16-30/3/2006.

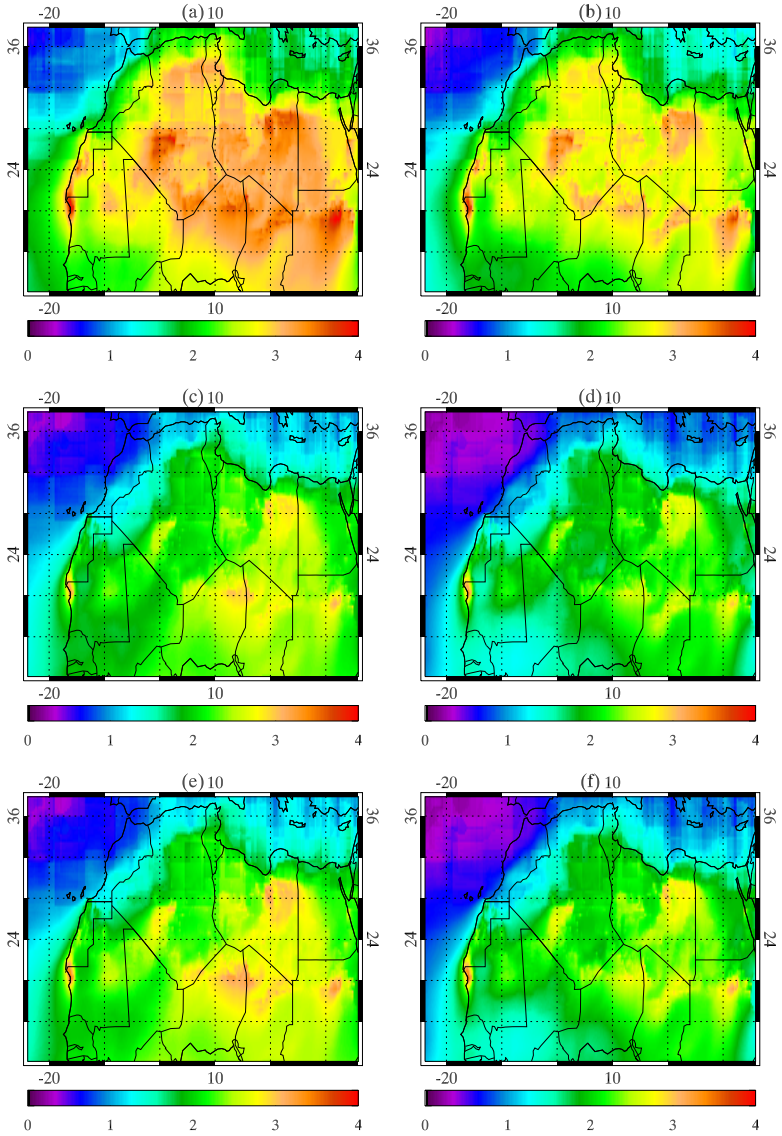

Figure 7.12: Effective radius (μm), March 2006, for the background model and the two assimilation schemes, and the two size distributions. On the left, $\bar{r}_{\text{clay}} = 1$ μm, and on the right, $\bar{r}_{\text{clay}} = 0.5$ μm.(a), (b): SHAMAL-high. (c), (d): SHAMAL-assim1. (e), (f): SHAMAL-assim6.

7.3.3 Size distributions and plume heights

A first look at the effect of the assimilation on the size distributions can be seen in the maps of mean effective radius for March, in figure 7.12. Obviously the effective radius is reduced in SHAMAL-r0.5 compared to SHAMAL-r1, but it is also reduced in SHAMAL-assim compared to SHAMAL-high, especially in SHAMAL-assim1. The reason for this reduction in the assimilation models is that in the assimilation process the whole size distribution is raised (or reduced) by the

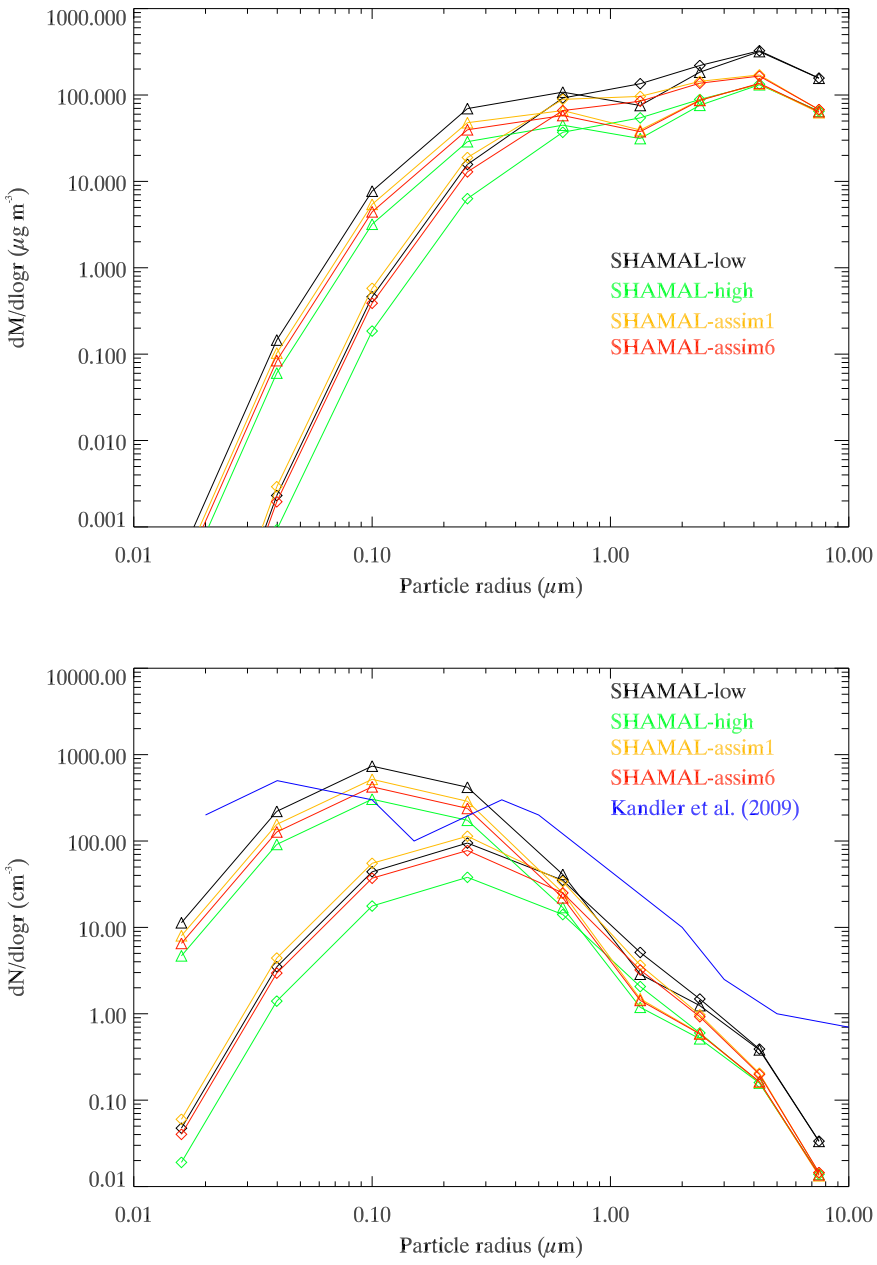

Figure 7.13: Mean number and mass distributions, March 2006, for the background model and the two assimilation schemes, and the two size distributions, in the lowest kilometre of the atmosphere. The two size distributions (SHAMAL-r1: diamonds; SHAMAL-r0.5: triangles) are distinct from each other: in the mass distribution, SHAMAL-r0.5 displays two peaks, with a dip at 1.33 μm; in the number distribution, SHAMAL-r1 is shown by the distributions peaking at 0.25 μm. The blue line is adapted from the 'dust wind' line from figure 7 of Kandler et al. (2009), also shown in figure 7.14.

same factor when carrying out the assimilation. The largest particles will drop out quickly, so their mass will quickly return to a negligible level; the smaller clay particles, however, have a longer atmospheric residence lifetime, and so their numbers do not relax as quickly to pre-assimilation levels (if the concentrations are raised; if they are reduced then we would see fewer small particles, and hence the size distribution would be shifted to the larger particles). Hence if the assimilation generally increases the optical depths and concentrations, then generally the effective radii will be reduced, whereas if it reduces the optical depth then the effective radius would be increased.

A closer look at the mass and number size distributions is presented in figure 7.13. A trivial observation is that the peak in number distribution for SHAMAL-r1 is at 0.25 μm, larger than for SHAMAL-r0.5, which is at 0.1 μm. Similarly, there is a drop in the mass distribution at 1.33 μm, in all versions of SHAMAL-r0.5, which is not really seen in SHAMAL-r1: this is due to the greater distinction between the clay and the silt size distributions in SHAMAL-r0.5. Note how the mass and number distributions increase in SHAMAL-assim much more for the smaller particles, whereas for the largest particles there is very little change. This shows how the assimilation schemes favour the smaller particles over the larger ones. The assimilation schemes show much more similarity to each other than they do to the associated background model, though SHAMAL-assim1 tends to be slightly larger than SHAMAL-assim6, for the sub-micron particles (since SHAMAL-assim6 often uses a smaller uncertainty on the model values, especially over the Mediterranean and the Atlantic, and so the model is less affected by the assimilation). The shape of these distributions agrees well with ground and aircraft (at $\sim$500 m) observations from the SAMUM 2006 campaign from Tinfou in Morocco (Kandler et al., 2009): mean observations are presented in figure 7.14, which show better agreement with SHAMAL-r0.5. The SAMUM observations are also overplotted on the number distribution in figure 7.13. Similarly, observations of dust events from Banizoumbou in Niger (Rajot et al., 2008), also presented in figure 7.14, show that dust events tend to have a 'coarse' mode (3.75-5 μm radius) and a 'fine' mode (2-2.5 μm radius). The coarse mode is well observed in the model, though the fine mode can only be seen in SHAMAL-r0.5, which locates the fine mode at 0.63 μm.

Due to the general increase in dust optical depth in the assimilation model, raising the baseline of the optical depth fields, more plumes are picked up by the assimilation model (since a cutoff of optical depth of 0.1 has been used to isolate significant dust plumes). Figure 7.15 maps the mean plume heights for March for the six ensemble model versions. Generally the plumes are also raised in altitude, a result of the decrease in the average particle size. Amongst the ensemble, the

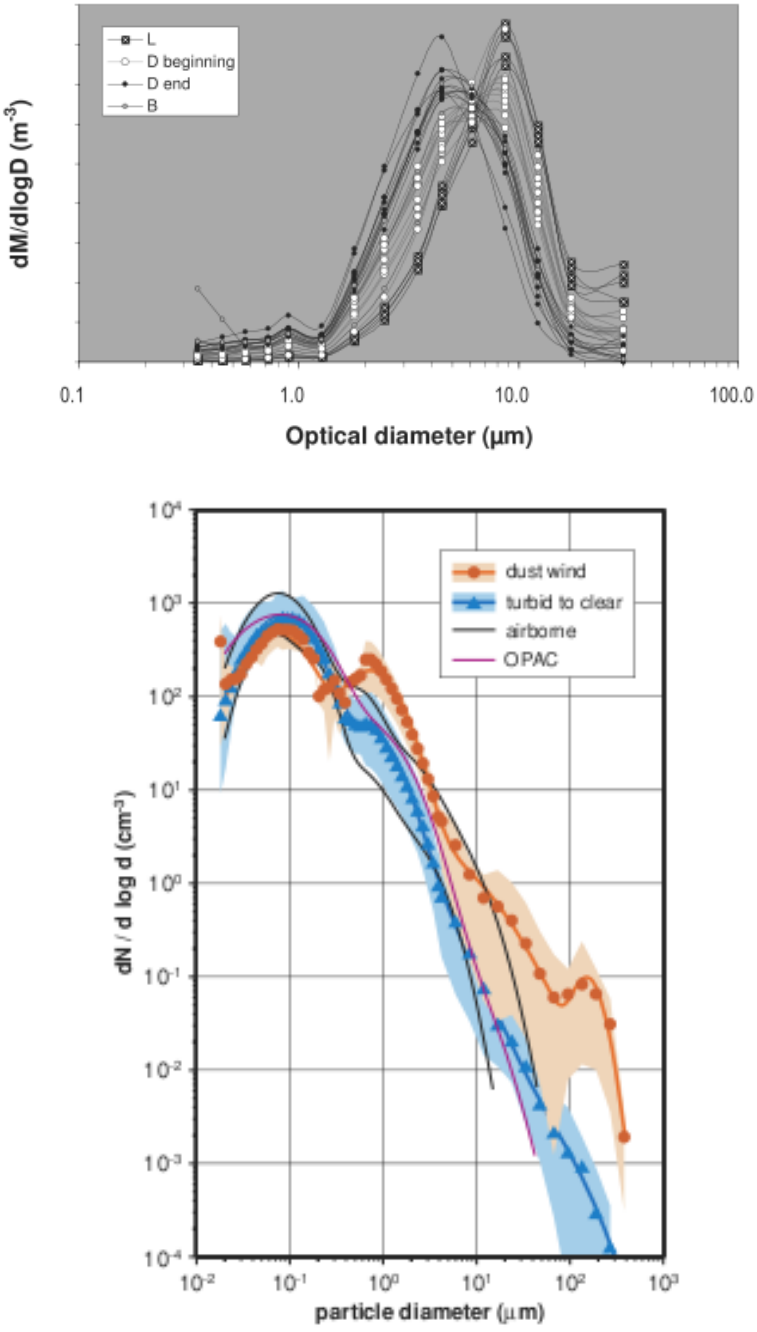

Figure 7.14: Top: normalised mass distributions of dust events over Banizoumbou (Niger), from figure 17 of Rajot et al. (2008). Bottom: mean aerosol number distribution observed during the SAMUM campaign over Tinfou (Morocco), May-June 2006, from figure 7 of Kandler et al. (2009).

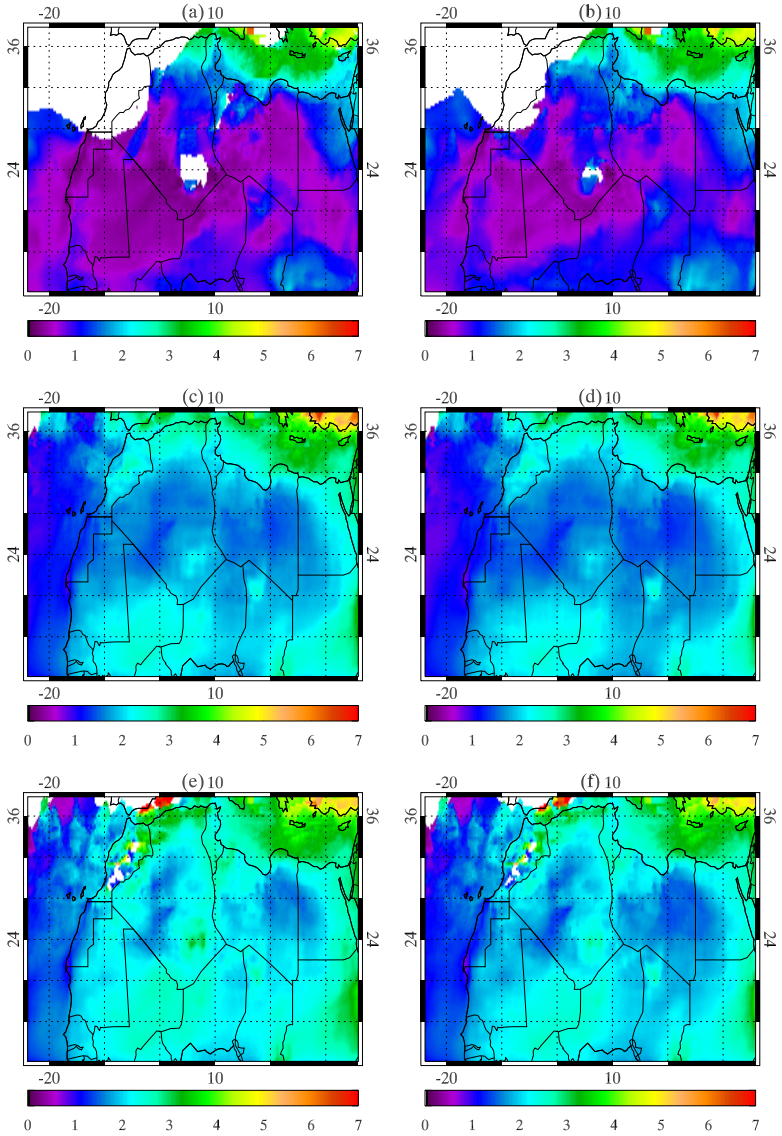

Figure 7.15: Plume height (km), March 2006, for the background model and the two assimilation schemes, and the two size distributions. On the left, $\bar{r}_{\text{clay}} = 1$ μm, and on the right, $\bar{r}_{\text{clay}} = 0.5$ μm.(a), (b): SHAMAL-high. (c), (d): SHAMAL-assim1. (e), (f): SHAMAL-assim6. White areas indicate where there are no observed plumes.

mean plume height ranges from 1.16 to 2.36 km. This compares favourably with observations from CALIPSO (from figure 5 of Vuolo et al. (2009)), which indicate that the typical height of dust occurrences in March (winter season) in the latitude range of ∼10-25 °N is between 1 and 2 km. In summer (June-September) the typical height between the latitudes of ∼10-30 °N is between 2 and 4 km, which also agrees well with the SHAMAL results for these months (2.42 to 3.24 km), as shown in table 5.5.

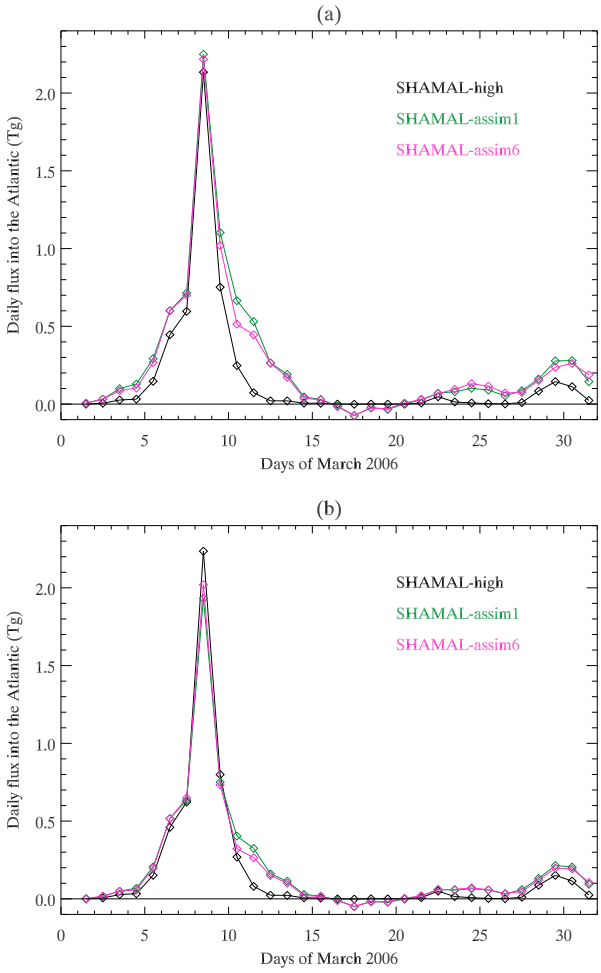

Figure 7.16: Daily dust flux into the Atlantic (Tg), during March 2006, for the background model and the two assimilation schemes. (a) $\bar{r}_{\text{clay}} = 1$ μm. (b) $\bar{r}_{\text{clay}} = 0.5$ μm.

7.3.4 Atlantic transport and deposition

The pattern of transport into the Atlantic is plotted in figure 7.16, for all six members of the model ensemble: it is immediately obvious that the days of the 5th-10th see the most transport into the Atlantic, which all members of the ensemble agree on. The total transport for the month is 6.37±1.33 Tg (where the uncertainty represents the spread of the ensemble model predictions). During March, the assimilation schemes do not increase the Atlantic transport substantially, the maximum increase from background to assimilation is from 4.96 to 8.18 Tg (table 7.2). There is even less difference in the predictions for transport on the 8th, at the peak. Generally the assimilation schemes increase the transport, though on the 8th they actually have a moderating effect on the model's over-prediction. The assimilation also broadens the duration of the 8th March

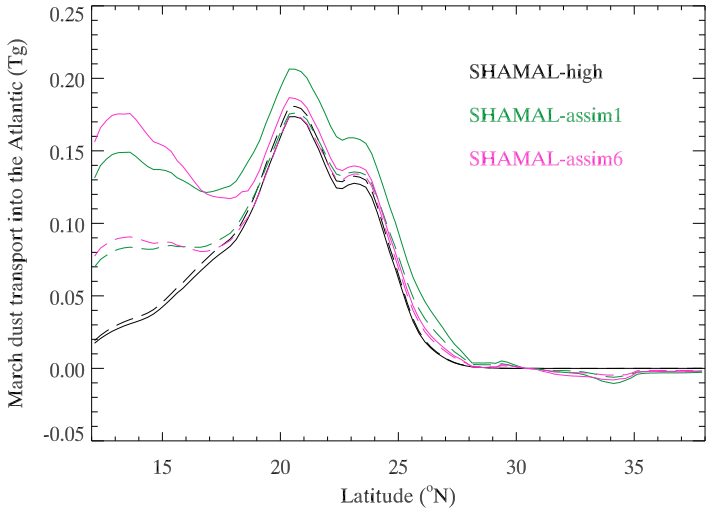

Figure 7.17: March 2006 dust flux into the Atlantic (Tg), across the 18 °W transect, for the six members of the model ensemble. Solid line: SHAMAL-r1. Dashed line- SHAMAL-r0.5.

event, so that dust is transported over a longer period, as late as the 13th (hence this widens the peak around the event). Assimilation also allows a noticeable quantity of dust to be transported back from the Atlantic to Africa: this occurs when the wind direction turns towards the coast, and there are sufficient quantities of dust still in the Atlantic atmosphere. This does occur in the background model, but the effect is much more pronounced in the assimilation experiments.

By latitude, dust transport is most concentrated at between 19 and 22 °N, along the Mauritanian and southern Western Saharan coasts. Figure 7.17 plots the dust transport as a function of latitude. In the background model, the transport peaks at ∼20.5 °N, and steadily drops off to the south. To the north, there is a much more rapid decrease in transport: north of 26 °N there is very little dust transport. There are two reasons for this: firstly, most of the dust sources and the transport pathways responsible for Atlantic transport are further to the south, over Mauritania and Western Sahara; secondly, the transect chosen for dust transport is 18 °W, which is just off the Mauritanian and Senegelese coast, much to the west of the Moroccan coast (hence most dust will be deposited in the oceanic and Moroccan source regions before the dust plumes reach the transect line). The north is also where most of the back-tracking occurs, where dust crosses east over the transect, since at this latitude the line is furthest from land.

The assimilation amplifies the model trend of latitude-dependent dust transport: in the south, the assimilation increases the transport, and in the north (north of 30 °N) the assimilation increases

the transport in the opposite direction. However, there is still very little dust transport in the north. Both assimilation schemes boost the transport in the far south (12-15 °N) along the Senegalese and Gambian coasts: this suggests that there should either be more emissions from southern sources (perhaps as far east as the Bodélé) or that the transport pathways should focus more dust to the south. Finally, the background model shows that there is a very slight increase in transport for SHAMAL-high-r0.5, since these particles are less susceptible to dry deposition. For the assimilation schemes however, SHAMAL-assim-r1 transports much more dust that SHAMAL-assim-r0.5, most noticeably in the south. This is further evidence evidence that SHAMAL-r1 is more sensitive to the assimilation process than SHAMAL-r0.5.

The total deposition into the Atlantic during the course of the month is mapped in figure 7.18, for the ensemble models. In total, there is 4.71±0.71 Tg of Atlantic deposition, across the ensemble. There is broad agreement amongst the background models about the geographical distribution, and amongst the assimilation models. Most of the dry deposition tends to take place over the subtropical north Atlantic, and there is good agreement between the background and the assimilation models on this, which helps to validate the model in this region, since it suggests that the model and the observations agree sufficiently in this region that the assimilation has little effect on the dust field. There is less agreement in the north however, where wet deposition becomes the dominant process. The observations suggest that there is much more dust in this region than does the model, hence there is more dust being deposited by precipitation scavenging in the assimilation (wet deposition is indicated by the frontal pattern in the background models and the spottiness of the pattern in the assimilation models). The magnitude of the difference in the North Atlantic compared to the subtropical north Atlantic is reduced in the assimilation models. Though the pattern in the increase is similar between the two assimilation schemes, it appears that in the North Atlantic there is less increase in the deposition when the sector-based errors approach is used. This suggests that SHAMAL-assim1 overestimates the model error in this region, and hence gives more emphasis to the observations than perhaps is justified. This is less important over the subtropical north Atlantic because here the modelled optical depths are much higher, and so the relative error is reduced, and the impact of the assimilation is correspondingly reduced. Finally, it can be seen that the deposition from the smaller clay size models is slightly less than that in the higher clay size models, since these particles are less susceptible to gravitational settling.

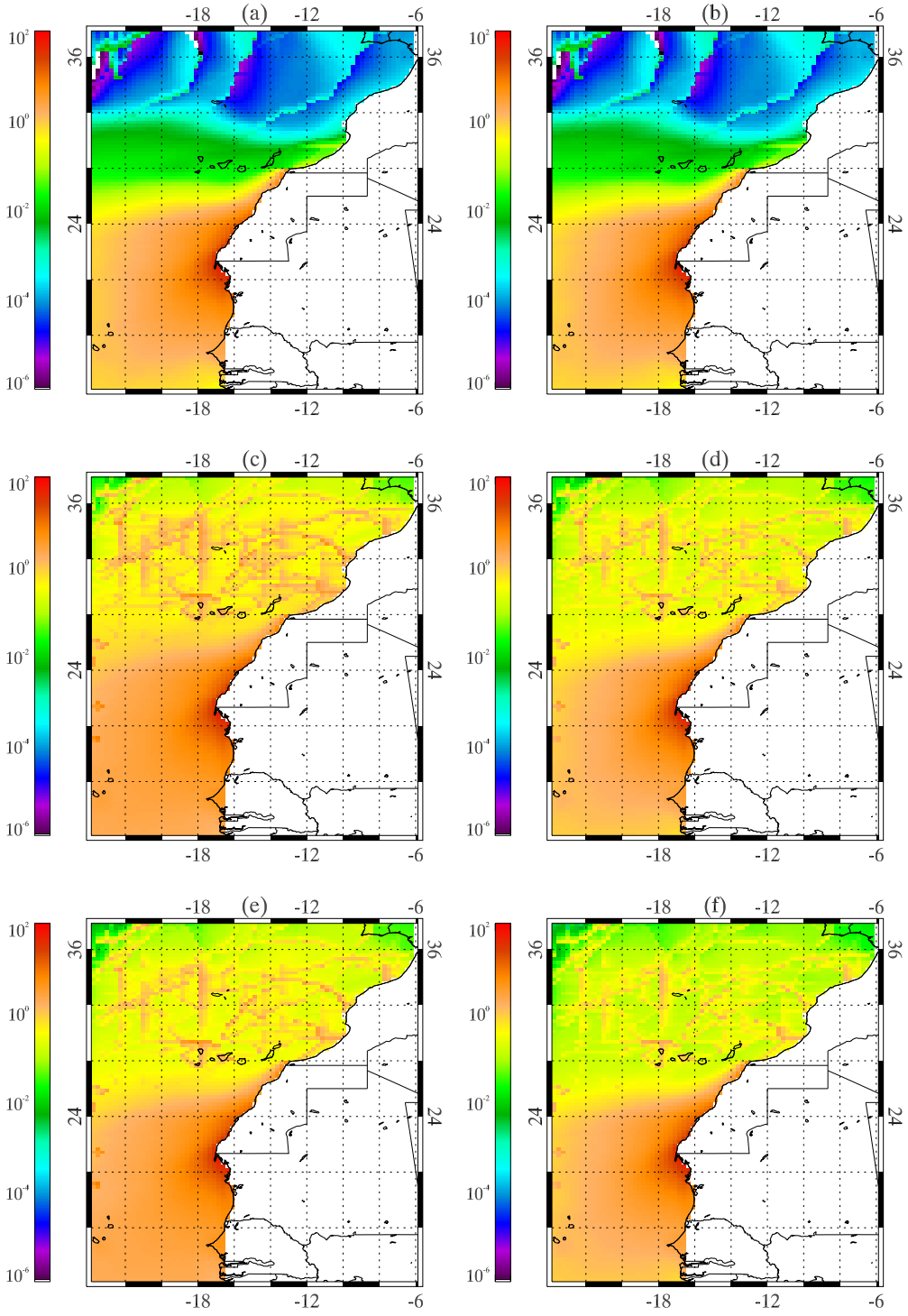

Figure 7.18: Atlantic deposition ($\mathrm{g\,m^{-2}\,month^{-1}}$), March 2006, for the background model and the two assimilation schemes, and the two size distributions. On the left, $\bar{r}_{\mathrm{clay}} = 1$ μm, and on the right, $\bar{r}_{\mathrm{clay}} = 0.5$ μm.(a), (b): SHAMAL-high. (c), (d): SHAMAL-assim1. (e), (f): SHAMAL-assim6. White indicate areas where the mean optical depth is less than 0.01.

7.4 The effect of data assimilation on the validation against AERONET

For the data assimilation scheme to be worthwhile, it must produce demonstrably better results compared to the background model. Again we compare the model output with AERONET data, to find the correlation. A problem to be aware of in this analysis is that the model uncertainty in the assimilation schemes is determined by comparison with AERONET, which is also used for validation. The DRI data is the data set used for the assimilation process (the observation values in the cost function analysis), and so this data set clearly cannot be used for validation: if we are allowing the background model to have some impact in the assimilation model, then the assimilation model would always be deficient if we regard the DRI data as our yardstick of the 'true' state of the atmosphere. Instead independent data (e.g. AERONET) should be used to validate the model results. Since the AERONET data are only used to estimate the model uncertainty, this is less of a problem; however, this still may produce a bias in the model, since if there is a significant difference between AERONET and SHAMAL, the model uncertainties will be high, and hence the assimilation will favour the DRI data (which are better correlated with AERONET than SHAMAL-high, see table 2.2). Though the effect may be minor, there may be a slight bias towards the AERONET data in the assimilation scheme, a possible artifact of a simple assimilation scheme which does not explicitly model the uncertainty.

Figures 7.19 and 7.20 plot time-series of the modelled optical depths for the ensemble against AERONET observations. Sites such as Blida, Ras El Ain, and Saada only have very weak signals (in both AERONET and model data), since there is very little significant dust activity. Lampedusa indicates a model predicted dust storm on the 19th (though there are no AERONET data), caused by dust source activation in northern Algeria on the 18th. In the north-east (Cairo EMA, Saada, and also Nes Ziona) the models generally over-predict compared to AERONET. However, the models (even the background models) predict very well the timings of dust events (such as on the 8th and the 13th), especially over Cairo EMA, which has more data. This is also true of Santa Cruz Tenerife, where the models and the AERONET agree on the timing of the 8th March event. Sahel and subtropical north Atlantic sites (Agoufou, Banizoumbou, DMN Maine Soroa, IER Cinzana, Capo Verde and Dakar) all show that the background model strongly under-predicts compared to AERONET, whereas the assimilation versions produce a much better fit to the data; only during the 8th March event are the assimilation models much lower than the observations. Over the Sahel

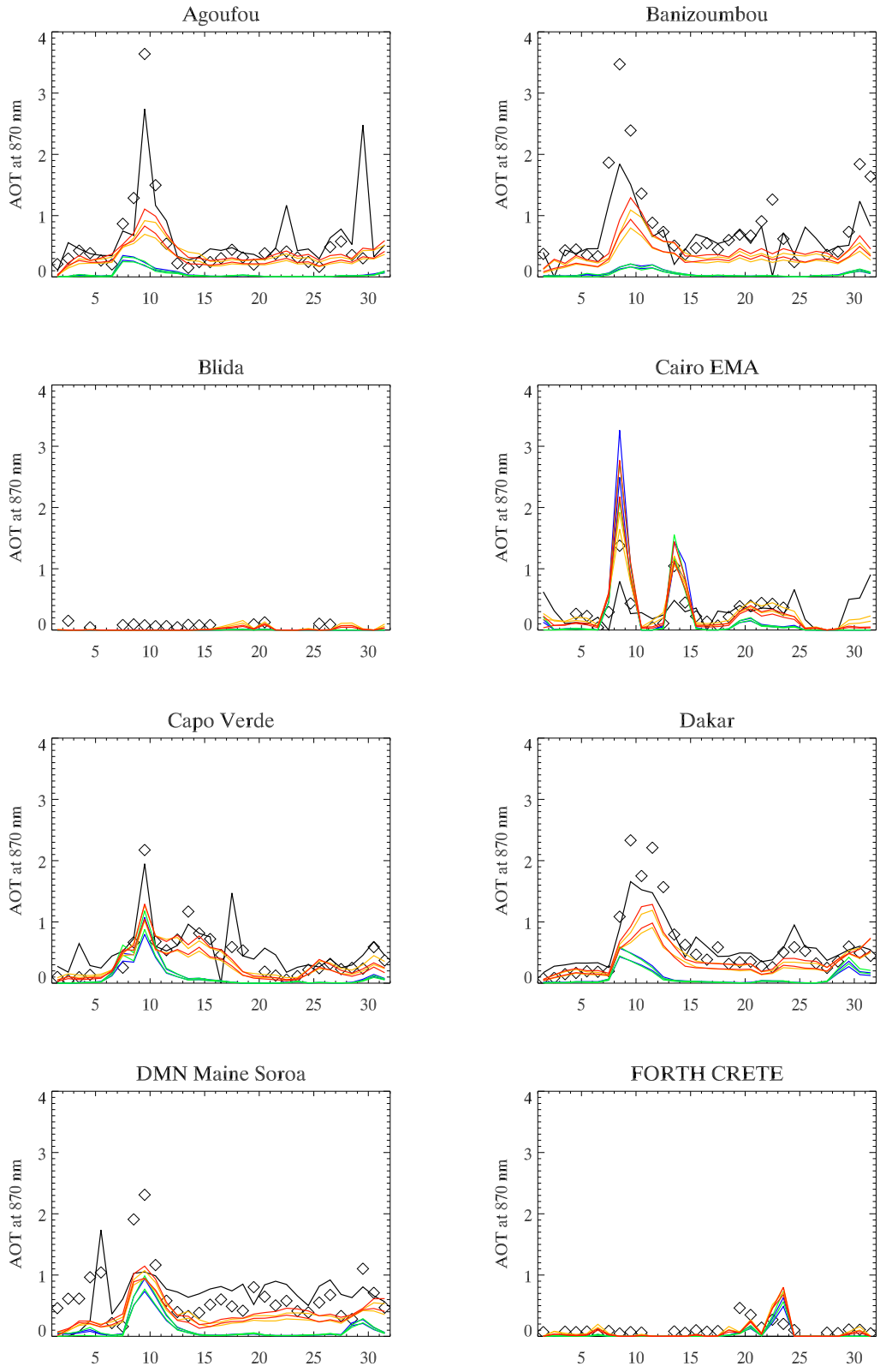

Figure 7.19: Daily averaged optical depth (at 870 nm), for eight AERONET sites, March 2006. Black diamonds: AERONET. Black line: DRI. Blue: SHAMAL-low. Green: SHAMAL-high. Orange: SHAMAL-assim1. Red: SHAMAL-assim6.

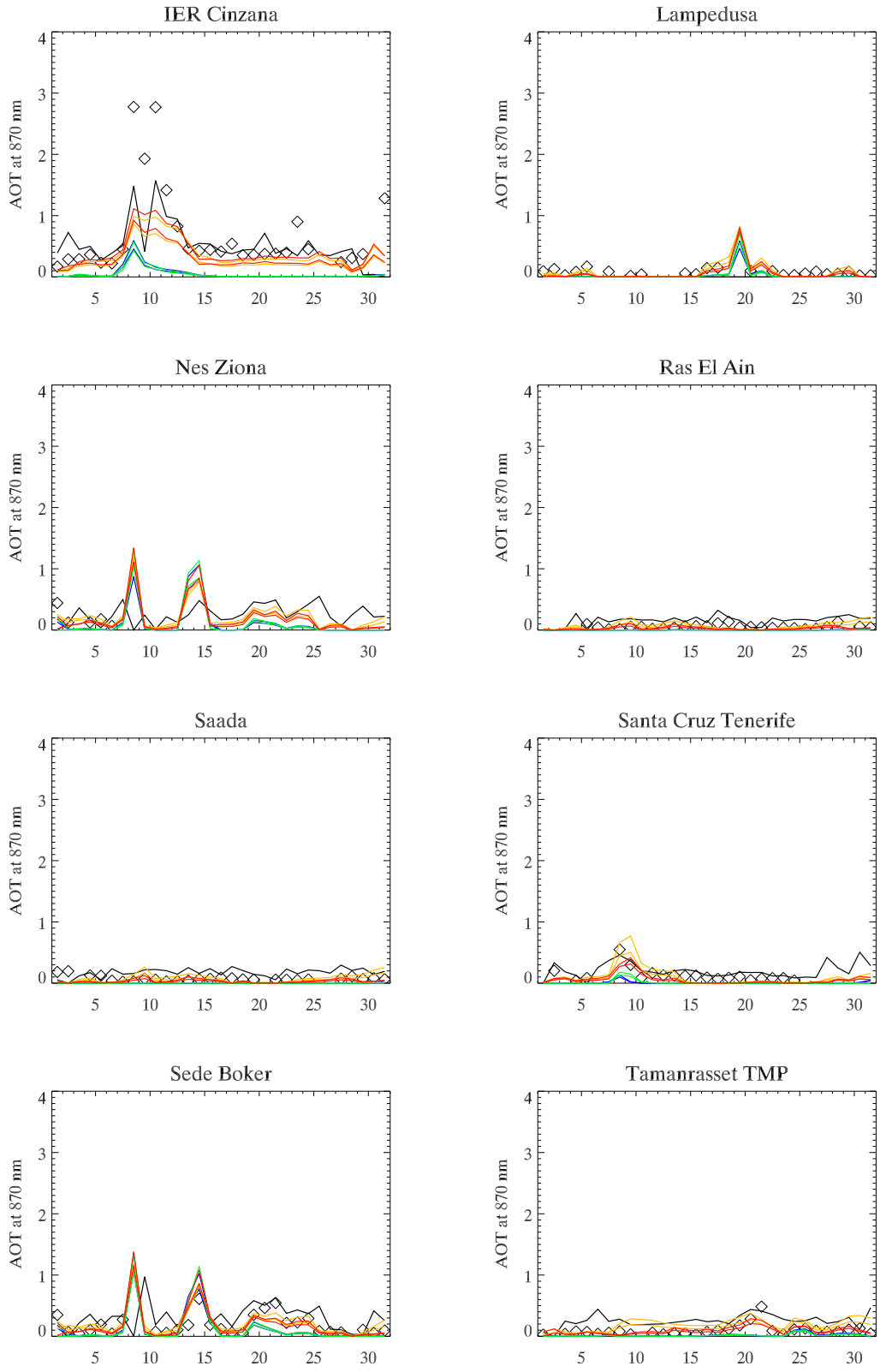

Figure 7.20: As figure 7.19. There is no available AERONET data for El Arenosillo, Niamey, Ouagadougou, or Ouarzazate. There are only three days of AERONET data for IMS-Metu-Erdemli, so this site has also been ignored.

sites the assimilation is particularly important, since the model may well be missing dust sources in this region.

The correlations between SHAMAL and AERONET during March 2006 are shown in table 7.3. The correlations vary significantly from site to site, and the most relevant comparisons that can be made are between the ensemble model output for each site. Across many of the sites in the Sahel, and the North Atlantic (e.g. Agoufou, Ras El Ain) the effect of the assimilation is quite unconvincing, with the correlation actually *decreasing*. Meanwhile over the two subtropical north Atlantic sites, most of the Mediterranean sites, and especially Tamanrasset in the central Sahara, the correlation is increased. The reason for the decrease in correlation in several of the sites, despite the fact that the magnitude of the optical depth shows better agreement, is that the temporal pattern is different. Consider the case of Agoufou: the baseline of SHAMAL-assim matches very well with the baseline of the AERONET data, but the peaks are often out of phase with each other (except on the 9th); though the pattern has not changed from the background model, there is more of a signal in the assimilated version, so this has more of an impact to degrade the correlation. Meanwhile over Capo Verde, the model more closely follows the temporal pattern of the AERONET observations. Across the domain, a weighted mean of the correlations indicates only a slight increase in the correlation from SHAMAL-high to SHAMAL-assim.

A more convincing improvement in the model quality due to the assimilation is revealed in table 7.4, which presents the RMS differences between the model and AERONET. Over almost all of the sites there is a clear decrease in the RMS difference (especially Agoufou, Banizoumbou, Capo Verde, Dakar and IER Cinzana), indicating that the magnitudes of the model and AERONET have been made more consistent by the assimilation. The domain RMS differences are most sensitive to the sites where there is the largest signal (since the RMS focuses on the square of the difference), and so the domain RMS differences are also decreased substantially (from an average of 0.497 amongst the background models, to an average of 0.334 amongst the assimilation models).

Due to the effect of the assimilation scheme on the model, we would expect that the model shows the highest correlation with the AERONET data in the early afternoon, at which time the model bias is minimised. Figure 7.21 plots the domain monthly averaged correlations and RMS differences between the model and AERONET over the course of the day. Immediately it is clear that the background model has a lower correlation than the assimilation schemes. Note also that the difference in correlations between the different schemes is much more substantial than the differences in correlation between the output for the different size distributions. For

	SHAMAL-low		SHAMAL-high		SHAMAL-assim1		SHAMAL-assim6	
Site name	-r1	-r0.5	-r1	-r0.5	-r1	-r0.5	-r1	-r0.5
Agoufou	0.74	0.74	0.75	0.76	0.61	0.70	0.67	0.75
Banizoumbou	0.70	0.68	0.73	0.71	0.61	0.67	0.68	0.72
Blida	0.31	0.31	0.30	0.31	0.31	0.30	0.30	0.30
Cairo EMA	0.80	0.80	0.79	0.79	0.84	0.80	0.84	0.82
Capo Verde	0.74	0.74	0.72	0.72	0.80	0.86	0.80	0.87
Dakar	0.64	0.65	0.56	0.57	0.85	0.87	0.85	0.87
DMN Maine Soroa	0.75	0.75	0.75	0.76	0.62	0.72	0.61	0.71
Forth Crete	0.48	0.48	0.42	0.42	0.38	0.40	0.40	0.41
IER Cinzana	0.81	0.81	0.83	0.83	0.81	0.86	0.83	0.87
IMS-Metu-Erdemli	0.99	0.99	0.98	0.98	0.99	0.99	0.99	0.999
Lampedusa	0.43	0.43	0.45	0.48	0.59	0.59	0.52	0.55
Nes Ziona	0.97	0.97	-0.46	0.97	-0.72	0.95	-0.69	0.97
Ras El Ain	0.22	0.22	0.14	0.13	0.00	0.02	0.02	0.04
Saada	0.11	0.10	0.06	0.05	-0.11	-0.09	-0.10	-0.09
Santa Cruz Tenerife	0.85	0.85	0.61	0.61	0.59	0.60	0.58	0.60
Sede Boker	0.58	0.58	0.60	0.63	0.67	0.74	0.70	0.70
Tamanrasset TMP	0.13	0.14	0.15	0.16	0.45	0.46	0.72	0.69
Domain	0.56	0.56	0.53	0.54	0.55	0.59	0.58	0.62

Table 7.3: Correlations between AERONET sites and the eight members of the model ensemble, for March 2006. The correlations for IMS-Metu Erdemli and Nes Ziona cannot be regarded as significant, since there are so few AERONET data points. The 'domain' value is a weighted mean of the correlations for all of the individual sites.

	SHAMAL-low		SHAMAL-high		SHAMAL-assim1		SHAMAL-assim6	
Site name	-r1	-r0.5	-r1	-r0.5	-r1	-r0.5	-r1	-r0.5
Agoufou	0.535	0.523	0.537	0.524	0.335	0.368	0.313	0.347
Banizoumbou	0.962	0.948	0.965	0.947	0.655	0.733	0.601	0.690
Blida	0.083	0.083	0.083	0.083	0.079	0.079	0.079	0.080
Cairo EMA	0.332	0.457	0.327	0.438	0.212	0.279	0.243	0.364
Capo Verde	0.468	0.431	0.463	0.428	0.248	0.285	0.248	0.276
Dakar	0.698	0.669	0.702	0.675	0.370	0.454	0.348	0.436
DMN Maine Soroa	0.625	0.589	0.625	0.580	0.428	0.461	0.414	0.448
Forth Crete	0.189	0.185	0.191	0.188	0.175	0.177	0.176	0.179
IER Cinzana	0.787	0.763	0.792	0.766	0.498	0.568	0.464	0.542
IMS-Metu-Erdemli	0.158	0.156	0.161	0.154	0.123	0.134	0.142	0.144
Lampedusa	0.085	0.084	0.086	0.085	0.065	0.059	0.064	0.068
Nes Ziona	0.174	0.140	0.276	0.117	0.261	0.077	0.260	0.085
Ras El Ain	0.061	0.061	0.061	0.061	0.097	0.062	0.054	0.049
Saada	0.075	0.075	0.076	0.075	0.111	0.070	0.061	0.060
Santa Cruz Tenerife	0.204	0.196	0.197	0.188	0.252	0.175	0.157	0.160
Sede Boker	0.198	0.203	0.204	0.199	0.147	0.129	0.145	0.155
Tamanrasset TMP	0.126	0.124	0.128	0.125	0.129	0.094	0.066	0.073
Domain	0.502	0.491	0.504	0.490	0.324	0.360	0.301	0.349

Table 7.4: RMS differences between AERONET sites and the eight members of the model ensemble, for March 2006.

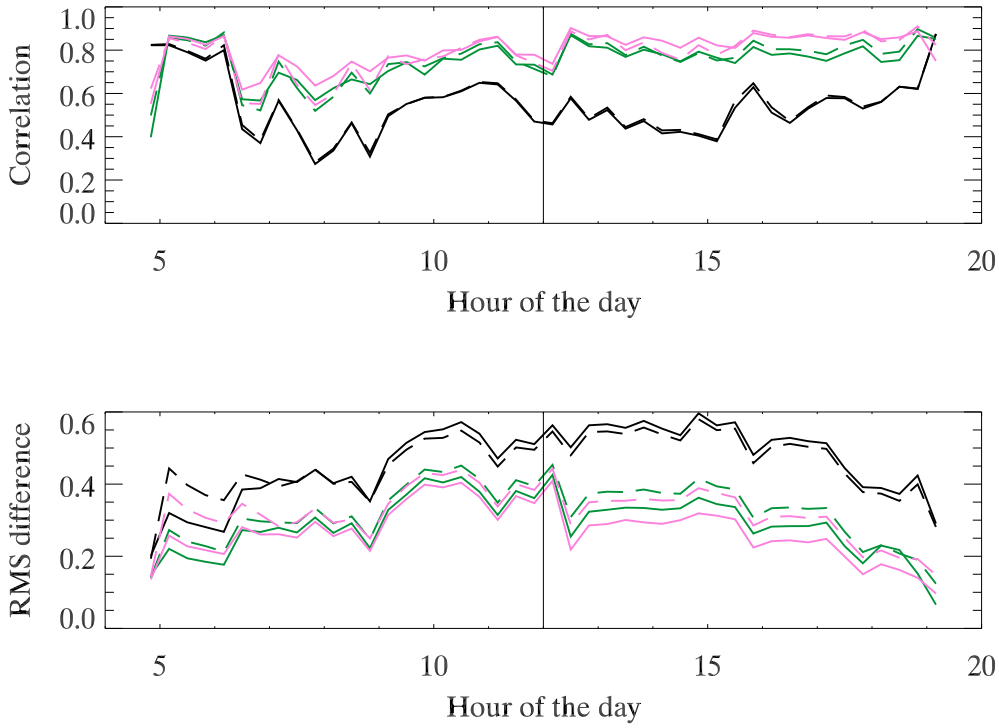

Figure 7.21: Mean correlation and RMS differences between AERONET and SHAMAL, on the diurnal cycle. Black line- SHAMAL-high; green line- SHAMAL-assim1; pink line- SHAMAL-assim6. Both size distributions are included (solid line: SHAMAL-r1; dashed line: SHAMAL-r0.5). There are no observations at night, so correlations can only be made between 0450 and 1910 (the spikes in correlation at the beginning and end of the day are artifacts caused by the small number of AERONET data points at times when the Sun is often below the horizon).

SHAMAL-high, the averaged correlation is 0.56 in the morning and 0.53 in the afternoon, so the model performs slightly less well in the afternoon. The difference between the two halves of the day is more pronounced in the assimilation schemes: in the morning it is 0.71 for SHAMAL-assim1 and 0.74 for SHAMAL-assim6, whereas in the afternoon it is 0.80 and 0.84. This is a noticeable increase, but the background model is still essential to these results: note that for all six versions of the model (background and assimilation), the correlation spikes at ∼12.30 pm (this spike may either be an artifact of the available AERONET data, or there is a particularly strong dust event that occurs at this time, on one or more days), with a corresponding drop in the RMS differences. Moreover, the agreement in shape between the background and the assimilation model shows that the assimilation only increases the *magnitude* of the correlation, but does not significantly affect the *pattern* of the dust activity.

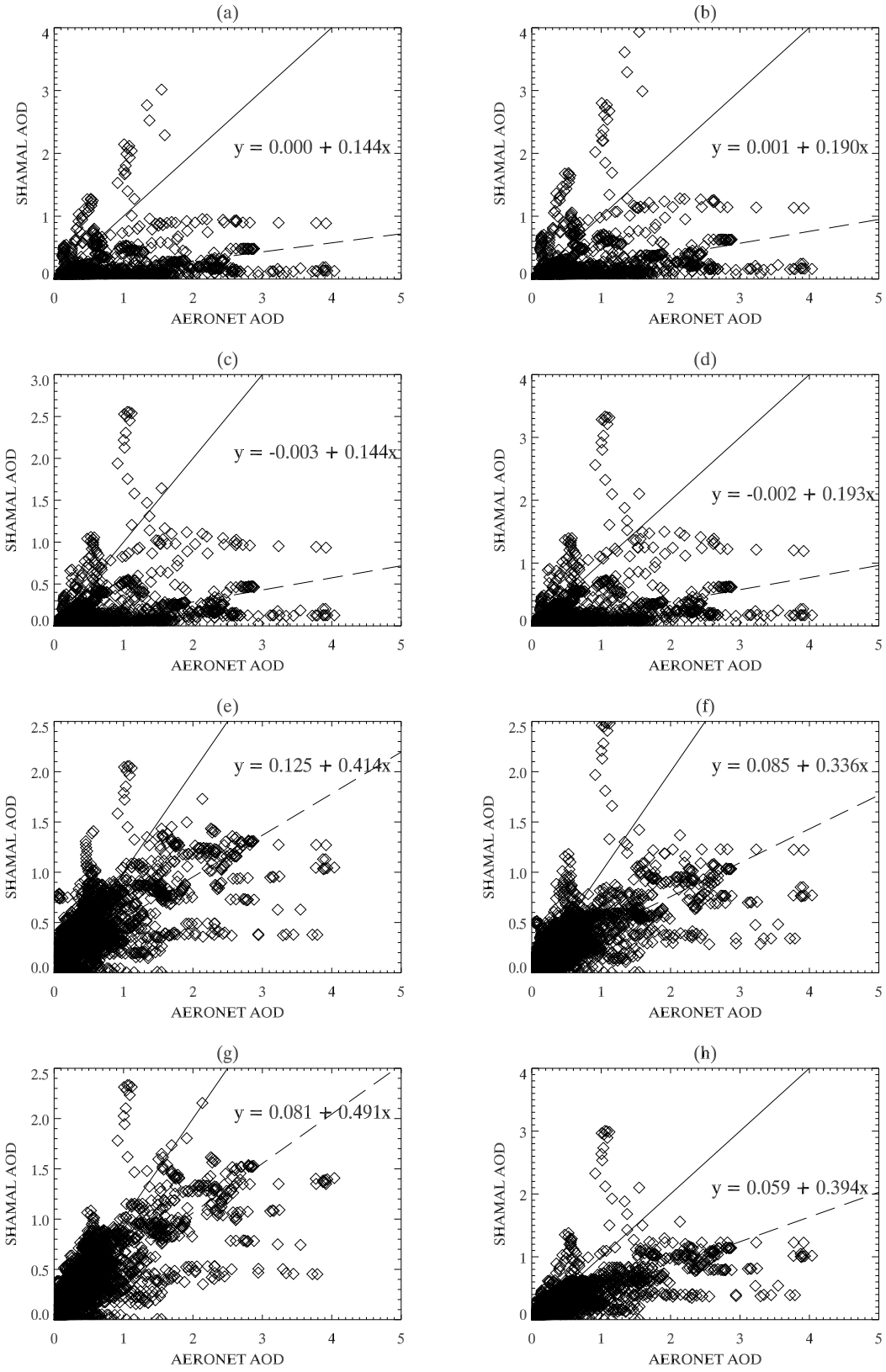

Figure 7.22: Comparisons between SHAMAL output AOD and AERONET AOD (at 870 nm), March 2006, for the background model and the two assimilation schemes, and the two size distributions. On the left, $\bar{r}_{\text{clay}} = 1$ μm, and on the right, $\bar{r}_{\text{clay}} = 0.5$ μm.(a), (b): SHAMAL-low. (c), (d): SHAMAL-high. (e), (f): SHAMAL-assim1. (g), (h): SHAMAL-assim6. The dashed line shows the fit to the comparison.

Direct comparisons between the SHAMAL output AOD and the AERONET observations are presented in figure 7.22, which shows the improvement in the comparisons produced by the assimilation schemes. Note the large number of points near the x-axis in the background versions (and the shallowness of the gradient of the fit): these indicate where SHAMAL substantially underpredicts compared to the AERONET observations. In the assimilation versions, many of these have been raised, so the gradient of the fit is rather higher. On this metric, SHAMAL-assim6-r1 performs the best, with a gradient of 0.491.

By region (figure 7.23), it is generally the case that the assimilation increases the agreement between the model and AERONET, and that the approach that uses the six sectors does provide a (slight) improvement in the predictions. Agreement is best over the South-East Mediterranean, but there is also good agreement for the Atlantic regions. The agreement is excellent over the North-East Mediterranean, except for a handful of outliers (where the model substantially underpredicts compared to AERONET) which skew the fit.

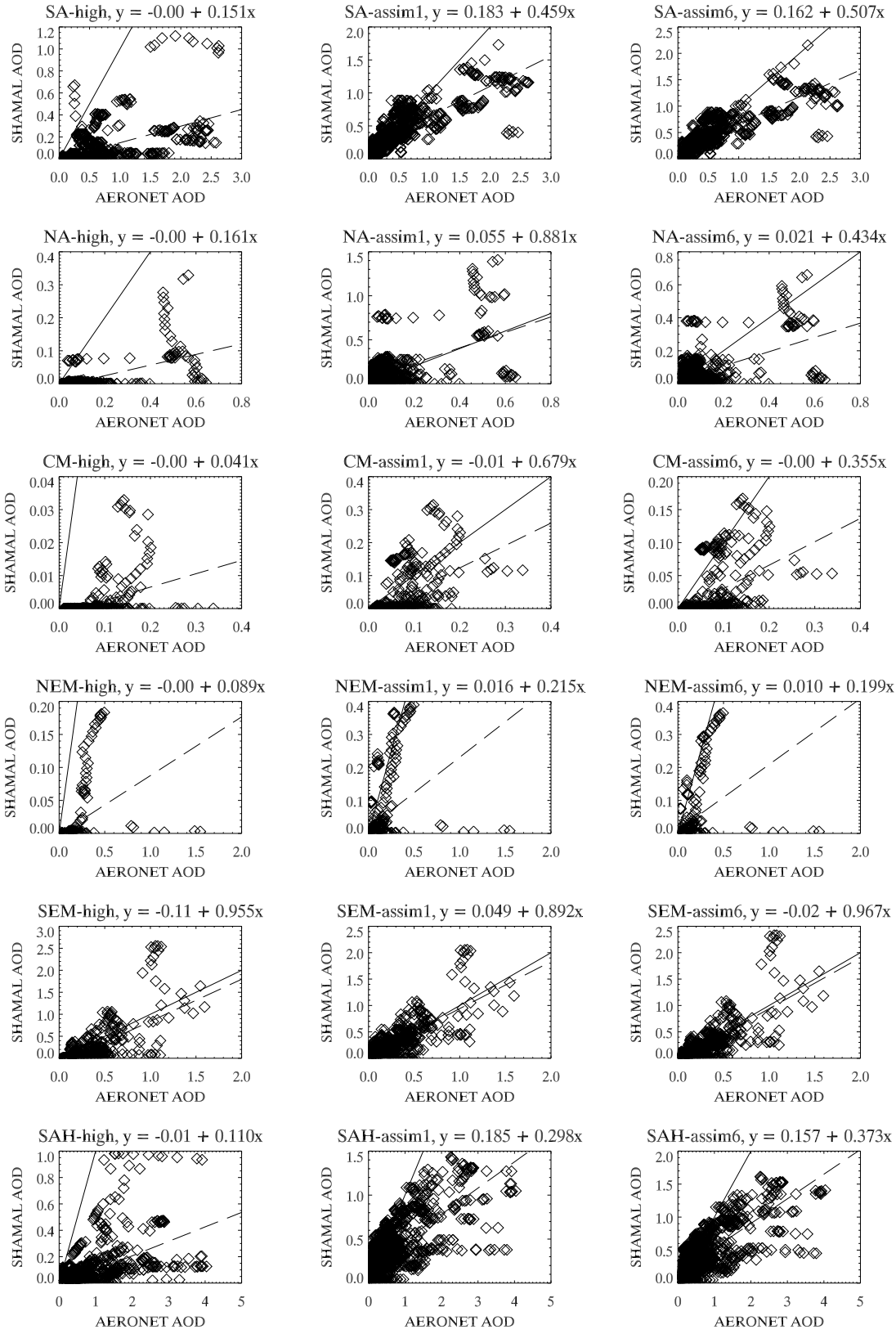

Figure 7.23: Comparisons between SHAMAL output AOD and AERONET AOD (at 870 nm), March 2006, for the background model and the two assimilation schemes ($\bar{r}_{\rm clay} = 1$ μm), over the six sectors of the domain. SA: subtropical north Atlantic; NA: North Atlantic; CM: Central Mediterranean; NEM: North-East Mediterranean; SEM: South-East Mediterranean; SAH: Sahara. The dashed line shows the fit to the comparison.

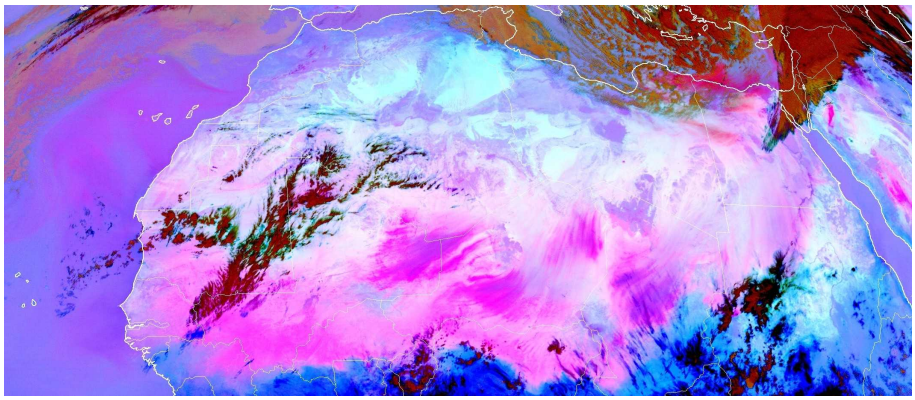

Figure 7.24: MSG-SEVIRI false-colour image of North Africa, from 1200 on 8/3/2006. Pink denotes dust, while red denotes thick high-level cloud, and brown and green denote mid-level clouds. Image courtesy of EUMETSAT [http://oiswww.eumetsat.org/WEBOPS/iotm/iotm/20060308_dust/20060308_ dust.html, last accessed 11/1/2010].

7.5 The 8th March 2006 dust event: anatomy of a dust storm

The modelled results from March 2006 (section 7.3) indicate the dominance of the 8th March event; this section will look into that event in more detail, describing how an example of a dust storm forms and evolves. Figure 7.24 shows a SEVIRI image of North African dust activity at noon on the 8th. Note how extensive the dust activity is, with thick dust plumes across Mauritania, Mali, southern Algeria, Niger, Chad, Libya and Egypt, and descending across Senegal, Burkina Faso, Nigeria, and Sudan. Compare with figure 7.1, where there are just one or two dust plumes, which is a more typical day.

This section will describe the chronology of the event in detail, from the initial storm development on the 5th to the end of the storm on the 9th.

7.5.1 Origins: the 5th-6th March

While the storm only starts to become particularly active on the 6th, the beginning of the event can be tracked back to the 5th, when a front from the Atlantic crossed over the Atlas mountains to the northern Algerian Sahara, instigating moderate dust emissions (1-10 $\mathrm{g\,m^{-2}\,day^{-1}}$) over the Grand Erg Occidental (near the Moroccan border) and the Grand Erg Oriental (near the Tunisian border). Daily emissions are mapped in figure 7.25. This source region for the 8th March event is well attested to in the literature (Slingo et al., 2006). Between these regions is a rocky hamada,

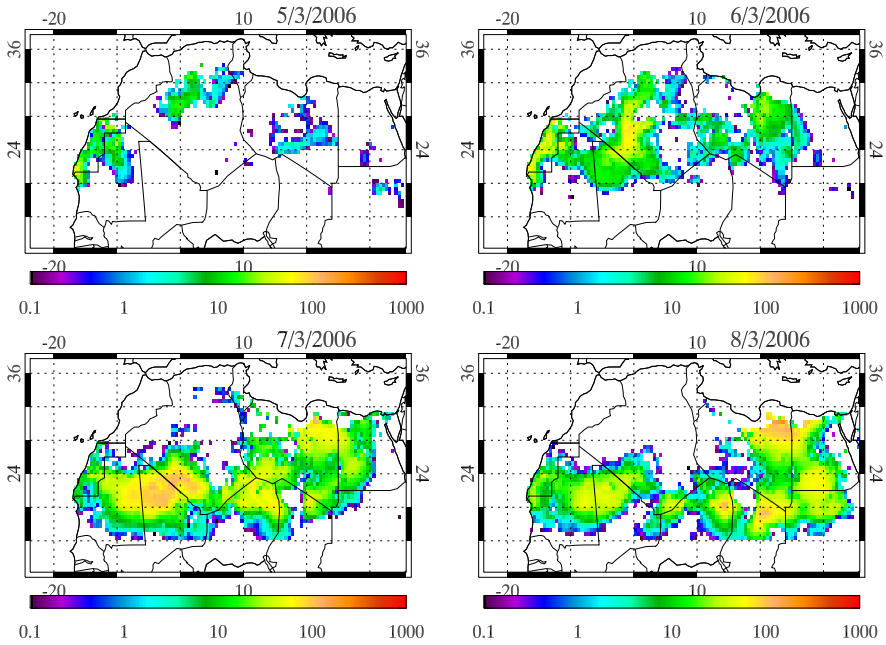

Figure 7.25: Daily emission ($\mathrm{g\,m^{-2}\,day^{-1}}$), SHAMAL-high-r1, for the 5th-8th March.

which is never susceptible to dust emission. Similarly extensive dust activity is also occurring at this time over Western Sahara and northern Mauritania. Figure 7.26 shows why: there are particularly strong winds over the south-western Mediterranean, pressing into northern Algeria, while a related wind system is pushing down the West African coast, cutting inland over Western Sahara.

On the 6th the dust sources are becoming rather more widespread and intense. The sources of the 5th remain active, but two new regions open up. The Algerian dust storm is being driven to the south, extending as far south as northern Mali, but is especially intense over Erg Chech in south-western Algeria. As the dust storm propagates southwards, not only does it emit fresh dust from the surface, but it retains substantial quantities of dust in the atmosphere from the more northerly sources. The other new source region is north-eastern Libya, which shows moderately strong emission (as much as $\sim$40 $\mathrm{g\,m^{-2}\,day^{-1}}$). By the end of the day, this event has become a moderately sized dust storm.

The weather system has now split into two. Originally the system was blown through the Straits of Gibraltar from the Atlantic, but it was split by the Algerian Atlas mountains (since the storm approached the mountain range end-on): the more intense storm headed westwards over the Mediterranean (causing precipitation as it moves, see figure 7.27), while the other, drier, front blew

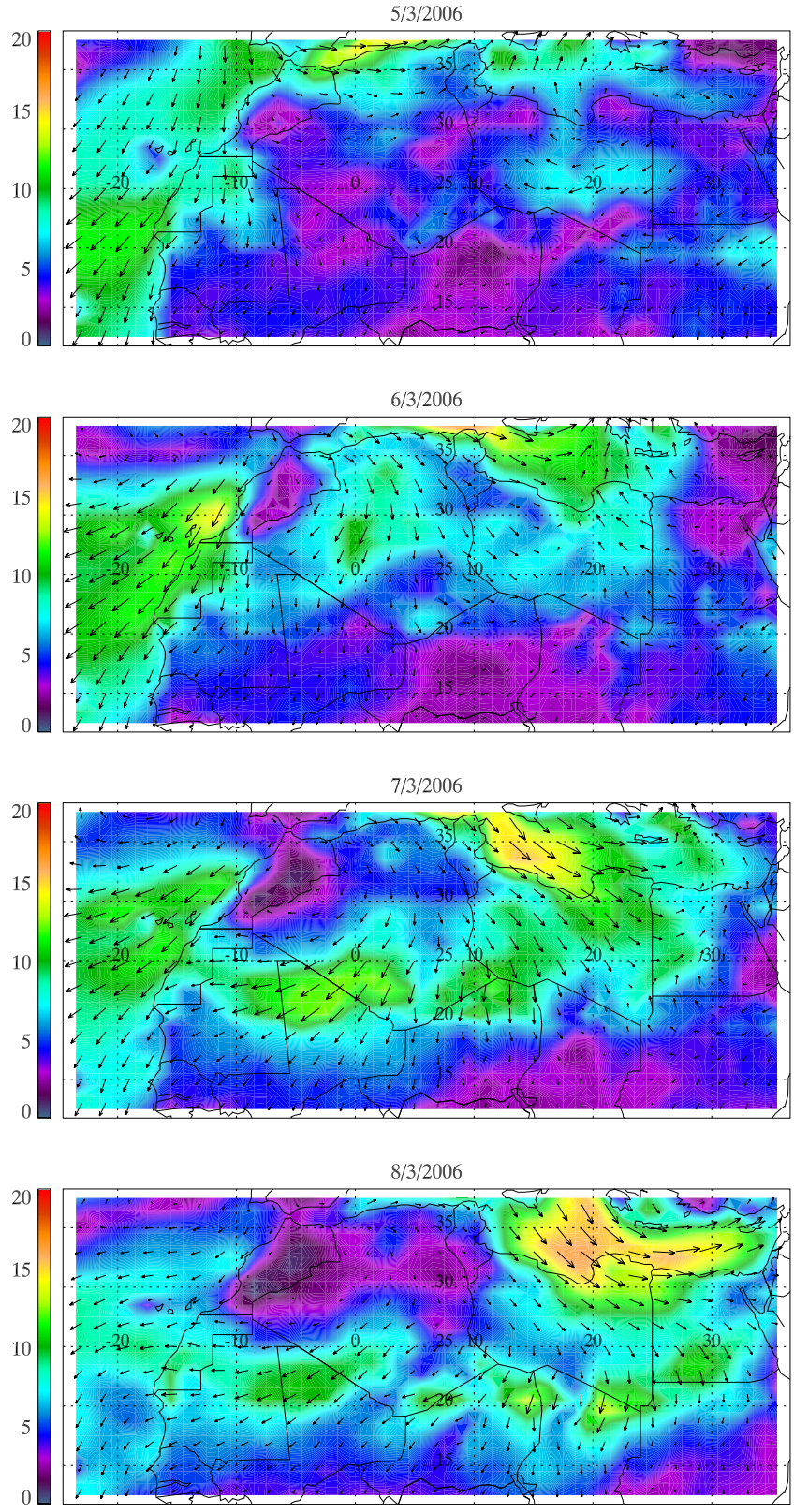

Figure 7.26: Mean daily surface wind speeds ($\mathrm{m\,s^{-1}}$), 5th-9th March.

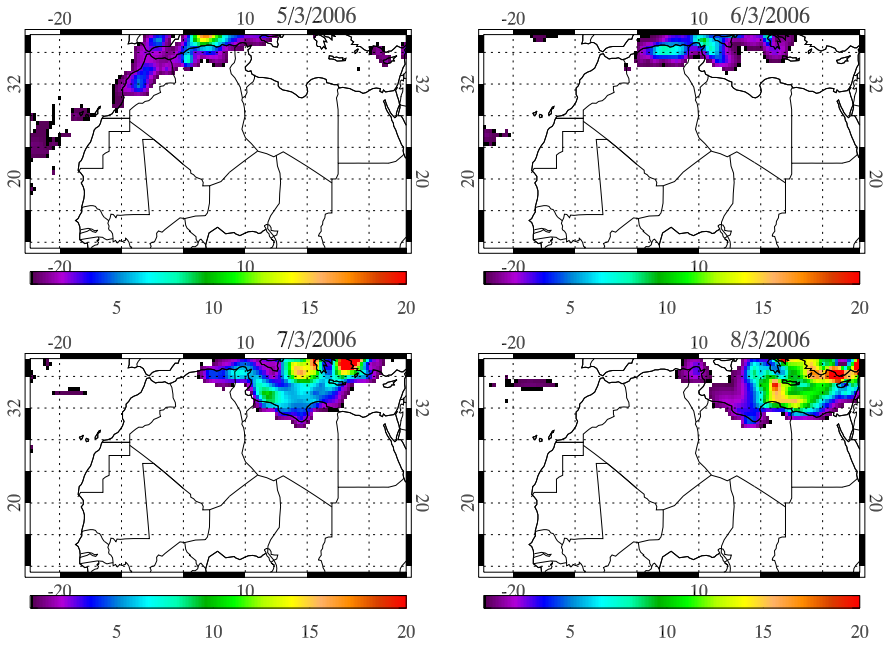

Figure 7.27: Total daily precipitation (mm), for the 5th-8th March. White refers to regions with less than 0.5 mm of rain.

southwards over Algeria. This front itself then starts to develop two distinct trajectories, heading southwards towards Mali, and south-eastwards across western Libya.

7.5.2 Growth: the 7th March

During the 7th, the event develops into a substantial dust storm. Dust sources have become much more widespread, and much more intense. While the original northern Algerian sources have faded, there is now a large swathe across the Erg Chech in south-western Algeria, northern Mali, and north-eastern Mauritania where the emissions reach 100 $\mathrm{g\,m^{-2}\,day^{-1}}$. The winds have been picking up speed as they head south and westwards. Sources in northern Niger are also activated (about 40-80 $\mathrm{g\,m^{-2}\,day^{-1}}$) by the winds from the middle system as they turn southwards, as is a much more extensive area of the Great Sand Sea (over eastern Libya and western Egypt). Over eastern Libya, the region is starting to be subjected to the full force of the front tracking its way eastwards across the Mediterranean (and entering eastern Libya through the Gulf of Sirte), bringing surface wind speeds of over 10 $\mathrm{m\,s^{-1}}$ across the source regions.

The magnitude of the increase in emissions from the 6th to the 7th is shown in figure 7.28. As the dust storm develops, the magnitude of the emission increases, and also the distribution shifts towards higher wind speeds (on the 5th the peak is at 10.25 $\mathrm{m\,s^{-1}}$, while on the 7th it is at 11.75

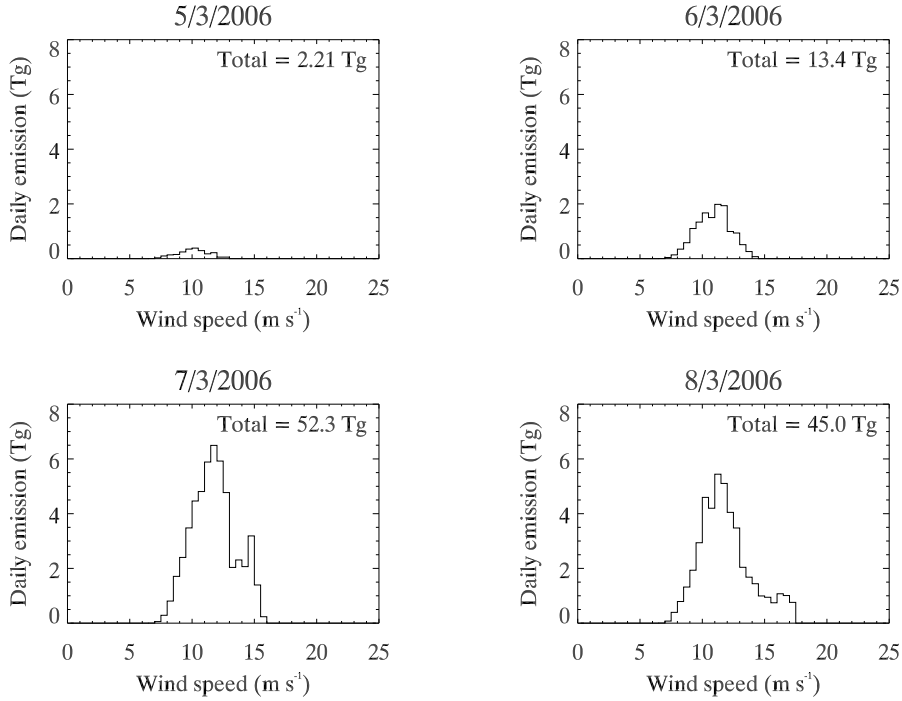

Figure 7.28: Daily emission (Tg), for the 5th-8th March, as a function of wind speed. The total for these four days is 112.97 Tg, 66.5% of the total for March 2006.

$\mathrm{m\,s^{-1}}$), which is a result of the increasing wind speeds over Mauritania and Libya.

Maps of dust optical depth for this day (figure 7.29) indicate just how thick and concentrated is the atmospheric dust loading. This is most concentrated over northern Mali and northern Mauritania, where the optical depths peak at 3.99: this storm is starting to curve to the south-west, following the winds. The picture over West Africa is complicated by a bank of mid- to high-level cloud (still present on the 8th) stretching from Algerian/Malian border across southern Mauritania towards Senegal. This is shown in the DRI data (2nd column, 3rd row) as a region of missing data, since cloud can block the retrieval of dust aerosol. Hence it is not possible to directly validate the intensity of the dust storm at its strongest, because the modelled peak is underneath a cloud layer, over a region with no AERONET sites; indirect comparisons can be made however, with the DRI data at the outliers of the storm, and with downwind AERONET sites such as IER Cinzana, Dakar, and Capo Verde (for the following day).

Comparisons with DRI show that there is good agreement between the modelled peaks of dust storm activity, and the peaks in the DRI data. The bulk pattern of the modelled dust storm is consistent with the DRI observations. On the 7th there is agreement on the three dust areas: West

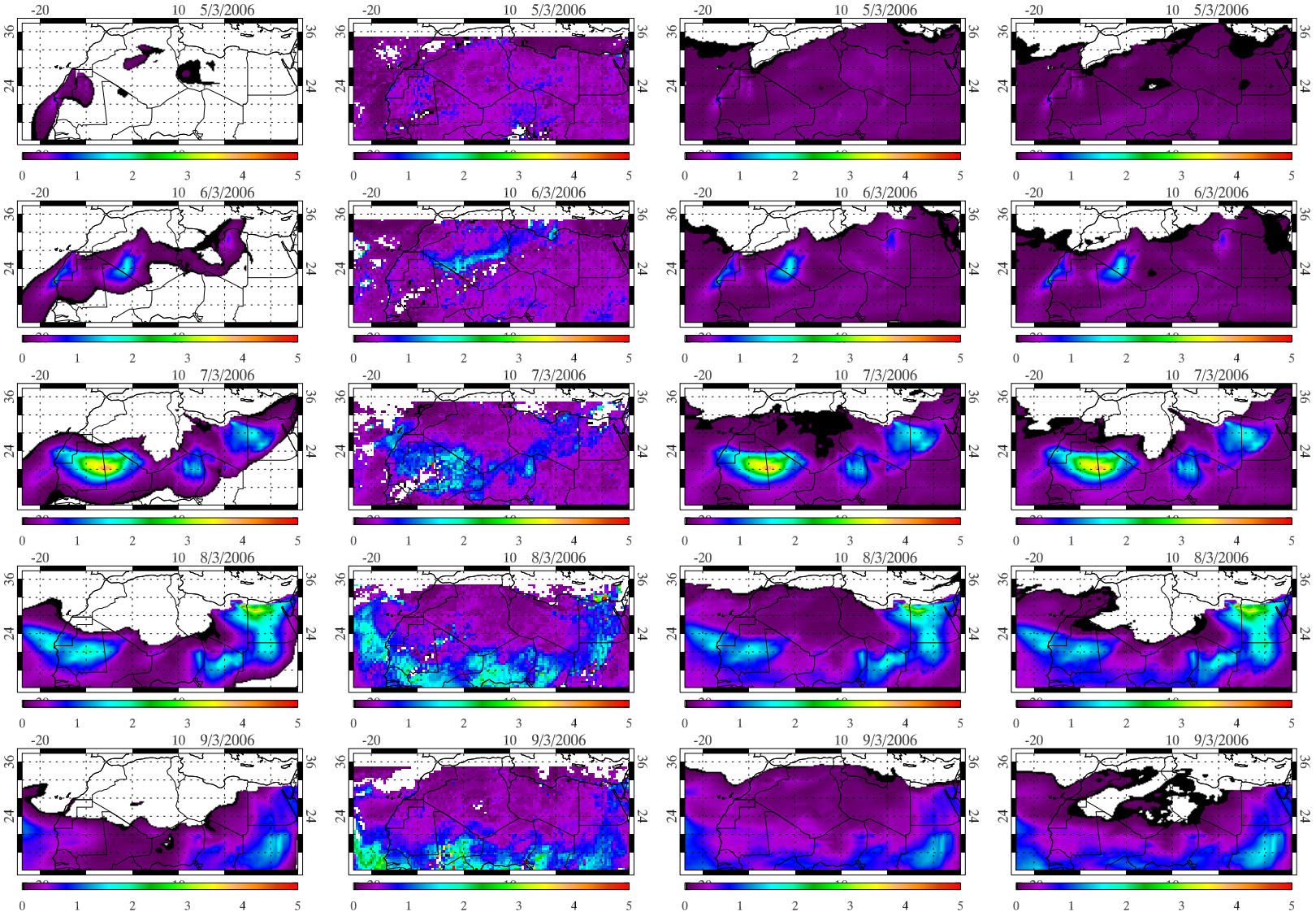

Figure 7.29: Mean daily AOD, 5th-9th March, for SHAMAL-r1. Column 1 (first from left): SHAMAL-high. Column 2: DRI. Column 3: SHAMAL-assim1. Column 4: SHAMAL-assim6.

Africa, the Nigerien/Chadian border, and over north-eastern Libya. There are five main points of disagreement.

(1) DRI data have a higher background level of dust aerosol: in most regions there is a thin haze of ambient dust observed. The fact that there is such a uniform haze may perhaps indicate a bias in the DRI observations, since the AOD is not significantly different over land and over ocean (whereas we would expect a rather higher dust loading/AOD over land). There could be possible interference from sea salt aerosol over the oceans, for example. Figure 7.20 indicates that AERONET data in some remote regions, e.g. Ras El Ain, Saada, Santa Cruz Tenerife, show rather closer agreement with the model (AOD < 0.2) than with DRI (AOD $\sim$ 0.3-0.4). This ambient haze is carried through into the assimilation models, since the higher DRI signal dominates over most of the domain. Only over the modelled dust storms do the assimilation models maintain fidelity with the background model.

(2) The DRI observations contain missing data, which either indicates the presence of clouds or the absence of any (reliable) satellite observations.

(3) Modelled dust storms are more continuous than the observed dust storms (which show more spatial variability at smaller scales). The homogeneity of the modelled storms is a consequence of the Eulerian grid modelling scheme, where the 0.25° resolution can often be larger than the spatial scale of some dust processes (e.g. emission).

(4) The DRI observations suggest that there are more dust sources and storms: for example, on the 8th, both the DRI and the model indicate the presence of dust storms over Mauritania, Chad, and Egypt; DRI data also indicate the presence of a dust storm over western Niger (presumably locally sourced, or from southern Algeria), which is not picked up by the model. Note that while this storm is very faint in the modelled AOD, it is much more noticeable in the modelled deposition (as will be presented in figure 7.31).

(5) There are differences in the magnitude of the major dust storms: often, the model over-predicts with respect to DRI.

The assimilation models tend to do one of two things, depending on the intensity of the modelled dust storm: where the model output is very low, the assimilation nudges the AOD up (to $\sim$0.2) due to the ambient dust observed in the DRI data, and where there is a substantial dust event (which may be over-predicted), the assimilation may help to moderate the predictions. In more specialised circumstances however, the assimilation models can exhibit more interesting behaviour. One example is the dust episode over the Great Sand Sea on the 7th, where the spatial extent of

the dust storm was increased by the assimilation, adding an extra tendril which crosses the border into Chad: here, the background model had been too conservative. Similarly on the 8th and the 9th, when dust storm activity crossed most of the Sahel, the assimilation raised the model from a conservative estimate of the AOD of ∼0.3 to more consistent values of a diffuse dust storm of over 1. Meanwhile there are also some minor differences between the behaviour of the two assimilation schemes. Where the AOD is very weak, SHAMAL-assim6 does not favour the DRI data as much as does SHAMAL-assim1: see the dust loading over Algeria from the 7th-9th, where SHAMAL-assim6 predicts much less ambient dust. Meanwhile where noticeable dust activity is observed (8th and the 9th in the Sahel) SHAMAL-assim6 is more responsive to the DRI data, adjusting the model more to the data. Hence there is more contrast in SHAMAL-assim6, a result of the more well-defined model errors calculated by the sector-based approach.

7.5.3 Maturity: the 8th March

During the 8th, the dust storm weakens slightly, but it is on this day that by far the most dust is transported into the Atlantic. Emission is still very extensive over the region of northern Mali, but is rather weaker than the day before. Sources further east become much more well defined, such as the Grand Erg de Bilma in eastern Niger and the Erg de Djourab in north-eastern Chad (which is generally upwind of the Bodélé), with emissions of ∼100 $\mathrm{g\,m^{-2}\,day^{-1}}$. The eastern Sahara generally has more emission than on the 7th, especially in north-eastern Libya, where the Mediterranean front is pressing on the Cyrenaican coast, bringing wind speeds of over 15 $\mathrm{m\,s^{-1}}$.

The dust storms have been travelling at low altitude (figure 7.30), especially the western and southern plumes. The typical height for these plumes is ∼500 m: this is confirmed by Slingo et al. (2006), who noted that the 'flow follow[ed] the lowest terrain and mov[ed] around the highest topography'. The influence of the topography can be seen in the Algerian storm, which split into two as it was deflected around the Hoggar massif: the larger dust storm travelled south-west to Mali, while the smaller one headed towards Niger. In the assimilation models, strong dust events can actually be seen in the plume height maps: as the storm expands, the plume heights get depressed to under a kilometre (whereas for ambient assimilated dust a more typical plume height is ∼2-3 km). For the southern and western storms, the plumes only seem to ascend at the extremities away from the source regions (into the Atlantic, the Sahel, etc.), where they can ascend to ∼1-2 km. The exception to this is over the north-eastern Sahara, where the plumes can rise to almost 3 km relatively quickly, a consequence of the precipitation which can wash out particles at

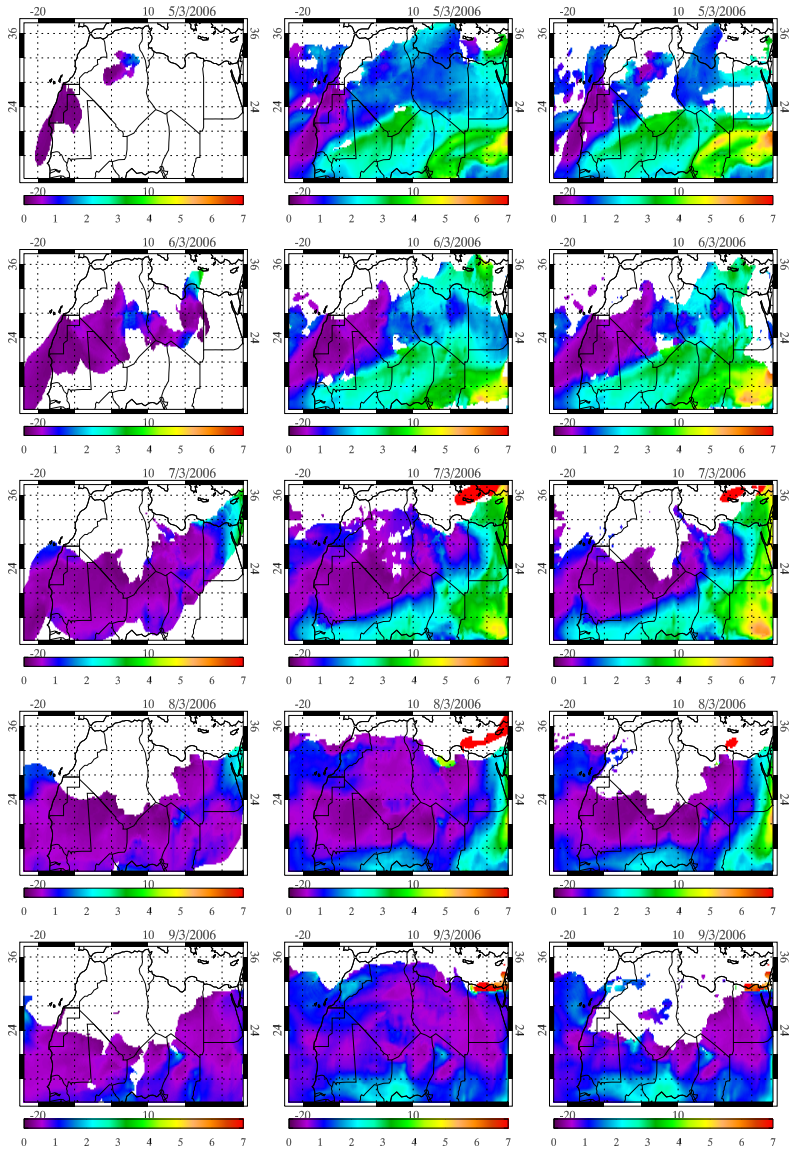

Figure 7.30: Mean daily plume height (km), 5th-9th March, for SHAMAL-r1. Column 1 (first from left): SHAMAL-high. Column 2: SHAMAL-assim1. Column 3: SHAMAL-assim6..

lower altitudes.

The north-eastern Sahara (north-eastern Libya, Egypt, and the eastern Mediterranean) presents a complicated picture of dust activity on the 8th, as shown both by the observations and by the model predictions. The SEVIRI observations (figure 7.24) show that there are several fronts of clouds over the eastern Mediterranean at this time, thickly scattered across the Mediterranean and jutting into north-eastern Libya. To the east, over eastern Egypt and the Levant, there is a particularly thick bank of cloud. The effect of this on the satellite observations is to regard many

pixels in this region to be too noisy: when there is cloud it becomes a substantial problem to obtain the *aerosol* optical depth (in the DRI data set, many of the pixels in this region have missing data). Hence while there may be a major dust storm present, it would be very difficult to observe using satellite instruments because there is so much cloud present. It is only where there are gaps in the cloud (mostly along the Libyan/Egyptian coastal border region) that we can observe the intensity of the dust storm.

The other challenge with the situation over north-eastern Libya and Egypt is that these clouds bring precipitation (figure 7.27), with between 4 and 15 mm of daily rainfall taking place in the Mediterranean just off the North African coast. This juts inland a short distance, with ∼1-10 mm of rainfall taking place over land within ∼50 km of the coast. The same weather system that brings the intensely strong winds ($> 15\ \mathrm{m\,s^{-1}}$) which allow the emission of extremely large quantities of dust over the Great Sand Sea also brings heavy rainfall, which can wash this dust out of the atmosphere and bind the soil together due to its moisture (which inhibits emission). Temporal resolution is therefore a problem here: the ECMWF model winds have a resolution of 6 hours, whereas the precipitation data are coarser, at 24 hours. Generally this is not a problem over the Sahara, but it can be for very specific events such as on the 8th in north-eastern Libya. The problem is that if there is too much of a lag in the model between the arrival of the strong winds and the arrival of the precipitation then the emissions can be over-predicted, possibly by a factor of two or three, depending on the time window. This can lead to excessively high optical depths.

7.5.4 Aftermath: the 9th March

On the 9th, the dust storm comes to the end of its life cycle, though ambient dust does remain over the southern Sahara and the northern Sahel over the following 2-3 days. By this stage the various weather systems have moved on and weakened, leaving behind remnant emissions in northern Mali, northern Niger, Chad, Egypt, but mostly in Sudan over Khartoum. Dust storm activity is now generally confined to the south, with relatively moderate amounts of dust aerosol over Cape Verde, and stretching across Senegal, Mali, Niger, Chad, Sudan, and arcing across Egypt: all of these areas are > 1000 km away from the original source region in northern Algeria. In summation, then, we see that the 8th March event expanded roughly in a southwards radial arc from its origin in Algeria, towards Cape Verde in the west and Israel in the east.

A consequence of the dust storm was the deposition, mapped in figure 7.31, for both dry and

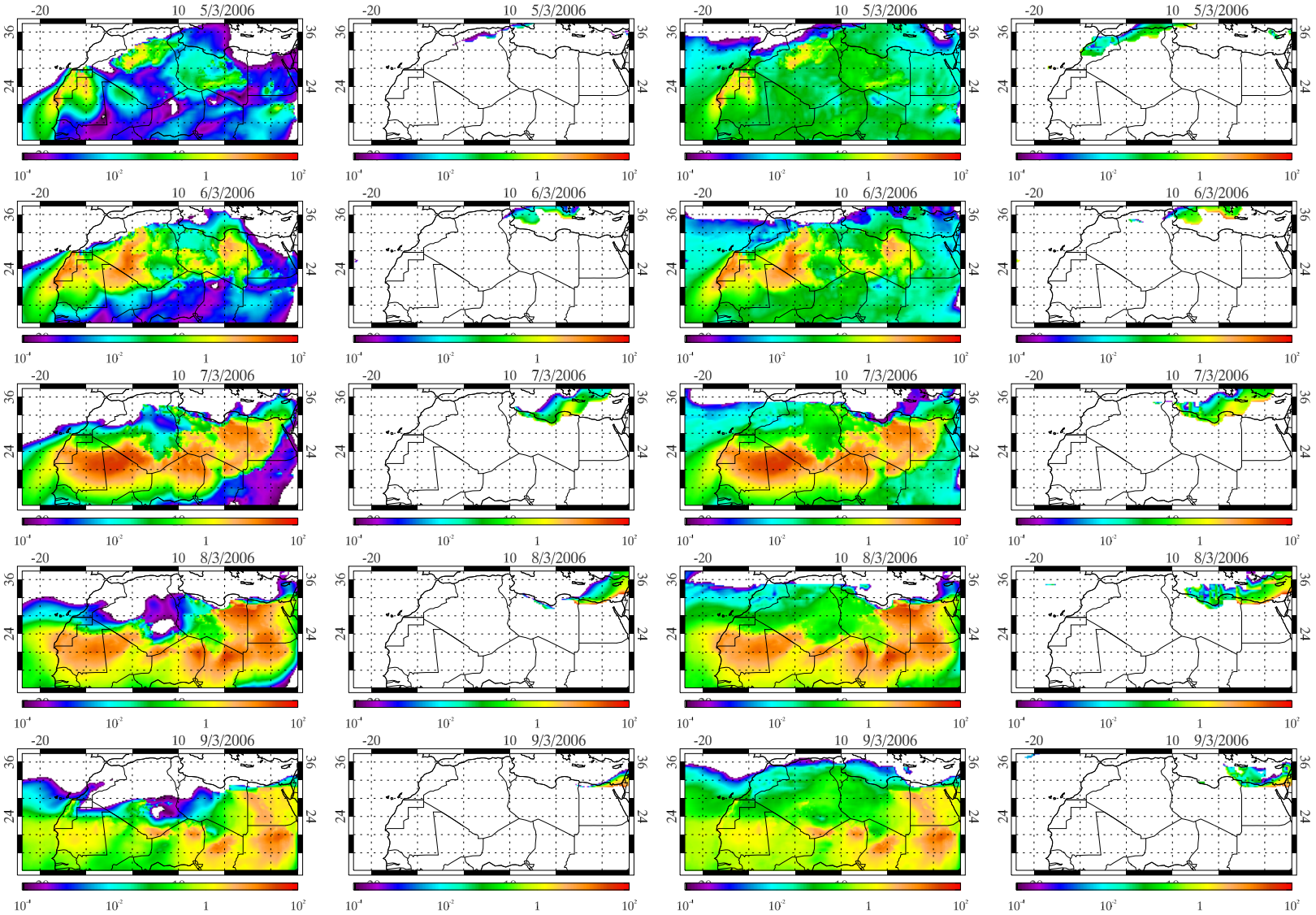

Figure 7.31: Total daily deposition ($\mathrm{g\,m^{-2}\,day^{-1}}$), 5th-9th March, for SHAMAL-r1, and for dry and wet deposition. Columns 1 and 2 (first from left): SHAMAL-high. Columns 3 and 4: SHAMAL-assim1.

wet deposition. These five days saw a substantial fraction of the total deposition for March, with 112.91±2.65 Tg of dust deposited (across the ensemble) during this period, 67.9±2.9% of the total for the month (on 16% of the days). Dry deposition accounts for 110.81±2.45 Tg of deposition, while wet deposition accounts for 2.11±0.37 Tg. Dry deposition takes place mostly over land and near the source regions, though its spatial extent is much larger than the source regions. Wet deposition is concentrated over the Mediterranean, over the Atlas mountains, and there is trace deposition over the North Atlantic. The path of the Mediterranean weather system is shown quite clearly: on the 5th there is wet deposition over the Atlas mountains (in both Algeria and Morocco), it crosses over Tunisia into the Central Mediterranean on the 6th, passing Libya and Egypt over the next couple of days before reaching Israel on the 9th. There can be a very clear distinction between the two modes of deposition: for example, on the 7th, the dividing line between the dry deposition over Libya and the wet deposition over the Mediterranean matches the line followed by the coast. Atlantic deposition also peaks during the 8th March event: across the ensemble, 2.69±0.22 Tg of dust is deposited into the Atlantic during the 5th-9th, 57.6±5.9% of the total for the month.

Dust transport into the Atlantic also peaked during this dust storm: during the 5th-9th, 4.38±0.40 Tg of dust were transported into the Atlantic, 70.2±9.6% of the total for the month. This indicates just how significant are such dust events to the monthly and yearly dust transport out into the Atlantic and beyond to the Americas. Previous work has been carried out using the RegCM3 model (Cavazos et al., 2009) which suggests that the daily dust transport into the Atlantic (at 15 °W, from 0-30 °N) during 6th-11th March was 1.9 Tg day^{-1}; for comparison, SHAMAL suggests that 0.88±0.08 Tg day^{-1} were transported across the line of 18 °W. The SHAMAL predictions are rather lower, one reason for which may be that the SHAMAL transect is further away from the source regions.

7.6 Summary

The two main aims of this chapter were to evaluate the dust assimilation schemes by studying the dust weather in March 2006, and to use these techniques to study the 8th March 2006 event in closer detail.

March 2006 saw substantial dust activity across the Sahara, and during one event on the 5th-9th March a series of inter-connected dust storms crossed the Sahara from the north (near or on the Mediterranean coast), and were carried out to the Atlantic in the west, the Sahel in the south,

and the Red Sea in the east. This storm provides an excellent case study of the dynamics of dust storms, from their inception to their aftermath, from their causes to their consequences. Moreover, given the strength of this event (e.g. 70.2±9.6% of the March transport into the Atlantic was from this period), studies of this event are useful for obtaining a better understanding of the monthly and seasonal cycles of dust activity. We find that emissions peaked on the 7th March (52.3 Tg, out of 172.6-172.7 Tg for the entire month), whereas peak dust transport occurred on the 8th March, when 2.13±0.13 Tg of dust were transported into the Atlantic.

Assimilation of this period provides enhanced estimates of quantities such as dust storm intensity, deposition, transport, and plume heights. The value of this approach has been shown by the improvements in the agreement between the model output and (semi-) independent observations (the RMS differences are reduced from 0.49-0.50 in the background models to 0.30-0.36 in the assimilation models). The correlations have also been improved (only marginally across the domain), but especially in the diurnal cycle (figure 7.21). This gives us extra confidence in the model's ability to predict the bulk transport of dust storm activity.

Amongst the assimilation schemes, it is clear that finding a more accurate estimate of the model uncertainty, on a regional basis, is preferable to using a crude single estimate over the entire domain. A simple approach of finding errors over six qualitatively defined areas (defined by the similarity in the dust activity and by the presence of AERONET sites) in North Africa has provided a quantitative increase in the correlation and decrease in the RMS differences between the model and the observations (correlations from 0.55/0.59 to 0.58/0.62, and RMS differences from 0.324/0.360 to 0.301/0.349). Optimally we would find a local uncertainty for every model grid point, which could perhaps be achieved by using satellite observations (since AERONET observations are too sparse geographically for such resolution to be possible).

Using the assimilation scheme, it has been possible to study the 8th March event in more detail than has been presented before. Estimates of emissions, transport, dust optical depths, plume heights, and deposition, have all been made. During the 5th-8th there was 113.0 Tg of emission, 66.5% of the total for the month. Meanwhile 4.38±0.40 Tg of dust were transported into the Atlantic from the 5th-9th, 70.2±9.6% of the monthly total. There is broad agreement with the work of Cavazos et al. (2009), in terms of the distribution of dust events during this event (for example, the intensity of the north-east Libyan event), while the estimates from SHAMAL for the dust transport are about half those quoted in previous work. The use of DRI data within the assimilation scheme has given improved confidence in the predictions produced by SHAMAL.

Chapter 8

Conclusion

8.1 Summary of the SHAMAL dust model

During the course of this thesis, a North African dust transport model (SHAMAL) has been developed, including three main components: the dust emission model; the dust transport model; and the data assimilation scheme. These three components build consecutively on each other. There have been five main science questions pursued by this project (as introduced in section 1.6):
(1) calculating the yearly and seasonal dust emissions from North Africa, and identifying source regions, as well as testing the various soil data sets and emission schemes;
(2) learning more about the behaviour of dust storms, including calculating dry and wet deposition, as well as plume heights and dust aerosol size distributions;
(3) calculating the mass transport and the deposition into the Atlantic;
(4) quantifying emission, transport, and deposition during the 8th March 2006 dust event;
(5) assessing the utility of including a data assimilation scheme.
These questions have been addressed during the course of this thesis, and are summarised below, with associated uncertainties. These uncertainties are derived from the spread of the predictions from the eight members of the parameter ensemble (consisting of both resolutions of the background model, both assimilation schemes and both possible initial clay size distributions).

8.2 Dust emission

The process of dust emission is the major factor in predicting the spatial distribution of dust storms. Simply put, dust storms tend to be strongest nearest the source regions, or immediately

downwind of the major source regions. The geographical distribution of emissions has a clear annual cycle. The major source areas are in West Africa, in Western Sahara, northern Mauritania, northern Mali, and south-western Algeria all of which are particularly active during the summer months. This compares well with previous observations, e.g. Schepanski et al. (2007). Other major source areas include the Bodélé Depression in Chad (during the winter), and a network of sources stretching from north-eastern Niger to north-eastern Libya (there is one source on the north-eastern Libyan coast which is exceptionally strong during ∼5 events during February-April 2006). Seasonally, spring and summer are the peak seasons for dust emission: during the spring the source regions are quite widespread (though the intensity is only moderate), strengthening during June, before shifting towards the west as the West African sources become very strong in July (when the North African emissions peak, at 233.5 Tg).

Dust emission is greatest where (and when):

(1) there is a high fraction of sand (the largest particles) in the soil available for saltation;

(2) the surface is smooth, i.e. the aerodynamic roughness length is low ($< \sim 0.1$ cm);

(3) the surface wind speeds are reliably strong, or where there can be particularly strong winds (even if just for a handful of events);

(4) the precipitation is very low (precipitation both binds the soil together, inhibiting emission, and washes out atmospheric dust by precipitation scavenging). There can be a very fine line between emissions and precipitation when cold fronts track across source regions, causing substantial emissions ahead of fronts of rainfall.

Peak emissions occur when all four of these conditions are met.

In total, 1225.2 Tg are predicted to have been lifted from the surface of North Africa during 2006, of which 34.8 Tg came from the Bodélé Depression, 24.6 Tg from northern Mauritania, 57.9 Tg from the coastal region of Western Sahara and Mauritania, and 21.9 Tg from north-eastern Libya. This highlights the importance of these sites as dust sources, and agrees well with previous model estimates (Laurent et al., 2008; Ginoux et al., 2004; Zender et al., 2003), between 585 and 1490 $\mathrm{Tg\,year^{-1}}$. The episodic nature of dust storms is also well-attested to by the quantities of emissions: the strongest ten days of emissions during 2006 emitted a total of 311 Tg, out of a yearly total of 1225 Tg. Hence 25.4% of the yearly emissions came from just 2.7% of the days. During 2006, 58% of the emissions were produced by surface wind speeds greater than 10 $\mathrm{m\,s^{-1}}$, the peak of the emissions distribution.

Tests carried out on the emissions produced by two soil data sets (IGBP-DIS and LISA) and

by two emissions schemes (power-law and MB95) indicate that MB95 emissions from LISA soils should be the preferred method of calculating emissions. Power-law schemes are very sensitive to the choice of soil properties, while also allowing emissions over an area that is too large, containing rockier regions which are not good dust sources. On the other hand, the MB95 emission scheme is more physical, taking into account saltation, the principal cause of dust emission to higher altitudes. Meanwhile LISA soils are preferred over the IGBP-DIS soils because the IGBP-DIS soils contain too much clay (a result of the measurements used to produce the data set). Hence the use of the MB95 scheme and of LISA soils is the most physical and reliable configuration of the emissions model.

Note that there are still uncertainties in emissions, especially because the soil properties are still not precisely known: for example, Sahelian sources are not modelled in this work, due to the highly seasonal nature of the surface properties during the year. Moreover, the meteorology is also an area of uncertainty: there can be a factor of 2 difference (section 3.8.3) in the modelled emissions when different meteorological models are used. This indicates a drawback of using the ECMWF Operational Analysis data set, which is that the model can get updated (and so can be an inconsistent data set). On the other hand, the Operational Analysis data set has the advantage over the earlier (and more consistent) ERA-40 data set in that the Operational Analysis model used to produce the data is improved and has a higher resolution than the ERA-40 model. This has an effect on small areas such as the Bodélé where there can be very localised strong winds leading to strong emissions; SHAMAL produces much stronger emissions here (which are more consistent with observations of the region's source strength) than do estimates such as those made by Laurent et al. (2008), who use ERA-40 data.

8.3 Dust storm activity

There are three properties/consequences of dust storms that identify where the most intense dust storms are located: emission, AOD, and deposition. These three are correlated with each other, on the yearly time-scale; emission and deposition have a very high correlation of 0.94, AOD and deposition have a correlation of 0.71, and emission and AOD have a correlation of 0.53. While emission is limited to very well defined areas, AOD shows a much more homogeneous spatial variability, since AOD reflects the distribution and mass of dust in an atmospheric column, during and after transport. Deposition is intermediate between emission and AOD, since deposition is strongest nearest the source regions where the largest dust particles have not ascended far, though

atmospheric transport does smear out the spatial distibution of deposition with respect to the distribution of emission. Deposition is dominated by low-altitude large particles, while AOD is dominated by higher-altitude sub-micron particles. As far as emission is concerned, since there is only a moderate correlation between the emissions and the AOD, it can be concluded that it would be very imprecise to use the AOD (e.g. from satellites) to determine the locations of dust source areas.

During March 2006 to February 2007, 995.0-1001.4 Tg of dust were deposited by dry deposition processes, and 45.3-46.4 Tg were deposited by precipitation scavenging. Dry deposition takes place nearest the source regions (correlation between emission and dry deposition of 0.940), whereas wet deposition tends to occur further away from the sources (correlation of -0.17), particularly over the Atlantic, the Mediterranean, and the Sahel.

Similarly, as with wet deposition, dust plume heights tend to be anti-correlated with source regions (correlation of -0.37) and with deposition regions (-0.47). Nearest the source regions the mass in an atmospheric column is weighted more towards the larger particles which have just been emitted from the surface. More long-lived dust plumes generally tend to be the higher ones, composed of smaller particles less susceptible to gravitational settling, and high enough to avoid turbulent interaction with the surface which also causes deposition; another feature affecting the longevity of high plumes is that they are also more likely to ascend above the cloud layer, rendering them less susceptible to wet deposition. The yearly mean plume height is 2.32-2.39 km. Spatially, the highest plume heights are over the Mediterranean, where they can exceed 6 km.

Particle size (effective radius) is positively correlated with emission (0.49), deposition (0.60), and AOD (0.72), and negatively correlated with plume height (-0.58). In SHAMAL-low ($\bar{r}_{\text{clay}} = 1$ μm) the peak in the emission and aerosol number size distributions is at 0.25 μm, whereas the peak in the AOD size distribution is at 0.63 μm. Meanwhile the peak in the mass loading distribution is at 4.22 μm. As for the distribution of particles with height, it is found that the scale height for clay and the smallest silt particles is 2.5 km, but this drops for the largest particles: for the 7.5 μm radius particles, the scale height is 1.1 km. The choice of clay mean radius in the soil size distribution has a negligible effect on mass properties such as deposition and mass fluxes, but has a significant effect on the AOD: the average AOD for $\bar{r}_{\text{clay}} = 0.5$ μm is double that of $\bar{r}_{\text{clay}} = 1$ μm. Hence the model-observation comparisons and validation is highly sensitive to the choice of soil size distribution. By comparing with AERONET observations (e.g. figure 5.33) and with in-situ measurements of size distributions (e.g. figure 7.14) it appears that the $\bar{r}_{\text{clay}} = 1$ μm distribution

may be more appropriate, since the peaks in the distributions match more closely, in terms of identifying the particle size at which the peaks occur.

Particle sizes have an influence on the scale height of dust in the atmosphere. On the yearly basis, the dust vertical profiles are well approximated by an exponential decrease with height, but these heights are dependent on particle size. For the smallest clay particles, the scale height is ∼2.65 km, which drops off quickly for the largest silt particles to just under 1 km. Extrapolating, we find that particles larger than 55 μm in radius do not tend to rise above an altitude of 10 m, the typical height of the saltation layer.

The model validity has been tested, primarily by comparison with AERONET observations. The dominant feature of these comparisons has been that, while SHAMAL tends to identify and reproduce the major dust storms, it cannot maintain the background dust level that is observed. Hence it tends to be the case that SHAMAL either produces substantial dust events or otherwise very low ambient dust. One possibility is that the deposition processes are too strong, or that the observations are biased towards a higher background aerosol loading (including from other species of aerosol). This feature of SHAMAL suggests that we should trust it most when there are substantial dust events; these are responsible for the bulk of the yearly transport, so this also gives confidence in estimates of properties such as the dust flux into the Atlantic.

8.4 Dust transport and deposition into the Atlantic

Atlantic dust transport and deposition is important for several reasons: firstly, deposited dust can be a fertiliser, both in the Amazon rainforest (phosphates, etc.), and over the oceans, where iron fertilises algae. Atmospheric dust may also influence the development of tropical storms off the coast of West Africa (affecting hurricane activity in North America).

During the year of March 2006 to February 2007, 62.0-64.2 Tg of dust were transported out from the coast of West Africa across the transect of 18 °W, using the SHAMAL-low model. The peak month for dust transport is July (when the West African dust emissions are strongest), during which 22.2 Tg of dust were swept into the Atlantic. During March 2006, 6.16±1.33 Tg (across the eight versions of the ensemble scheme) of dust were calculated to have left the coast of West Africa. Scaled up to the yearly basis, it can be extrapolated that the yearly dust transport is 75.9±16.4 Tg.

In SHAMAL-low, it is predicted that 27.6-27.9 Tg of dust were deposited into the Atlantic, peaking in July (5.68 Tg). During March 2006, 4.71±0.71 Tg of dust were calculated to have been

deposited, so we can make an estimate of 36.16±8.55 Tg for the yearly deposition. Hence, of the order of half the dust that leaves West Africa for the Atlantic is deposited into the east Atlantic, as far west as 24 °W.

8.5 The 8th March 2006 dust event

The dust event on the 8th March 2006 has been extensively studied by satellite instruments, due to the spatial extent of the event, spanning at least 30 ° of longitude, and at least five countries.The 8th March was a day of particularly strong dust emission: 45.2 Tg of dust were emitted that day, compared to the 2006 average daily emission of 3.36 Tg (on only 4 days of the year did the emission exceed 30 Tg). However, the 7th March was even stronger (emitting 52.3 Tg), resulting from an unusually frequent occurrence of strong wind speeds (10-20 $\mathrm{m\,s^{-1}}$). These days were the second and third most active source days during 2006 (the highest was the 23rd February, when 57.6 Tg of dust were emitted).

Per day, the 8th March saw the most dust leave the coast of West Africa during March 2006: 0.88±0.08 $\mathrm{Tg\,day^{-1}}$ of dust were transported, 70.2±9.6% of the total for March 2006. Similarly, 2.69±0.22 Tg of dust was deposited into the Atlantic during the 5th-9th, 57.6±5.9% of the total for the month. Across the domain, 112.91±2.65 Tg of dust was deposited, 67.9±2.9% of the monthly total. This indicates both the strength of this one dust outbreak (and helps to quantify the observed dust transport), and how important just a handful of dust events are for the monthly and yearly dust budgets.

8.6 The value of data assimilation

Satellite data can improve the estimates of dust transport, using the technique of data assimilation. By making use of the observations (and taking into account the limitations of these) the estimates of dust tranport can be made more consistent with the observations, since the observations are used as initial conditions. Hence the results of the assimilation scheme provide estimates for properties that the observations cannot directly measure (e.g. mass fluxes) from satellite measurements that the observations do measure (e.g. optical depth). The assimilation scheme extrapolates what the dust transport, the dust deposition, etc. should be, given the observations.

It can be argued that these estimates are *improved* estimates. The data assimilation scheme constrains the model using the observations, and so this should minimise any model bias. This

makes the model output more consistent with other observations, such as AERONET, and so we should have more confidence in its ability to quantify the actual dust activity. This can be seen by the fact that the background model RMS difference with AERONET (DRI data cannot be used for comparison with the assimilation model, since the assimilation model is not independent of the DRI observations) is 0.497±0.007, whereas the assimilation model RMS difference is 0.334±0.026 (amongst the four versions). This is a substantial improvement in the RMS difference, and shows the extra value added to the model by the observations.

8.7 Directions for future work

One of the most pressing needs for improving model estimates of dust transport is in improving our knowledge of the surface characteristics. Dust emission is sensitive to surface properties such as roughness length and sand-blasting efficiency. There are two general ways in which the soil data can be improved. Firstly, improved parameterisations of the soil properties, which may require further field measurements in source regions. Secondly, improved resolution may well be useful. Currently the soil resolution is 0.25 ° (∼25 km), which may be too coarse for some source regions (wadis, for example, may have a width of only a kilometre or two), and so the dust emission scheme may miss some sources.

A drawback of the soil data set used in SHAMAL is that it does not include soil properties in the Sahel, south of 16 °N, despite the fact that there are numerous known source areas in this region, and which have been measured in sites such as Banizoumbou (Rajot et al., 2008). As a result of this, the SHAMAL model often under-predicts dust loading over the Sahel. A reason why this area may have been omitted from the data set is that the surface properties change during the seasonal cycle (much more so than the northern Sahara, which is dry year-round) as the monsoon comes and goes, causing vegetation to flourish. During the monsoon, the surface roughness length will be rather greater than during the dry season (and hence there should be no emission), and there would be a greater fraction of vegetation in the soil. Since there is no single value of the various soil properties which would be applicable to both the dry and the wet seasons, this region should not be included in a static soil data set (otherwise the emissions and the dust loading could be indicative of the wrong season). An improvement which would allow this region to be included in the soil data set would be to add temporal resolution to the soil data set, for example on the monthly or seasonal time-scale. The properties would change very little over the northern Sahara, but in the Sahel there would be more variability.

Further improvements can be made to the atmospheric components of the SHAMAL model. One of these is the parameterisation of wet deposition, which was crudely calculated by washing out all dust underneath the cloud top when a certain threshold of rainfall was exceeded. In reality, only a fraction of the dust would be washed out at lower rainfall rates: in reality there would be a smoother relationship between rainfall rates and precipitation scavenging. An improvement to the modelled deposition would be to include such a relationship in the wet deposition scheme. However, since dry deposition is the dominant deposition process over the domain (and especially over the Sahara and the source regions), the effects of adjusting the wet deposition may be marginal (and hence has not been included in the SHAMAL model).

The main improvement that could be made to the assimilation scheme is to create an adjoint modelling scheme (as mentioned in section 6.1.4) to identify the source regions and to produce new estimates of the dust emission, using the satellite observations. This would require an accurate and precise inverse modelling scheme, which would also have to take into account sinks and anti-diffusion, both of which could be significant challenges to the accuracy of the model. For this reason (the inherent instability of an inverse modelling scheme) the adjoint model has not been included in the current work. The advantage of using a reliable adjoint model, however, is that the emission is influenced by the observations (and hence produces a more consistent set of values of the aerosol transport), and allows us to find improved values of surface properties, e.g. roughness length.

A simpler improvement that can be made is to run the assimilation scheme over a longer timescale. Using SEVIRI data, which is available for all of 2006, the assimilation scheme could be used to enhance the model estimates of dust activity on the yearly timescale. While the SEVIRI data have higher uncertainties on the observations compared to DRI (which uses other satellite instruments to produce a more complete observational data set), assimilation with SEVIRI should nudge the model towards the observations and enhance the correlation with AERONET.

One of the main advantages that a simple model such as SHAMAL has over more complex and coupled models is its flexibility, its ability to test the effects of varying different parameters quickly and easily. By varying the parameters we can build up a model ensemble. Examples of this in chapter 7 are the use of two different initial soil size distributions, and the use of two assimilation schemes, which vary according to the geographic region of interest. The model ensemble could be extended substantially using many other parameters, for examples by varying the effects of precipitation, the soil properties, the emission schemes, the turbulent dry deposition,

the model resolution, the satellite instruments used for data assimilation (amongst many others), to investigate the consequences of these on dust transport. In so doing, the parameters which the model is most sensitive to can be identified and quantified. Those parameters which the model is found to be the most sensitive to may be those parameters which give the greatest uncertainties in the model simulations. By validating the members of the ensemble against observations from AERONET and from other satellite instruments, we can come to a better understanding of the most accurate configuration of the parameters included in SHAMAL, and why this might be.

As well as improving the model so as to make better estimates of dust sources, sinks, and atmospheric transport, the model could be used to study further aspects of dust storms, as yet unexplored in this thesis. One of these possibilities would be to extend the model westwards (and southwards) across the Atlantic to the Amazon, to measurement sites such as Barbados (Ellis and Merrill, 1995), and to the coast of the US. The main purpose of this study would be to make measurements of Saharan dust deposition over the Amazon, which could indicate just how much dust is deposited there, and when it is deposited on the seasonal basis. Using this information it could be estimated just how significant Saharan dust transport is to the Amazon region, and its provenance in the Sahara (Koren et al. (2006) argue that the primary source is the Bodélé Depression). This method would also allow estimates of dust transport to the Caribbean, as well as more complete estimates of dust deposition into the Atlantic, over a wider area. This has not been included in the SHAMAL model, due to the computational expense required (it would have to go as far west as $\sim$80 °W and $\sim$10 °S, though if the model resolution over the Atlantic and the Americas were degraded, then this might be more feasible).

The model could also be extended northwards, across the Mediterranean into Europe. Particularly over southern Europe, Saharan dust can have a significant impact on local air quality, so estimates of dust deposition and near-surface dust concentrations could indicate the potential severity of the problem. For the same reason, it may also be useful to extend the model domain across the Middle East (including Arabia, Iraq and the Syrian desert as sources), so that the effect of dust storms on air quality throughout the region could be assessed. For example, the July 2009 dust storm that swept Iraq and Iran (figure 1.6) caused a substantial degradation in air quality across the two countries, especially in Baghdad and Tehran (in Tehran this may also have had political implications, since it coincided with anti-government demonstrations and planned strikes; the government closed all public buildings, ostensibly because of the dust pollution, which was mixed with the vehicle pollution that already blights the city's air quality).

Since the model can be extended further north into Europe, then it may also be useful to consider SHAMAL's applications to dust forecasting. To do this, we would require accurate knowledge of the current state of dust in the atmosphere: data assimilation would be carried out over the preceding days, using data from SEVIRI for example, to give us our best guess of the current conditions (i.e. at $t = 0$). As the model moves into the forecasting stage, forecast meteorological data from ECMWF would be required (as opposed to the hindcasts used in the model up to now) to drive the dust forecasts. Meanwhile, the lack of future satellite observations removes the possibility of using satellite data for the purposes of data assimilation; these would be used over the following days for the purposes of model validation only. This forecast will be most reliable over the first few days, the period when the SEVIRI observations are at their most influential. In so doing, warnings could be made of dust storm activity, from the perspective of its implications for local air quality and for aviation, for example.

Further work could also be carried out on the radiative effects of the dust, which would indicate the impact of dust on the heat budget of the atmosphere. Though this project has mainly concerned itself with the physical impacts of dust (deposition over land and the oceans, surface concentrations, etc.), dust also has radiative effects: for example, during the March 2006 dust event, surface temperatures at Niamey dropped by 10 °C (Slingo et al., 2006). By calculating the radiative effects, it could be established what the contribution of Saharan dust to the atmosphere is, and its effect on climate change.

Feedbacks between Saharan dust aerosol and climate change suggest further possible case studies, experimenting with possible scenarios for future (and historic) climate and surface properties over the desert: using such scenarios to calculate the dust mass budget, we can determine the effect of climate change on Saharan dust activity. This would highlight the links between Saharan dust and global climate.

8.8 Overview

The dust transport model SHAMAL has been used to make predictions of dust emission, transport, and deposition, using the technique of data assimilation, centred on the March 2006 test period. Modelling of emissions and of atmospheric transport has shown considerable sensitivity to the surface conditions and the meteorology, but assimilation using DRI satellite data has reduced the uncertainties in the dust loading. These estimates of dust transport indicate the importance of dust storms, particularly in the regional context, but also in a wider context: dust transport into the

Atlantic is substantial, as is dust transport across the Mediterranean. As well as North Africa and the Middle East, other regions such as Europe, the Atlantic, and the Americas can be influenced by Saharan dust.

References

Abdou, W. A., Diner, D. J., Martonchik, J. V., Bruegge, C. J., Kahn, R. A., Gaitley, B. J., and Crean, K. A. (2005). Comparison of coincident Multiangle Imaging Spectroradiometer and Moderate Resolution Imaging Spectroradiometer aerosol optical depths over land and ocean scenes containing Aerosol Robotic Network sites. *Journal of Geophysical Research*, 110(D10S07).

Abed, A. M., Al-Kuisi, M., and Khair, H. A. (2009). Characterization of the Khamaseen (spring) dust in Jordan. *Atmospheric Environment*, 43:2868–2876.

Allen, D. J., Kasibhatla, P., Thompson, A. M., Rood, R. B., Doddridge, B. G., Pickering, K. E., Hudson, R. D., and Lin, S.-J. (1996). Transport-induced interannual variability of carbon monoxide determined using a chemistry and transport model. *Journal of Geophysical Research*, 101(D22):28,655–28,669.

Almeida, M. P., Jr., J. S. A., and Herrmann, H. J. (2006). Aeolian Transport Layer. *Physical Review Letters*, 96(018001).

Andrews, D. G. (2000). *An Introduction to Atmospheric Physics*. Cambridge University Press, Cambridge.

Bagnold, R. A. (1941). *The Physics of Blown Sand and Desert Dunes*. Methuen, London.

Barrot, G. (2010). GlobColour: An EO based service supporting global ocean carbon cycle research. Product User Guide.

Bessagnet, B., Hodzic, A., Vautard, R., Beekmann, M., Cheinet, S., Honoré, C., Liousse, C., and Rouil, L. (2004). Aerosol modeling with CHIMERE- preliminary evaluation at the continental scale. *Atmospheric Environment*, 38:2803–2817.

Blackadar, A. K. and Tennekes, H. (1968). Asymptotic Similarity in Neutral Barotropic Planetary Boundary Layers. *Journal of Atmospheric Science*, 25:1015–1020.

Bousserez, N., Attié, J. L., Peuch, V. H., Michou, M., Pfister, G., Edwards, D., Emmons, L., Mari, C., Barret, B., Arnold, S. R., Heckel, A., Richter, A., Schlager, H., Lewis, A., Avery, M., Sachse, G., Browell, E. V., and Hair, J. W. (2007). Evaluation of the MOCAGE chemistry transport model during the ICARTT/ITOP experiment. *Journal of Geophysical Research*, 112(D10S42).

Bouttier, F. and Courtier, P. (1999). Data assimilation concepts and methods. *ECMWF*, http://www.ecmwf.int/newsevents/training/lecture_notes/pdf_files/ASSIM/Ass_cons.pdf.

Brasseur, G. P. and Madronich, S. (1992). *Chemistry-transport models*, chapter 15. Cambridge University Press, Cambridge, UK.

Brown, R. A. (1974). *Analytical Methods in Planetary Boundary-Layer Modelling*. Adam Hilger Ltd, 29 King Street, London.

Callot, Y., Marticorena, B., and Bergametti, G. (2000). Geomorphologic approach for modelling the surface features of arid environments in a model of dust emission: application to the Sahara desert. *Geodinamica Acta*, 13:245–270.

Carboni, E., Thomas, G., Sayer, A., Poulsen, C., Grainger, D., Siddans, R., Ahn, C., Antoine, D., Bevan, S., Braak, R., Brindley, H., DeSouza-Machado, S., Deuze, J., Diner, D., Ducos, F., Grey, W., Hsu, C., Kalashnikova, O. V., Kahn, R., Salustro, C., Tanré, D., Torres, O., and B.Veihelmann (2009). Desert dust satellite retrieval intercomparison. In *European Geosciences Union*.

Cavazos, C., Todd, M. C., and Schepanski, K. (2009). Numerical model simulation of the Saharan dust event of 6-11 March 2006 using the Regional Climate Model version 3 (RegCM3). *Journal of Geophysical Research*, 114(D12109).

Chatenet, B., Marticorena, B., Gomes, L., and Bergametti, G. (1996). Assessing the microped size distributions of desert soils erodible by wind. *Sedimentology*, 43:901–911.

Chin, M., Ginoux, P., Kinne, S., Torres, O., Holben, B. N., Duncan, B. N., Martin, R. V., Logan, J. A., Higurashi, A., and Nakajima, T. (2002). Tropospheric Aerosol Optical Thickness from the GOCART Model and Comparisons with Satellite and Sun Photometer Measurements. *Journal of Atmospheric Science*, 59:461–483.

Chin, M., Rood, R. B., Lin, S.-J., Muller, J.-F., and Thompson, A. M. (2000). Atmospheric sulfur cycle simulated in the global model GOCART: Model description and global properties. *Journal of Geophysical Research*, 105(D20):24,671–24,687.

Claquin, T. (1999). *Modelisation de la mineralogie et du forcage radiatif des poussieres desertiques*. PhD thesis, Univ. of Hamburg, Hamburg, Germany.

Curier, L., de Leeuw, G., Kolmonen, P., Sundström, A.-M., Sogacheva, L., and Bennouna, Y. (2009). *Aerosol retrieval over land using the (A)ATSR dual-view algorithm*, chapter 5. Springer-Praxis Publishing Ltd, Chichester, UK.

D'Almeida, G. A. (1986). A Model for Saharan Dust Transport. *Journal of Applied Meteorology*, 25:903–916.

D'Almeida, G. A. and Schütz, L. (1983). Number, Mass and Volume Distributions of Mineral Aerosol and Soils of the Sahara. *Journal of Applied Meteorology*, 22:233–243.

Dubovik, O. and King, M. D. (2000). A flexible inversion algorithm for retrieval of aerosol optical properties from Sun and sky radiance measurements. *Journal of Geophysical Research*, 105(D16):20,673–20,696.

Ellis, W. G. and Merrill, J. T. (1995). Trajectories for Saharan Dust Transported to Barbados Using Stokes' Law to Describe Gravitational Settling. *Journal of Applied Meteorology*, 34:1716–1726.

Engelstaedter, S., Tegen, I., and Washington, R. (2006). North African dust emissions and transport. *Earth-Science Reviews*, 79:73–100.

Engelstaedter, S. and Washington, R. (2007a). Atmospheric controls on the annual cycle of North African dust. *Journal of Geophysical Research*, 112(D03103).

Engelstaedter, S. and Washington, R. (2007b). Temporal controls on global dust emissions: The role of surface gustiness. *Geophysical Research Letters*, 34(L15805).

Errico, R. M. (1997). What is an Adjoint Model? *Bulletin of the American Meteorological Society*, 78(11):2577–2591.

Fécan, F., Marticorena, B., and Bergametti, G. (1999). Parameterization of the increase of the aeolian erosion threshold wind friction velocity due to soil moisture for arid and semi-arid areas. *Annales Geophysicae*, 17:149–157.

Fernald, F. G., Herman, B. M., and Reagan, J. A. (1972). Determination of Aerosol Height Distributions by Lidar. *Journal of Applied Meteorology*, 11(3):482–489.

Forster, P., Ramaswamy, V., Artaxo, P., Berntsen, T., Betts, R., Fahey, D. W., Haywood, J., Lean, J., Lowe, D. C., Myhre, G., Nganga, J., Prinn, R., Raga, G., Schulz, M., and Dorland, R. V. (2007). *Changes in Atmospheric Constituents and in Radiative Forcing*, chapter 2. Cambridge University Press, Cambridge, United Kingdom and New York, NY, USA.

Giles, J. (2005). The dustiest place on earth. *Nature*, 434:816–819.

Gillette, D. A. (1979). *Environmental factors affecting dust emission by wind erosion*, pages 71–94. John Wiley, New York.

Ginoux, P., Chin, M., Tegen, I., Prospero, J. M., Holben, B., Dubovik, O., and Lin, S.-J. (2001). Sources and distributions of dust aerosols simulated with the GOCART model. *Journal of Geophysical Research*, 106(D17):20,255–20,273.

Ginoux, P., Prospero, J. M., Torres, O., and Chin, M. (2004). Long-term simulation of global dust distribution with the GOCART model: correlation with North Atlantic Oscillation. *Environmental Modelling and Software*, 19:113–128.

Ginoux, P. and Torres, O. (2003). Empirical TOMS index for dust aerosol: Applications to model validation and source characterization. *Journal of Geophysical Research*, 108(D17).

Goudie, A. S. and Middleton, N. J. (2006). *Desert Dust in the Global System*. Springer, Heidelburg, Germany.

Grini, A., Myhre, G., Zender, C. S., and Isaksen, I. S. A. (2005). Model simulation of dust sources and transport in the global atmosphere. Effects of soil erodibility and wind speed variability. *Journal of Geophysical Research*, 110(D02205).

Grini, A., Tulet, P., and Gomes, L. (2006). Dusty weather forecasts using the MesoNH mesoscale atmospheric model. *Journal of Geophysical Research*, 111(D19205).

Grini, A. and Zender, C. S. (2004). Roles of saltation, sandblasting, and wind speed variability on mineral dust aerosol size distribution during the Puerto Rican Dust Experiment (PRIDE). *Journal of Geophysical Research*, 109(D07202).

Guerzoni, S., Molinaroli, E., and Chester, R. (1997). Saharan dust inputs to the western Mediterranean sea: depositional patterns, geochemistry and sedimentological implications. *Deep-Sea Research II*, 44(3-4):631–654.

Hall, F. G., Collatz, G., Los, S., de Colstoun, E. B., and Landis, D. (2005). ISLSP Initiative II. *NASA*, DVD/CD-ROM.

Haltiner, G. J. and Williams, R. T. (1980). *Numerical prediction and dynamic meteorology*. John Wiley & Sons, New York.

Haustein, K., Perez, C., Baldasano, J. M., Muller, D., Tesche, M., Schladitz, A., Esselborn, M., Weinzierl, B., Kandler, K., and von Hoyningen-Huene, W. (2009). Regional dust model performance during SAMUM 2006. *Geophysical Research Letters*, 36(L03812).

Heinold, B., Helmert, J., Hellmuth, O., Wolke, R., Ansmann, A., Marticorena, B., Laurent, B., and Tegen, I. (2007). Regional modeling of Saharan dust events using LM-MUSCAT: Model description and case studies. *Journal of Geophysical Research*, 112(D11204).

Heintzenberg, J. (2009). The SAMUM-1 experiment over Southern Morocco: overview and introduction. *Tellus*, 61(1):2–11.

Holben, B. N., Eck, T. F., Slutsker, I., Tanré, D., Buis, J. P., Setzer, A., Vermote, E., Reagan, J. A., Kaufman, Y. J., Nakajima, T., Lavenu, F., Jankowiak, I., and Smirnov, A. (1998). AERONET- A Federated Instrument Network and Data Archive for Aerosol Characterization. *Remote Sensing of Environment*, 66(1):1–16.

Holtslag, A. A. M. and Boville, B. A. (1993). Local Versus Nonlocal Boundary-Layer Diffusion in a Global Climate Model. *Journal of Climate*, 6:1825–1842.

Iversen, J. D. and White, B. R. (1982). Saltation threshold on Earth, Mars and Venus. *Sedimentology*, 29:111–119.

Jaenicke, R. (1993). *Tropospheric Aerosols*, chapter 1. Academic Press, San Diego, California.

Jickells, T. D., An, Z. S., Andersen, K. K., Baker, A. R., Bergametti, G., Brooks, N., Cao, J. J., Boyd, P. W., Duce, R. A., Hunter, K. A., Kawahata, H., Kubilay, N., laRoche, J., Liss, P. S., Mahowald, N., Prospero, J. M., Ridgwell, A. J., Tegen, I., and Torres, R. (2005). Global Iron Connections Between Desert Dust, Ocean Biogeochemistry, and Climate. *Science*, 308(67):67–71.

Justus, C. G., Hargreaves, W. R., Mikhail, A., and Graber, D. (1978). Methods for estimating wind speed frequency distributions. *Journal of Applied Meteorology*, 17:350–353.

Kallos, G., Papadopoulos, A., Katsafados, P., and Nickovic, S. (2006). Transatlantic Saharan dust transport: Model simulation and results. *Journal of Geophysical Research*, 111(D09204).

Kalma, J. D., Speight, J. G., and Wasson, R. J. (1988). Potential wind erosion in Australia: a continental perspective. *International Journal of Climatology*, 8:411–428.

Kalnay, E. (2003). *Atmospheric Modeling, Data Assimilation and Predictability*. Cambridge University Press, Cambridge.

Kandler, K., Schütz, L., Deutscher, C., Ebert, M., Hofmann, H., Jäckel, S., Jaenicke, R., Knippertz, P., Lieke, K., Massling, A., Petzold, A., Schladitz, A., Weinzierl, B., Wiedensohler, A., Zorn, S., and Weinbruch, S. (2009). Size distribution, mass concentration, chemical and mineralogical composition and derived optical parameters of the boundary layer aerosol at Tinfou, Morocco, during SAMUM 2006. *Tellus B*, 61(1):32–50.

Kasten, F. (1968). Falling Speed of Aerosol Particles. *Journal of Applied Meteorology*, 7:944–947.

Kaufman, Y. J., Koren, I., Remer, L. A., Tanré, D., Ginoux, P., and Fan, S. (2005). Dust transport and deposition observed from the Terra-Moderate Resolution Imaging Spectroradiometer (MODIS) spacecraft over the Atlantic Ocean. *Journal of Geophysical Research*, 110(D10S12).

Kaufman, Y. J., Tanré, D., Remer, L. A., Vermote, E. F., Chu, A., and Holben, B. N. (1997). Operational remote sensing of tropospheric aerosol over land from EOS moderate resolution imaging spectroradiometer. *Journal of Geophysical Research*, 102(D14):17,051–17,067.

Knippertz, P., Deutscher, C., Kandler, K., Muller, T., Schulz, O., and Schütz, L. (2007). Dust mobilization due to density currents in the Atlas region: Observations from the Saharan Mineral Dust Experiment 2006 field campaign. *Journal of Geophysical Research*, 112(D21109).

Knippertz, P. and Todd, M. C. (2010). The central west Saharan dust hot spot and its relation to African easterly waves and extratropical disturbances. *Journal of Geophysical Research*, 115(D12117).

Kokhanovsky, A. A. (2008). *Aerosol optics: light absorption and scattering by particles in the atmosphere*. Springer- Praxis Publishing Ltd, Chichester, UK.

Koren, I., Kaufman, Y. J., Washington, R., Todd, M. C., Rudich, Y., Martins, J. V., and Rosenfeld, D. (2006). The Bodélé depression: a single spot in the Sahara that provides most of the dust to the Amazon forest. *Environmental Research Letters*, 1.

Laurent, B., Marticorena, B., Bergametti, G., Léon, J. F., and Mahowald, N. M. (2008). Modeling mineral dust emissions from the Sahara using new surface properties and soil database. *Journal of Geophysical Research*, 113(D14218).

Levy, R. C. (2009). *The dark-land MODIS collection 5 aerosol retrieval: algorithm development and product evaluation*, chapter 2. Springer- Praxis Publishing Ltd, Chichester, UK.

Lin, S.-J. and Rood, R. B. (1996). Multidimensional flux-form semi-Lagrangian transport schemes. *Monthly Weather Review*, 124:2046–2070.

Liou, K. N. (1980). *An Introduction to Atmospheric Radiation*. Academic Press (An imprint of Elsevier Science), San Diego.

Liousse, C., Galy-Lacaux, C., Assamoi, E., Ndiaye, A., Diop, B., Cachier, H., Doumbia, T., Gueye, P., Yoboué, V., Lacaux, J.-P., Guinot, B., Guillaume, B., Rosset, R., Castera, P., Gardrat, E., Zouiten, C., Jambert, C., Diouf, A., Koita, O., Baeza, A., Annesi-Maesano, I., Didier, A., Audry, S., and Konaré, A. (2009). Integrated Focus on West African cities (Cotonou, Bamako, Dakar, Ouagadougou, Abidjan, Niamey): Emissions, Air quality and Health Impacts of gases and aerosols. In *Third International AMMA Conference*.

Mabbutt, J. A. (1977). *Desert Landforms*. The MIT Press, Cambridge, Masachusetts.

Mahowald, N. M., Baker, A. R., Bergametti, G., Brooks, N., Duce, R. A., Jickells, T. D., Kubilay, N., Prospero, J. M., and Tegen, I. (2005). Atmospheric global dust cycle and iron inputs to the ocean. *Global Biogeochemical Cycles*, 19(GB4025).

Marticorena, B. and Bergametti, G. (1995). Modeling the atmospheric dust cycle: 1. Design of a soil-derived dust emission scheme. *Journal of Geophysical Research*, 100(D8):16,415–16,430.

Marticorena, B., Bergametti, G., and Aumont, B. (1997). Modeling the atmospheric dust cycle: 2. Simulation of Saharan dust sources. *Journal of Geophysical Research*, 102(D4):4387–4404.

Marticorena, B., Chazette, P., Bergametti, G., Dulac, F., and Legrand, M. (2004). Mapping the aerodynamic roughness length of desert surfaces from the POLDER/ADEOS bi-directional reflectance product. *International Journal of Remote Sensing*, 25(3):603–626.

Martonchik, J. V., Kahn, R. A., and Diner, D. J. (2009). *Retrieval of aerosol properties over land using MISR observations*, chapter 9. Springer- Praxis Publishing Ltd, Chichester, UK.

McKendry, I. G., Strawbridge, K. B., O'Neill, N. T., Macdonald, A. M., Liu, P. S. K., Leaitch, W. R., Anlauf, K. G., Jaegle, L., Fairlie, T. D., and Westphal, D. L. (2007). Trans-Pacific transport of Saharan dust to western North America: A case study. *Journal of Geophysical Research*, 112(D01103).

McTainsh, G. H., Nickling, W. G., and Lynch, A. W. (1997). Dust deposition and particle size in Mali, West Africa. *Catena*, 29:307–322.

Meehl, G. A. (1992). *Global coupled models: atmosphere, ocean, sea ice*, chapter 17. Cambridge University Press, Cambridge, UK.

Menut, L. (2008). Sensitivity of hourly Saharan dust emissions to NCEP and ECMWF modeled wind speed. *Journal of Geophysical Research*, 113(D16201).

Middleton, N. J. (1985). Effect of drought on dust production in the Sahel. *Nature*, 316:431–434.

Middleton, N. J. and Goudie, A. S. (2001). Saharan dust: sources and trajectories. *Transactions of the Institute of British Geographers*, NS 26:165–181.

Mie, G. (1908). Beiträge zur Optik trüber Medien speziell kolloidaler Metallösungen. *Ann Phys.*, 25:377–445.

Miller, A. A. (1961). *Climatology.* Methuen, London.

Miller, R. L., Cakmur, R. V., Perlwitz, J., Geogdzhayev, I. V., Ginoux, P., Koch, D., Kohfeld, K. E., Prigent, C., Rudey, R., Schmidt, G. A., and Tegen, I. (2006). Mineral dust aerosols in the NASA Goddard Institute of Space Sciences ModelE atmospheric circulation model. *Journal of Geophysical Research*, 111(D06208).

Munoz, O., Volten, H., Hovenier, J. W., Nousiainen, T., Muinonen, K., Guirado, D., Moreno, F., and Waters, L. B. F. M. (2007). Scattering matrix of large Saharan dust particles: Experiments and computations. *Journal of Geophysical Research*, 112(D13215).

Myhre, G., Grini, A., Haywood, J. M., Stordal, F., Chatenet, B., Tanré, D., Sundet, J. K., and Isaksen, I. S. A. (2003). Modeling the radiative impact of mineral dust during the Saharan Dust Experiment (SHADE) campaign. *Journal of Geophysical Research*, 108(D18).

Nickovic, S., Kallos, G., Papadopoulos, A., and Kakaliagou, O. (2001). A model for prediction of desert dust cycle in the atmosphere. *Journal of Geophysical Research*, 106(D16):18,113–18,129.

Niu, T., Gong, S. L., Zhu, G. F., Liu, H. L., Hu, X. Q., Zhou, C. H., and Wang, Y. Q. (2008). Data assimilation of dust aerosol observations for the CUACE/dust forecasting system. *Atmospheric Chemistry and Physics*, 8:3473–3482.

Prandtl, L. (1935). *The mechanics of viscous fluids*, volume III, pages 34–200. Springer, Berlin.

Prospero, J. M., Ginoux, P., Torres, O., Nicholson, S. E., and Gill, T. E. (2002). Environmental characteristics of global sources of atmospheric soil dust identified with the Nimbus 7 Total Ozone Mapping Spectrometer (TOMS) Absorbing Aerosol Product. *Reviews of Geophysics*, 40(1).

Rajot, J. L., Formenti, P., Alfaro, S., Desboeufs, K., Chevaillier, S., Chatenet, B., Gaudichet, A., Journet, E., Marticorena, B., Triquet, S., Maman, A., Mouget, N., and Zakou, A. (2008). AMMA dust experiment: An overview of measurements performed during the dry season special observation period (SOP0) at the Banizoumbou (Niger) supersite. *Journal of Geophysical Research*, 113(D00C14).

Rasch, P. J., Mahowald, N. M., and Eaton, B. E. (1997). Representations of transport, convection, and the hydrologic cycle in chemical transport models: Implications for the modeling of short-lived and soluble species. *Journal of Geophysical Research*, 102(D23):28,127–28,138.

Sayer, A. M. (2008). *Aerosol Remote Sensing Using AATSR*. PhD thesis, University of Oxford.

Schepanski, K., Tegen, I., Laurent, B., Heinold, B., and Macke, A. (2007). A new Saharan dust source activation frequency map derived from MSG-SEVIRI IR-channels. *Geophysical Research Letters*, 34(L18803).

Seinfeld, J. H. and Pandis, S. N. (2006). *Atmospheric Chemistry and Physics: from Air Pollution to Climate Change*. John Wiley Sons, Inc., Hoboken, New Jersey, USA.

Selvam, A. M. (2007). *Chaotic Climate Dynamics*. Luniver Press.

Shao, Y. (2000). *Physics and Modelling of Wind Erosion*. Kluwer Academic Publishers, Dordrecht, The Netherlands.

Shao, Y. (2001). A model for mineral dust emission. *Journal of Geophysical Research*, 106(D17):20,239–20,254.

Shao, Y. (2004). Simplification of a dust emission scheme and comparison with data. *Journal of Geophysical Research*, 109(D10202).

Shao, Y., Raupach, M. R., and Findlater, P. A. (1993). Effect of Saltation Bombardment on the Entrainment of Dust by Wind. *Journal of Geophysical Research*, 98(D7):12,71912,726.

Slingo, A., Ackerman, T. P., Allan, R. P., Kassianov, E. I., McFarlane, S. A., Robinson, G. J., Barnard, J. C., Miller, M. A., Harries, J. E., Russell, J. E., and Dewitte, S. (2006). Observations of the impact of a major Saharan dust storm on the atmospheric radiation balance. *Geophysical Research Letters*, 33(L24817).

Solmon, F., Chuang, P. Y., Meskhidzhe, N., and Chen, Y. (2009). Acidic processing of mineral dust iron by anthropogenic compounds over the north Pacific Ocean. *Journal of Geophysical Research*, 114(D02305).

Sow, M., Alfaro, S. C., Rajot, J. L., and Marticorena, B. (2009). Size resolved dust emission fluxes measured in Niger during 3 dust storms of the AMMA experiment. *Atmospheric Chemistry and Physics*, 9(12):3881–3891.

Stier, P., Feichter, J., Kinne, S., Kloster, S., Vignati, E., Wilson, J., Ganzeveld, L., Tegen, I., Werner, M., Balkanski, Y., Schulz, M., Boucher, O., Minikin, A., and Petzold, A. (2005). The aerosol-climate model ECHAM5-HAM. *Atmospheric Chemistry and Physics*, 5:1125–1156.

Swap, R., Garstang, M., Greco, S., Talbot, R., and Kallberg, P. (1992). Saharan dust in the Amazon Basin. *Tellus*, 44B:133–149.

Tanskanen, A., Krotkov, N. A., Herman, J. R., , and Arola, A. (2006). Surface Ultraviolet Irradiance From OMI. *IEEE Transactions on Geoscience and Remote Sensing*, 44(5):1267–1271.

Tegen, I. and Fung, I. (1994). Modeling of mineral dust in the atmosphere: Sources, transport, and optical thickness. *Journal of Geophysical Research*, 99(D11):22,897–22,914.

Tegen, I., Harrison, S. P., Kohfeld, K., Prentice, I. C., Coe, M., and Heimann, M. (2002). Impact of vegetation and preferential source areas on global dust aerosol: Results from a model study. *Journal of Geophysical Research*, 107(D21).

Thomas, G. E., Carboni, E., Sayer, A. M., Poulsen, C. A., Siddans, R., and Grainger, R. G. (2009). *Oxford-RAL Aerosol and Cloud (ORAC): aerosol retrievals from satellite radiometers*, chapter 7. Springer- Praxis Publishing Ltd, Chichester, UK.

Todd, M. C., Washington, R., Martins, J. V., Dubovik, O., Lizcano, G., MBainayel, S., and Engelstaedter, S. (2007). Mineral dust emission from the Bodélé Depression, northern Chad, during BoDEx 2005. *Journal of Geophysical Research*, 112(D06207).

Troen, I. B. and Mahrt, L. (1986). A simple model of the atmospheric boundary layer: sensitivity to surface evaporation. *Boundary-Layer Meteorology*, 37:129–148.

Van de Hulst, H. C. (1957). *Light Scattering by Small Particles*. John Wiley & Sons, Inc., New York.

Vuolo, M. R., Chepfer, H., Menut, L., , and Cesana, G. (2009). Comparison of mineral dust layers vertical structures modeled with CHIMERE-DUST and observed with the CALIOP lidar. *Journal of Geophysical Research*, 114(D09214).

Warner, T. T. (2004). *Desert Meteorology*. Cambridge University Press, Cambridge, UK.

Warren, A., Chappell, A., Todd, M. C., Bristow, C., Drake, N., Engelstaedter, S., Martins, V., M'bainayel, S., and Washington, R. (2007). Dust-raising in the dustiest place on earth. *Geomorphology*, 92:25–37.

Washington, R. and Todd, M. C. (2005). Atmospheric controls on mineral dust emission from the Bodélé Depression, Chad: The role of the low level jet. *Geophysical Research Letters*, 32(L17701).

Washington, R., Todd, M. C., Lizcano, G., Tegen, I., Flamant, C., Koren, I., Ginoux, P., Engelstaedter, S., Bristow, C. S., Zender, C. S., Goudie, A. S., Warren, A., and Prospero, J. M. (2006). Links between topography, wind, deflation, lakes and dust: The case of the Bodélé Depression, Chad. *Geophysical Research Letters*, 33(L09401).

White, B. R. (1979). Soil Transport by Winds on Mars. *Journal of Geophysical Research*, 84(89):4643–4651.

Zakey, A. S., Solmon, F., and Giorgi, F. (2006). Implementation and testing of a desert dust module in a regional climate model. *Atmospheric Chemistry and Physics*, 6:4687–4704.

Zender, C. S., Bian, H., and Newman, D. (2003). Mineral Dust Entrainment and Deposition (DEAD) model: Description and 1990s dust climatology. *Journal of Geophysical Research*, 108(D14).

Zobler, L. (1986). A world soil file for global climate modeling. *NASA Tech. Memo.*, 87802.